LASER SURFACE ENGINEERING FOR IMPROVED WEAR RESISTANCE

by

Nicola Mckeown

September 1992

A thesis submitted for the degree of Doctor of Philosophy of the University of Liverpool

Laser Division
Department of Mechanical Engineering

University of Liverpool
Liverpool L69 3BX

Declaration

I declare that no part of this thesis has been submitted in support of any other qualification

Signed 

Nicola McKeown

September 1992

To my parents, Joyce and Kevin McKeown
and my husband, Steven Plant

LASER SURFACE ENGINEERING FOR IMPROVED WEAR RESISTANCE

ABSTRACT

Laser transformation hardening using a 2kW continuous wave CO laser was used to investigate the hardening characteristics of two engine valve steels, EN24 - 1 Ni Cr Mo and EN52, a high chromium steel.

The percentage absorptivity of the steel surfaces to 10.6μm radiation was measured experimentally for a number of different surface coatings and the optimum conditions for case hardening determined. The results were compared with data calculated using an empirical, an analytical, and a finite difference model. Comparison of experimental results with the model showed fairly good correlation for the finite difference and analytical models but poor correlation with the simple empirical model. Modification of the finite difference model to allow for the finite component size in this study yielded excellent correlation between theory and experiment. The spheroidised carbide starting structure of these steels resulted in more uniform hardening than the usual ferrite/pearlite structure. Analysis of the as-hardened microstructures revealed the presence of undissolved Fe-Cr carbides in the case of EN52 steel, whereas the carbides were completely dissolved in the hardened zone for EN24.

Wear testing of laser hardened valve stems under simulated engine conditions has been carried out and the results compared with previous tests on induction hardened samples. The laser hardened samples exhibit excellent wear characteristics. Similar wear tests on stem lengths hardened in a spiral pattern produced high resistance to wearing.

Blown powder laser cladding was also investigated for application to valve seat faces, with a view to improving the wear properties. Stellite 6, the conventional hardfacing material for this application was used to clad premachined valve seat faces. The process was successful and resulted in the production of uniform low dilution layers. The process was extended to investigate Ni-based Stellite 35 and to incorporate ceramic particles into the melt pool via particle injection.

Wear testing of the clad layers revealed improved wear characteristics, especially on addition of chromia or silicon carbide powders to the Stellite 35 alloy.

ACKNOWLEDGEMENTS

There are a number of people whom I would like to thank for their help, guidance and support during the course of this work.

Firstly, my academic and industrial supervisors, Prof. W.M.Steen, Dr. G. McCartney and Dr. D.R.Bury (T&N Technology Ltd.) whose advice and encouragement have been invaluable.

My thanks also to Arthur.Green and Pat Mitchell (Materials Science), Graham Nurse (T&N Technology), Steve, Jack and Andy for their patience and help in the laboratory and to Heather Garnett, Andrea Jones and Jenny Kaye for their secretarial support.

I am also most grateful to my friends in the Laser Group, Materials Science and at home - especially Karen Williams, Sarah Sharkey (fellow suffragettes), Angela Hampton (sympathiser) and the girls - who have kept me sane and sometimes sober.

Finally, my special thanks go to my parents who have made many sacrifices to allow me the privilege of such an education, to my husband Steve who has endured endless sleepless nights and to my sister Kerry for her encouragement and chicken tagliatelli. Finally thanks Beryl for the sunday roast during the busier weekends..

Thanks are also due to the Science and Engineering Research Council and to T&N Technology for funding this research project.

Contents

	Abstract	i
	Acknowledgements	ii
	Contents	iii
	List of Figures	vi
	List of Tables	ix
	Nomenclature	x
	General Introduction	1

Chapter 1
The Engine Valve - a Metallurgists View

1.1	Engine operation - the basic principles	2
1.2	The poppet valve	2
1.3	Valve failure	3
1.4	Valve operating mechanism	4
1.5	Valve design considerations	4
	1.5.1 Valve temperature effects	4
	1.5.2 Valve stress effects	5
	1.5.3 Volumetric efficiency effects	6
	1.5.4 Other effects	6
1.6	Valve production	6
	1.6.1 Material selection	6
	1.6.2 Material properties	7
	1.6.3 Valve manufacture	8
1.7	Towards the future	9

Chapter 2
Literature Review. Surface Treatment for Wear Resistance

2.1	Introduction	15
2.2	The CO2 laser	15
2.3	Output properties of the CO2 laser	16
	2.3.1 Mode structure	17
	2.3.2 Beam radius	17
	2.3.3 Polarisation	18
2.4	Interaction of the CO2 laser with materials	18
2.5	Reflectivity	19
	2.5.1 Wavelength of the incident light	19
	2.5.2 Angle of incidence of laser light	20
	2.5.3 Temperature	20
	2.5.4 Surface condition	21
	2.5.5 Use of surface coatings	21
	2.5.6 Surface oxidation	22
2.6	The nature of wear	22
	2.6.1 Wear resistant materials-selection & properties of powders	25
	2.6.2 Wear resistance of laser treated surfaces	27
2.7	Surface Modification to resist wear	29
	2.7.1 Laser transformation hardening	29
	2.7.2 Laser cladding	30
	2.7.3 Associated laser surface treatments	30
2.8	Other techniques for surface hardening	33
	2.8.1 Hardening treatments involving thermal transformation	33
	2.8.2 Treatments involving diffusion of elements at surface	36
	2.8.3 Metalliding and similar techniques	39
	2.8.4 Surface plating techniques	40
2.9	Other techniques for wear resistant coating production	40
	2.9.1 Oxy-acetylene welding	40
	2.9.2 Tungsten inert gas hardfacing	41
	2.9.3 Plasma transferred arc welding	41
	2.9.4 Spraying/fusion hardfacing	42
2.10	Metallurgical considerations of laser surface hardening	42
	2.10.1 Mechanism of transformation hardening ferrous materials	42
	2.10.2 The Fe-C system	42

2.10.3 The Fe-C-Cr system 43
2.10.4 The formation of austenite 44
2.10.5 The martensite transformation 50
2.10.6 The effect of surface melting 50
2.10.7 The effect of rapid heating on AC_1, AC_3 52
2.10.8 Laser transformation hardening-a review of previous work 52
2.11 Metallurgical considerations of laser cladding 54
2.11.1 Rapid solidification 54
2.11.2 Laser cladding with Stellite 55
2.12 Residual stresses due to laser treatment 57
2.12.1 Laser clad coatings 57
2.12.2 Laser hardened surfaces 58
2.13 Process control 59
2.13.1 Laser beam monitoring 59
2.13.2 Use of different optics for process optimisation 60
2.13.3 Case depth control 60
2.13.4 Surface temperature control 60

Chapter 3
Theoretical Analysis of the Laser Heating Cycle

3.1 Introduction 70
3.2 Background to heat flow models 70
3.3 Theoretical discussion of models used in this work 74
3.3.1 Numerical model 74
3.3.2 Simple empirical model 77
3.3.3 Finite difference numerical model 77
3.4 Use of the models 80
3.4.1 Calculation of operating window using Shercliff & Ashby model 81
3.4.2 Modifications to the finite difference model 81

Chapter 4
Experimental Procedures

4.1 Equipment used for laser treatment 86
4.1.1 Lasers used 86
4.1.2 Beam delivery system 87
4.1.3 Laser beam alignment 88
4.1.4 Lens focussing assembly 88
4.1.5 Mirror focussing assembly 89
4.1.6 Safety 89
4.1.7 Determination of process variables 89
4.1.8 Equipment specific to laser hardening experiments 93
4.1.9 Equipment specific to laser cladding experiments 93
4.2 Materials and substrate preparation 95
4.2.1 Transformation hardening 95
4.2.2 Laser cladding 99
4.3 Experimental procedures 100
4.3.1 Laser transformation hardening 100
4.3.2 Laser cladding and particle injection 102
4.3.3 Wear tests 104
4.3.4 Metallographic examination and analysis 105

Chapter 5
Experimental Results - Laser Transformation Hardening

5.1 Introduction 116
5.2 Results of calculations to define the operating window for LTH 116
5.2.1 Temperature determination using thermocouples 116
5.3 Results of absorptivity determinations for different surface coatings 117
5.4 Results of transformation hardening En52 and En24 valve steels 118
5.4.1 Transverse tracks across substrates 118
5.4.2 Variation of hardness-longitudinal tracks 118
5.4.3 Variation of hardness-spiral tracks 119
5.5 Microstructural evolution during the heating and cooling cycles 119

5.5.1 As-received steels 119
5.5.2 Microstructure of laser hardened steels 122
5.6 The effect of surface melting 123
5.7 Effect of mode structure on hardened track profile 124
5.8 Reproducibility 124
5.9 Wear test results 125
5.9.1 Single track tests 125
5.9.2 Valve stem tests 126
5.10 Summary 127

Chapter 6
Discussion - Laser Transformation Hardening 166

Chapter 7
Results - Laser Cladding
7.1 Introduction 191
7.1.1 Development of optimum gas flow system for THS 192
7.2 Cladding of Stellite 6'W' 192
7.2.1 Flat plate clads 192
7.2.2 Valve cladding with Stellite 6'W' 192
7.3 Cladding of Stellite 35 193
7.3.1 Stellite 35 on mild steel 193
7.3.2 Stellite 35 on 21-4N 193
7.4 Cladding of Stellite 35 and SiN 194
7.5 Cladding of Stellite 35 and Alumina 194
7.6 Cladding of Stellite 35 and SiC 195
7.7 Cladding of Stellite 35 and Chromia 197
7.8 Wear testing of clad samples using hammer drill rig 198

Chapter 8
Discussion - Laser Cladding

8.1 Cladding of Stellite 6'W' on mild steel 224
8.2 Valve cladding 225
8.3 Laser cladding of Stellite 35 228
8.3.1 Microstructure 228
8.3.2 Porosity 229
8.3.3 Cracking 230
8.3.4 Dilution 230
8.3.5 Powder feed system 230
8.4 Solidification 231
8.5 Addition of ceramic particles 233
8.6 Wear resistance of clad layers 235

Chapter 9
Conclusions and Future Work
9.1 Laser transformation hardening 242
9.2 Laser cladding 243
9.3 Valve cladding 244
9.4 Future work 244
9.5 Publications 245

Appendix A
Block diagram for F.D. model

Appendix B
Operating parameters for LTH

References

List of Figures

1.1	Sequence of piston strokes for combustion cycle	10
1.2	The important parts of a poppet valve assembly	10
1.3	Typical valve lifting assembly	11
1.4	Temperature profile for diesel engine exhaust valve	11
1.5	Illustration of heat flows in the valve	12
1.6	Valve modifications using liquid sodium	12
1.7	Typical stress contour of a valve head with pressure	12
1.8	(a) Inclusion of carbon relief to remove valve wall deposits	12
	(b) Undercut neck to remove valve wall deposits	12
2.1	Interaction spectrum for laser materials processing	61
2.2	Low order TEM modes obtained for cicular beams	61
2.3	Variation of reflectivity with wavelength	61
2.4	Dependence of absorptivity on angle of incidence	61
2.5	Variation of absorptivity of metal surfaces with temperature	62
2.6	Improvement in absorptivity with surface coatings	62
2.7	2-D schematic of laser supported absorption wave	62
2.8	Wear resistance of heat treated steels	63
2.9	Relationship between original hardness and weight loss for steels of various carbon content	63
2.10	Comparison of wear resistance of laser deposited and plasma sprayed layers	64
2.11	Results of 2-body abrasive wear teste for prcipitation hardened, plasma sprayed and laser clad surfaces	64
2.12	Schematic showing principle surface treatments	64
2.13	Path of magnetic flux through bar during induction hardening	65
2.14	Flame hardening operation - progressive technique	65
2.15	Fe-C equilibrium diagram	65
2.16	Cr-Fe binary system	66
2.17	Constitution diagram for Fe-C-Cr alloys	66
2.18	Comparison of volume percent austenite formed from pearlite and speroidised eutectic steel structures	67
2.19	Possible nucleation sites for carbide containing steels	67
2.20	Concentration of carbon vs distance along a radius from centre of spherical carbide particle	67
2.21	Variation of r_a and r_b for values of r_o during austenite formation	68
2.22	Hardness of steel phases as a function of carbon content	68
2.23	Comparison of hardness profiles for different steels	68
2.24	Specific volumes of steel phases as a function of carbon content	69
3.1	Shercliff and Ashby master plot for case depth prediction	83
3.2	Hardened depth correlation according to Steen and Courtney	83
3.3	Variation of reflectivity with temperature	84
3.4	Sample output from modified mathematical model	85
3.5	Faces and index points for subroutine CALC	84
4.1	Alignment path and operating arrangement for Laser Ecosse AF5L	108
4.2	Lens holding asssembly used for initial hardening trials	108
4.3	2-D schematic for calculation of beam diameter	108
4.4	Rotating jig used for valve stem hardening	109
4.5	Argon cooling assist device designed for valve stem hardening	109
4.6	Powder feed hopper device	109
4.7	Experimental arrangement for laser cladding	110
4.8	Tripple hopper powder feed system	110
4.9	Shrouding device designed for laser cladding	111
4.10	Rotating jig for cladding of poppet valves	111
4.11	Schematic showing 3-D surface profiling rig	111
4.12	Mounting fig and experimental set-up for absorptivity determination	112
4.13	Example of trace produced from experiments to determine absorptivity	112
4.14	Dimensions of poppet valves used in the study	112
4.15	Holes drilled in valve stems for temperature determination	112

4.16 Geometry of twin feed cladding system 113
4.17a Boundary lubrication wear rig - schematic 113
4.17b Boundary lubrication wear rig - photograph 113
4.18 Hammer drill rig for wear testing of clad samples 114

5.1 Plot of required absorbed power versus traverse speed upto 1000 W 128
5.2 Plot of required absorbed power versus traverse speed upto 1400 W 128
5.3 Plot of required absorbed power versus traverse speed upto 2000 W 128
5.4 3-D surface profiles of En24 steel surfaces 129
5.6 Relationship between surface hardness and interaction time En24 133
5.7 Relationship between surface hardness and interaction time En52 133
5.8 Plot of case depth vs interaction time for En 24 grit blasted 134
5.9 Plot of case depth vs interaction time for En 52 grit blasted 134
5.10 Plot of hardness vs depth below surface for grit blast En24 135
5.11 Plot of hardness vs depth below surface for graphite coated En24 135
5.12 Plot of hardness vs depth below surface for graphite coated En52 136
5.14 Motor calibration curves 132
5.15 Hardness profiles for spiral tracks 137
5.16 Optical micrograph showing A-R En52 steel 138
5.17 SEM showing A-R En52 steel 138
5.18 TEM showing grain precipitates in A-R En52 steel 139
5.19 TEM showing intra-granular precipitates in A-R En52 steel 139
5.20 TEM showing SAD pattern from carbide and EDX trace 140
5.21 TEM showing CBED pattern from carbide 141
5.22 SAD pattern for $(Fe,Cr)_{23}C_6$ generated using Macdiffract 142
5.23 Optical micrograph showing A-R En24 steel 143
5.24 SEM showing A-R En24 steel 143
5.25 TEM showingelongated spheroidal precipitates in A-R En24 144
5.26 TEM showing SAD pattern, carbide and EDX trace for En24 145
5.27 TEM showing carbide and CBED pattern for En24 146
5.28 Optical micrograph showing 2-zone microstructure of En52 after LTH 147
5.29 Optical micrograph showing upper layer of HAZ in En52 147
5.30 Lower layer of HAZ in En52 148
5.31 TEM showing coarsening of grain boundary precipitates, En52 148
5.32 SEM showing martensitic surface of laser hardened En24 149
5.33 TEM showinf precipitates in En24 after LTH 149
5.34 Optical micrograph showing structure obtained after melting, En52 150
5.35 SEM showing microstructural changes in En52 151
5.36 SEM showing dendritic zone in surface melted En52 152
5.37 SEM of partially transformed zone in En52 153
5.38 SEM of partially transformed zone in En52 153
5.39 Wear test results - A-R and conventionally heat treated En24 154
5.40 Wear test results - grit blasted En24 154
5.41a Wear test results - DAG coated En24 155
5.41b Wear test results - spray coated En24 155
5.42 Wear test results - DAG coated En24 156
5.43 Wear test results - excimer pretreated En24 157
5.44 Wear test results - A-R and conventionally heat treated En52 158
5.45 Wear test results - grit blasted En52 158
5.46 Wear test results - DAG coated En52 158
5.47 Wear test results - spray coated En52 159
5.48 Wear test results - excimer pretreated En52 160
5.49 Wear test results - excimer pretreated En52 161
5.50 SEM micrographs showing wear scar on pin and substrate after BLWR 162
5.51 SEM micrographs showing wear scars at high magnification 163
5.52 3-D surface profiles of En24/52 before and after wear testing 164

6.1 Isothermal section of Fe-C-Cr system at 873K 178
6.2 Isothermal section of Fe-C-Cr system at 1273K 178
6.3 Influence of alloy additions on eutectic temperature and C content 179
6.4 Relationship between hardness, C content and amount of martensite 179
6.5 Calculated critical thermal cycles for En52 sample sp1 180
6.6 Calculated critical thermal cycles for En52 sample sp3 180

6.7	Calculated critical thermal cycles for En24 sample s3	181
6.8	SEM micrograph showing initiation of austenite at carbides	182
6.9	CCT diagrams for En52/24 steels	183
6.10	Schematic of four zone microstructure found in surface melted En52	182
6.11	SEM micrographs showing partially transformed zone in En52	184
6.12	Plot of $P/\sqrt{dv}$ against hardness for En24/52 steels	185
6.13	Plots of theoreticla and experimental case depths (Shercliff model)	185
6.14	Experimental and F.D. model results plotted on Shercliff master plot	186
6.15	3-D heat flow pattern from F.D. model with x-axis temperature profiles	187
6.16	3-D heat flow pattern for modified boundary condition model	188
	with x axis temperature profiles	189
6.17	Comparison of heat flows for original and modified F.D. models	190
7.1	Dimensions of laser deposited tracks	199
7.2	Examples of valve clads	200
7.3	Dendritic nature of Stellite 6 clad onto valve seat face	199
7.4	Interface microstructure of Stellite 6 clad on valve seat	201
7.5	Turbulent mixing in melt pool of clad	201
7.6	Hardness of Stellite 6 layers on valve seat faces	202
7.7a	Microstructure os Stellite 35 layer	203
7.7b,c	Effect of velocity on clad height and hardness	203
7.8	EPMA traces for Stellite 35 clads on 21-4N	204
7.9	Dot maps for Stellite 35 clad on 21-4N	206
7.10	Geometry using twin feed tubes for cladding Stellite 35+alumina	207
7.11	SEM showing upper and lower surface of slagged alumina layer	208
7.12	Dimensional relationship of St.35+alumina clads with Wt% alumina	209
7.13	Change in shape of clad with Wt% alumia addition	211
7.14	Attack of alumina on 21-4N surface	207
7.15	Example of pulsed deposit due to irregular powder flow	212
7.16	SEM showing SiC particles at clad surfaces	212
7.17	EPMA traces for St.35+5,10 and 20 Wt% SiC addition	213
7.18	Dot maps for 5 Wt% addition of SiC to Stellite 35	214
7.19	Examples of dissolved/partly dissolved SiC particles	215
7.20	Experimental geometries for cladding trials	216
7.21	Hardness of deposit with Wt% SiC addition	217
7.22	EPMA traces for Stellite 35+10 Wt% chromia	218
7.23	EPMA traces for Stellite 35+chromia (twin feed system)	219
7.24	Dot maps for Stellite 35+chromia (10 Wt%)	220
7.25	Hardness of deposit with Wt% chromia addition	217
7.26	Typical chrmia containing clads	221
7.27	Relationship between wear scar diameter and Wt% ceramic addition	222
7.28	Relationship between wear scar diameter and velocity for Stellite 35	222
7.29	Examples of wear scars on pin and substrate after hammer drill test	223
8.1	Bead shapes for laser cladding	237
8.2	Isothermal section of the C-Co-Cr system	237
8.3	Interfacial force balance for valve groove cladding	238
8.4	Spheroidised clad due to poor wetting	238
8.5	Isothermal section of the Ni-B system	238
8.6	Photograph showing cracking of clad bead	238
8.7	Dependence of solidification morphology on temperature gradient	
	and solidification velocity	239
8.8	Ellingham Richardson diagram for the oxides	239
8.9	Standard free energy of formation of carbides	239
8.10	Ektapro photographs of melt pool as a function of SiC addition	240
8.11	Confocal laser scanning micrographs showing SiC particle	241

List of Tables

1.1	Chemical compositions of exhaust valve steels	13
1.2	Chemical composition of some hardfacing materials	14
2.1	Salient features of chromium carbides	69
3.1	Thermal properties of En24 and En 52 steels	84
4.1	Manufacturers data for ceramic powders	114
4.2	Sieve analysis for ceramic powders used	115
5.1	Peak temperatures recorded 1mm below surface during LTH	130
5.2	Absorptivities of various surface coatings	130
5.3	Motor calibration data	132
5.4	Composition of steel phases	142
5.5	XRD data for steels	142
5.6	Wear test results - valve stem tests	165
7.1	Operating parameters - Stellite 6 on mild steel	223a
7.2	Operating parameters - Stellite 6 on valve seat faces	223b
7.3	Operating parameters - Stellite 6 on valve seat faces	223c
7.4	Operating parameters - Stellite 35 on mild steel	223c
7.5	Elemental analyses for clad layers	223a

Nomenclature

Symbols other than those listed here are defined where they occur in the text.

I	Intensity of laser at a point	$W\,m^{-2}$
I_o	Peak intensity at laser beam centre	$W\,m^{-2}$
T	Temperature	K
T_o	Ambient temperature	K
q	Laser power	W
λ	Thermal conductivity	$J\,m^{-1}\,s^{-1}\,K^{-1}$
R	Radius of spherical surface drawn around heat source	mm
v	Traverse speed	$mm\,s^{-1}$
E	(E=x-vt) distance considered from point source	mm
a	Thermal diffusivity	$m^2\,s^{-1}$
C_p	Specific heat of steel	$J\,kg^{-1}\,K^{-1}$
x,y,z	Cartesian coordinates (origin = beam centre)	mm
r_B	Radius of Gaussian beam	mm
A_1	A_1 temperature of a steel	K
A	Surface absorptivity	
t	Time	s
t_o	Heat flow time constant	s
z_o	Calibration distance	mm
T_p	Peak temperature	K
T_s	Surface temperature	K
C_1	Constant	
ρ_c	Volumetric specific heat	$J\,m^{-3}\,K^{-1}$
z_{01}, z_{02}	Calibration distance (near and far field)	mm
T_c	Critical temperature	K
q^*	Normalised beam power	
v^*	Normalised beam speed	
x^*,y^*,z^*	Normalised x,y,z coordinates	
z_o	Normalised calibration distance	
t^*	Normalised time	
z_{01}^*, z_{02}^*	Normalised calibration distances (near and far field)	
q_m	Beam power for temperature equal to A_1	W
q_m^*	Normalised beam power for temperature equal to A_1	
k	Heat conductivity	$J\,m^{-1}\,s^{-1}\,K^{-1}$
d_B	Beam diameter (Gaussian beam)	mm
T_m	Melting temperature of steel	K
t_p	Time to reach peak temperature	s

INTRODUCTION

The increasing requirement for higher performance, efficient and "environmentally friendly" combustion engines has led to an increased interest in improving the wear properties of engine components to meet these demands. The valve train components have assumed particular importance. The subject of this study is the engine exhaust valve which must perform for thousands of hours under high pressure and temperature and corrosive/erosive conditions.

The capital cost of these components can be lowered by using a method of surface treatment to improve the wear resistance of relatively inexpensive bulk materials. One group of such techniques utilises the high power CO_2 laser to effect surface treatment. The literature survey is concerned with describing the metallurgical requirements of engine valves, and the materials and processes available to perform surface treatment, with particular emphasis on lasers for surface engineering. Also included are the metallurgical consequences of rapid thermal treatments.

The thesis thereafter is divided broadly into three main areas, a theoretical study of the thermal cycle, laser transformation hardening of valve stem materials, En24 and En52 and laser cladding of valve seat faces using cobalt and nickel based Stellite alloy powders (Stellite 6 and 35 respectively) including an investigation of the addition of ceramic particles to the melt pool.

CHAPTER 1

THE ENGINE VALVE - A METALLURGISTS VIEW

1.1 Engine Operation - the basic principles

In piston engines, valves are required to control the intake and exhausting of gases. There are two valves to each combustion cylinder in most engines, although some have three or four for optimum gas flow. An inlet valve, to admit the combustible mixture of gas and air and an exhaust valve to allow the escape of the burned gases. The burning gases of the fuel/air mixture create a high temperature, causing expansion of the gases. Since this burning occurs above the pistons, a high pressure is generated, forcing the piston down on its cylinder.

In diesel engines, air is drawn into the combustion chamber and compressed before the fuel is injected. Ignition of the diesel fuel occurs immediately on injection into the hot compressed air.

In a petrol engine however, air and fuel are drawn simultaneously into the chamber and compressed. An electric spark is then passed through the mixture to effect combustion.

The reciprocating piston motion produced by this sequence of events is converted into rotary motion by the connecting rods and crankshaft.

Most engines use four piston strokes to complete the cycle, these being; inlet, compression, power and exhaust. The sequence is shown in Fig. 1.1.

The role of the valve therefore, is to open and close at the correct moment so that the combustion cycle can be maintained.

1.2 The Poppet Valve

There are various types of engine valve, including rotary, sleeve and reed valves, in two stroke engines the pistons themselves act as valves covering and uncovering ports in the cylinder walls. The work covered in this research project considers the "poppet" type of exhaust valve which is used in all four stroke engines, and certain two stroke diesel engines, and is relatively economical to manufacture. The important parts of a poppet valve assembly are illustrated in Fig. 1.2 (after ref.2).

Although simple in appearance, there are four fundamental requirements of an engine valve;

(1) endurance at high temperatures (typically >500^{o}C for exhaust valves). A valve must retain its shape and strength at elevated temperature

(2) endurance under rapid movement (valves will open and close around 33 times/s in a typical engine travelling at motorway speeds)

(3) capability to withstand pressures up to 14MPa in a diesel engine cylinder

(4) resistance to burning, corrosion and erosion

The most severe conditions correspond with the start of opening of the valve, when the pressure and temperature of the gases can reach 0.4MPa and 1650^{o}C respectively. At this point the velocity of the exhaust gases approaches that of sound and can have an extreme cutting or erosive action on the valve seat.
A valve must also be able to resist wear, especially on the sealing face where there is little or no lubrication, and on the valve stem due to reciprocating movement against the valve guide. To meet the above requirements, and others imposed by engine design, the valve is in fact a more sophisticated component than it seems on first inspection.

1.3 Valve Failure

Valve life is known to be one of the contributory factors limiting the time between engine overhauls, for heavy fuel engines. Valve life is dependent on both operational factors - engine load, number of stops and starts - and on fuel quality.
Valve failures may be broadly divided into several classes, according to Mogford and Ball (1), as follows:

1) Stem breakage - usually due to fatigue or corrosion fatigue
2) Stretching - between the stem and head, due to operating temperature being too high for material selected
3) Tuliping - often accompanying (2), due to poor resistance of the material to bending stresses in the valve head
4) Radial cracking of valve seat - due to high alternating hoop stresses in the presence of corroding deposits (cracks often extend well into the valve head)
5) Cracks between centre of head and rim - occurring with (4), due to bending stresses in the head in presence of corroding agent
6) Deposit cracking - causing guttering of the seat
7) Burning of valve seat - (at one time accounting for > 50% of valve failures (2) but less common now as fuels and lubricants have improved) occurring usually due to the valve sticking as a result of deposits

Type (2) and (3) failures can be avoided by regular adjustments of the tappets and by grinding the valves in before operating the engine. Negligence in this respect leads to burning of the valve seat.
Assuming that the mechanical properties of the valve materials are acceptable, the majority of failures are a result of corrosion of the alloy. Frequently, tuliping and stretching of the valve results in insufficient contact of the valve seat and cylinder head, the consequence of which is a rapid increase in the seat temperature, far in excess of the scaling temperature. In view of this, materials possessing a low coefficient of expansion and suitable hot strength are desirable.
The presence of lead oxide exacerbates the problems caused by oxidation due to the burning process. The reason for this is two-fold, firstly, it absorbs oxygen from the exhaust gases and transfers it to the valve surface, and secondly, lead oxide tends to

remove the metallic oxide and render fresh surfaces open to oxidative attack. This second phenomenon is thought to be more pronounced for iron based valve alloys than for nickel or cobalt alloys due to the higher solubility of iron oxides in lead oxide.
In addition to the above, certain materials have a predisposition for crack formation and growth under the influence of stress, corrosion and temperature, hence the importance of the material to be resistant to corrosion fatigue. Obviously wear is a significant problem but generally one which leads to a decrease in efficiency before failure.

1.4 Valve Operating Mechanism

The valve opening mechanism must be precise for the efficient operation of an engine. It is also important that the operating assembly be of light weight when engine performance is particularly critical. Valve movement is controlled by the cams, which are designed to rapidly open the valve, hold it open for a fixed amount of time and allow it to be closed by the spring. A typical lifting assembly is illustrated in Fig. 1.3. Correct design and material selection is vital for efficient operation, and the valve train components must be manufactured to high tolerances.

1.5 Valve Design Considerations

In order to discuss the importance of valve design, it becomes necessary to scrutinise the operating environment for the exhaust valve and to assess the effect of design both on the temperatures and stresses induced in the valve and on the volumetric efficiency of the engine.

1.5.1 Valve Temperature Effects

Control of valve temperature is one of the most effective ways of reducing hot corrosion and thus prolonging valve life. The temperature pattern in the valve head is constantly changing throughout the operating cycle.
An exhaust valve is more prone to the effects of temperature than an inlet valve as there is generally no cooling mechanism available to protect it from the hot and corrosive gases. Whereas inlet valves are air cooled when open as the air is drawn into the combustion chamber. The temperature of an exhaust valve seat can range from 350 - 550^{o}C. A typical plot of the temperature profile for a diesel exhaust valve is shown in Fig. 1.4 (3).
Heat flows into the valve during combustion by radiation, and also during the exhaust stroke by conduction. Heat flow into the valve by conduction is limited by the area of the valve head, it is therefore advantageous to design a valve with the minimum head area.
The temperature and velocity of the exhaust gases and the presence of oxides and

surface deposits will influence the amount of heat flowing into the valve during the exhaust stroke.

The cooling of an exhaust valve occurs only by conduction, from the centre of the valve head to the seat when closed, or from the stem to the valve guide (4). The flow of heat from the valve is illustrated in Fig. 1.5.

Of the two cooling mechanisms, the heat flow through the seat is the greater, accounting for some 75% of the cooling effort, and is dependent on a number of factors, which include contact area, temperature differential, presence of deposits and the thermal properties of the valve materials.

Although a reasonable contact area is needed, it is important that the valve diameter be kept to a minimum, to minimise conduction. Good contact between the valve and its seat insert can then be assured by seating the valve concentrically.

Three important factors govern heat flow via the valve stem, namely, thermal conductivity of the material, stem diameter and clearance between the valve stem and guide. Therefore unless weight is a determining factor, a larger stem diameter is advantageous, and a material with suitable thermal properties should be selected.

The difficulty of achieving satisfactory cooling of valves is the overriding determinant in most valve failures, and this prompted the introduction of the sodium filled valve for certain engine applications - particularly aero-engines and high performance auto-engines, where the temperatures are abnormally high, or where the hot strength of the material is marginal. This modification is illustrated in Fig. 1.6(a). It consists of a hollow stem partially filled with sodium which becomes molten shortly after engine start-up, this allows increased heat transfer from the valve head to the stem and guide by means of the displacement of the molten sodium. A further modulation was the hollow-head, hollow-stem valve, also illustrated in Fig. 1.6(b), which has a greater capacity for sodium. The relative merits of these two designs, and others are discussed by Worthen and Tunnecliffe (5), who also report some interesting results relating to valve temperatures. The authors used quasi-steady state finite element heat transfer analysis to define heat flows in the valve and established that significant changes in surface temperatures of the valve could be induced by the addition of heat barrier coatings to the head and fillet radius.

1.5.2 Valve Stress Effects

Stresses in the valve seat are either residual stresses resulting from the manufacturing process, low frequency occurring when starting and stopping the engine or substantially changing the load and due to the thermal gradient between the head and edges, or high frequency as a result of valve distortion, cyclic heating and cooling, valve hitting the seat and seating stresses due to gas pressure.

Thermal stresses account for the greatest proportion of the total stress and are a function not only of the thermal gradient but also of the coefficient of thermal expansion and Young's modulus of the material. A typical stress contour of the valve head is presented in Fig. 1.7, after Worthen and Rauen (6) who investigated valve temperatures and strains under various operating conditions.

1.5.3 Volumetric Efficiency Effects

A discussion of the major design details for poppet valves and the valve port, with respect to engine efficiency is given by Giles (3).
The most important points being:

(1) valve openings must be large enough to accommodate air flow necessary to achieve desired output power
(2) valve seat angle must be chosen to allow adequate flow through the opening, and to reduce cylinder head distortion and seating pressure
(3) suitable arrangement of valves in cylinder must be determined so that heat is evenly distributed between the valves
(4) guide length should generally be as long as possible to minimise side thrust from the rocker arm against the valve tip
(5) stem diameter should be selected for maximum durability
(6) valve head shape must be such that effective port sealing is assured and stress and temperature effects are minimal; this decreases the risk of fatigue crack initiation by ensuring that the underhead bending stresses are low in magnitude

1.5.4 Other Effects

Valve rotators may be used to further equilibrate the temperature distribution around the valve and hence minimise thermal stresses. Such rotators work using either a ratcheting action or a grinding action, and can also prevent the development of areas of damage on the seat and seat insert as they ensure that the valve seats in a continually different position. Rotators also allow a small amount of wiping between valve seat and face which removes deposit formations.
Valve stem seals are often used to restrict the amount of lubricating oil available thus limiting deposit formation.
The inclusion of a carbon relief, as shown in Fig. 1.8(a) (after ref.3) is sometimes effective in scraping deposits from the guide wall.
Some manufacturers prefer to use an undercut neck, Fig. 1.8(b), for the same purpose.

It is clear that attention to the design of an efficient engine cannot be limited to the valve, but must also extend to the associated components of the valve train.

1.6 Valve Production

1.6.1 Material Selection

The choice of material for a particular application frequently presents a problem in engineering. Incorrect selection can result in deterioration of a component, particularly in an aggressive environment, to the point where it becomes unreliable. Wear resistance of a material is a function not only of the material properties, but also of the environmental conditions and loading situation. It is therefore

necessary to completely evaluate materials so that expensive or even dangerous mistakes can be avoided. The requisite tests for such determinations are discussed by Ball and Ward (7), who recommend material selection based on a combination of laboratory and in-situ testing. The philosophy, which is used to illustrate a rock-conveying system, may be applied to similar systems requiring wear resistance, allowing an informed decision to be made.

A closer look at the poppet valve reveals the areas which are subject to wear and how this may be counteracted.
Valve stems are manufactured from materials possessing intrinsic wear resistance, but this is often augmented by the addition of surface coatings such as chromium plating, phosphate treatment or nitriding.
In some cases bimetal valves are preferred. They incorporate a steel resistant to the aggressive combustion environment forming the head, friction welded to a highly wear resistant material as the stem, and thus represent the optimum properties for each area.
The wear resistance of a valve seat may be improved by the use of coatings, usually one of the Stellite range of hardfacing materials, which are welded into a semi-circular groove in the valve face and machined flat.
The tip of an engine valve receives continual hammering from the rocker. The wear resistance in this area can be enhanced by hardening the tip if the alloy is hardenable, by welding a piece of hardenable material to the stem to form the tip, or by protecting the tip with a replaceable cap of wear resistant material.

1.6.2 Material Properties

A valve must possess sufficient tensile strength, ductility, and fatigue resistance. It must have good thermal conductivity, but not too good as this encourages sticking due to the more ready formation of deposits from exhaust gases or due to oxidation of the lubricating oil. It must exhibit a low coefficient of expansion so that constant clearance between the stem and guide is maintained, and also suitable hot strength. In addition, a valve must be resistant to abrasion and corrosion (especially with respect to lead and sulphur compounds).

The chemical analyses of some common exhaust valve alloys are shown in Table 1.1. Of the alloys included in the Table, En59 (XB), 21-4N and Nimonic 80A are the ones used in heavy duty diesel engines, the others are used for low duty diesel and petrol engine exhaust valves. En24 and En52 are usually used to form the stems of bimetal exhaust valves in either type of engine.

The initial valve materials were low alloy steels, hardened and tempered to suit the engine, e.g. En24. With the introduction of the first British Standards in the 1920's, steels with a chromium content in the range 2.2 - 11.0 %, and 0.2 - 0.4 % silicon were developed (8).
Silchrome I (En52) became the industry standard in 1930 and still remains in

regular use, for diesel engine intake valves, along with XB type steel (En59), which is also used for petrol engines. XCR steel is more popular in the USA for these applications (9).
The incorporation of tetra-ethyl lead to fuel in the 1920's allowed engine output power to virtually double. This led to the first use of heat resistant austenitic steel for exhaust valves, now denoted En54. This steel is still employed in motorcycle, high performance diesel and aero-engines.
Later developments included the use of some stainless steels, but the cobalt-chromium and tungsten types are less corrosion resistant in the presence of lead and sulphur compounds.
Addition of nitrogen to the austenitic steels led to the evolution of 21-12N and 21-4N which became popular due to their superior heat and corrosion resistance. 21-4N has precipitation hardening characteristics and first found use in valves at Armco Steel Company, USA. It is primarily used for heavy duty exhaust valves alongside the nickel-base alloys, Nimonic 70, 80A and Inconel M (8). The latter of which generally forms the hollow head and stem, sodium-cooled valves and has been found to reduce valve failure by a factor of seven over austenitic steel valves (9). The Nimonic alloys are widely used in motorcycle and high performance racing engines as they possess higher hot strength.

Valve seats often require a hardfacing to attain the necessary wear and corrosion resistance. In general, natural/LPG gas engines use the same type of valve materials as diesel engines. Face wear is a recurring problem, especially in leaded fuel and heavy duty diesel engine applications, and hardfacing is the rule. Hardfacing alloys for valve coating are expected to possess a wide variety of properties including high compressive strength, low coefficient of friction, metal-metal wear resistance, resistance to cavitation erosion, impact resistance, corrosion resistance and good hot hardness.
One particular problem concerning the valve industry is galling (10). This describes the interfacial damage which often occurs when two metallic surfaces are brought together under high load and relative motion. Cobalt-based Stellite 6 alloy has traditionally been used to face valve seats using plasma or oxy-acetylene welding. More recently, in the wake of a 1978 price increase for cobalt, nickel- and iron-base alloys have been developed to minimise the use of the strategic material cobalt. In addition, Ni-based material is often easier to weld. Table 1.2 shows the chemical compositions of some of the more common valve facing materials.

1.6.3 Valve Manufacture

Valves are currently manufactured from lengths of material which is cut into rods. The rods are rolled whilst hot to ensure the stem is straight. At this stage, two alloy rods may be friction welded, should a bi-metal valve be required.
The valves are then hot upset forged to shape the head and impart high strength to the component. This is achieved by applying heat (usually via induction coils) and pressure to one end of the rod which forms a tulip shape.

The valve head and neck may need no further machining, but the face is always machined. The stems are usually machined circular and to the desired finish by centreless grinding. Attention to the wearing areas is then given.

1.7 Towards The Future

It would seem at present that extensive research into the life and efficiency of the poppet valve is somewhat unnecessary, since the valve tends to last for a reasonable period of engine lifetime. However, when this work is placed into the context of future expected trends in the automotive industry, one sees that such investigation is both necessary and worthwhile.

The 1990's have witnessed the birth of a more environmentally conscious population. This in turn has led to worldwide interest in measures related to the motor industry which will effectively lead to a reduction in the amount of potentially hazardous or harmful emissions and to a healthier environment. The British Government spurred interest in unleaded fuels with the introduction of a tax saving for consumers. It is thought that the trend towards unleaded fuels can only increase in the future, as the public becomes better informed of the advantages of its use. The gradual decline of leaded fuel usage has been further influenced by a ruling in California, USA, that from 1993, all fleet and rental vehicles must run on clean burning fuels.

Materials must be resistant to hot corrosion by the combustion by-products of methanol, i.e. formaldehyde and formic acid, whose effects may be worse than those caused by existing fuels.
So, the automotive design engineer must consider the effects of different fuels on the life and efficiency of materials chosen for engine applications. In this respect, the internal combustion engine poppet valve becomes highly significant. The challenge to improve the wear resistance of such valves has been addressed in this work. The lead compound, tetra-ethyl lead, added to petrol as an anti-knocking agent, also acts as a lubricant. Removal of this leaves the engine components operating in an unlubricated state, which greatly increases the potential wear problems. Not only is the valve in a hostile atmosphere in terms of temperature and corrosion, but it now has the added disadvantage of minimum lubrication.

The CO_2 laser is the ideal tool for application to wearing surfaces. The highly monochromatic, focussable nature of laser energy renders it available for a wide range of surface treatments, which may improve the wear properties of a material. These include transformation hardening, laser cladding, surface alloying and melting. Since high tolerances are required for a valve, the minimum distortion offered by laser treatment when compared to more conventional methods is an obvious advantage.

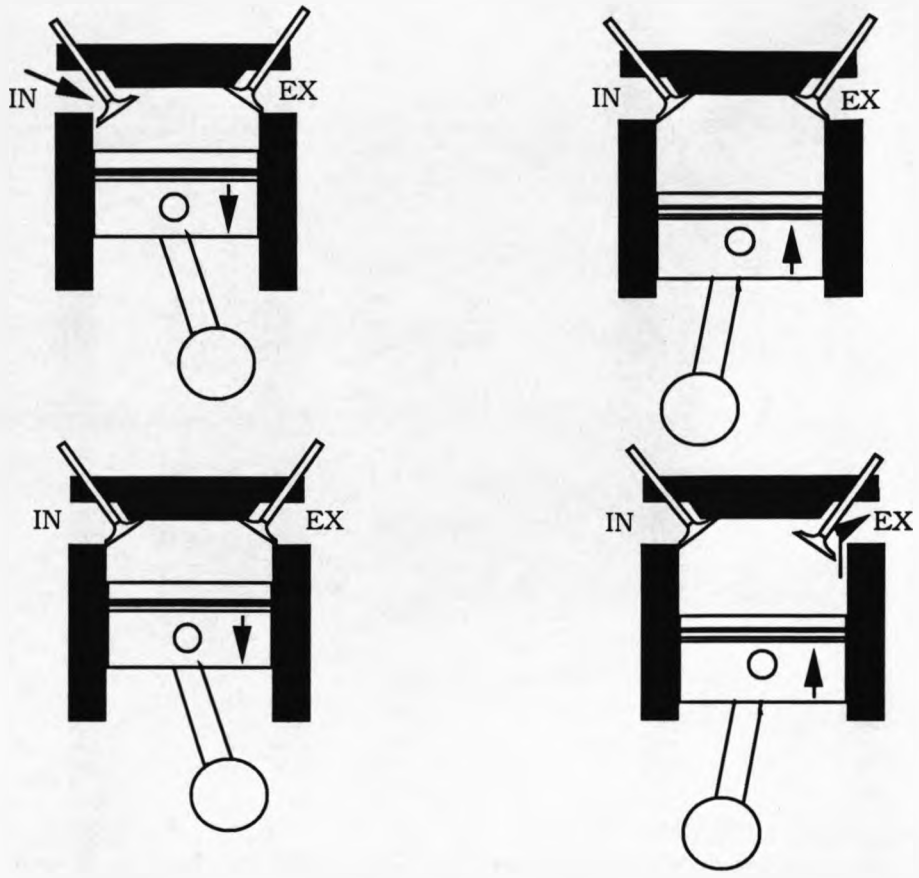

Fig. 1.1 Sequence of Piston Strokes for Complete Combustion Cycle

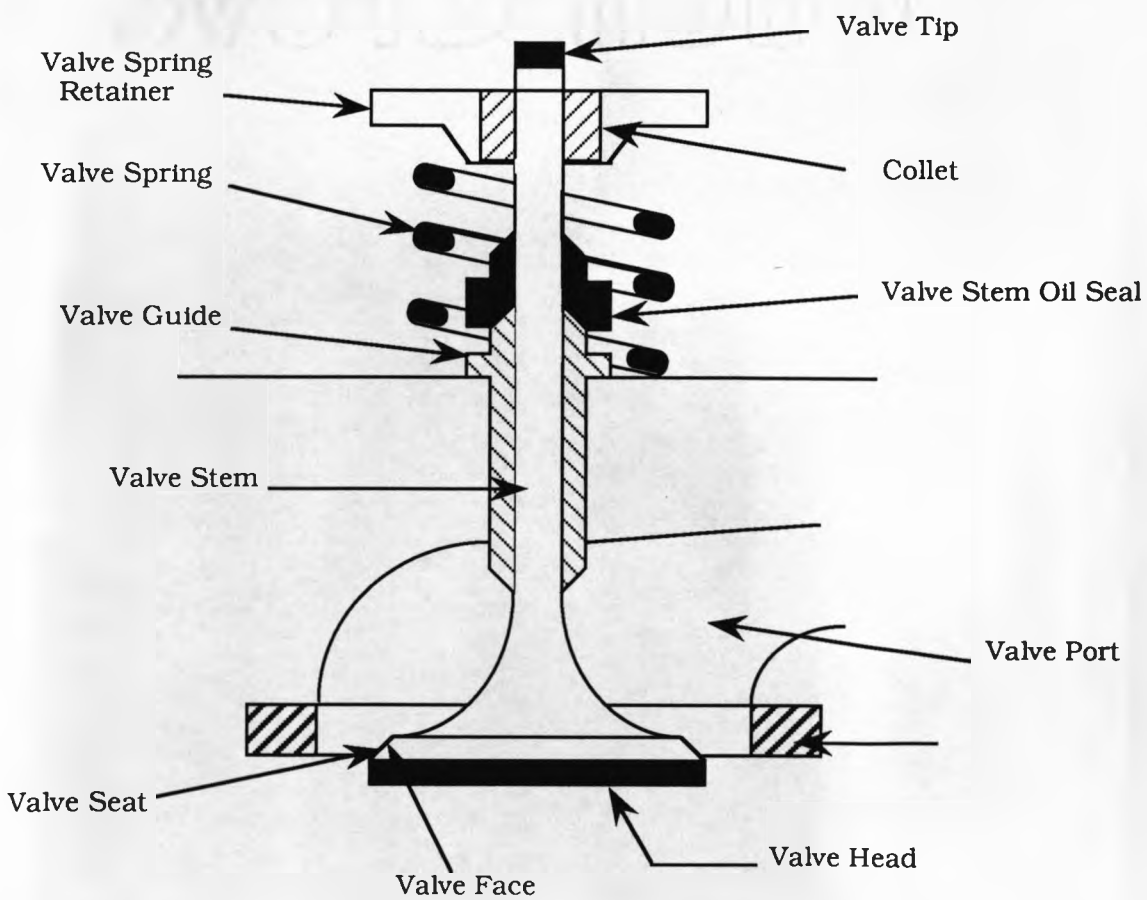

Fig. 1.2 The important parts of a poppet valve assembly

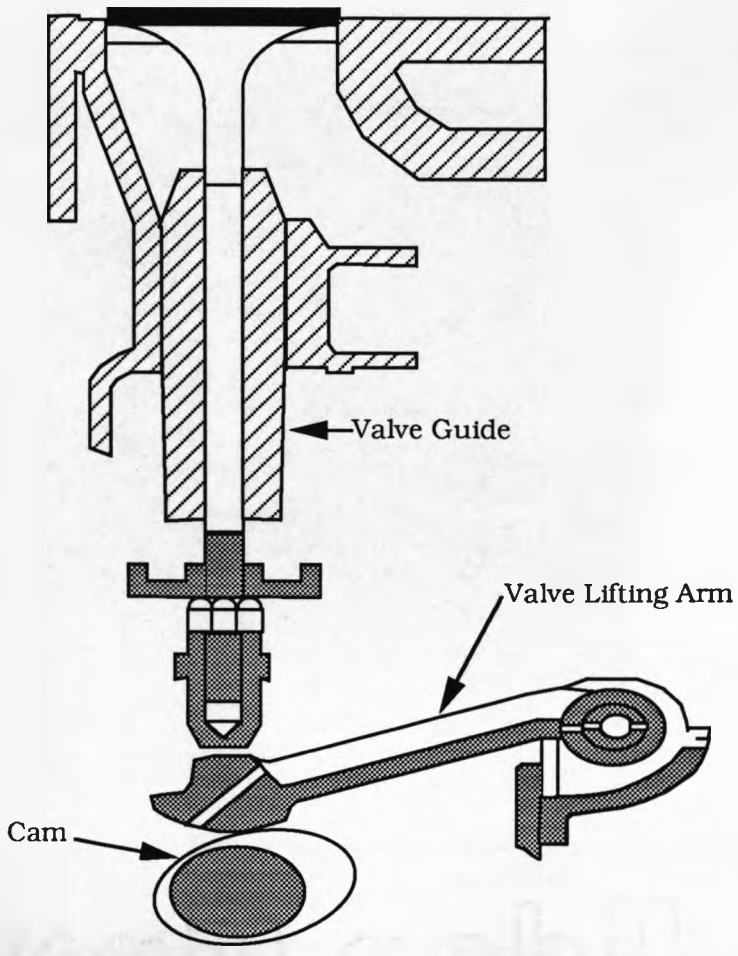

Fig. 1.3 Typical valve lifting assembly

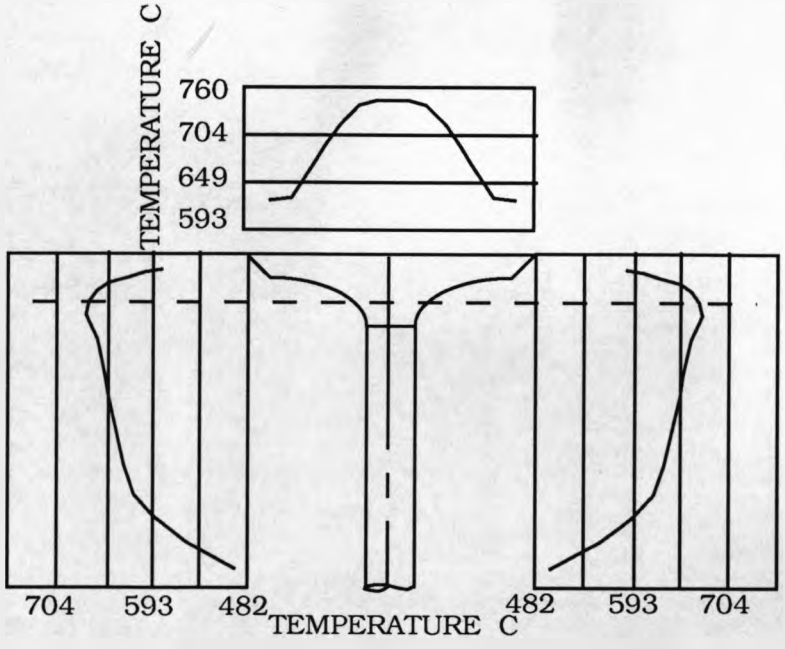

Fig. 1.4 Temperature profile for diesel exhaust valve (after ref. 3)

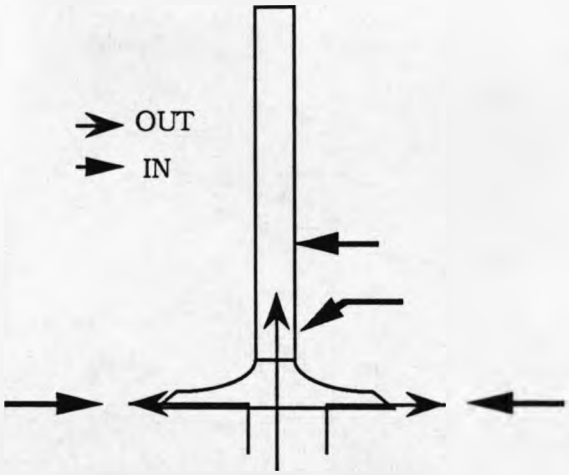

Fig. 1.5 Illustration of the heat flows in the valve

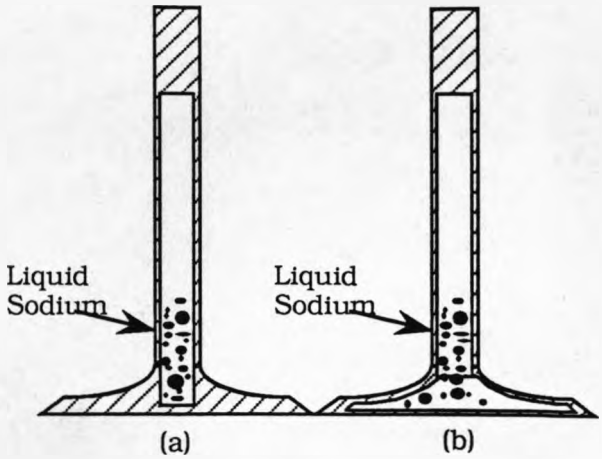

Fig. 1.6 Valve modifications-using liquid sodium (a) hollow stem, (b) hollow head and stem

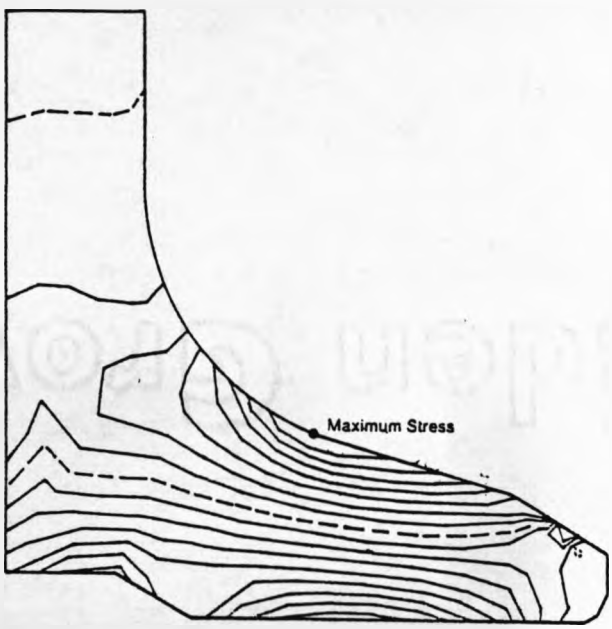

Fig. 1.7 Valve head stress contour with combustion pressure

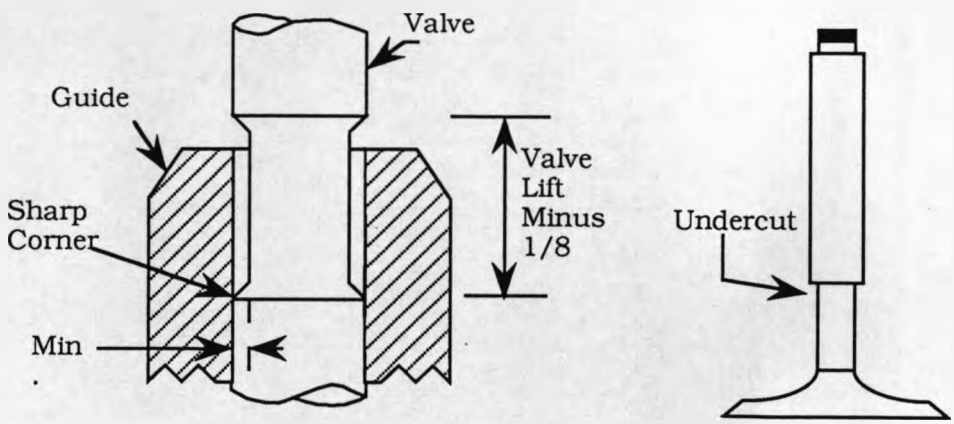

Fig. 1.8 (a) Inclusion of a carbon relief to remove deposits from valve walls, (b) Undercut neck used for same purpose

	En52	En59	XCR	21-12N	21-4N	Nimonic 75	Nimonic80A	Inconel M	En24
C	0.40 - 0.50	0.76 - 0.82	0.40 - 0.50	0.20 - 0.30	0.48 - 0.58	0.10	0.05	0.05	0.36 - 0.44
Si	3.00 - 3.75	1.95 - 2.25	1.00 max	1.00 max	0.25 max	1.00	0.60	0.10	0.10 - 0.35
Mn	0.30 - 0.75	0.20 - 0.60	1.00 max	1.50 max	8.00 - 10.00	1.00	1.00	2.00	0.45 - 0.70
Cr	7.50 - 9.50	19.00-20.50	23.00-24.50	20.00-22.00	20.00-22.00	20.00	20.00	15.70	0.45 - 0.70
Ni	0.50 max	1.15 - 1.60	4.50 - 5.00	11.50-12.50	3.25 - 4.50	Balance	Balance	Balance	1.00 - 1.40
Fe	Balance	Balance	Balance	Balance	Balance	1.00	3.00	6.00	Balance
N	-	-	-	0.15 - 0.25	0.38 - 0.50	-	-	-	-
Al	-	-	-	-	-	-	1.20	-	-
Co	-	-	-	-	-	-	2.00	-	-
Ti	-	-	-	-	-	0.50	2.50	2.80	-
S	0.03max	-	-	-	-	-	-	-	0.04max
Mo	-	-	2.50 - 3.00	-	-	-	-	-	-
P	0.04max	-	-	-	-	-	-	-	0.035max

Table 1.1 Chemical compositions of exhaust valve steels

	Stellite 1	Stellite 6	Stellite 12	Stellite F	Stellite 35
C	2.80	1.05	1.40	1.75	0.20
Mn	1.00max	0.50	1.00	0.30	-
Si	1.50max	1.10	1.00	1.10	3.21
Cr	30.00	28.00	30.00	25.50	5.50
Ni	3.00max	3.00max	3.00max	22.50	Balance
Mo	1.00max	1.00max	-	0.60max	-
W	12.80	4.50	9.00	12.00	-
Fe	3.00max	3.00max	3.00max	1.35max	1.85
B	-	0.01max	-	0.01max	1.58
Co	Balance	Balance	Balance	Balance	-
Others	1.00max	-	1.00max	-	-

Table 1.2 Chemical composition of some hard facing materials

CHAPTER 2

LITERATURE REVIEW

SURFACE TREATMENT FOR WEAR RESISTANCE

2.1 Introduction

An expanding future for the laser in materials processing has been predicted (11). In addition to the growing list of users, the automotive industry features prominently. Manufacturers whose need for flexible, cost-effective, high-productivity systems drives the market place are looking towards laser technology as a new tool. Current uses in motor manufacture are mainly restricted to cutting and welding, where cost reductions and improved quality are possible. However, future applications for surface treatments seem highly likely (12). Examples include hardening the inside walls of cylinders, valve stems and drive shafts, cladding valves and alloying valve seats. The following chapter discusses the use of the CO_2 laser for surface modification, why modification is necessary from the point of view of wear on component lifetime and a review of other possible methods of treatment to achieve surface hardness and wear resistance.

2.2 The CO_2 Laser

The carbon dioxide laser represents a means of supplying a high density energy source to a localised area. It is a molecular laser, the lasing medium provided by CO_2, N_2 and He. The laser beam is monochromatic, parallel and can be focussed to near diffraction limits (~0.1mm spot size), the power is easily shaped and travels well, rendering it suitable for robotic control. In addition to the more popular cutting and welding applications, the laser has found uses in many surface treatment techniques. The laser beam is defocussed for surface engineering applications which cover the following processes (13):

Transformation Hardening
Surface Melting
Surface Alloying
Surface Cladding
Particle Injection
Laser Chemical Vapour Deposition (CVD)
Laser Physical Vapour Deposition (PVD)
Enhanced Plating
Shock Hardening

These processes range from simple surface modification without a phase change,

through the addition of 'foreign' particles to the existing surface, to the production of a completely new surface layer. Control of the power density and interaction time of the laser beam governs the process. Fig. 2.1 shows the interaction spectrum for materials processing.

The principles of operation and the lasing mechanism for the CO_2 laser are discussed elsewhere (14,15), but the advantages of laser surface treatment over other methods in general are given below (16):

(1) the process is chemically clean
(2) thermal penetration and therefore component distortion is controllable
(3) thermal profile is controllable (i.e. shape & location of heat affected zone)
(4) less after machining is required
(5) remote processing is possible
(6) process is easily automated
(7) beam can be shared between workstations for different functions

In addition to these general features, there are a number of more pertinent advantages of laser processing for the transformation hardening and cladding techniques in question (17).
Laser transformation hardening allows selective hardening, often of inaccessible areas, without the use of a quenchant. In addition, the case depth is controllable and the process often results in an improvement of the fatigue life of the component (18).
The laser cladding process enables thin layers to be produced. These layers exhibit low dilution, low porosity and high hardness. The low heat input results in a very small heat affected zone (HAZ) and the process decreases the alloy cost and allows automatic alloy feed with less post-processing clean-up required than conventional processes.

On the negative side, the capital cost of the equipment for laser treatment is high, processing rates and coverage areas may be quite slow and absorbent coatings may be necessary in some cases to improve the coupling of the laser beam with the substrate.

However, the use of lasers for material processing applications is becoming more widespread. At present the CO_2 and the solid state Nd:YAG laser are in use but there are major advantages for the lower wavelength lasers as the optics are less expensive and the problem of reflectivity is greatly reduced.

2.3 Output Properties of the CO_2 Laser Beam

The beam produced by the laser is monochromatic, highly coherent (laser light exhibits both high spatial and high temporal coherence) and has a low divergence angle. These factors are discussed in depth by Ready (14). The characteristics of the output beam affecting its application to surface treatment are discussed below.

2.3.1 *Mode Structure(19,20,21)*

Beam mode structure or power distribution is a function of the laser cavity and optics. The power distribution of the output beam is determined by the spatial arrangements of the light within the resonator cavity. Two kinds of mode exist, these being longitudinal and transverse. Longitudinal (parallel to the optical axis) variations are much smaller than transverse variations, which determine the spatial profile of the beam. The transverse modes represent configurations of the electromagnetic field in the cavity determined by boundary conditions imposed by the cavity.

The transverse electromagnetic modes commonly occurring are termed TEM_{pq} where subscripts p and q represent the number of nulls in the spatial pattern in two orthogonal directions. The spatial intensity patterns for some low order modes are shown in Fig. 2.2. TEM_{01}^{*} corresponds to a linear superposition of like modes, i.e. TEM_{01} and TEM_{10}, rotated by 90^{o}.
The intensity profile of the incident light strongly affects the processing ability of the laser. For cutting and welding applications where high power densities and focussed beams are required, TEM_{00}, the Gaussian mode is favoured. For lower power density treatments such as surface treatments, a more diffuse laser mode is required. The donut or TEM_{01}^{*} mode is usually chosen due to its more uniform heating effect.

The effect of mode structure on materials processing has been studied by a number of authors. Sharp *et al* (22) looked at the effect of power distribution on laser welding, and found that Gaussian beams do produce narrower welds with increased penetration. Sharp (23) also studied the effect of mode on laser transformation hardening, and concluded that for the donut mode, there was less likelihood of surface melting due to the more uniform intensity profile. An additional benefit of this mode was to increase the coverage rate due to the more diffuse beam. A similar study by Weerasinghe (24) showed that the more intense distributions led to uneven melt depths and increased levels of dilution for clad layers.

2.3.2 *Beam Radius*

The spot size of the laser beam is an important factor for materials processing applications. The absence of any strict mathematical boundaries for a particular intensity distribution (23) makes the definition somewhat difficult. The generally adopted convention is for a characteristic radius to be specified, this is usually expressed as the radius at the point where the intensity has fallen to $1/e^2$ its maximum value. In terms of the intensity then for a Gaussian beam, the intensity (I) is given by:

$$I(r) = I_o \exp\left(\frac{-2r_o^2}{r_o^2}\right) \qquad (2.1)$$

Where I_0 is the intensity at the centre. The point at which the intensity has diminished to e^{-2} of its central intensity looks like the edge of the beam to the eye. For this reason it is deemed reasonably accurate to assume that the radius can be determined by single isotherm methods such as charring wood or burning perspex. A more sophisticated method of beam radius determination using the time taken for a spot to rise to 90% of equilibrium and comparing to a calculated Gaussian diameter to deduce an effective radius was proposed by Courtney and Steen. (25). This method gives an absolute measurement rather than a comparative one and eliminates the complexities encountered using multiple isotherm techniques. When considering higher order modes, the intensity distribution becomes much more complicated and is described by Laguerre polynomials (26). In this case the characteristic radius may not realistically represent the spot size as the power contained within the defined radius depends upon the mode, and higher order modes have an effective spot size which is much greater than the characteristic radius. Sharp (22) defined a mode factor K, to overcome this problem, where K is defined as:

$$R = K r \qquad (2.2)$$

And R and r are the beam radius and the characteristic radius respectively. For a TEM_{01} mode, the mode factor becomes 1.32, assuming that the value for a Gaussian beam is 1.00.

2.3.3 Polarisation

A laser beam may or may not be polarised depending upon the application. For this work on surface treatment the laser beam was polarised. This would have been of significance if the beam had been used at glancing angles of incidence. Since in this study it was not, there is no relevance in polarisation here. The beam was polarised within the laser cavity due to the fold mirrors in the Electrox laser or a single 45^0 reflector in the Laser Ecosse cavity.

2.4 Interaction of the CO_2 Laser with Materials

When a laser beam falls on a metallic surface, a portion of it is absorbed and the remainder is reflected. Absorption of the energy occurs via interaction of the photons with electrons in the target which may be either free or bound (14). Electrons absorb quanta of light energy and are consequently raised to a higher energy state within the conduction band. On collision, the electrons rapidly give up this energy to return to their ground state in a time period of the order of 10^{-12}s. The

energy absorbed is converted into lattice vibrations (heat). The increase in temperature in the metal is a function of the incident energy, the amount of energy absorbed, the interaction time and the material properties, absorption coefficient, specific heat and thermal diffusivity (27).

Ready (14) summarises the laser-material interaction into three categories:

(1) Heating without phase change
(2) Heating with solid-liquid phase change
(3) Heating with solid-liquid phase change plus plasma formation

However, an additional category, omitted from this list, is heating with a solid state phase change (as in transformation hardening). The physics of the laser-material interaction is very different for each case. Laser cladding, discussed later in this work falls into the type (2) thermal regime.

Energy input to the material surface can be defined as P/vd, where P is the incident power, v the traverse speed and d the diameter of the beam. The quantity P/vd is known as the specific energy. As its value increases, the effect of the laser beam on the material changes from one of simple surface heating through melting to vaporisation.

The interaction of a laser with a substrate is not only determined by the laser beam parameters, but also by a number of material properties (28). The laser beam parameters of importance are wavelength, spot-size and mode structure. The material parameters include specific heat (α), thermal conductivity (k), thermal diffusivity (a, where $a=k/\alpha$), latent heat (if phase change occurs) and transformation temperatures.

2.5 Reflectivity

The efficiency of a laser process depends upon the amount of light energy absorbed by the substrate. This presents a particular problem for surface treatment processes where deep penetration is undesirable and insufficient absorptivities are generally found. The absorption process is governed by a number of factors as follows:

2.5.1 Wavelength of the Incident Light

All metals have highly reflective to radiation in the long infrared (IR) region of the spectrum. The variation of reflectivity of various metals at room temperature is shown in Fig. 2.3. (20,29). For most metals, reflectivity increases with increasing wavelength, for example the reflectivity of iron increases from around 45% at 1.06μm to 90% at the CO_2 wavelength of 10.6μm. At wavelengths >5μm, reflectivity is depends on electrical conductivity, and is highest for those metals with the

highest values of electrical conductivity.
Roessler (20) defines reflectivity in terms of a coupling coefficient (γ), which represents the fraction H/H_0. Where H represents the absorbed intensity, and H_0 the incident intensity. Then for samples which do not transmit any of the incident light,

$$\gamma = (1 - R) \qquad (2.3)$$

Where R is the surface reflectivity.

For metals processing, the high reflectivity at the CO_2 wavelength poses a significant problem. There are a number of options possible for improving the coopling of the radiation to the metal, which can be divided into three categories: The first, and most obvious thing to do would be to process at a wavelength more compatible with metallic surfaces. Dausinger *et al* (30) investigated the effect of wavelength on absorption rates and found remarkable improvements with the shorter wavelength CO (5.4μm) and Nd:YAG (1.06μm) lasers which showed almost 20% improvement in absorption of steel at normal incidence.

2.5.2 Angle of Incidence of Laser Light

Absorption of laser light also depends on the angle of incidence. Light which is linearly polarised in the plane of incidence undergoes a strong absorption near the so-called Brewster angle, approximately 85^{o} from the normal for steel. This peak in the absorptivity is clearly illustrated for steel at different incidence is shown in Fig. 2.4 (30) for s and p polarised light.

Dausinger and Rudlaff (31) concluded from experiments on inaccessible areas, bore walls and complex shaped components that the use of the oblique incidence technique is practicable and offers many advantages over conventional hardening.

2.5.3 Temperature

The absorptivity of a metal increases with increasing temperature. This is due to an increase in the phonon population at higher temperatures, with a corresponding increase in the number of electron-phonon interactions per unit time.Typically, a steady increase in reflectivity upto the melting point occurs for metals. The start of melting corresponds with a rapid increase in the coupling coefficient, which becomes complex as a result of non-specular reflections by the molten metal surface and changes in the optical properties of the liquid and solid phases. Further heating leading to vaporisation may result in plasma formation. In this incident, free electrons in the plasma render it more able to absorb IR radiation than the metal, which may result in decoupling of the laser beam. Fig. 2.5 shows the effect of surface temperature on the coupling coefficient (absorptivity) of some metals.

2.5.4 *Surface Condition*

Another important determinant for surface absorptivity is the surface condition of the metal. In general, rougher surfaces increase the absorptivity as they provide greater surface area for absorption and a series of peaks and troughs which may trap the incident radiation, resulting in multiple reflections. Additionally, surface defects may be in low thermal contact with the bulk metal and may therefore raise the surface temperature (33). A study by Dekumbis (34) on the surface absorptivity (A) of aluminium and steel as a function of surface roughness (R_z) revealed a gradual increase in A with R_z for both metals, with the absorptivity value for Al peaking at 10.6μm, the CO_2 laser wavelength. Experimental work on polished, ground and milled surfaces (35), also indicated a strong dependence of absorptivity on surface condition.

However, these enhancements in absorptivity due to surface roughening not maintained at temperatures above 600^{o}C (36) as surface defects induced by roughening are annealed out.

The reliance of many CO_2 laser treatments on improved absorptivity values calls either for surface roughening (which may disrupt a machined component) or the use of surface coatings.

2.5.5 *Use of Surface Coatings*

The application of thin coatings with high absorptivity to CO_2 radiation is a common method employed for decreasing the reflectivity of metallic surfaces. For processes which do not involve melting, such coatings may be used without altering the near-surface composition.

In general, a suitable coating would be absorbent to I.R. radiation, a good thermal conductor, adherent, easily applied and with a high melting point.

The use of coatings, however, does have some disadvantages which include an extra processing step (not easily automated), obstruction to surface temperature control with pyrometers and residues remaining on the surface which may require further machining. Another inherent problem with coatings is the degradation of the coating at higher interaction times and intensities.

Colloidal graphite, zinc-phosphate and black spray paint are among the more common coatings currently in use. The effectiveness of these and others on the reflectivity of a steel surface is shown in Fig. 2.6 (after ref.31,37).

The physical behaviour of painted surfaces can be explained as follows (38): Incident energy >100Wcm^{-2} decomposes the paint leaving a charred residue. The amount of charring determines the flow of energy from the coating to the metal. Since the thickness and nature of the residue are controlled by the incident energy, absorption is intensity dependent. At high intensities, the coating is often removed and the absorptivity of the metal returns to its original value (39).

For high volume industrial application, coatings become inefficient in terms of the additional time required to complete processing.

2.5.6 Surface Oxidation

Another method for improving surface absorptivity without the use of coatings is to induce the formation of a thin coating of surface oxide. This can be achieved by raising the temperature of the surface to promote oxidation. One way of inducing oxidation is to use an excimer laser (operating in the U.V. region of the spectrum), which has been shown (40,41) to greatly enhance the coupling of CO_2 laser radiation to the metal when a pretreatment of overlapping excimer pulses is employed. This increase in coupling arises from a combination of laser-induced oxidation and roughening, the degree of which depend on the total excimer fluence (Jcm^{-2}) delivered. Varying the number of overlapping pulses per unit area allows the balance between roughening and oxidation to modified so that the required level of coupling can be achieved.

The mechanism of the oxidation/roughening process relies on the production of a surface plasma by inverse Bremsstrahlung (42), followed by the formation of a laser-supported absorption wave (LSC)(41). This further couples the radiation to the metal - by means of thermal coupling or more likely, radiation to the surface - and increases the rate of material removal. This is illustrated in Fig. 2.7 (33). The shock wave associated with the plasma forces liquid to be expelled from the focus. The liquid droplets are then oxidised (probably by atomic oxygen in the plasma(41) and the resultant surface consists of small oxide particles in a rough metal matrix. In this case, the coupling coefficient will depend upon the absorptivity of the metal target to the wavelength of the plasma re-radiation. A full explanation of this phenomenon can be found in reference 33.

2.6 The Nature of Wear

Wear can be defined as the progressive loss of material from the operating surface of a body as a result of interaction with another surface (43). Such interactions, usually loads or motions produce adhesion, abrasion or fatigue. Wear is one of the three most commonly encountered industrial problems leading to the replacement of components in engineering environments, according to Eyre (44). The extent of wear in any given situation will be a function of the loading method, speed, temperature, presence (or absence) of lubrication and its type and quantity, the chemical nature of the environment and the materials present. Wear is not generally catastrophic, but leads to marked reductions in operating efficiency and necessitates more frequent part replacement.

In order to select materials for a particular application, the wear mechanisms must be correctly diagnosed. A review of the symptoms of various wear mechanisms is given by Godfrey (45), who recommends optical and scanning electron microscopy and X-ray techniques for identification of the mechanisms. In the case of the engine exhaust valve, the three areas affected by wear and the respective types of wear are as follows (46):

(1) Valve tip - impact wear between the tip and tappet
(2) Valve stem - sliding wear between stem and valve guide
(3) Sealing face - erosion and corrosion by combustion gases and contaminants

The severity of wear at each of these points depends on the duty. Impact wear at the tip is a form of fatigue wear, which can be further classified as percussive wear. This type of wear tends to lead to deformation cracking when successive impacts at a stress above the yield strength of the material cause continual permanent deformation. Should the impact stress be below the yield strength, surface fatigue may occur on repeated impact. In the case of the valve tip, a hard surface may be applied, which must be thick enough to distribute local stresses at the surface to a large area of the softer substrate to aid in absorbing the impact load.

Sliding wear occurs between the stem and its guide (usually cast iron) This is a form of low stress abrasive wear which usually occurs with lighter loads under minimal impact. The most important property for wear resistance to low stress abrasion is hardness, which for pure and annealed surfaces is proportional to the abrasive wear resistance. However, for heat treated steel surfaces, the relative improvement in wear resistance with hardness is much lower, as illustrated in Fig. 2.8 (46) Heat treating or hard chromium plating of the stem is generally used to improve the wear resistance, where the thickness of the chromium plate can vary from 1-2μm in petrol engines to 300μm in heavy duty diesel engines.

The wear affecting the sealing face is a combination of several types of wear in which more than one process occurs simultaneously. The corrosive conditions require hot corrosion resistance to lead and sulphur compounds. Also, the sealing face must be resistant to indentation by hard particles carried in the combustion gases. Galling is a particularly insidious problem for the valve industry.

A thorough discussion of the different types of wear and their subdivisions is given in references 46 and 47.

Attempts to define wear resistance in terms of a physical quantity usually refer to the Rabinowicz equation (48), where for a load L (in kg) applied to a surface of hardness H, the wear volume, V, is given by:

$$V = \frac{k\,L\,S}{H} \qquad (2.4)$$

Where k is the wear coefficient, and S is the sliding distance in mm. A similar equation was derived by Archard (49), for two body abrasive wear, where:

$$V = \frac{k\,L\,S}{3\,H} \qquad (2.5)$$

The variation with both load and sliding distance has been shown to be linear, therefore, if the hardness of the test material approaches that of the indenter, an increase in wear resistance should occur. These equations have been applied to sliding, adhesive and abrasive wear. It must be noted, however, that the equations are simplified and take no account of ploughing or material build-up ahead of the indenter. Additionally, the wear coefficient, k, may be of limited use as it may change with the load, sliding speed and temperature. Jahanmir (50) suggests combining k and the hardness, H to form a wear constant K which can be experimentally determined. However, some authors (51) propose that wear coefficients can be predicted from published tables, assuming conditions are similar to those under which the coefficients were measured.

Considerable interest in hard coatings and surface treatments has resulted from the need to improve wear resistance of automotive engine components. The work undertaken here is concerned with ferrous materials which to date represent the largest proportion of components used in abrasive situations. For these materials, microstructure, hardness and interstitial content are the metallurgical parameters relating to wear resistance. Of course, the operating conditions and cost effectiveness are also important and the final choice of material would take all of these factors into consideration.

The effect of hardness on wear resistance has already been discussed, abrasive wear resistance being directly proportional to hardness. The effect of microstructure follows an expected trend, a hard martensitic structure showing superior wear resistance to gouging than the softer transformation structures, which decrease in both wear resistance and hardness in the following order:

Decreasing		martensite
wear resistance	↓	bainite
and hardness		ferrite and pearlite

In addition, the level of carbon has been found to be critical (52). This is a result of the interference of interstitial carbon atoms, coherent precipitates and carbides (incoherent precipitates) with the passage of a dislocation, and thus with the process of plastic flow. Interstitial carbon intensifies the work hardening process and therefore is important in determining abrasion resistance. Data presented by Borik is illustrated in Fig. 2.9 which clearly shows that high carbon levels greatly improve the wear resistance. Similar results from Steven and Caitlin (53) measured after adhesive wear tests show the dominant role of carbon. Borik (52) also found that wear resistance increased with increasing volume of carbides, providing that the hardness of the carbides exceeds that of the abrading medium

It follows therefore, that efforts have concentrated on producing hard martensitic surfaces in steels for improved wear resistance.

2.6.1 Wear Resistant Materials - Selection and Properties of Alloy Powders

Hardfacing or cladding of a selected alloy onto a substrate provides a protective layer which can resist wear. The use of powders facilitates uniformity of composition and microstructure within the coating. The factor most influential in determining the properties of the deposit is chemical composition. The composition of an alloy is chosen in response to the service conditions, i.e. the type of wear encountered, the equipment available and the cost and scale of the process necessary to achieve a suitable deposit. As a general guide, the impact resistance of an alloy decreases with the proportion of carbides present (54). Glaeser (55) recommends a systematic approach to materials selection, for wear resistance, in which the specific property requirements are compared with those of candidate materials and the material chosen using a priority system. Materials can be used as-recieved, heat treated, diffusion treated or coated. Powders are usually classified by their alloy content. A summary of the properties of surface alloy systems is given in reference 54.

Alloys based on iron are the most commonly used hardfacing materials, offering low cost and a wide range of properties. However, in general, the Fe based alloys are unsuitable for combating wear in the presence of high temperatures, oxidative or corrosive conditions. Low alloy ferrous alloys have high impact resistance but low hardness. Alloying elements are mostly of the following types: Cr, Mn, Mo, Si and C where carbon is influential in controlling the hardness and chromium is the main alloying element. This type of material usually contains a dispersion of chromium carbides. The low cost of such alloys accounts for their frequent use in applications where regular resurfacing is necessary.

The high-alloyed steels have major additions of either chromium or molybdenum and offer considerable impact and abrasion resistance coupled with high strength. The main disadvantage of this group of materials is their tendency to soften at temperatures above 250^{o}C. Also included in this category are the modified high speed steels which are tough and wear resistant upto 600^{o}C and the austenitic manganese steels which are often used for applications involving metal-metal wear and impact. These steels are work-hardenable (allowing improvement on the as-deposited hardness which is low) (56), do not crack but are embrittled at temperatures >250^{o}C.

The next most widely used alloys are those based on cobalt which perform excellently at high temperature and in corrosive/erosive conditions. The alloys are based on the Co-Cr-W-C system often with small additions of other elements. The

microstructure consists of carbides in a cobalt-based matrix. These carbides impart wear resistance to the alloys. The composition (weight percent) of Co-based systems ranges from 19-35 % Cr, 0.7-2.5% C and 0-15% W. The presence of carbides and solid-solution strengthening mean that these alloys retain their hardness at elevated temperature, but cracking of Co-based alloys on cooling is an inherent problem. The advantages of the Co alloys must be tempered by the fluctuating cost of cobalt which is more expensive than iron and nickel and the fact that cobalt is often supplied by politically unstable nations. Reliance on cobalt without a substitute is therefore quite dubious and there has been considerable interest in the automotive industry in the development of substitute alloys containing little or no cobalt.

One such group of alloys are those based on nickel. They exhibit high metal-metal wear resistance, abrasion, corrosion and oxidation resistance and retain their hardness upto about $550^{o}C$. These alloys are based on the Ni-Cr-B-Si system with a range of alloy contents (in weight percent) as follows: 0-17% Cr, 1.5-3.5%B, 0.2-1.4%C and 2.0-4.5% Si. Boron and silicon have the advantage of lowering the melting point of the alloy for ease of welding. The alloys are also self-fluxing (54), the low melting eutectic combining with surface oxides to facilitate wetting of the substrate surface. Ni-based powders generally solidify on melting to form a solid solution of chromium in nickel and a eutectic of nickel boride (Ni_3B), chromium borides (CrB, Cr_2B and Cr_5B) and other complex borides as the hard phase.

For severe abrasive/cutting applications, carbide powders are usually used, the most popular being tungsten carbide. The carbides are mostly used in a binding material of mild steel or a Ni- or Co-based alloy and are not widely used in powder form. Tungsten carbide contains WC and W_2C particles. In a high alloy matrix, carbides provide high hot hardness, wear resistance and resistance to both oxidation and corrosion.

It is important to consider the compatibility of candidate alloys with the substrate material when selecting an alloy. The two should be compatible in terms of composition, melting point, coefficient of thermal expansion and oxidation/corrosion. Ensuring compatibility not only prolongs service life but leads to a minimum stress condition in the coating. Similarly, the choice of deposition process must be chosen on the basis of cost, speed, ease of use, versatility and its ability to produce low dilution coatings with minimum distortion of the component.
Two principal cladding materials have been investigated. The first, Stellite 6'W', a cobalt-based alloy is widely used for hardfacing engine valve sealing faces and the use of lasers for the deposition process has been evaluated. The second is a Ni-based alloy, Stellite 35, which is new to the application and may provide better performance in the presence of combustion products from the unleaded and clean-burning fuels. This alloy has been mixed with various ceramic powders to study the effect on microstructure, weldability and wear.

2.6.2 Wear Resistance of Laser Treated Surfaces

The CO_2 laser offers the advantage of rapid surface modification with the possibility of local improvements in wear resistance. The mechanism by which such improvements are effected depends on the process. Melting, alloying and cladding are the main areas of interest in terms of laser induced improved wear resistance, but transformation hardening can also offer considerable improvements.

2.6.2 (i) Wear Resistance of Laser Hardened Surfaces

The use of laser transformation hardening to improve the wear resistance of components has been discussed by a number of authors (13, 18, 32). The production of hard martensitic surface improves hardness but does not necessarily imply an increase in wear resistance. However, it is generally accompanied by an increase in resistance to abrasion and surface fatigue.
The composition of En52 steel can give rise to a hardened layer consisting of a fine dispersion of Fe,Cr carbides in a martensitic matrix after laser treatment. This multiphase structure would be expected to be highly resistant to abrasion.

2.6.2 (ii) Wear Resistance of Laser Clad Surfaces

A number of workers have studied the abrasive wear resistance of Stellite alloys deposited by conventional methods (56, 57) and laser techniques (51, 58).

Antony (57) investigated the effect of hardness and carbide volume fraction on the abrasive wear of a number of Stellite alloys deposited by gas tungsten arc welding and oxyacetylene welding. The results for the gas tungsten arc welded deposits showed the greatest improvement in wear resistance (attributed to slight carbon pickup during oxy-acetylene welding) wear loss being inversely proportional to hardness. Wear resistance was greater for the more coarse structures, and a general trend of increased wear resistance with both the size and volume fraction of carbides was observed.

Silence, (56) studied the abrasive wear resistance of various cost, wrought and hardfaced Stellite alloys using a dry sand rubber wheel test. Samples with larger carbides showed less wear loss than those with finer structures for all types of structure. There did not appear to be a relationship between hardness and wear resistance for any of the alloys

Work done by Monson and Steen (59) on a Co- and Ni- based Stellites showed that laser processed deposits had better abrasive wear resistance than those deposited conventionally, despite the finer distribution of carbides in the laser samples, this was thought to be due to solid solution hardening of the matrix and formation of a fine dendritic microstructure due to the rapid cooling rates associated with laser

cladding. In fact, the laser samples showed improved wear resistance with structural refinement. Similar results were reported by Lugscheider (60). Eiholzer et al (61) studied the wear properties of an Fe-Cr-Mn-C alloy deposited by laser cladding and found superior wear resistance compared to a traditional Stellite increased alloy. The authors found that laser power and transverse speed had very little influence on friction and wear for the data they considered (q = 4 - 6kW) (V = 8.5 - 10.5 mm/s). These results are encouraging in the light of the strategic nature of cobalt supply. Lugscheider et al (62) found a large increase in wear resistance for laser clad NiCrN6B and NiCrTaB layers over plasma sprayed layers of the same alloys (Fig. 2.10).

The introduction of hard phase particles into a metallic matrix by laser cladding is another method by which wear and erosion resistance can be improved. Tucker et al (63) investigated laster cladding of varying mixtures of carbides WC and TiC Co based alloy powders and found the erosive wear behaviour varied with the carbide species, WC being preferable to TiC. Dekumbis (64) reports interest in Co-based matrices with additions of up to 83% by weight WC for the wear protection of tools. The results of two body abrasive wear tests as part of this study Fig. 2.11 (64) illustrate the reduction in wear due to coating, the greatest reduction shown for the laser coated samples.

Most work in this area has centred around ceramic particle injection into a melt pool on the substrate surface. Cooper and Ayers (65) found significant improvements in erosion wear resistance of TiC injected surface Ti-6AL-4V and AL alloys with as little as 25-30 volume percent carbide in the injected layer. Improvements in relative wear rates of 7-38 times were found depending on the alloy type and processing conditions. However, particle injection did not appear to be suitable for impact wear applications. Similar results (66) point to the improvement in wear resistance due to ceramic particle-injection. It has been suggested (67) that the process may not be suitable for applications involving high level cyclic stress as there is a tendency towards cracking for some carbide injected metals.
An interesting adaptation by Puig *et al* (68) showed that laser fusion of an initially graphitised $Ni_{70}Cr_{30}$ substrate produced surfaces equally resistant to wear as those produced by particle-injection of chromium carbide powders on nimonic 80A.

Belmondo & Castagna (69) compared the wear resistance of laser possessed plasma sprayed metal + carbide powders. The powder, 70% Mo, 1.2% Cr, 18.8% Cr-carbide, 5% Ni and 5% Si (Wt. %) was pre-placed onto cast iron and melted using a CO_2 laser beam. Reciprocating motion wear tests showed a marked reduction in abrasive wear for laser coatings, especially at higher applied pressures (800-1000 N/cm^2).
A recent study by Abbas et al (70, 71) on the wear resistance of incorporated SiC particles in a Stellite 6 laser clad matrix showed a marked improvement in wear resistance and hardness for the composite Stellite 6/SiC clads compared to Stellite

6 alone. Cladding with a mixture of 10% SiC + Stellite achieved an approximately twofold increase in wear resistance and hardness compared to Stellite clads, attributed to carbon enrichment of the Stellite by dissolution of SiC rather than the presence of undissolved SiC particles. however, at levels less than 19 Wt.% SiC, the level of dilution of the clad was found to increase.

2.7 Surface Modification to Resist Wear

The material properties required to resist wear can be achieved either within the bulk material by heat treatment, which may or may not involve diffusion of additional elements, or in layers produced on the surface. The principal processes of each category are shown in Fig. 2.12 (46). This introduces the techniques of laser transformation hardening and laser cladding for wear resistance and compares these methods firstly with other surface treatment techniques effected by laser and secondly with the more conventional techniques suitable for application to the poppet exhaust valve. For a comprehensive review of the applicability, advantages and disadvantages of each method, Gabel and Donovan (72) should be consulted.

2.7.1. Laser Transformation Hardening (LTH)

This section serves as an introduction to LTH, which is discussed in more detail in Chapter 3. Laser heat treatment is primarily used on steels and pearlitic cast irons whose transformed structures quench to a harder structure. The first use of the laser for hardening dates back to the 1960's, when Speich *et al* (73) started metallurgical research of the process. The first application was in the Saginaw Steering Gear Division of General Motors in 1970 (74). Since then the use of lasers for surface hardening has spread rapidly and is widely used in production, a comprehensive list of the applications is given by Gregson (75). The initial aim of laser transformation hardening was to harden against wear, but the practical uses have been greatly extended to encompass a range of metallurgical problems including:

(1) Increasing hardness, strength and fatigue life
(2) Wear reduction (76)
(3) Rehardening martensitic steels
(4) Facilitating lubrication
(5) tempering metals
(6) Creation of surface carbides
(7) Creation of unique wear patterns

The experimental arrangement for transformation hardening consists of a defocussed laser beam which is passed over the surface of the material increasing the temperature as it does so. A thin surface layer is rapidly heated above the austenitisation temperature. Quenching via the bulk metal after the beam has passed effects hardening by the formation of martensite. Surfaces to be hardened are usually treated to reduce the reflectivity.

2.7.2 *Laser Cladding*

Laser cladding and hardfacing using the powder injection technique are fusion welding processes. The laser is used to produce a weld pool which travels over a substrate surface, into which is blown powders to produce low dilution, fusion bonded deposits (77). The process is fully discussed elsewhere (24) and is reviewed in Chapter 3.

Laser cladding is a process which can be fully automated to produce high quality deposits with low porosity and good interface strength, especially for the coverage of small thermally sensitive areas. Basic bead shapes have been identified (78) for the production of successul overlapping tracks and Steen (79) outlines three limits for the production of low dilution fusion bonded layers as follows:

(1) onset of porosity - aspect ratio, porosity parameter = $^{PV}/_{m}$, $JSmm^{-1}g^{-2}$

(2) onset of dilution - upper energy balance, dilution parameter = $^{P}/_{md}$, $Jg^{-1}mm^{-1}$

(3) loss of continuity of clad - lower energy balance = P(1-r-s), Jmm^{-2}

Where P = incident power, W, M = powder feed rate, gs^{-1}, D = beam diameter, mm, V = traverse speed, mms^{-1}, r = reflectivity and s = shadow effect of particles in screening subs. surface

These 3 parameters define the operating region for the process. The process is also suitable for rapid alloy scanning (79)

2.7.3 *Associated Laser Surface Treatments*

A comprehensive review of surface treatments using high power CO_2 lasers is given by Steen (80). The techniques discussed below are those laser surface methods which have been considered for the treatment of engine valve steels in place of LTH or laser cladding.

2.7.3 (i) *Laser Surface Melting*

The laser surface melting process is conducted in the same way as transformation hardening but with the use of a near focussed beam, and an inert atmosphere to prevent surface oxidation. The process is extremely flexible and the rapid solidification rates produce very fine, almost homogeneous structures to a surface finish of ~25μm. The residual compressive stresses developed in the treated layer due to the formation of martensite are thought to improve not only hardness and fatigue properties, but also resistance to corrosive, erosive and abrasive wear (81). The convective flow responsible for homogenisation may also cause a solute banding effect (82), which is undesirable. Surface melting is generally confined to

inhomogeneous materials such as cast irons, tool steels and stainless steels which can be homogenised in this way. It is therefore not ideal for the treatment of the valve steels En24 and En52. A further drawback of utilising the process for the valve steels is the flow of material at the surface during melting which requires a further machining step of a hardened surface.

2.7.3 (ii) Laser Surface Alloying

Addition of another material to the laser induced melt pool forms the basis of the surface alloying technique. The process allows control of the surface composition so that an enhanced surface layer can be produced at minimal cost. There are a number of methods for introducing particles to the melt pool which are discussed by Chen (83). The process is versatile, with many systems possible. The fluid flow problem at the surface is the main disadvantage of the process.

2.7.3 (iii) Particle Injection

Similar to laser cladding, this technique involves blowing powder into the melt pool without the powder melting. The process is aimed at improving hardness and wear. Although still in its infancy, particle injection has been applied to aluminium and its alloys and to stainless steel (84). The important requirements for an effective coating are sufficient wetting of particles by the matrix, good bonding to the matrix and minimum dissolution of particles in the melt pool. These restrictions require a clean surface and low level of superheat. The principles of this technique apply to the mixed powder cladding experiments performed in this work.

2.7.3 (iv) Shock Hardening

A short pulse of high power radiation incident on a metal surface generates a high temperature plasma. The blow off from such a plasma can induce a shock wave in the substrate which is reflected within the substrate generating very high pressure. There is little surface disruption, but the phenomenon can induce metallurgical and mechanical changes such as stress hardening. A study of the effect of shock hardening on Ni-based superalloys (85) found that the main physical parameter is the impulse momentum given to the material, which is related to the strain microstructure.

2.7.3 (v) Laser Enhanced Plating

The use of lasers to irradiate substrates in plating baths greatly increases the plating speed in the irradiated region during both electro- and electroless plating. This technique allows modification of existing deposits and also the deposition of patterned areas on substrates. Nd:YAG and argon ion lasers have been used to effect enhanced plating but CO_2 lasers are not effective as plating solutions are not transparent to 10.6μm radiation.

2.7.3 (iv) Laser Physical Vapour Deposition(LPVD)

This technique involves the use of lasers to vaporise material for deposition or to control the location of vapour condensation by substrate heating. Vaporisation is performed either by simple heating of coating materials by continuous wave laser to form a substantial amount of non-ionised vapour - which results in fairly even coverage, or by plasma condensation using short, high energy laser pulses to form a mixture of liquid, ionised and non-ionised vapour phases, in this case, coatings are rougher and metallic deposits may exhibit unusual electrical properties. Similarly, deposition can be achieved by laser heating a substrate, over which thermally sensitive vapour is blown to produce deposition by pyrolysis. This process is very slow.
Alternatively, the laser can be used as a clean heat source to evaporate a target under vacuum for deposition. e.g. excimer laser ablation (86).

2.7.3 (vii) Laser Chemical Vapour Deposition(LCVD)

This is the process whereby a laser beam is used to drive a chemical reaction by pyrolytic or photolytic processes to form a solid film on a substrate. Laser assisted CVD offers the advantages of high deposition rates, small heat affected zone, cleanliness and control over conditions when compared with other methods of CVD. The process is used mainly for microelectronics applications but is also useful for the production of wear resistant hard coatings, such as TiC, TiN, Ti(C,N), Al_2O_3, W_2C, W_3C, W, Cr_3C_2, SiC, $(HfN)^2$, $(TiB_2)^3$ (46). These layers are frequently applied to metal cutting tools and occasionally to dies and cold extrusion punches. CVD coatings tend to be dense and highly adherent, but due to the high temperatures involved (500-1000^{0}C) substrate distortion may be a problem for steel components.

2.7.3 (viii) Coating Consolidation

Similar to laser cladding, this technique utilises the CO_2 laser to consolidate coatings applied by some other method. The coatings may be hardfacings in their own right and are effectively sealed on the outer surface by the laser, which reduces the level of porosity. Successful consolidation of corrosion resistant plasma sprayed coatings has been achieved (87) but hardfacing materials can be problematic. Thermal stresses lead to solidification and cooling cracking in low ductility coatings rendering the technique effective only for thin layer consolidation.

2.8 Other Techniques for Surface Hardening

There are a number of surface hardening techniques which can be used in the treatment of valve stems or other components requiring localised hardening. In general these methods involve one of three basic processes. The first involves

raising the temperature of the surface above the austenitisation temperature and rapidly quenching to produce a martensitic surface i.e. a thermal treatment, the second involves the addition of elements to the surface by diffusion combined with thermal treatment i.e. a thermochemical hardening treatment,and the final process involves plating the surface with a hard or wear resistant metal. The production of engine valves requires the use of one of these techniques, the most popular being either induction hardening or hard chromium plating. Current methods of surface hardening are discussed below

2.8.1 Hardening Treatments Involving Thermal Transformation

Laser transformation hardening falls into this section, the advantages, disadvantages and principles have already been discussed.

2.8.1 (i) Induction Hardening (88, 89, 90)

An alternating current flowing through an inductor (work coil) generates a highly concentrated, rapidly alternating magnetic field within the coil. This field induces eddy currents in the surface of the component, an electric potential is induced in the part which represents a closed circuit, hence the induced voltage causes the flow of current. The resistance of the component to the flow of current results in heating. The strength of the magnetic field is largely dependent on the magnitude of the current in the coil.

The pattern of hardening will be determined by the shape and number of turns in the inductor, the frequency and power of the A.C. input, the length of the heating cycle and the nature of the work piece. An example of the path of magnetic flux through a bar is given in Fig. 2.13 (90). The coil can be chosen to accommodate the part to be heated and the heating pattern desired, and are usually water cooled. The depth of heat penetration will be a function of the resistivity and permeability of the component and also of the frequency of the A.C. current. The latter being the main variable. Simplified relationships exist for the approximate calculation of penetration depth as follows (90):

$$d_c = \frac{20}{\sqrt{f}} \qquad d_h = \frac{500}{\sqrt{f}} \qquad (2.6)$$

cold state ($20^{o}C$) hot state ($800^{o}C$)

Where d is the penetration depth (mm) and f the frequency (Hz)
Conduction in the material will in fact increase the depth of penetration by a factor d_1 given by:

$$d_1 = 0.2\sqrt{t} \qquad (2.7)$$

Where d_1 is the penetration depth (mm) and t is the duration of heating (s).
The total penetration depth is thus $d + d_1$. As a general guide, the conditions required for a minimum depth if heating will be maximum power density, high frequency and minimum duration.

In summary this technique is versatile, relatively cheap to operate, easily automated, causes minimal distortion, surface oxidation and decarburisation and is a clean, quick method of selective hardening.
Induction hardening generally produces an increase in fatigue strength of the part. Surface heating produces compressive stresses in the skin of the component, opposed by tensile stresses in the core, as a result of the volume increase occurring with the transformation to martensite. Should surface decarburisation occur during the treatment, quench cracking may be a problem as a result of the formation of a rigid pearlitic surface which will be in tension when the material below undergoes the martensite transformation.
The major disadvantages of the method are the capital cost of equipment and the restrictions imposed by component shape and the grade of steel, which is usually limited to the 0.3-0.5% carbon range.

2.8.1 (ii) Flame Hardening (90, 91)

This involves the direct impingement of a high temperature flame and then a quench in water or oil, to produce the desired level of hardness. The high temperature flame is obtained from a mixture of oxygen or air and a combustible gas which are burned using flame heads. The depth of hardness in this case depends on the type of fuel used, the duration of heating, the part geometry and the method and medium for quenching. The hardenability of the component will also be a factor. The flame hardening technique is extremely versatile and there are a wide range of heating conditions possible, including spot or stationary heating, spinning, progressive and a combination of spinning and progressive. The method selected depends on the size and shape of the component and the pattern of hardening required. The flame hardening operation is illustrated in Fig. 2.14.

The advantages of the technique include low capital costs, high versatility and the ability to treat large parts or those requiring accurate treatment of selected areas.
However, the operating costs are somewhat higher than for induction hardening.

2.8.1 (iii) Electron Beam Hardening (EBH) (88, 92, 93, 94)

The electron beam process is also suitable for selective hardening. The surface of a ferrous alloy is rapidly heated above the austenitisation temperature by the

impingement of an accelerated stream of electrons. Heating occurs by the transfer of kinetic energy of the electrons to the atomic structure of the component in the form of heat. Self-quenching occurs when the electron beam is switched off, in a similar manner to laser transformation hardening.
The resultant surface is again compressively stressed and martensitic. For selective treatment the power density is usually about 3 kW/cm^2 and is achieved by restoring. In general, the transition in properties from the hardened layer to the base depends on the conditions of preheating employed (94).

The electron beam technique is a highly controllable method of hardening which usually removes the need for post heat treatments. There are however, a number of process restrictions as follows:

(1) the electron stream requires line of sight access to the surface and a minimum impingement angle of 25°
(2) components must be demagnetised to avoid magnetic interactions with the beam and unnecessary beam deflection
(3) mass of part must be sufficient to facilitate self-quenching
(4) treatment may need to be done in vaccuo

Surface finish is important for EBH as ridges in the surface may promote melting. For the short austenitisation times employed, an isothermal prior heat treatment may increase the hardenability of the steel (92).

2.8.1 (iv) High Frequency Resistance Hardening (46, 93)

This process consists of a water cooled 'proximity conductor' placed close to the surface of the component is connected to the workpiece by a pair of contacts at the edges and to a high frequency (~400kHz) power supply. Surface heating occurs beneath the conductor followed by self-quenching when the power is switched off. The depth of hardening is controlled by the frequency, heating time and power level but is typically 0.37-0.75mm. This method of hardening is rapid (<0.5s for a typical cycle) and can be applied to most medium/high carbon or low alloy steels. It offers a real competitor to LTH and EBH as the capital outlay is low and there is no requirement for a vacuum or surface coating.

2.8.2 Treatments Involving Diffusional Addition of Elements to the Surface (88, 46, 93, 90)

These treatments are performed on steels in either the austenitic or ferritic condition, depending on the process.

2.8.2 (i) Carburising or Case Hardening

This process involves heating low carbon, low alloy steel to the austenite phase field in the presence of a carburising medium, which may be a solid media, in salt baths or in gases in the temperature range 825 - 925^{o}C. Carbon diffuses into the surface from the carburising medium, and at levels upto the eutectoid level of the particular steel.will increase the hardness of the martensite produced on quenching. Water or oil quenching is used depending on the steel which is to be treated. Low alloy steels can usually achieve maximum hardness with an oil quench, thus minimising cracking problems associated with water quenching. Carburisation always takes place via a gaseous phase regardless of the method used. The three production methods are outlined below:

Carburising via a Solid Substance (Pack Carburising)

Components are packed into carburising compound in steel boxes. Carbon monoxide derived by the reaction of oxygen (enclosed in the box) with carbon dioxide decomposes at the surface of the steel to form carbon and carbon dioxide. This nascent carbon is dissolved by the austenite phase of the steel, whilst the carbon dioxide reacts with carbon on the carburising compound to replenish the supply of carbon monoxide. An energiser or catalyst of $BaCO_3$, $CaCO_3$ or $NaCO_3$ is added to the charcoal to reduce the level of carbon dioxide in the system and produce more CO. The process can therefore continue until the required case depth is achieved. Subsequent cooling is followed by austenitising and quenching to further harden the case. This method is not widely used due to the poor control of case depth and the large degree of manual labour required.

Salt-Bath or Liquid Carburising

The carburising agent used for this technique is either sodium or potassium cyanide and compounds of the alkaline earth metals. The chemistry of the system is fairly complex but carbon diffuses from the bath into the surface as well as nascent nitrogen from the system. The temperature of the bath as well as the constituents determine the case depth produced. Salt baths are usually classified as low (850-900^{o}C) or high (900-950^{o}C) temperature for shallow and deep cases respectively. The liquid method is quicker and more versatile than pack carburising and the operator has more control over the case depth. However, the salts used are toxic and disposal presents a problem.

Gas Carburising

The gaseous carburising process is controllable and reliable. It utilises carbon from hydrocarbons to produce the hardened layer. Control of the gas composition allows more accurate control of the carbon concentration. Methane is the most commonly used hydrocarbon and is supported by a carrier gas of nitrogen or a reducing gas mixture witha carbon potential, such as class 302 gas, an endothermic gas which allows a wide range of carbon control. During the process, there are a number of

simultaneous reactions occurring, the exact sequence of which is not known. However, the reactions can be summed to give:

$$CH_4 \rightarrow C\,(\text{in Fe}) + 2H_2$$

And in some cases, the methane content is high enough to produce this reaction directly on the steel surface. A number of methods for controlling the surface carbon content, and thus the case depth and hardness.

2.8.2 (ii) Carbonitriding

The carbonitriding process is a modification of the carburising process in which carbon and nitrogen are absorbed into the steel surface simultaneously. The process is effected using either a salt bath or gas method. The addition of nitrogen to the surface increases the hardness and allows oil quenching to reach full hardness even in plain carbon steels. It is thus suitable for a range of applications and is most commonly associated with shallower case depths due to the lower temperatures and shorter durations than gas carburising. The addition of nitrogen also improves the wear resistance relative to carburised steel surfaces. This is an austenitic thermochemical treatment. The salt bath method is basically the same as cyanide bath hardening where carbon monoxide and nascent nitrogen are liberated from sodium cyanate. This process has the disadvantage of waste disposal. The more common gas carbonitriding technique involves the addition of ammonia to the carburising atmosphere. The ammonia content is usually 3-8%. Nascent nitrogen is formed at the component surface and diffuses into the surface with the carbon. The addition of ammonia is often delayed until the last 30-60 minutes to avoid the development of a soft skin as a result of internal oxidation in the surface layer.

2.8.2 (iii) Nitriding

Nitriding is a ferritic thermochemical treatment i.e. it involves the introduction of atomic nitrogen into the ferrite phase field and requires no phase change. Nitriding is applicable all steels, but is more frequently confined to low alloy and tool steels, it imparts a number of desirable characteristics to the steel surface (90):

(1) Improved hardness and wear resistance
(2) Improved corrosion resistance for non-stainless steels
(3) Dimensional stability
(4) Increased resistance to fatigue
(5) High-temperature hardness and resistance to tempering

The improved hardness observed can be attributed to the formation of a fine dispersion of nitrides and carbo-nitrides. Nitriding can be carried out in a gaseous environment, using salt baths or powder, in each case the case depth depends upon

the time and temperature of the treatment, the steel composition and the nitrogen activity.

Gas Nitriding

Ammonia at a temperature between 495 and 565^{o}C is allowed to flow over the components. In contact with the steel surface, the ammonia dissociates to form nascent nitrogen and hydrogen. Atomic nitrogen occurring instantly on dissociation diffuses into the steel surface to form nitrides in the surface layer. Case depths of 0.2-0.7mm are generally possible, although the process takes many hours to complete. Less common variations on the gas nitriding process include the use of ammonia and nitrogen or ammonia and hydrogen mixtures, or the addition of hydrocarbons to the ammonia stream (usually propane) to aid carbon diffusion. In this case the nitriding temperature is increased to around 570^{o}C.

Ion Nitriding (Plasma Nitriding)

This process was originally called glow-discharge nitriding (88), and allows accurate control over the depth and growth of the nitride layer. The components are connected to a power supply in vacuum and they act as a cathode. The steel surface is observed to form a plasma, causing ionisation of ammonia gas applied to the system. Nitrogen ions are produced and accelerated to impinge on the surface of the steel, the surface is cleaned and heated and the active nitrogen is absorbed as before. The process is more rapid than conventional gas nitriding, requires lower temperatures and is more versatile metallurgically.

Salt-Bath Nitriding

Liquid nitriding is carried out at similar temperatures to gas nitriding, and offers the same advantages in terms of the resultant case. The salt bath consists primarily of cyanates and due to the sub-critical temperature employed is suitable for finished components. The process also results in more nitrogen, less carbon absorption than the higher temperature techniques, and is much more rapid than the gaseous nitriding process. Another advantage, is that the brittleness sometimes inherent with gas nitriding is avoided. On the negative side, salt bath nitriding can be dirty and treatment in excess of 4 hours results in pore formation. The hardened layer may be less tough than a gas nitrided case due to the rapid cooling cycle employed. Variations on the composition of the salt baths used have trade names such as Sulfinuz and Tufftride, which are well discussed in reference 90. In certain applications, the process is accelerated by aerating the salt bath with anhydrous ammonia or air.

Since the primary objective of this work is to improve wear resistance, a further problem of the nitriding method should be addressed. Gas nitriding results in the formation of brittle compounds of nitrogen at the surface of parts. This effect is termed the 'white layer effect', and it is only possible to avoid this by very accurate process control. The layer must be removed before the part goes into service by

grinding or chemical methods, and makes the total cost of the process high. An interesting point to note is that liquid nitriding increases the amount of ε–carbonitride formed which provides a corresponding increase in the wear resistance. Similar increases in the ε-carbide level can only be obtained during gas nitriding if hydrocarbons are added to the system.

2.8.2 (iv) Nitrocarburising

This technique is a ferritic treatment, for the addition of carbon and nitrogen to a ferrous surface. The process is quick (<3 hours), and results in a compound surface layer which possesses improved wear and friction resistance, higher resistance to fatigue, and anti-scuffing properties. Retention of nitrogen in solid solution beneath the compound layer further improves the material properties, and is achieved by an oil or water quench immediately after treatment. The furnaces tend to be very similar to those used in carburising, with an atmosphere of ammonia in endothermic carrier gas (type 302 as for carburising). Variations on the basic process use different carrier gases and slightly higher operating temperatures. Again, ε-carbide is present in the surface layer.

2.8.3 Metalliding and Similar Techniques (91, 93, 89, 46)

A wide range of metals (Cr, Co, Al, Ni, Nb, Zn, V) and metalloids (B, Si) can be deposited on steel surfaces by diffusion techniques. These processes have not been widely used, chromising, boriding and the Toyota Diffusion process being the most promising.

Chromising

Generally applied to carbon or tool steels this process deposits Cr on the surface from 900-1020^{o}C for about 12 hours to give a 0.02-0.04mm thick layer. Chromium diffusion is limited, but C from within the steel diffuses to the surface to form chromium carbides, hence carburising to enrich the surface C-content is often applied as a pretreatment. A simple Cr layer is possible if required. Chromium carbide layers are hard (>1500HV) and wear resistant upto ~700^{o}C. Pack or gaseous methods are available. On the negative side, deposits are less adherent than those produced by thermochemical methods and component distortion may occur at these high temperatures.

Boriding

This technique produces extremely hard (1500-1900HV) coatings which are wear and corrosion resistant and have excellent frictional and anti-galling properties (93). Applicable to any ferrous metal, this technique deposits boron in the form of a paste or powder at about 950^{o}C to form a layer of iron borides. Layers upto 0.15mm thick are possible. Boriding via pack, paste, salt bath, plasma or gaseous means are

available, these are reviewed by Dearnley and Bell (95).

Toyota Diffusion (TD) Process

Layers of Ti, Nb, Cr and V carbide, 5-10μm thick have been produced by the TD method. The very high hardness of such layers provides excellent wear and corrosion properties with toughness and a low friction coefficient (91). The process is carried out in a fused borax salt bath at 800-1050^{o}C for 1-10 hours for the formation of a pure carbide layer which grows by reaction of the carbide former with carbon atoms diffusing from the substrate.

2.8.4 Surface Plating Techniques

The only plating metal of interest in terms of wear resistance is hard chromium plating. Nickel plating can be used but is primarily applied for its resistance to corrosion, rather than its wear properties.

Chromium Plating

Hard chromium plating is formed by electrodeposition from a solution of chromic acid and a catalytic anion. The process is very popular for the treatment of valve stems as the coating produced is hard, resistant to corrosion and wear, reduces friction and prevents galling and seizing. Another application of this technique, the coating of piston rings is said to improve lifetime by five times, for a 100-175μm layer (88).

The conventional plating bath contains a mixture of chromic acid and sulphate to act as a catalyst. The ratio of the constituents varies but the ratio of chromic acid to sulphate radicals is in the range 75:1, to 120:1, the mid-range providing optimum plating distribution. Other process variables are the current density, temperature and nature of the anodes, (insoluble lead alloy anodes are the norm), which can be selected to give the plating thickness required.

2.9 Other Techniques for Wear Resistant Coating Production

Some of the various processes used for hardfacing are shown in Fig. 2.12. A hardfacing technique should be able to minimise dilution with the base metal, to preserve deposit properties and to be effective at high deposition rates to preserve the economic advantage. Most welding processes are adaptable to hardfacing providing preheating and other techniques are employed to prevent 'stress cracking', and minimise dilution.

2.9.1 Oxy-acetylene Welding

Oxy-acetylene welding can be performed with either bare wire or powder, filler material and involves heating the substrate in an oxy-acetylene gas flame and then

melting the coating onto the surface. If the coating is highly oxidation resistant, the surface is first heated with the flame using excess acetylene to produce a thin carbonised layer which has a lower melting point than the substrate bond and bonds well with the alloy. This is a low-cost versatile process which is also portable and can produce high quality coatings. However, deposition rates are low unless automated feed is used and highly skilled operators are needed. In addition, component preheating is often required to promote fusion (51) which leads to slow cooling and deposition rates. The technique is widely used for the deposition of nickel and cobalt based powders.

2.9.2 Tungsten Inert Gas (TIG) Hardfacing

This process uses bare cast filler rods which are fed either manually or automatically into an arc struck between a non-consumable tungsten electrode and the substrate. An argon shield gas is generally used to prevent oxidation and a DC polarity. The capital outlay is higher than for oxy-acetylene welding and the equipment less portable but the process is compatible with a wide range of alloy powders to produce uniform deposits at a rate which is slow manually but acceptable with automatic feed. The process requires little back-machining but due to the higher temperature involved, tends to lead to higher levels of dilution of oxy-acetylene welding. TIG welding is often used for coating small areas especially with high alloy materials as oxidation is less of a problem.

2.9.3 Plasma Transferred Arc Welding

This process involves the use of a plasma heat source generated from a restricted DC TIG arc. The plasma is formed when the gas ionises as it passes through the orifice. The hardfacing material, in the form of wire or powder, is then fed into the plasma stream with an additional flow of Shield gas. A D.C. power supply connects the tungsten electrode (+ve polarity) and workpiece and a second DC supply connects the electrode tot he restricting orifice. Support is a non-transferred arc which supplies additional energy and acts as a pilot to initiate the transferred arc. The process is controllable, easily automated and offers a method for producing smooth, low dilution deposits at a high deposition rate. It is widely used for hardfacing with Ni-Cr or Co-Cr alloys or for mixing tungsten carbide particles with alloys to produce heterogeneous deposits for abrasion resistance (46). In this case, the carbides are fed separately behind the arc to limit layering of the deposit and carbide melting.

PTA welding has replaced TIG and oxy-acetylene techniques in many high-volume applications, inducing the coating of engine valves as discussed by Matlock *et al* (96). However, deposits may be overly thick (97) and overspraying is a problem. The process is suitable for a wide range of alloy deposition and produces microstructures similar tot hose achieved using TIG welding (10).

2.9.4 Spraying/Fusion Hardfacing

This technique involves the fusion of sprayed coatings via a heat source and is limited to low melting point (<1250^{o}C) alloys, (51), oxidation and excessive melting is a problem for the higher melting point alloys). Spraying is achieved by one of the following methods: arc, plasma, flame, detonation gun or the cheapest and most common method of flame spraying.

Flame spraying is achieved using an oxyacetylene flame with powder supplied in a jet of compressed air. The resultant mechanically deposits are bonded upto 25mm thick (51), 80% dense and are formed from impacted molten or semi-molten powder. Fusion via oxyacetylene torch, induction fusion or vacuum fusion is then completed, the method depends on the volume of components of the coating thickness. In all cases, preheating is required which results in slow cooling therefore minimal cracking. Spray/fusion techniques produce metallurgically bonded coatings with negligible dilution, as the substrate never becomes molten. This technique is especially useful for inclusion of carbide particles in the deposit.

There are a number of other hardfacing techniques which are covered elsewhere (46) but which are unsuitable for the hardfacing of poppet valves.

2.10 Metallurgical Considerations of Laser Surface Hardening

2.10.1 Mechanism of Transformation Hardening in Ferrous Materials

Transformation hardening of ferrous materials involves raising the temperature of the material above the austenitisation temperature followed by rapid quenching to produce a hard martensitic structure. The microstructure is transformed by a phase change which occurs without melting.

The process is the same whether complete hardening or selective surface hardening is required. Examination of the process involves looking at the nature of the iron-carbon binary system to understand the phase changes which occur on heating and rapid cooling.

2.10.2 The Fe-C System

Microstructures resulting from the heat treatment of steel consist of one or more phases containing iron, carbon and other elements. Consider the Fe-C phase diagram shown in Fig. 2.15, which illustrates the phases present under equilibrium conditions at different temperatures and compositions. The critical transformation temperatures A_1 and A_2 are also shown. This diagram illustrates the correlation between structure and heat treatment and shows the relationship between the allotropic forms of iron. The body centred cubic α-iron (ferrite) is stable

below 910°C whilst above this temperature, the face centred cubic γ-iron (austenite) becomes stable, and at temperatures above 1400°C, δ-iron (b.c.c.) is stable. The versatility of heat treatments available for steels relies on the retention of this allotropy in the presence of considerable amounts of alloying elements.

The presence of alloying elements, other than carbon results in unique shifts of the phase field boundaries in the Fe-C diagram due to the widely differing solubilities of the elements in ferrite and austenite. The elements fall into two classes, the austenite stabilisers, such as Mn, Ni and the more common ferrite stabilisers e.g. Si, Cr, W, Mo etc. Relatively large amounts of these elements can be added to the Fe-C system without significantly changing the structures which are developed during heat treatment. The presence of a single-phase austenite field at higher temperatures allows the production of a single phase microstructure, and cooling from this field makes possible a wide range of microstructures depending on the rate and duration of the heating/cooling cycles.

A purchased plain carbon steel consists of a mixture of ferrite (almost pure iron) and cementite (Fe_3C) and inevitably also contains traces of other elements and non-metallic impurities. The proportion of Fe_3C is a function of carbon content (Fe_3C is always the prevalent carbide in plain carbon and low alloy steels). This is due to the limited solubility of carbon in ferrite (about 0.020% maximum at 1340°C)(98). Carbon is dissolved in octahedral interstitial sites in the iron lattice which are much smaller in ferrite than in austenite. Hence on slow cooling from the austenite phase field, cementite is formed as a result of the decreasing solid solubility of carbon with temperature. The process is accompanied by a characteristic time lag due to the formation of nuclei. The dispersion of such carbides depends upon the diffusivities of the elements present, particle sizes ranging from a few to 25μm diameter, finer distributions exhibiting higher hardness values.

2.10.3 The Fe-C-Cr System

To examine the effect of significant amounts of alloying elements on the microstructure of a steel, it is necessary to consult the appropriate ternary phase diagram for the system. In this case the Fe-C-Cr system is the pertinent one. This system is discussed by Rivlin (99) and Lundberg *et al* (100). The phase diagram for the C-Cr system is shown in Fig. 2.16 (101). In a pure Cr-C system (Fig. 2.17), three types of carbide exist (98), $Cr_{23}C_6$, Cr_7C_6, and Cr_3C_2. The crystal structures, composition limits and lattice parameters of each type of carbide are given in Table 2.2. It has been pointed out however (102) that the lattice parameters may change in relation to the steel composition e.g. $(Cr,Fe)_{23}C_6$ a=10.589Å for a high chromium, low nickel steel, whereas for a similar carbide in a chromium-nickel steel the lattice parameter becomes a=10.598Å.
The structure of $Cr_{23}C_6$ allows chromium in the lattice to be replaced by iron upto

around 30 weight %, above this level, some tungsten must be present in the lattice to enable it to dissolve more iron - otherwise, cementite forms instead. Referring then to Fig. 2.17, one would expect En24 (1.4% Cr) to have $(Fe,Cr)_3C$ type carbides, and En52 (8.5-9.5% Cr) to have $(Fe, Cr)_{23}C_6$ type carbides. This is further borne out by an investigation by Vitek and Klueh (103) into the precipitation reactions of a 9Cr-1Mo-V-Nb alloy, which revealed a combination of chromium-rich $M_{23}C_6$ precipitates and vanadium-niobium-rich MC carbides, with $M_{23}C_6$ type carbides as the primary precipitate. These precipitates were shown to contain 63% Cr, 29% Fe and 7% Mo. An interesting point to note from the Fe-C-Cr phase diagram, is that the α solid solution in the equilibrium $\alpha+M_7C_3+M_{23}C_6$ becomes richer in iron at lower temperatures; consequently, $M_{23}C_6$ may appear in alloys with <10 wt. % Cr, e.g. En52.

2.10.4 The Formation of Austenite

At temperatures above the A_3 temperature of a steel, austenite is formed by the solid solution reaction of ferrite and carbide. The rate of austenitisation , above A_3, increases with increasing temperature. The heating process is important in determining the final microstructure of the steel as the properties depend largely upon whether complete carbide dissolution occurs and the level of homogeneity of dissolved elements in the austenite. Equally important is the initial microstructure, which determines both the mechanism and speed of austenite formation. For dual-phase spheroidal carbide/ferrite steels like En24/52, austenite formation begins at the ferrite-carbide interface by classical heterogeneous nucleation (104). The carbide particles become enveloped by austenite, subsequent transformation depending on the rate carbon diffusion through the austenite as the carbides dissolve.

2.10.4 (i) The Effect of Initial Microstructure

The effect of microstructure on austenite formation was discussed by Roberts and Mehl (105) who found that the rate of both nucleation of austenite and the subsequent growth of austenite nodules were structure sensitive.

The relative rates of austenite formation for a pearlitic and a spheroidised steel were measured by Grossman and Bain (106). The results, plotted in Fig. 2.18, show a much faster rate of transformation for the pearlitic steel. Seaman (107) observed the effects of initial microstructure during the short austenitisation times (typically 0.01-1.0s) encountered with laser transformation hardening to be a major factor in controlling case depth and the hardness gradient between the heat affected zone and the base metal. In general, the shorter cycle times characteristic of laser hardening minimise grain coarsening leading to higher strength and fatigue resistance in steels, and allow the formation of martensite in normally non-hardenable steels (107). However, rapid heating rates lead to a number of drawbacks

depending on the initial microstructure. Coarser structures may not dissolve to form homogeneous austenite which may lead to softer areas within the heat affected zone. In addition, complex alloy carbides may have insufficient time to dissolve so that the overall carbon level may seem to be somewhat less actually exists. A similar dissolution problem can occur with pro-eutectoid grain boundary constituents which may be retained in the treated zone.

Initial microstructure is therefore critical. A study of the hardness/depth profiles for a coarse pearlitic/blocky ferrite structure and a fine spheroidal carbide/martensite structure by Seaman yielded the results were summarised (107) below:

(1) A more gradual transition to base hardness occurs for the coarser structure due to the longer diffusion paths over which uniform austenitisation must be achieved. This effect is also common to higher carbon and alloy steels.

(2) Finer structure leads to a greater effective case depth, although the surface hardness for the two structures is roughly equal as homogenisation may occur due to the high temperatures achieved at the surface.

(3) The width of any softened region at the base of the heat affected zone (often undetectable by microhardness measurements) is less for the finer structure).

An examination by Karmazin (108) of the austenitisation process for spheroidised structures of 0.80% C, 2.02% Si, 2.06% Mn, 1.05% Cr (all weight %), not only in terms of the cementite particles but also the size and morphology of ferrite grains. A comparison of two structures, one produced by tempering martensite and the second by high temperature transformation of inhomogeneous austenite, reveals that the kinetics of the $\alpha \rightarrow \gamma$ transformation strongly depend on initial structure. The morphology of ferrite grains and the location of carbide particles with respect to grain boundaries are also important. Karmazin attributes this to two factors:

(1) Si has the opposite influence to carbide forming elements on the activity of C in austenite. Consequently, there is a decreasing driving force for C-diffusion across the composition gradients close to dissolving carbides.

(2) Ferrite is stabilised by a redistribution of Si and Mn on the moving $\alpha \rightarrow \gamma$ interface. This stabilisation depends on the morphology and properties of the ferrite grain boundaries in the initial structure.

2.10.4 (ii) Mechanism of Austenite Nucleation in Spheroidised Steels

There is general agreement in the literature that austenite nucleation occurs at

carbide particles. Paxton (109) observed that for ferrite-carbide steels, with carbide diameters of around a few microns, a spectrum of nucleation times exists, and that growth may advance at a sufficiently fast rate to eliminate the necessity for further nucleation. The results of Garcia and DeArdo (110) also show that austenite is nucleated at carbide particles for a 1.5%Mn steel, with nucleation occurring over a range of times.

Speich and Szirmae (111) observed preferential austenite nucleation at junctions between carbides and ferrite grain boundaries, for spheroidised plain carbon steels. Further, they noted that primary nucleation occurred at the intersection of a cementite particle and two ferrite grains, where the available surface free energy is higher than for other sites. Similar observations were made by Dirnfield *et al* (112) for a low alloy tool steel. Site saturation was found to occur early in the reaction.

According to Paxton (109), there are three important factors governing the preferred nucleation site:

(1) the free energy change per unit volume
(2) the contribution due to strain energy
(3) the net increase in surface energy for a given volume of austenite

Since the free energy change is related to the composition of the austenite nucleus, the free energy change will always be less than the maximum attainable for alloy steels whose constituents diffuse more slowly. Judd and Paxton (113) found that austenite nucleation rate was considerably slower for a 0.5% Mn alloy than for a similar Fe-C alloy.

The possible nucleation sites for a spheroidised structure are shown in Fig. 2.19. Nucleation at carbides is preferred (111) as austenite can be stable with this structure at lower temperatures than it can in pure iron due to an increase in its carbon content as the carbides dissolve. Nucleation is especially preferential at grain boundary carbides where the free energy change is larger. Therefore sites 2 and 3 in Fig. 2.19 would be favoured over site 1. The density of grain boundary carbides thus controls the number of nucleation events. It has been shown (113) that the austenite nucleation rate at grain boundary carbides is 3-8 times greater than for matrix carbides.

2.10.4 (iii) Growth of Austenite

After austenite has nucleated and enveloped the carbides, growth proceeds by the diffusion of carbon through the austenite. Judd and Paxton (113) developed a model to explain this diffusion as follows. With reference to Fig. 2.20, consider a spherical carbide particle, radius r_0 which nucleates a spherical austenite shell after time t_0. Carbon diffuses outward from the carbide and ferrite is simultaneously consumed. C and C_a represent the solubility of carbon in ferrite and the weight percent carbon

in cementite and r_a and r_b represent the limits of austenite stability range at 775°C. The values of r_a and r_b were calculated (113) as a function of time after t_o, the results are plotted in Fig. 2.21 (109).

On the assumption that carbon diffusion is the rate controlling step, Judd and Paxton found excellent agreement between the predictions and experimental results for a zone refined 0.1%C steel. However, this was not the case for a similar alloy with 0.5%Mn addition, where a much slower growth rate than predicted and relatively poor agreement was found. Their explanation was based on the preferential partitioning of alloying elements to the carbide phase which reduces the diffusion gradient in austenite by changing the carbon activity at the $\gamma-\alpha$ interface. The model, based on boundary conditions defined by binary phase diagrams is therefore inaccurate when the presence of alloying elements alters the boundary conditions. Since carbide dissolution is time and temperature dependent, carbon concentration gradients exist for appreciable times after the carbides are no longer visible in the microstructure. Therefore, the austenite formed may not be homogeneous (114).

A study of the transformation to austenite in a fine grained ferrite/globular carbide tool steel (112) established that the rate law for the reaction was controlled by growth and was independent of the nucleation rate, the growth controlling mechanism being the advancing ferrite-austenite interface reaction. Agren *et al* (115) noted that a fine structure of spherical cementite particles in ferrite yields a more rapid increase in the amount of carbon dissolved at short times. However, when the steel had been previously annealed, to enrich the cementite in manganese, the reaction was strongly displaced towards longer times. Additions of alloying elements upto 1 atomic percent were found to produce systematic changes in the pattern of austenite growth (116). Ni, Co or Mn additions were not found to influence the growth pattern to any significant extent, whereas V, Ti, Cr Si and Al additions reduced the rate of austenite growth, producing a ragged interface and increasing austenite penetration along ferrite grain boundaries, ahead of the rim.

Under normal circumstances, the growth of austenite grains proceeds both into the ferrite matrix and along the grain boundaries, the distance of growth being larger in the latter direction. The difference in growth rate is thought (110) to be caused by the difference in diffusion coefficients perpendicular to and parallel to the ferrite grain boundaries. The formation of austenite in an Fe-10Cr-0.2C alloy was investigated by Lenel and Honeycombe (116). The results indicated that nucleation was sluggish compared to a low alloy steel whilst the growth rate of austenite was rapid and increased with temperature. (Carbide dissolution is obviously more rapid in austenite than in ferrite due to the increased solubility of carbon in austenite. This means that unless carbon can diffuse into adjacent austenite grains, carbide dissolution in ferrite is inhibited). For the alloy under discussion, carbide dissolution was notably slow and incomplete at temperatures upto 900°C.

Growth of the austenite grains after impingement is followed by grain coarsening, if the temperature is maintained for sufficient time (long interaction times) and provided that the boundaries are not locked by dispersed particles.

2.10.4 (iv) Effect of Alloying Elements on Austenite Formation

The condition of the austenite formed on heating steels affects the resultant properties of the steel. Both composition and grain size are important factors and are influenced by the presence of alloying elements. The heating process should therefore be tailored to allow for the different diffusivities of the elements present.

The effect of Cr on the formation of pure austenite (i.e. without any carbides) is to shrink the phase field by higher Cr content until pure austenite is eliminated at around 20% Cr, this is shown in Fig. 2.16 (101). Similarly, Mo has the effect of shrinking the pure austenite phase field and raising the transformation temperature.

The elements can be arranged in order of relative effectiveness in retaining carbon in combination (98) as follows:

Mn, Cr, W, Mo, Ta, V, Co, Ti

$\rightarrow$

increasing effectiveness

The fact that austenitisation depends on the diffusion of the alloying elements, which is slow compared to that of carbon, means that the heat treatment must be selected carefully.
Bowen and Leak (117) calculated the diffusion rates for Cr in alpha and gamma iron by radioactive tracing techniques and found the following room temperature values:

$$D_{Cr}(\alpha\text{-Fe}) = 8.52 \exp^{-59,000} \qquad D_{Cr}(\gamma\text{-Fe}) = 10.80 \exp^{-69,700}$$

The diffusion rate of Cr decreases by approximately two orders of magnitude with the ($\alpha-\gamma$) transformation. This compares with diffusion rates for carbon of 1 $\exp^{-2,700}$ in austenite and 6 $\exp^{-1,590}$ m^2/s in ferrite.

The degree of solution of the more slowly dissolving alloying elements will also affect the hardening of a steel. The presence of undissolved alloy carbides in a steel decreases to the concentration of carbon in the austenite to a level which is below that of the bulk steel.
Hillert *et al* (118) conducted a theoretical examination of the effect of alloying elements on the various reactions occurring during austenitisation, assuming that

local equilibrium is established at all phase interfaces. The numerical calculations for three chromium alloyed steels were found to correspond well with experiment for the various reactions. This supports the local equilibrium model as opposed to a theory proposed by Nolfi *et al* (119), whereby local interfacial equilibrium is not assumed and dissolution is entirely controlled by a slow interfacial reaction. Further support of the local equilibrium model is provided by Nemoto (120) and Beswick (121). Beswick noted that for a 0-1.42 wt.% Cr, 1.0 wt.% C steel, the ferrite-austenite transformation temperatures were increased due to the presence of chromium and that the chromium content of the residual spheroidal $(Fe,Cr)_3C$ increased during austenitisation. An equilibrium was observed between the carbon and the chromium matrix composition, regardless of the austenitising conditions.

An interesting comparison of the hardening response of Fe-0.5C-0.8Mn and Fe-0.5C-0.8Mn-).8Cr steels using a CO_2 laser has been made by Bradley and Kim (122). The initial microstructures of both steels consisted of fine pearlite and proeutectord ferrite. Almost uniform hardness, with a sharp transition was found for the Cr containing alloy whereas the Fe-C-Mn steel showed a much greater variability in hardness and a more gradual transition due to the presence of partially transformed regions of pro-eutectoid ferrite within the heat affected zone. The Fe-C-Mn-Cr steel contained a lesser and more finely dispersed amount of pro-eutectoid ferrite initially and had a more uniform microsturcure in the HAZ. Additionally, slightly deeper hardening occurs in the plain carbon steel, this becomes more pronounced at longer interaction times. Complete carbide dissolution at the surface is characteristic of the two steels but towards the lower edge of the heat affected zone, there are some undissolved carbides in the Cr-containing steel. However, at higher scanning rates in complete carbide dissolution at the surface was observed for the Fe-C-Mn-Cr alloy.

A similar result is obtained for a high-purity Fe-0.38C-2.8Cr alloy (123), where a two layer microstructure is seen, the upper zone fully martensitic and the lower, undissolved cementite plates in a martensite matrix. Partitioning of Cr and Mn to the cementite provides stability. However, at <1%, their effect on the transformation temperature and the thermodynamic driving force for diffusion controlled transformation should be negligible (124).

The hindrance on the kinetics of the reaction may not be negligible, in fact, Mn additions have been noted to lower the austenite growth rate assuming that C-diffusion is rate controlling(113). However, for higher chromium contents, the kinetics of Cr carbide dissolution are controlled by Cr diffusion in austenite. Slower dissolving carbides can be engulfed by growing austenite during salt bath re-austenitisation of Fe-0.2C-10Cr alloy with a resultant microstructure similar to that produced by LTH. This explains why the Cr-containing alloy used by Bradley & Kim does not undergo complete austenitisation. The diffusivity of Cr (and Mn) in austenite is much lower (by several orders of magnitude) (117) than that of carbon. Calculation of the thermal cycles for the process led the authors to conclude that the

depth of complete austenitisation agrees with the calculated depth, assuming that cementite dissolution is Cr-diffusion controlled. The presence of chromium also decreases the activity of carbon giving rise to a martensitic near-surface microstructure with an under layer of partially dissolved carbides in a low carbon martensite matrix. The mixed layer will be lower in hardness and strength (104) but the performance has not been fully investigated (124). Hence alloying elements conventionally added to increase hardenability may in fact be detrimental to the rapid thermal cycles characteristic of LTH.

2.10.5 The effect of surface melting

Laser surface melting is a complete field of study in itself and is discussed here purely to aid understanding of the structures found when melting occurs during transformation hardening.

Rapid surface melting of iron alloys by laser can lead to the production of thin, soft layers of large grained austenite in the upper part of the solid state transformed regions (125). these so-called 'white layers' were observed under certain conditions in graphite coated (1.0C, 0.35Si, 0.4Mn, 1.48Cr) AISI 52100 steel but not in similar samples coated with phosphate compounds. For AISI 1040 (0.4C, 0.3Si, 0.8Mn, 0.1Cr, 0.1, Ni) and 9840 (0.4C, 0.3Si, 0.Mn, 0.8Cr, 0.8Ni) steels however white layers are seen for all processing conditions leading to surface melting but never when no melting occurred. In the case of the 1% C alloy, the increased C content favours surface melting. the melt may be enriched in carbon from the graphite coating. Carbon easily diffuses in the underlying solid region allowing stabilisation of austenite during cooling. this only occurs for high thermal gradients as the carbon profile is not allowed to decrease gradually and a high concentration is preserved beneath the melt. The thickness of these white layers increases with incident power to a point after which it decreases to zero. Such layers may be detrimental to the mechanical properties and can be eradicated by suitable choice of material, coating and processing parameters.

2.10.6 The Martensite Transformation

Rapid cooling of a steel from the austenite phase field prevents diffusion and results in a diffusionless, shear transformation to martensite. Martensite is a metastable, body-centred tetragonal phase which is a supersaturated solid solution of carbon in body centred cubic α-iron. The martensite reaction is a nucleation and growth process where the barrier to nucleation is very large. Martensitic transformations therefore only occur at temperatures which correspond to a very large undercooling below the equilibrium transformation temperature. Conversely, the barrier to growth is negligible and growth rates can approach the speed of sound (126).

The hardness of martensite is reduced by slow cooling, however, rapid cooling can

produce microscopic cracks when the grain is coarse. The composition of austenite also influences the hardness of martensite. Elements other than C exert a hardening effect when the C content is low and the quench develops maximum hardness. Alloying elements make it improbable that the pure (Fe-C) martensitic hardness is reached but probably do not actually lower the pure martensitic hardness. Carbon is the most influential element in terms of hardness. Heat treatments to form martensite are usually applied to steels containing <0.73%C as the gains in hardness for such steels are more substantial (105). Above the eutectoid point (0.77%C), hardenability decreases with C content due to the presence of retained austenite. The effect of carbon content on the hardness of different phases is shown in Fig. 2.22 (90).

Hardenability decreases with decreasing austenite grain size. This is because a smaller grain size supplies more grain boundaries available for the nucleation of ferrite/pearlite which in turn reduces hardenability. Hardenability also increases with increasing homogeneity of austenite as areas lean in alloying elements transform to fine pearlite at high quench rates. The presence of some alloying elements may extend the range of sample sizes which can be substantially hardened by a specific quench.
In essence, there are three factors which increase hardenability:

(1) dissolved elements in austenite (except Co and B)
(2) coarse austenite grain size
(3) homogeneous austenite

The carbide-forming elements restrict austenite grain growth as long as some carbide particles remain. When dissolved, they are powerful deep-hardening elements (98).

The high hardness (strength) of martensite may be attributable to solid solution strengthening of the structure by carbon, which makes the movement of dislocations and/or fine twins contribute to the strength in a smaller way (104). The crystallography of the martensitic transformation is a complex subject and is not strictly necessary for the purposes of this discussion. Two major morphologies of martensite, lath and plate, develop in heat treatable carbon steels (where lath and plate describe the 3-D shapes of individual martensite crystals). For Fe-C alloys, lath martensite is formed from 0-0.6%C, plate martensite from 1.0%C upwards and mixed in between. These boundaries may shift in alloy steels.

The temperature at which martensite starts to form in an alloy is designated the martensite start temperature (M_S), which reflects the amount of thermodynamic driving force needed to initiate the transformation. M_S decreases with carbon content in Fe-C alloys, as carbon increases the strength of the austenite and greater undercooling is required to initiate the shear transformation. Similarly, the martensite finish temperature (M_f) is a function of C-content. If M_f drops below

room temperature, untransformed (retained) austenite will be present. This becomes significant above approximately 0.4%C (104). M_S is also influenced by alloying elements. The alloy content is related to M_S by the following equation(127):

$$M_S (^oC) = 512 - 453C - 16.9\,Ni + 15\,Cr - 9.5\,Mo + 217(C)^2 - 715(C)\,(Mn) - 67.6(C)(Cr)$$

2.10 7 The Effect of Surface Transformation hardening on A_1, A_3

LTH is characterised by rapid heating rates. This not only affects the austenitisation temperature but also, the homogeneity of austenite in the HAZ. Conventional austenitisation begins at the A_1, temperature of the steel and is complete at the A_3 temperature. At high heating rates, the system is not able to establish equilibrium. This means that the temperatures induced by rapid heating must be higher than the conventionally accepted temperatures to produce austenitisation.

2.10.8 Laser Transformation Hardening - A Review of previous work

The principles and mechanisms of LTH have already been discussed. This section contains a review of the findings of previous authors in the field.

Research into laser hardening dates back to the 1960's with the first application (74), the hardening of gears, reported in 1970. The laser is now used to harden many steels for a whole range of applications. Ricciardi and Cantello (128) reviewed the use of the laser for the surface treatments of automobile parts. The laser hardening of a number of components was investigated.

The tooth sides of carbon steel gears (129) were hardened without affecting the tooth base. This high toughness of the teeth was maintained without thermal distortion, using extremely short interaction times, as the tooth thickness of 3mm leaves only a 1.5mm thickness available for self-hardening when the 2 sides are treated simultaneously.

Laser hardening of crankshafts aimed at replacing the traditional nitriding method for producing a compressively stressed surface layer was also successful. A laser power of 2.2 kW and interaction time 0.9s was used to produce a 0.6mm case depth composed of martensite and a thin layer of Cr carbides. This compressive-stressed layer is capable of reducing microcrack propagation. Similarly, the inner surfaces of cast iron cylinder liners were treated to improve life, reduce wear and friction coefficients and to obtain liners suitable for high pressure engines (e.g. turbo diesel engines). In this case. 2.1kW and an interaction time of 0.65s were the optimum parameters. A martensitic case consisting of dark and white regions was formed, beneath which was a bainitic layer of slightly lower hardness and a soft

layer lower in hardness than the base. Hardening of camshafts by surface remelting was also used to achieve high quality surfaces with a surface structure consisting of cementite, ledeburite and refined austenite. Below this a martensitic zone was observed.

Surface hardening of the leading edge of martensitic stainless steel turbine blades (130) to withstand corrosion are also encouraging, the steel (0.12C, 1.0Mn, 1.0Si, 13.0Cr) retaining corrosion resistance upto 700 C in continuous use. Hardening at specific power of 2700Wcm2 and 0.4s interaction time yields a HAZ 100-600 μm deep with a refined structure absent of micro-cracks. Additionally an increase in hardness from 240-500HV_{10} and a decrease in manufacturing time of over 90% compared to other techniques (induction hardening and Stellite brazing) is observed.

Bach et al (131) used a faceted mirror to achieve uniform intensity distribution for their examination of laser hardening for a number of tool steels. A small number of hardness profiles were found. The heat -treatable steels show a plateau-like shape with a narrow transition zone and a rapid decrease to the base hardness. Plain carbon and low alloy steels show a pronounced transition zone exhibiting incomplete hardening (austenitisation) and a lower region where hardness decreases almost linearly with depth below the surface. For lower C contents, hardness can be increased by increasing the amount of C in solid solution. For higher C contents however, the presence of retained austenite overwhelms this effect, the decrease in transformed volume decreasing the hardness. A third profile for ledeburitic Cr steels exhibits a dramatic decrease in hardness close to the surface. In this case, selective melting is a problem and the presence of austenitic structures in the resolidified melt is responsible for the reduction in hardness.

Similarly, Menin et al (132) report different hardness profiles for the steels C43 normalised (coarse ferrite/pearlite), C43 quenched and tempered (fine ferrite/pearlite) and 40CrMo4 quenched and tempered (sorbitic) - initial structures indicated in brackets. The profiles are illustrated in Fig. 2.23 (132). Normalised C43 transforms to a heterogeneous structure of high and low carbon martensite and untransformed ferrite, whereas Q+T C43 forms an almost completely martensitic hardened zone with some bainite and ferrite in the lower region. 40CrMo4 forms a fairly homogeneous zone of fine martensite. In addition to selecting the correct treatment parameters to avoid surface melting, the tendency of a steel to retain austenite must be borne in mind. This tendency increases with increasing alloy and carbon contents (104).

Laser transformation hardening of M2 high speed tool steel (133) is accompanied by the formation of martensite and the precipitation of M_2C, MC and M_6C special carbides with structural heterogeneity having a negligible effect on the hardness of the HAZ.
A study of the effect of LTH on En8 steel (134) relates the depth of hardening to the

parameter $P/\sqrt{dv}$ and the onset of surface melting to the parameter P/d^2v. Two distinct microstructures are found for this steel. For low speed runs, a fully martensitic case of uniform hardness with an interface layer of martensite/pro-eutectoid ferrite is seen whilst high speed runs yield an inhomogeneous austenite due to the rapid austenitisation time. It has been suggested (109) that at very high heating rates the alpha-gamma transformation proceeds by diffusionless shear giving austenite of a different morphology. This was the case for most of the experimental runs. There is very little literature relating to the transformation hardening of ferrite/spheroidised carbide steels. Transformation hardening of sorbitic 0.4% C steel is also reported as being successful (135), leading to fully hardened surface layers.

2.11 Metallurgical Considerations of Laser Cladding

Laser cladding (and hardfacing) involves the addition of a material to a surface to improve the properties of the surface. This can include modifications to improve wear, corrosion, magnetic properties or the creation of a thermal barrier coating on the surface. Laser hardfacing is a term generally used to describe coatings which are applied to improve wear resistance. To distinguish laser cladding from the other laser processes, Powell (16) defined it as

> "*the laser fusing of a cladding material to a substrate producing asubstantial (0.5mm thick) deposit with a low level of substrate-deposit dilution (<10%).*"

Ideally then, the process requires minimum mixing between the deposit and substrate, minimum heat input to the substrate and the production of a uniform defect-free deposit. For industrial use, there are the additional requirements, that the process is cost effective and offers a high degree of reproducibility. The advantages of using a laser have been discussed previously (section 2.2).

Monson (51) prepared a comparative study of laser cladding and conventional coating processes and found the laser deposits superior in terms of hardness, microstructure and wear.

2.11.1 Laser Cladding with Stellite

Stellite alloys date back to 1900, when they were developed by Elwood Haynes. The early alloys were of the binary cobalt-chromium system and were improved by the addition of molybdenum, tungsten and/or nickel (57). There are some twenty or more Stellite alloys available today, which are either cobalt- or nickel-base. Stellite alloys are extensively used in wear applications, where their high strength, hot-hardness, wear and corrosion resistance can be exploited. Stellite 6 is the alloy normally used for valve seat applications as it shows particularly high resistance to galling (10). The chemical compositions of the more common Stellite alloys are

indicated in Table 1.2 (Chapter 1).

2.11.2 Methods of Laser Cladding - A Review of Previous Work

Three methods of cladding using a laser beam, have been used to date as follows:

1 Wire Fed Laser Cladding

This method was patented in 1976 by Gnanamathu (136). Impingement of the laser beam on a wire in contact with the substrate surface causes melting of the wire and surface. A fusion bond is created on re-solidification. The technique is clean and involves no wastage. However, a high degree of accuracy in placing the wire is necessary, and some more recent work by Matthews (137) has shown the coupling of the laser beam to the surface to be inefficient due to the shielding effect of the wire. The following two methods are in much wider use.

2 Laser Cladding with Pre-placed Powder

The pre-placed powder technique is very simple. A powder, usually held in an inert binder is placed on the substrate surface and melted by the scanning laser beam. The method was used by Steen and Courtney (138) to produce a 1-2mm thick layer of Stellite 12 on nimonic 75 substrates. An investigation of the process by Matthews (137) for a number of alloys revealed some difficulty in obtaining a uniform layer. This problem was also pointed out by Powell (16) who found the method poor for maintaining constant clad thickness. A theoretical model (139) developed for the analysis of thermal cycling during preplaced powder cladding with a scanning defocussed or rastored laser beam has been used to explain the low dilution levels obtained as follows. By identification of the molten front at various interaction times, the authors were able to follow the movement of the front with time and found a retreat of the front from the clad-substrate interface after initial contact. Subsequent re-melting is therefore slow and the amount of dilution limited.

3 Laser Cladding with Powder Feed

The problems encountered with the previous laser cladding techniques led to the development of blown powder laser cladding. Clarke *et al* (140) are the first reported workers in this field. They used a modified oxyacetylene torch to deposit stainless steel and nickel based monel powders on mild steel substrates. Subsequently, there has been much interest in this area, with the first patent by Rolls Royce in 1980 (141), for the coating of high pressure turbine blades, using the Stellite 12/ nimonic 75 system previously investigated by Steen and Courtney (138). Rolls Royce reported (141) an 85% cost reduction over the T.I.G. welding technique previously in use. Similar work on turbine blade shroud interlocks using blown powder cladding (142) produced sound deposits which were tested extensively and found to exceed part requirements.

The powder feeder used by Clarke *et al* was also used by Powell (16) for coating exhaust valves with nickel-based Stellite SF40. Powell found the feed system

inflexible, which led to interest in developing an improved delivery method. The screw fed powder feed evolved from the work of Weerasinghe and Steen (143) and is able to provide uniform flow over a wide range of flow rates, allowing control of dilution and deposit thickness. A completely different innovation by Tucker *et al* (144) is the coaxial feed system which is reported to be more energy efficient and produces an omni-directional powder flow.

The main body of the cladding work detailed here involves the use of more than one powder feeder. Takeda *et al* (80) used a multi-hopper feed system to clad mild steel substrates with Fe-Cr-Ni alloys. The system was used either to feed the powders into a single delivery tube, or through separate delivery tubes to the workpiece surface. In-situ alloys were produced, the homogeneity of which was dependent on the cladding speed (e.g. at 1.7kW, 8mm beam diameter and a flow rate of $0.293gs^{-1}$, lack of homogeneity occurred at speeds $>7mms^{-1}$). Layered structures were also prepared with the aim of eliminating deposit cracking by the inclusion of a soft 'buffer' layer.

Clads having controlled variable composition using the Ni-Cr-Si-C-B and Colmonoy 5 systems were reported by Monson *et al* (145). Hardness is related to B content for the former alloy. However, above 450HV, the incidence of cracking increases with hardness. The latter alloy shows hardness increasing with Mo content, with two peaks in hardness at 25 and 55 weight percent Mo. This alloy was deemed suitable for the production of crack free deposits at room temperature.

In essence then, the laser provides a suitable energy source for the production of low dilution, fusion bonded clads. This is due to the rapid solidification rate at the clad-substrate interface which prohibits convective stirring (146). The coupling efficiency of the beam to the substrate is enhanced for the blown powder technique. The main disadvantage of this coating method is the spraying of powder to surrounding areas when it bounces off the surface. This can lead to pollution of the local operating environment and powder wastage. Reclamation of this powder is both difficult and time consuming if mixed powders are employed.
A review of methods of improving clad quality and operating efficiency is given by Li (147 thesis). This includes such modifications as vibro laser cladding (ultrasonically vibrating the substrate whilst cladding to eliminate cracking and porosity) (16), the use of uniform beam profiles for uniform energy distribution across the beam diameter and the use of a reflective dome to further increase the coupling efficiency. Finally, Li *et al* (148) have developed a computer model which aims to select the optimum operating parameters and maintain clad quality throughout the process.

Industrial applications of the process include cladding valve seats and seals, the leading edge of turbine blades, the inside of small diameter pipes and for salvaging undersized components. The first patent relating to cladding was filed by the Caterpillar Tractor Company, U.S.A. (149), for the preplaced powder cladding of the

wearing surface of engine valves. The technique involved pre-placing Stellite 6 powder onto the austenitic Cr-Si-Ni valve steel as it rotated beneath the laser beam. The results were very encouraging, uniform clads with a fine-grained structure and excellent bonding were formed. The deposits were far superior to those produced by the previous gas welding method, which exhibited large areas of segregation due to the slow cooling rates associated with the process, lower hardness and were approximately twice as costly to produce.
A more recent use of CO_2 laser cladding for coating valve seats with continuous powder feed (150) has produced high quality deposits 1.5-3mm wide and 0.5-1mm high, with excellent wear resistance and high hardness. However, in this instance the authors needed 2-4 beads for complete coverage.
Powell (16) successfully clad spheroidised Stellite SF40 powder into grooved engine valve seats to form a uniform bead with a flat surface, minimising the need for post-process grinding. Similarly, Kupper *et al* (151) studied blown powder cladding of Stellites F and C and Celsite F (a coarse-grained variant on Stellite 6) on engine valves. The results showed deposits with fine microstructures, a high degree of homogeneity and 3% dilution. The authors used a power ramping facility on the laser to optimise the overlap zone to give a uniform flat deposit.

Assessment of a process for industrial acceptance must include a feasibility study. A direct cost saving of laser cladding over conventional T.I.G. welding due to a reduction in processing time has been reported (141). Blake and Mangalay (152) reported technical and economic advantages of the process despite higher capital costs. A feasibility study of the process for hardfacing exhaust valve sealing faces, in conjunction with this project (153) suggests substantial advantages for laser cladding compared with the more traditional plasma spray coating process. The infancy of laser coating technology requires education of potential users in the manufacturing industry on the capabilities and potential cost savings of the process. The introduction of more job-shop facilities for testing an application, and the availability of fully automated workstations with in-process monitoring and closed loop control should further expand the acceptance and use of laser coating in industry.

2.12 Residual Stresses due to Laser Treatment

The distortion and fracture of heat treated components is a major industrial problem and therefore of significant economic importance. Laser transformation hardening and cladding produce residual stresses in treated areas which may affect the performance of components.

2.12.1 Laser Clad Coatings

During cladding, residual stresses are set up in the clad layer and substrate as a result of substrate deformation. This is due to differential expansion of the substrate caused by the temperature gradient across its thickness (24). The residual

stresses obtained are tensile in the coating and compressive in the substrate (154), their magnitude depending on the level of substrate distortion and hence the thickness of the base material. For example, a large plate thickness generates high resistance to contraction of the clad layer on cooling and a high residual stress will be set up in the clad, with minimal distortion.

Post-annealing for stress relief is generally only applicable if the coating material has a lower coefficient of thermal expansion than the substrate. Tensile stresses in the layer can then be transformed to compressive stresses whose magnitude can be controlled by appropriate selection of the annealing conditions. If this is not the case, post-annealing is ineffective as further stresses are set up on cooling due to the differential expansion of the clad and substrate. Preheating, shot-peening and pre-tensioning are possible methods of relieving residual stress. Pretensioning of the substrate by welding it to a retaining base plate before treatment (24) was found to reduce surface residual stresses from 285MPa to 8MPa, for a 1.3mm thick clad of Stellite 6 on a mild steel substrate.

2.12.2 Laser Hardened Surfaces

In common with other methods of surface heat treatment, laser treatments in the solid state which lead to martensite formation produce compressive residual stresses in the near-surface region, due to the volume expansion occurring with the austenite-martensite phase change (155). These stresses, which depend upon the microstructural state of the steel, are very important and must be considered when a heat treatment process is selected (156). Localised surface hardening sets up both thermal and transformation stresses in a steel (90). If a bar is considered, surface layers expand plastically when heated and are restrained by the colder core. This sets up tangential thermal stresses in the bar, the magnitude of which increases with increasing bar diameter and also with increasing effectiveness of the quenchant. On quenching, the surface layer contracts initially and expands again with the formation of martensite. There is always an increase in volume when austenite transforms to other structures, as illustrated by the specific volumes of steel phases, in Fig. 2.24 (91).

In addition to the residual stresses, surface hardening is an excellent method of improving the endurance limit and service life of components (90). However, this is only the case if all working faces are treated. Compressive stresses at the surface also provide enhanced fracture resistance. There is no available data regarding the stress distribution generated during laser hardening when a fully martensitic case is formed (157). It is therefore not possible to compare the residual stresses induced with those generated by more established techniques. The laser hardening process may improve the fatigue life of a component by changing the surface topography, surface hardness and residual stress (158). An investigation, (159) of the wear and mechanical fatigue behaviour of 32 CDV 13 steel (0.32% C, 2.91% Cr, 0.05% Ni, 0.85% Mo, 0.46% Mm, 0.29% Si in wt. %) subjected to nitriding or laser hardening

revealed that although laser hardening produce the deeper case depths, the maximum hardness obtained was much lower (HV 600 compared to HV 950 for nitrided specimens). Laser hardening was found to induce a deep compression zone accompanied by a high tensile stress sub-layer, zone related to overtempering. The lower hardness values for the laser processed medium carbon steel samples were too low to provide any significant increase in fatigue lifetime and also led to lower wear resistance.

2.13 Process Control

Process control of laser transformation hardening and cladding is necessary so that trial and error methods can be eliminated and the laser can become a more acceptable industrial tool. Laser parameters can be controlled by computer, therefore, real-time feed-back control is a reality. A number of aspects of the process have been examined with a view to establishing and maintaining the optimum processing conditions.

2.13.1 Laser Beam Monitoring

A laser beam analyser, developed by Lim and Steen (160), allows in-process beam sampling for beam analysis without interfering with the beam itself. This consists of a reflective rotating rod which reflects a small percentage of the beam energy into a pyroelectric detector in two orthogonal directions.

A second technique for monitoring the laser beam is the acoustic mirror (161). This records a signal due to 'ringing' of mirrors reflecting high power laser beams. This phenomenon was first observed by Beyer et al (162) in 1984. In essence, a mirror reflecting a high power CO_2 laser beam rings at a frequency far above its resonant frequencies and this generates an event which is detectable via an acoustic sensor. The nature of the signal is not precisely understood. Analysis of acoustic emission signals for LTH of the En8 stainless and 0.25% mild steels (163) showed that En8 and mild steel emitted signals which could be used as part of a feed-back loop to control the extent of the process. The authors proposed that the source of the acoustic emissions was the martensitic transformation and that the technique could also be used to detect the extent of transformation from the amplitude of the signal and the onset of melting or cracking. For laser cladding monitored using this method, it was not possible to detect the behaviour of the deposit whilst the feed and feed plus ultrasonic vibrator were operating. However, deposits were found to be acoustically active over a ten minute period after the runs had finished but it was difficult to differentiate between cracks and pores in the deposit using this technique. A system of beam shaping by combining scanning of the beam with simultaneous microprocess power control is currently under investigation (164) for improvement of the efficiency of laser processing.

2.13.2 Use of Different Optics for process Optimisation

Juptner et al (165) discussed the use of a number of optical arrangements for producing a rectangular intensity distribution of the laser beam. Techniques suggested include a light pipe beam integrator, rotating mirrors and segmented mirrors. A technique of mirror oscillation (166) was successfully used to obtain and control the beam width to produce a wider transformation zone. Successful progressive hardening of a uniform surface layer of steel bars using a 'so-called' toric mirror - this reflects an annular laser beam onto the surface so that a continuous ring shaped band can be hardened - was achieved by Melander and Chang (167).

2.13.3 Case Depth Control

A potentiometric non-destructive technique for case depth control has been investigated (168). The method is based on an increase of the specific resistivity of the sample after martensitic transformation of the original structure. The experimental arrangement consists of a number of electrodes generating electrical contact at various points on the sample surface. A correlation between case depth and electric signal was found, the best results being those obtained by detecting the ratio of two potential differences.

2.13.4 Surface Temperature Control

Demands for high quality industrial manufacturing can only be met by online process control. A stationary absorbed power density is a prerequisite for homogeneous case depth along a track (169). Fluctuations in laser output power and absorptivity require control of the power and, therefore, the surface temperature. This allows uniform case depths to be produced on irregular work pieces and also allows fine tuning of the process parameters for more economic processing, and the production of a wide range of hardnesses (170).

A number of authors have successfully addressed this problem (169,170), using a feed-back loop consisting of a pyrometer, a controller and a flexible laser handling system. However, problems occur with the use of absorbent coatings. The surface temperature depends not only on the processing parameters and the thermophysical properties of the substrate, but also on those of the coating. Drenker et al (171) overcame this problem for successful hardening of complex geometries using a recursive process identification and control algorithm to control the surface temperature allowing for the disturbances caused by a coating.

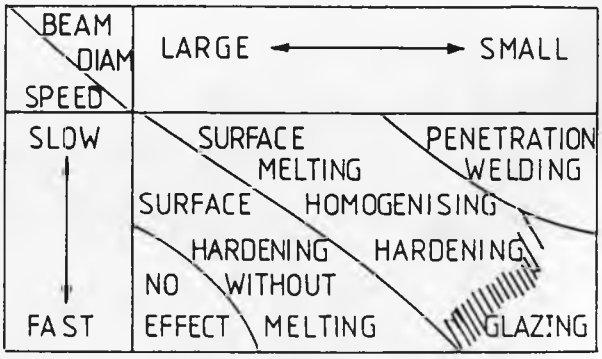

Fig. 2.1 Interaction spectrum for laser materials processing

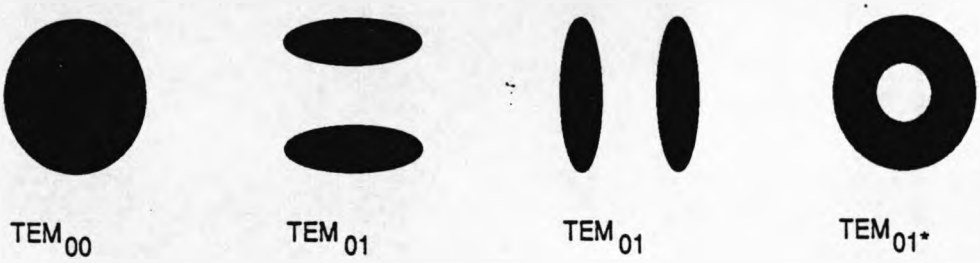

Fig. 2.2 Low order TEM modes obtained for circular beams

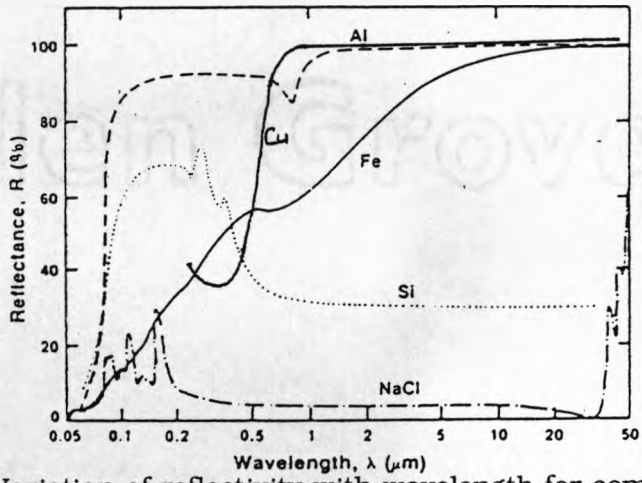

Fig. 2.3 Variation of reflectivity with wavelength for common materials at room temperature (20, 29)

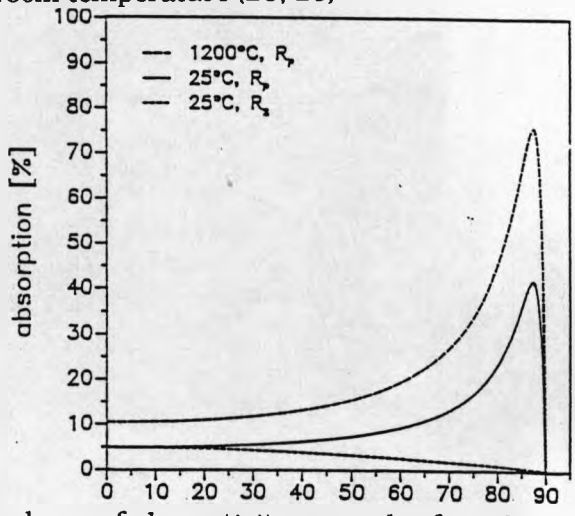

Fig. 2.4 Dependence of absorptivity on angle of incidence for s and p polarised light (30)

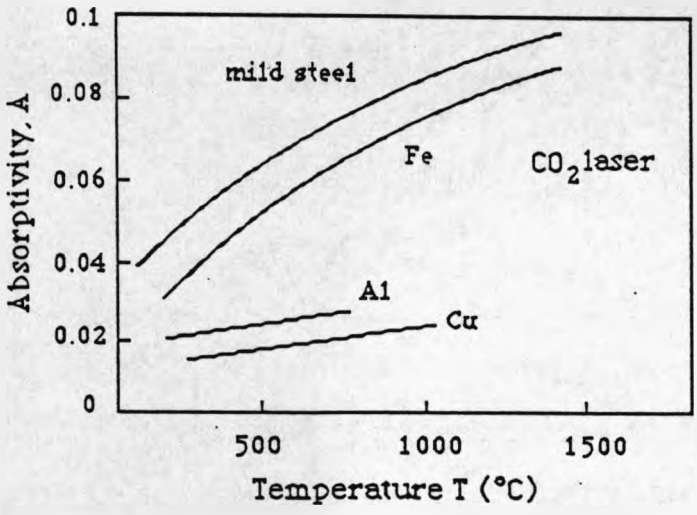

Fig. 2.5 Variation of absorptivity of different metal surfaces with surface temperature (29)

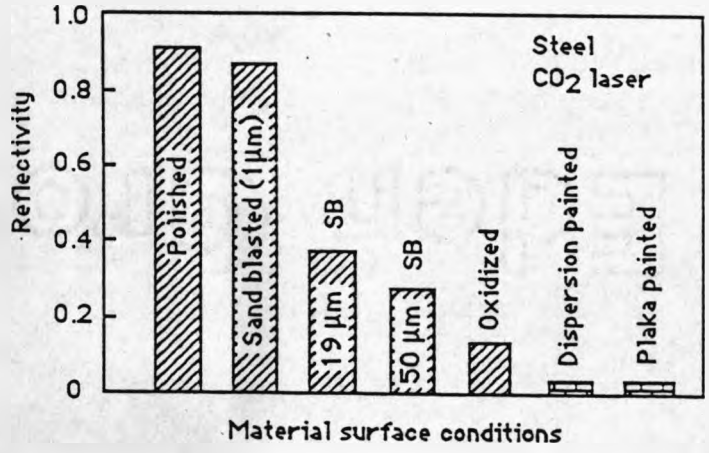

Fig. 2.6 Decrease in reflectivity of steel surfaces to CO_2 radiation with various surface coatings (31, 37)

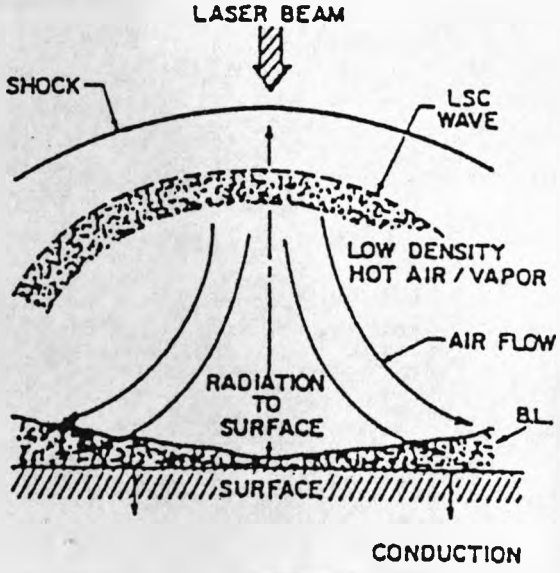

Fig. 2.7 2-D schematic of laser supported absorption wave (combustion) (33)

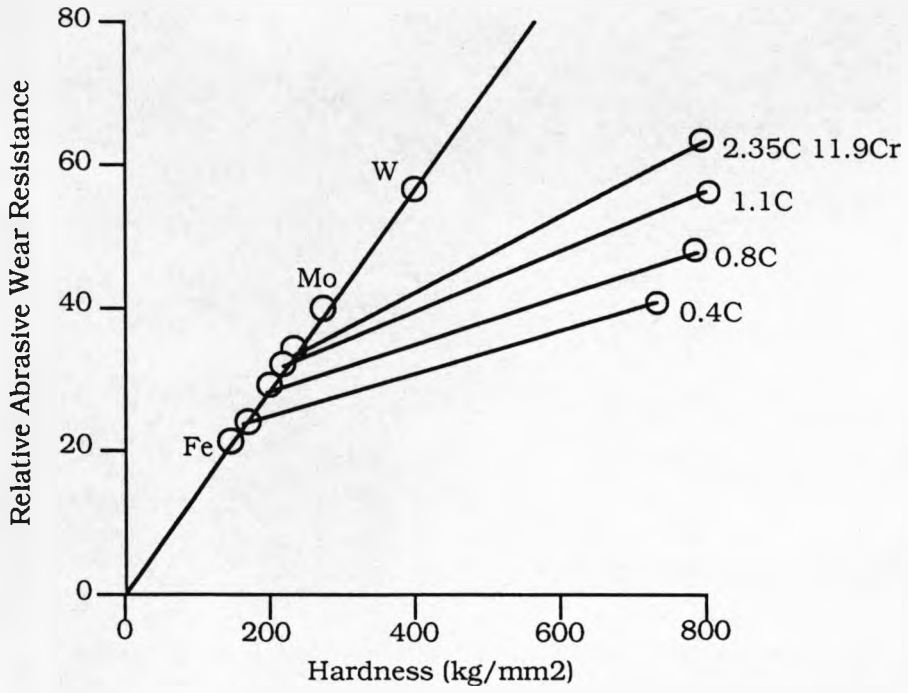

Fig. 2.8 Wear Resistance of Heat Treated Steels (46)

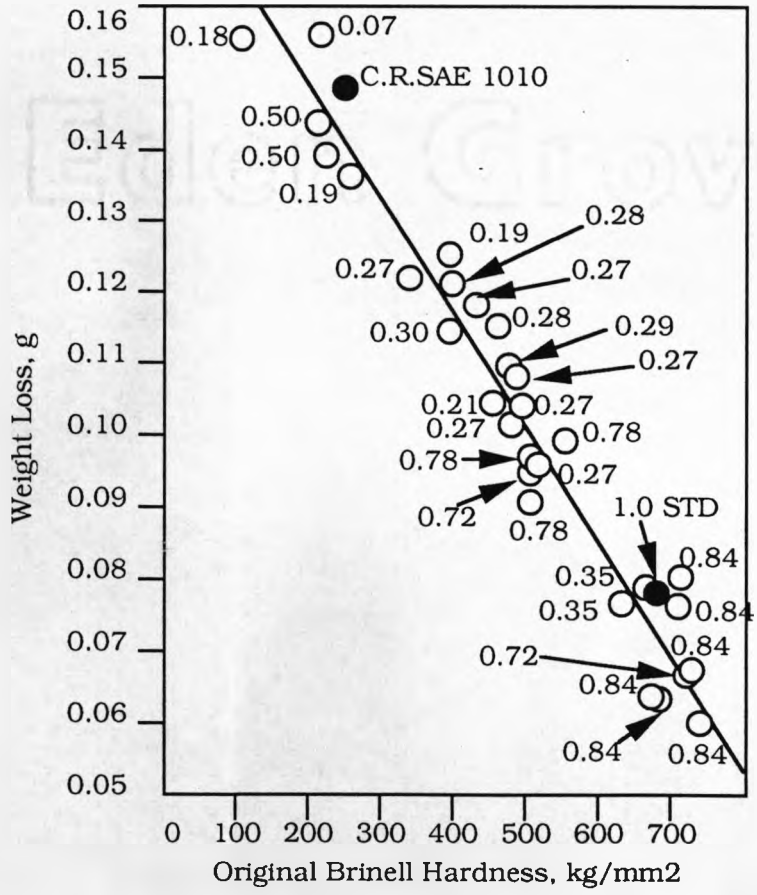

Fig. 2.9 Relationship between Original Hardness and Weight Loss in the Pin Abrasion Test for Steels of Various Carbon Content (80μm particle size alumina cloth) (52)

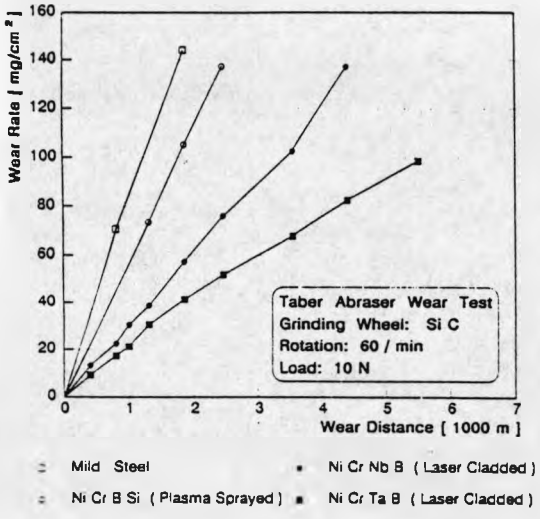

Fig. 2.10

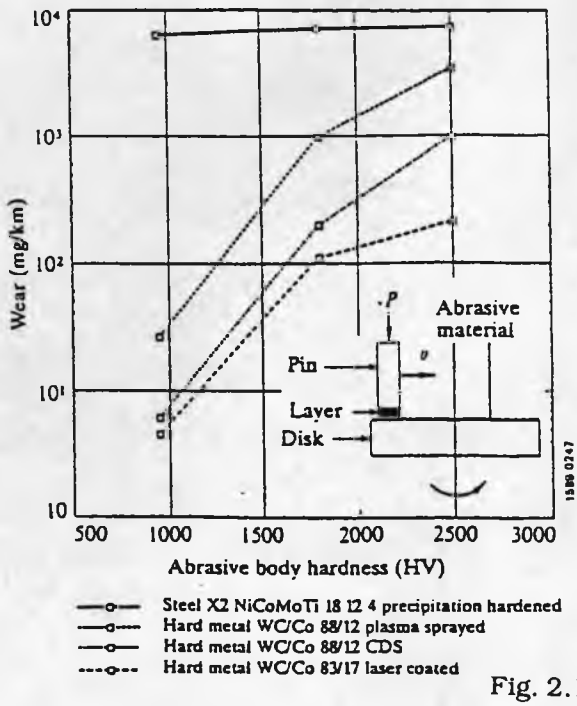

Fig. 2.11

Fig. 2.10 Comparison of wear resistance of laser deposited and plasma sprayed layers (62)

Fig. 2.11 Results of 2-body abrasive wear tests for precipitation hardened, plasma sprayed laser clad surfaces (64)

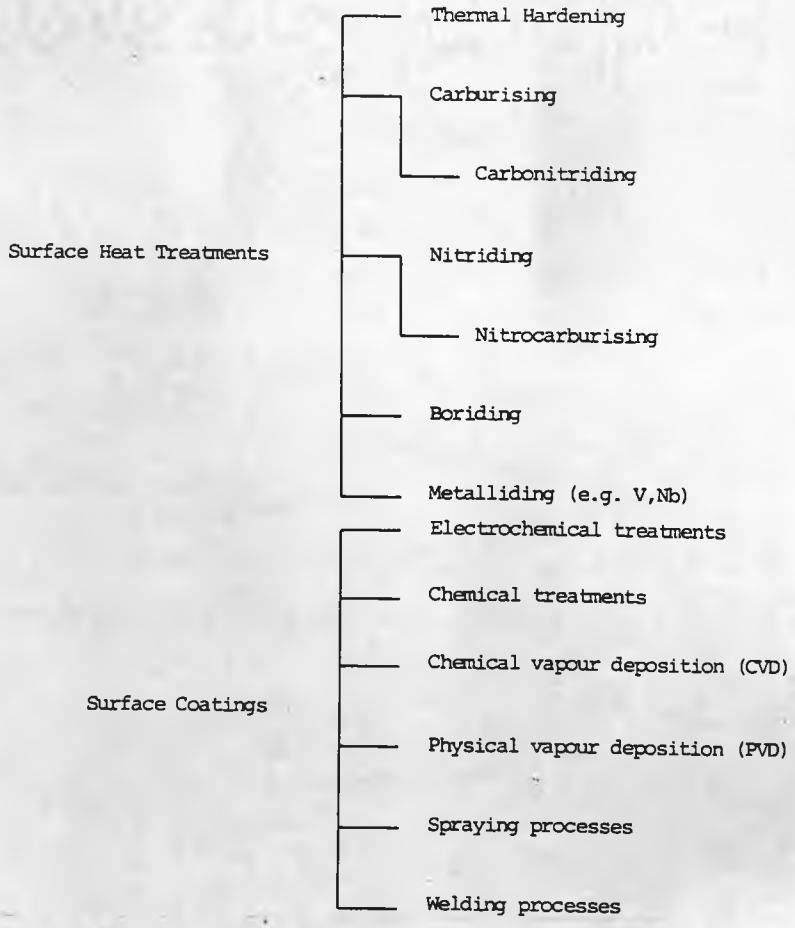

Fig. 2.12 Schematic showing principal surface treatments (46)

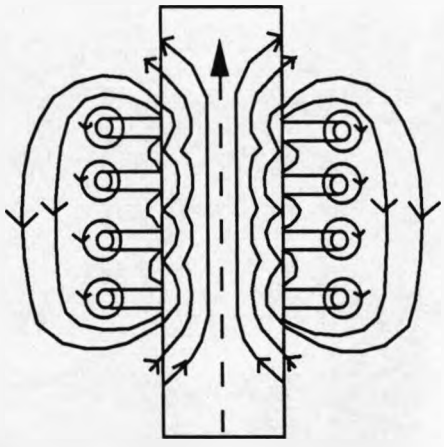

Fig. 2.13 Path of magnetic flux through bar during induction hardening (90)

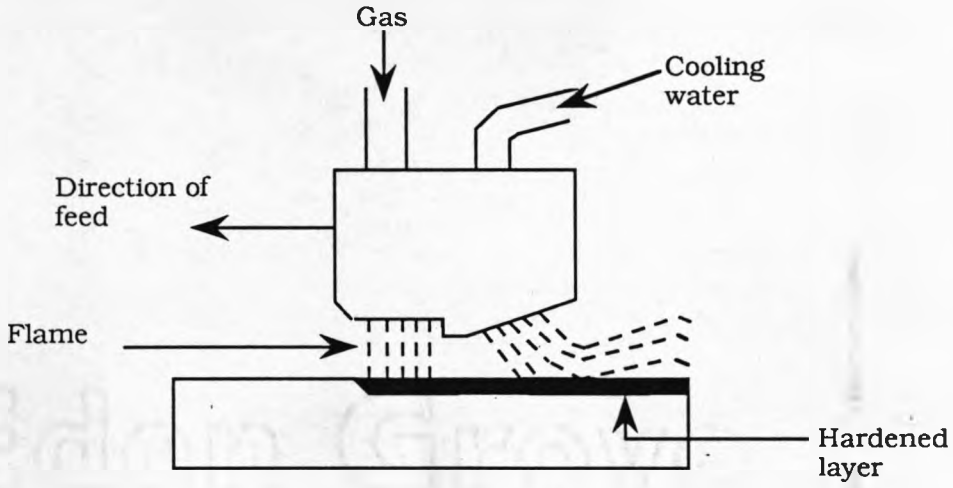

Fig. 2.14 Flame hardening operation - progressive technique

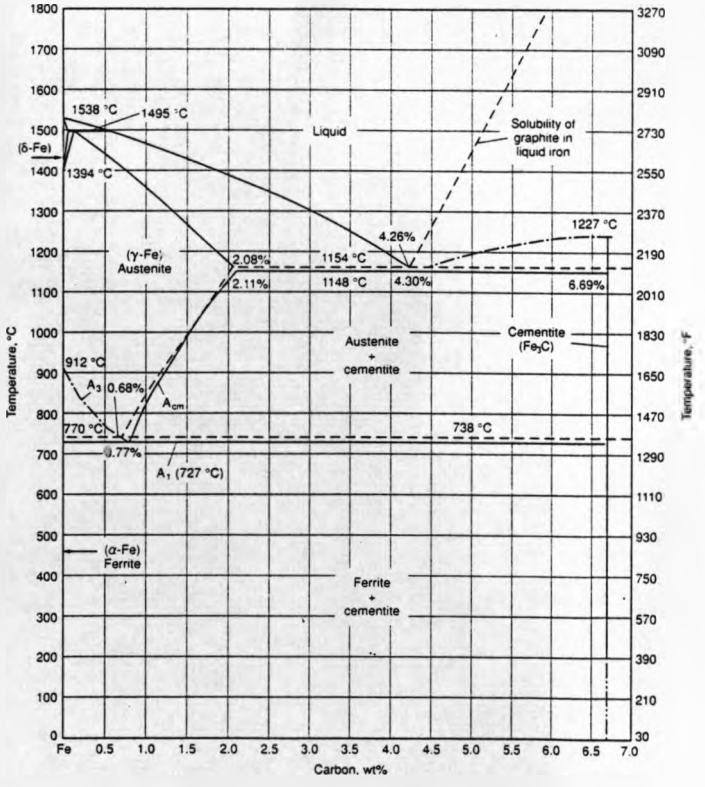

Fig. 2.15 Fe-C equilibrium diagram up to 6.67 Wt.% carbon (98)

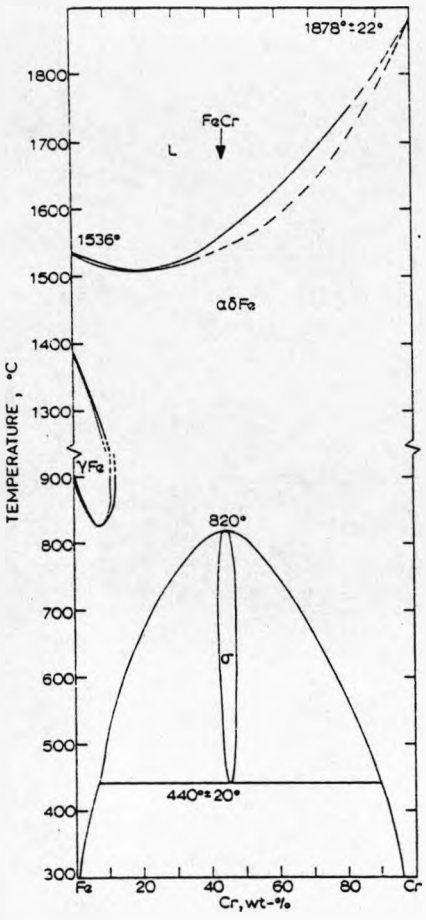

Fig. 2.16 Cr- Fe binary system (99)

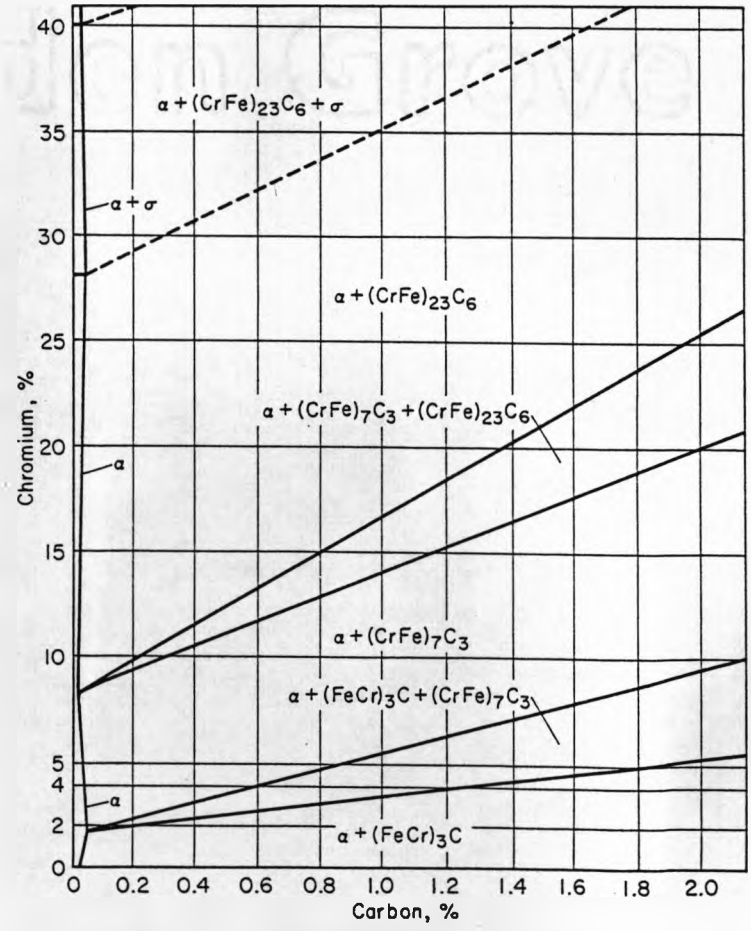

Fig. 2.17 Constitution diagram for Fe-C-Cr alloys (98)

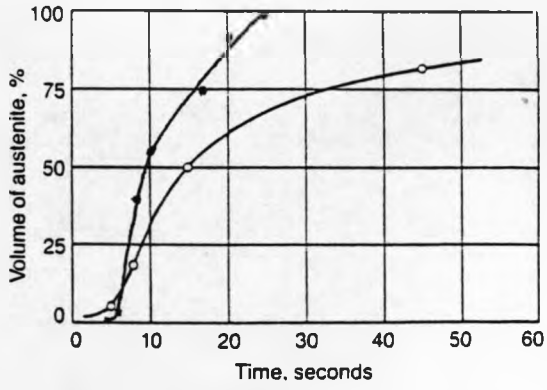

Fig. 2.18 Comparison of volume percent austenite formed from pearlitic and spheroidised eutectic steel structures (106)

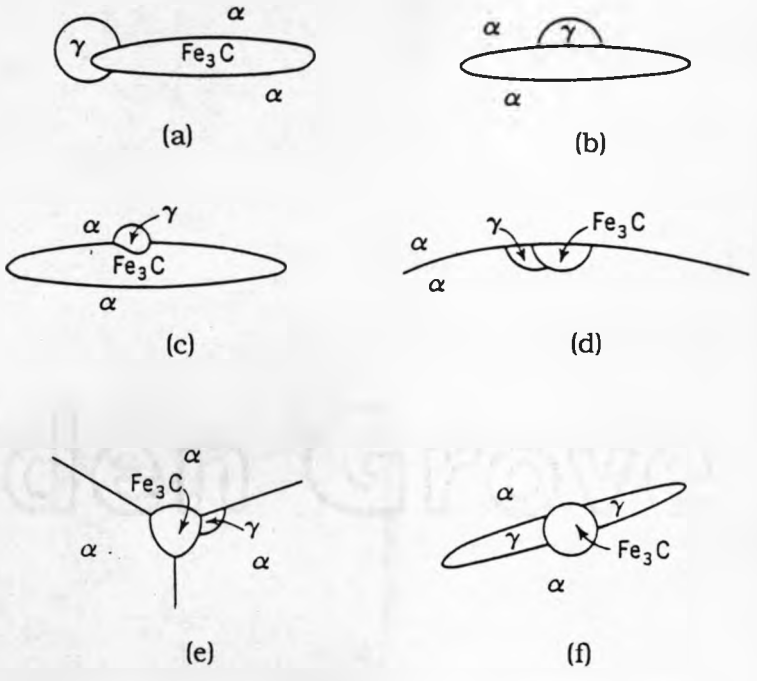

Fig. 2.19 Possible nucleation sites for carbide containing steels (109)

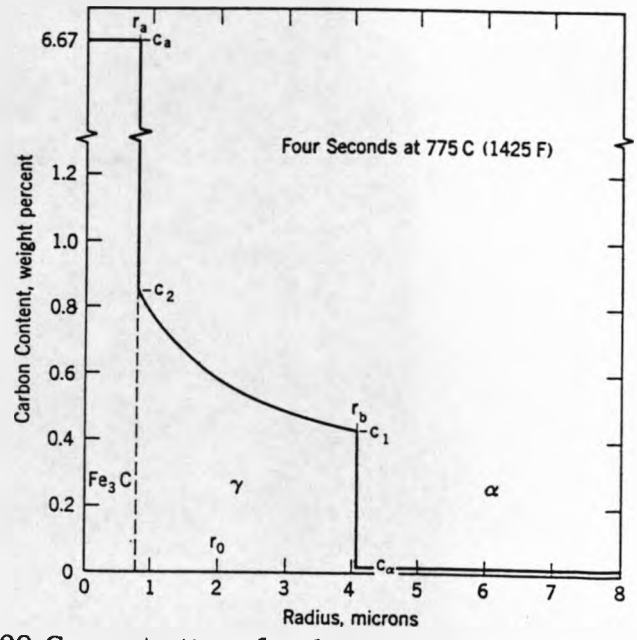

Fig. 2.20 Concentration of carbon vs distance along a radius from centre of spherical carbide particle (113) 67

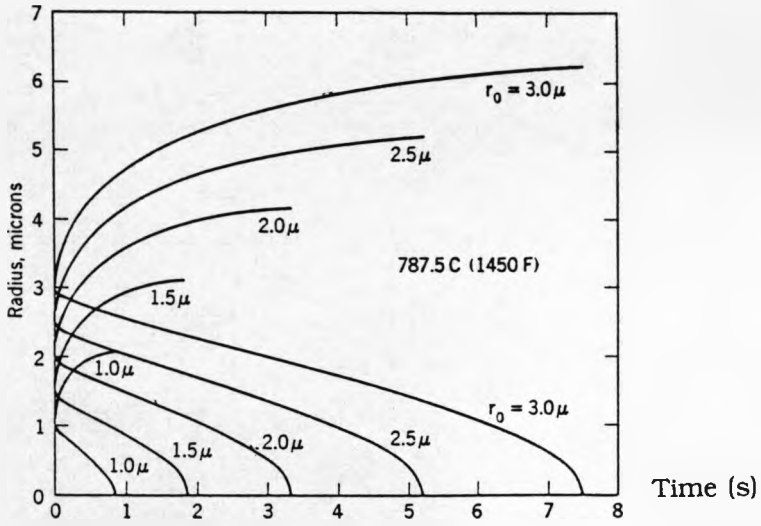

Fig. 2.21 Variation of r_a and r_b for typical values of r_o during austenite formation at 787.5°C (109)

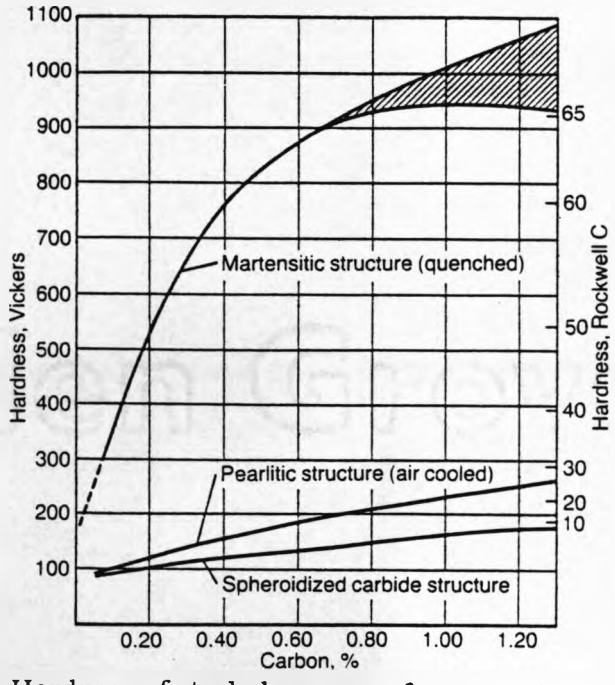

Fig.2.22 Hardness of steel phases as a function of carbon content (104)

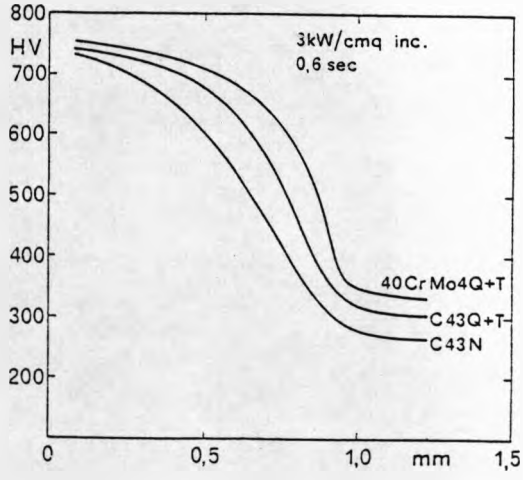

Fig. 2.23 Comparison of obtained hardness profiles for steels C43 N, C43 Q&T and 40CrMo4 Q&T (132)

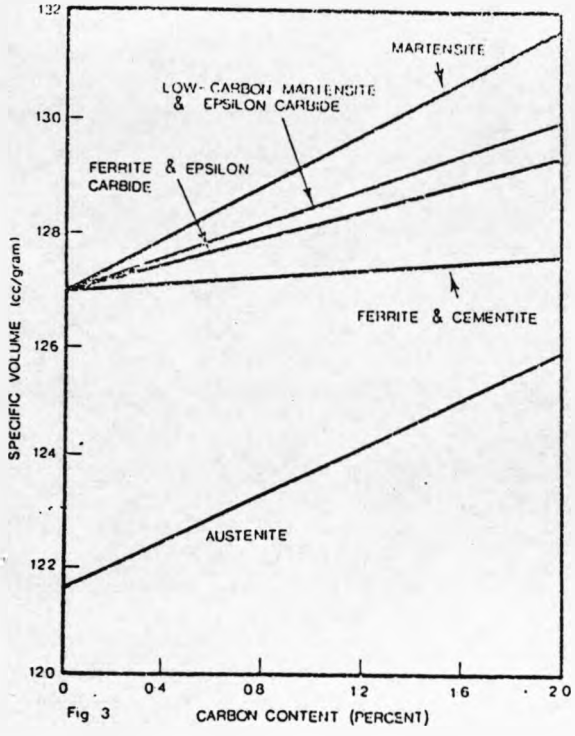

Fig. 2.24 Specific volumes of steel phases as a function of carbon content (91)

	Cementite, Fe3C	Cr23C6	Cr7C3
Symmetry	Orthorhombic	Cubic	Hexagonal (trigonal)
Space group	Pbnm	Fm 3m	C_{3o}^{4}
Unit cell dimensions	a=4.5144, b=5.0787, c=6.7297	a=10.638-10.51	a=13.98, c=4.523
Volume of unit cell	154	1204-1160	489
No. atoms per unit cell	16=12 Fe, 4 C	116=92 metal, 24 C	80=56 metal, 24 C

Table 2.1 Salient features of chromium carbides (102)

CHAPTER 3

THEORETICAL ANALYSIS OF THE LASER HEATING CYCLE

3.1 Introduction

Modelling of the laser heating effect during processing is crucial to the further understanding of the process and to the prediction of effects in new systems. A comparison of the results obtained in this project has been made with three different types of model: a simple empirical model by Courtney and Steen (134), an analytical model of the temperature field produced by a laser beam proposed by Shercliff and Ashby (172,173) and a more complex numerical thermal model discussed by Sharpe (23) which has been modified in a number of ways to model the exact situation encountered during the laser hardening of engine valve stems. This is discussed in Chapter 5.

3.2 Background to the Heat Flow Models

The theories presented by Rosenthal (174) in 1946 provide the most frequently used basis for predicting the heat flow in a substrate due to a moving source. Rosenthal presented solutions of the heat flow equations for a 1-dimensional heat flow model, a moving point source model and a moving line source model. This work is concerned with surface heating and melting so the only relevant model is the moving point source for determining the temperature cycle induced by a laser beam scanning the surface.

The moving point source Rosenthal solution is based on the following assumptions:

1) The physical characteristics of the metal are independent of temperature
2) The speed and rate of heat input are constant during the treatment cycle
3) Heat is supplied by a point source
4) Quasi-stationary state is quickly attained within the metal
5) Latent heat of fusion is negligible
6) Cooling occurs by conduction through the metal

A full derivation of this theory is given in reference 174 is not necessary for the purposes of this discussion, it is sufficient to quote the solution for the temperature field due to a moving point source with the above assumptions (expressed in rectangular co-ordinates and the Shercliff and Ashby nomenclature) as:

$$T - T_o = \frac{q}{4 \pi \lambda R} . e^{-\frac{vE}{2a}} . e^{-\frac{vR}{2a}} \qquad (3.1)$$

The assumption of a point source means that this temperature distribution reaches infinity when R=0. Therefore, the accuracy of the model decreases as R→0, and only points distant from the source may be examined to determine the temperature field. This shortfall can be overcome by assuming that the heat source has a non-zero finite size - thus avoiding infinite temperature.

The next major step in this direction was made by Cline and Anthony (175) whose solution allowed for the finite spot size of the beam. In this model, the energy distribution within the beam was assumed to approximate to a Gaussian intensity distribution for a semi-infinite substrate geometry. The model is used to solve the transient problem with a moving Gaussian source. The central result of the paper - a solution of the transient problem with a moving Gaussian beam - gives the following equation for the steady state temperature:

$$T = \frac{q}{C_p} \int_0^{\infty} \exp \left[\frac{-(x + Rt)^2 + y^2}{(2 r_B^2 + 4at} \right] \left[\frac{dt}{(\pi^3 at)^{.05} (2 r_B^2 + 4at)} \right] \qquad (3.2)$$

Where R is the characteristic beam radius. Clearly, this simplifies to the well known Carslaw and Jaeger moving point source solution (176) in the limit of zero spot size (which is also the same as the Rosenthal (174) solution), given as:

$$T(x,y,z) = \frac{q}{4 \pi \lambda R} . e^{-v(R+x)/2a} \qquad (3.3)$$

The authors also calculated penetration depths and cooling rates. However, Cline and Anthony pointed out the asymmetry of the temperature distribution with respect to x due to a source moving in the x-direction. As the velocity increases, the maximum temperature shifts behind the centre of the moving beam. It is not possible then to determine the maximum depth of penetration of an isotherm unless the variation of some depth parameter with x is known.

Ashby and Easterling (177) solved the quasi-steady state problem to obtain the temperature field produced by a moving beam by integrating the temperature field over the surface, with a view to examining the microstructural changes occurring in hypo-eutectoid steels during rapid heating. The solution is based on the following assumptions:

1) All of the absorbed energy goes into raising the temperature of the material with negligible latent heat of transformation
2) The solid is large enough that its average temperature is unchanged
3) The thermal properties of the material are constant
4) The surface absorptivity is constant
5) The eutectoid transformation temperature, A_1, is as given by the phase diagram

Using a similar basis as Cline and Anthony (175), the authors derive an approximate temperature field by considering the Gaussian beam as a line source of finite width in the y-direction but infinitessimally thin in the x-direction. The solution is based on Rykalin's analytical solution (178) for the temperature field due to a line source given in equation (3.4);

$$T - T_o = \frac{\frac{Aq}{v}}{2\pi\lambda\,[t(t + t_0)]^{0.5}} \exp\left\{ - \frac{1}{4a}\left[\frac{z^2}{t} + \frac{y^2}{t + t_0}\right]\right\} \qquad (3.4)$$

Where

$$t_o = \frac{r_B^2}{4a}$$

and is the time taken for the heat to diffuse over the beam half width.
Again, the surface temperature reaches infinity at the point where the beam impinges on the surface. To overcome this, Ashby and Easterling introduce an apparent line source in the plane $z=z_0$ (above the surface) to replace the real source in the z=0 plane.
This is justified by the fact that the beam has a finite width (x-direction), hence heat is input to a surface point over a period of time (the interaction time), during which, heat is conducted away from the surface leading to a finite surface temperature. The modified temperature field is then given by;

$$T - T_o = \frac{\frac{Aq}{v}}{2\pi\lambda\,[t(t + t_0)]^{0.5}} \exp\left\{ - \frac{1}{4a}\left[\frac{(z + z_0)^2}{t} + \frac{y^2}{t + t_0}\right]\right\} \qquad (3.5)$$

and directly below the beam centre, at y=0;

$$T - T_0 = \frac{\frac{Aq}{v}}{2\pi\lambda\,[t(t + t_0)]^{0.5}} \exp - \{\frac{1}{4a} \cdot \frac{(z - z_0)^2}{t}\} \qquad (3.6)$$

Where t_0 is given by the expression stated previously (Equation 3.4).
Now, differentiating Equation (3.6) with respect to time gives:

$$\frac{dT}{dt} = \frac{T - T_0}{t}\,[\,\frac{(z + z_0)^2}{4at} - \frac{1}{2}\,(\frac{2t + t_0}{t + t_0})\,] \qquad (3.7)$$

heating cooling

And the peak temperature, T_p, occurs when $dT/dt = 0$, i.e.

$$\frac{t(2t + t_0)}{t + t_0} = \frac{(z + z_0)^2}{2a} \qquad (3.8)$$

Ashby and Easterling go on to calculate z_0 for two limits using an equation by Bass (179) for the peak surface temperature, T_s, produced by a stationary Gaussian beam of average intensity, $q/\pi r_B^2$, applied for a time t_B. This equation is given as:

$$T_s - T_0 = \frac{2\,A\,q}{\pi^{1.5}\,r_B^2\,\lambda}\,(at_B)^{0.5} \qquad (3.9)$$

The solutions derived for the near-field ($t<<t_0$) and far-field ($t>>t_0$) are given below:

a) $t<<t_0$, Equation (3.8) becomes

$$t = \frac{(z + z_0)^2}{2a} \qquad (3.10)$$

Therefore, z_0 is given by:

$$z_0^2 = (\frac{\pi}{2e})\,(\frac{a\,r_B}{C_1 v}) \qquad (3.11)$$

b) $t >> t_0$. Equation (3.8) becomes

$$t = \frac{(z + z_0)^2}{4a} \tag{3.12}$$

And z_0 is given by:

$$z_0^2 = \left(\frac{\pi^{0.5}}{e}\right) \left(\frac{a\, r_B}{C_1 v}\right)^{.05} . r_B \tag{3.13}$$

The energy which just causes the surface temperature to exceed some critical temperature, T_c, is then expressed as:

$$\left(\frac{q}{v\, r_B}\right) = \frac{\pi^3}{4} \left[\frac{(T_c - T_0)\, r_B}{A}\right]^2 . \frac{\rho_c \lambda}{C_1 q} \tag{3.14}$$

Ashby and Easterling (177) also demonstrated the accuracy of the equations - within the realms of experimental error - for the prediction of case depths, cooling rates and the composition of hardened zones by examining the metallurgical transformations occurring as a result of the thermal cycle. A further refinement of this model by Shercliff and Ashby has been used in this work and will be discussed in the following section.

3.3 Theoretical Discusssion of Models Used in This Work

3.3.1 Numerical Model - Shercliff and Ashby (2)

The model derived by Ashby and Easterling has since been modified by Shercliff and Ashby and has been used in this work to calculate the operating window for transformation hardening, to compare theory with experimental results and to look at the thermal cycle and metallurgical transformations in more detail. The master plot resulting from the Shercliff and Ashby (180) analytical model for predicting case depths in laser surface treatment is shown in Fig. 3.1. The plot can be difficult to interpret and the following section aims to explain the plot by briefly discussing its derivation.

The derivation is very similar to that described previously with the exception that a more general equation by Bass (179) is used to calculate an expression for z_0. Instead of Equation (3.9), the following equation is used:

$$T_s - T_0 = \frac{A\,q}{\pi^{1.5}\,\lambda\,r_B}\,.\,\tan^{-1}\left(\frac{4at_B}{r_B^2}\right)^{0.5} \qquad (3.15)$$

(This reduces to Equation (3.8) in the limit $t_B << r_B^2/4a$.)
The new expressions for z_0 are then:

a) $t << t_0$ (near-field, close to source)

$$z_{01} = \left(\frac{2\pi}{e}\right)^{0.5}.\frac{a}{v\tan^{-1}\left(\frac{8a}{v\,r_B}\right)^{0.5}} \qquad (3.16)$$

b) $t >> t_0$ (far-field, remote from source)

$$z_{02} = \left(\frac{2\pi^{0.5}\,a\,r_B}{e\,v\tan^{-1}\left(\frac{8a}{v\,r_B}\right)^{0.5}}\right)^{0.5} \qquad (3.17)$$

And the expression for q, the energy required to just exceed a critical surface temperature, T_c, is:

$$q = \frac{\pi^{1.5}\,\lambda\,r_B}{A}\,.\,\frac{T_c - T_0}{\tan^{-1}\left(\frac{8a}{v\,r_B}\right)^{0.5}} \qquad (3.18)$$

Equations (3.6), (3.16) and (3.17) allow prediction of the temperature below a moving laser beam at any depth and reduce to the stationary source solution at the surface or the Rosenthal moving point source for large depths.

One further important modification made by Shercliff and Ashby was the reworking of the derivation using a system of three dimensionless variables. By grouping the six process variables (beam characteristics; power, diameter and speed and thermal properties of the steel; thermal conductivity, volumetric specific heat and minimum temperature required for martensite formation) and the dependent variable, case depth into three dimensionless variables according to Buckingham's Rule, the general temperature field was redefined in dimensionless terms using the following dimensionless groups:

$$\frac{1}{q^*} = \frac{r_B \lambda (T - T_0)}{Aq} \qquad v^* = \frac{v\, r_B}{a} \qquad t^* = \frac{t}{t_0} \qquad y^* = \frac{y}{r_B}$$

$$z^* = \frac{z}{r_B} \qquad z_0^* = \frac{z_0}{r_B} \qquad \text{and} \qquad x^* = \frac{x}{r_B} \tag{3.19}$$

The temperature field is therefore given by:

$$\left[\frac{v^*}{q^*}\right] = \frac{2/\pi}{\{t^*(t^* + 1)\}^{0.5}} \cdot \exp - \left[\frac{(z^* + z_0^*)^2}{t^*} + \frac{(y^*)^2}{(t^* + 1)}\right] \tag{3.20}$$

An approximate solution to the temperature field in the near and far field respectively yields the following:

$$t_p^* = 2\,(z^* + z_{01}^*)^2 \qquad\qquad t_p^* = (z^* + z_{02}^*)^2 \tag{3.21}$$

near-field far-field

And therefore the normalised expressions for z_0 become:

a) near-field solution

$$z^* + z_{01}^* = \left[\frac{2}{e\pi^2}\right]^{.05} \left[\frac{q_m^*}{v^*}\right] \tag{3.22}$$

b) far-field solution

$$[z^* + z_{02}^*]^2 = \left[\frac{2}{e\pi}\right] \left[\frac{q_m^*}{v^*}\right] \tag{3.23}$$

Where q_m^* and v^* are independent groups since z_{01}^* and z_{02}^* are functions of v^*. The surface temperature was calibrated using the general Bass equation (Equation 3.15) and again the results shown to be accurate within experimental error.

Examination of the the master plot which is a plot of z_c^* against v^* with contours of constant q^* on log scales shows that for any steel, there is a critical value of q^*

($q^* \approx 7.5$, for a medium carbon steel) below which melting will not occur and a mimimum value of q^* required to just cause hardening ($q^* \approx 3.5$, for a medium carbon steel). The master plot therefore allows the operating window to be defined.

3.3.2 Simple Empirical Model - Steen and Courtney (1)

A simple empirical relationship for case depth was formulated by Courtney and Steen (134), on the basis of statistical analysis of results from LTH of En8 steel. The theoretiacl basis for the analysis is the unique relationship between the dimensionless temperature , T^* and the dimensionless time θ^*, for a stationary spot with a certain surface heat loss, as discussed by Steen (11), where;

$$T^* = \frac{T\pi k\, d_B}{Aq} \qquad \text{and} \qquad \theta^* = \frac{4\,\alpha t}{z^2} \tag{3.24}$$

Since the heating time in a moving system is proportional to d_B/v, the depth, z, is proportional to $\sqrt{d_B/v}$ and the associated value of T means that T is proportional to q/d_B. Now z is a function of T and t for a given material thus z can be related to the parameters as follows:

$$z \propto z\,(\frac{q}{d_B})\sqrt{\frac{d_B}{v}} = \frac{q}{\sqrt{d_B v}} \tag{3.25}$$

Comparison of this parameter with the experimental results by a least squares fit gave the following:

$$z_c = -\,0.10975 + 3.02\,(\frac{q}{\sqrt{d_B v}}) \tag{3.26}$$

With a standard error on Y, 0.094, and a correlation coefficient of 0.88. The plot of hardened depth versus $P/\sqrt{d_B v}$ for En8 steel is shown in Fig. 3.2, the result is more than acceptable when the experimental scatter is considered. Similarly, the onset of surface melting was correlated to the parameter $P/d_B{}^2 v$ which is constant for a given material. Process operating charts developed using this data showed a small operating region for small beam diameters for large case depths.

3.3.3 Finite Difference Numerical Model - Sharpe (23)

The third and final theoretical model used in this work is due to Sharp (23). This finite difference numerical model, GLAB1, runs on the VAX/VMS mainframe and

was initially used as a predictive tool and then modified to model the application of LTH to engine valve stems. Models of surface sources where the substrate is assumed to be semi-infinite may decrease in accuracy for components such as valve stems where the geometry has finite thickness. The finite difference model has been modified to study the effect of this finite thickness on non-linear heat transfer at conductive and radiative boundaries, as the beam scans the surface. In addition the output nodal temperature data from the program has been modified so that it can be read into a Femview 5 program which converts the original printout (cross-sectional isotherm profiles and thermal histories at different depths) to a 3-dimensional temperature grid of the substrate. This allows the observer to view quickly and clearly the heating effect of the beam and to extract temperature profiles in any plane without the need for cumbersome data extraction and manual graph plotting previously necessary. A block diagram constructed from the original code is given in Appendix A. A full theoretical analysis is too wieldy for this section which gives a brief description of how the model operates and the main principles.
Numerical modelling of the heating process can be more accurate than less complex analytical models. This F.D. model applies to all continuous wave laser processes with the exception of laser cutting. The model was initiated by Steen in 1977 (181) and subsequently modified by a number of authors the most recent ammendments being those of Sharp (23).

A substrate moving beneath the laser beam will undergo a thermal cycle, developing a stationary temperature field relative to the beam. This steady state field is approximated using a transient solution. A uniform cartesian grid is employed and the intensity profile of the beam is assumed to be radially symmetric - therefore, only points for $y>0$ need be considered. The distance between grid points in each direction is uniform. Following the block diagram (Appendix A), the initial set of calculations is performed on a rough grid. After a chosen number of iterations, the extent of the temperature field is determined and a finer grid set to cover the heat affected zone. Heat flow into the surface is governed by the incident power, convective and radiative heat losses and the variation of surface relectivity. The latter being the most influential parameter. For the purposes of this model, the variation of reflectivity is assumed to be a stepwise linear function of temperature, as shown in Fig. 3.3 (where T_2 is the boiling point). The heat flows from the surface source, heat transport due to substrate motion and Fourier conduction of heat between points are derived by heat balance techniques. For heat flow with surface melting latent heat effects become considerable. There is also heat flow by convection within the melt pool. This model is capable of modelling phase changes, keyholing, variable reflectivity and arbitrary mode structure, although models based on heat flow without melting can approximate surface melting with a reasonable degree of accuracy.

The model uses a uniform 3-dimensional mesh with a variable number of points in orthogonal directions so that the region of interest is most effectively covered. The maximum number of grid points is set to 9000 and the grid point temperatures are

stored in an array TEMP.

Parameter and control data are read from a data file or entered via an input command. The size of the initial region of interest (DLENX x DWIDY x DTHIZ) is contained within the data statement. A suitable mesh size to cover this region is calculated by subroutine RANGE which gives the mesh size (decreased to fall just below 9000), DELTA and the number of points in each direction, IX, IY, IZ. IZ is set to 3 should it fall below, then IX and IY determined in the correct ratio to give <9000 grid points. The grid point index of the beam centre is KI and is set approximately one third of the way along the x direction.

With the initial grid defined, the power distribution of the beam is calculated by subroutine POWDIST and the results stored in a 2-dimensional array, (IX,IY)POWER. This subroutine sets power to zero for elements > 4(beam radius) away from the beam centre. (This is justified by the fact that all TEM modes have an exponential factor thus elements towards the edge of the region recieve only a minute fraction of the power. POWERIN is a numerical integration function which calculates the average power falling on any element and allows for the mode structure.

A value for the time step (DELTIME) is calculated by sunroutine DELTIM using the grid which has been generated and the traverse speed given.

The number of grid points (and therefore the execution time) for which the finite difference calculations are performed is limited by subroutine GRDLIM. It does this by finding the indices of the outermost elements in all directions for which the temperature rise is ≥ 20K. The variables $1 \leq KS \leq KF \leq IX$, $1 \leq IYL \leq IY$ and $1 \leq IZL \leq IZ$ are set and the heat transfer calculations are carried out in the region defined by KS, KF, IYL and IZL.

Subroutine CALC carries out the main heat transfer calculations and is called once each iteration. The six Fourier heat flows are calculated and stored in the variables DXEF, DXWF, DYNF, DYSF, DZUF and DZDF. Where surface elements DZUF or DZDF are calculated as having convective and radiative heat transfer. It is assumed that the outermost elements in the X and Y directions conduct heat into the surrounding material which remains at ambient temperature.

DELCOND stores the convective heat transfer term due to the substrate motion and the variable FLUX stores the flux from the beam (FLUX is calculated from the POWER array for surface elements, allowing for the temperature dependent reflectivity function RF. For other elements, FLUX is obtained from the surface power intensity reduced by the Beer-Lambert coefficient, or from the average transmitted power.

HFLOW is the overall Fourier heat flow which is used to calculate the rate of temperature rise RESDU and the temperature rise of an element during the iteration, RES. A temporary new value for the temperature of the element is stored in TEMPT.

Subroutine LATTRAP corrects for any latent heat effects and then corrections for keyholing and latent heat of vapourisation are dealt with. This section is not relevant for transformation hardening, it is sufficient to say that it is controlled by a Fortran DO-loop and places the revised values for the temperature rise (RES) and temperature (TEMPT) in the array TEMP. The maximum temperature rise for any grid point (IPK, IPI, IPL) in an iteration is stored in the variable BIG for use in determining the convergence of the model. The value of BIG is printed periodically so that progress can be monitored.

On completion of the given number of iterations (IJRESET), subroutine RESET is called. This modifies the grid to the developing temperature field by examining the extent of significant temperature rise (10K > ambient). Although simple to determine in the X direction, a second subroutine, PROFILE is needed for the Y and Z directions since the positions in Y and Z where the maximium temperature rise occurs are not implicitly known due to the temperature field being swept behind the beam centre. The maximum temperatures reached for Y and Z values along the X axis are stored in a cross-sectional, temperature array, PROF. The ranges of significant temperature rises are then stored in the variables XL, XR, YR, and ZR and the total range in XT. (Setting IWELD=1, modifies the Z range should the points span two physical boundaries.

The procedure described above for setting a new grid, calculating the array POWER and setting DELTIME using the initial settings (DLENX, DWIDY, DTHIZ) isnow employed using the new values, XT, YR, ZR. The TEMP array is reset to the initial temperature and the loop begins again.

A model run is terminated by (a) no significant temperature rise occurring, (b) reaching the number of cycles set (LIMIT) or (c) convergence occurring. A dynamic convergence criterion is employed whereby the variable CONVTEM is set to the maximum temperature rise occurring at any point in the main run and if the maximum temperature rise falls to < 1/500(CONVTEM) the run is terminated and the convergence criterion printed. The model output gives the temperature reached at points in the X, Y and Z directions.

There are two post processing programs which analyse the thermal data to produce isotherm positions from the data in the PROF array (Isotherm Program) and thermal histories at various depths within a zone defined by a certain temperature e.g. the melting isotherm (Thermal History Program). Source code listings of all of these programs are included on microfiche inside the back cover.

3.4 Use of the Models

The following section descrbes the use of and modicications made to the models. The Steen and Courtney (134) model was used simply to compare with experimental results and is therefore omitted from this section.

3.4.1 Calculation of Operating Window Using Shercliff & Ashby Model(2)

The Shercliff and Ashby model (172,173) was used to calculate the operating window for laser transformation hardening, for En24 and En52 steels. Using the assumption that a 0.5mm case depth was required, the dimensionless equation (Equation 3.20) was manipulated to enable the velocity required to produce this case depth to be calculated over a range of powers, absorptivities and beam diameters. This gave an operating matrix and therefore an indication of the parameters required for successful hardening, eliminating the trial and error method.

A computer program in Basic has been written to solve equation (3.20) for v^* using an iterative technique with the Newton-Raphson approximation. The code for this program is presented on microfiche inside the back cover of the thesis. The program was used to calculate a complete series of tables showing the traverse speed necessary to give the desired case depth, for each steel with any possible combination of q, r_B and A. The values used for the material properties of the steels are given in Table 3.1 (all units are as given in nomenclature).

Obviously, certain combinations of parameters will lead to surface temperatures in excess of the melting point. Therefore, a second series of calculations have been performed using a Basic program to calculate the surface temperature for each set of conditions. Those combinations of parameters leading to surface melting were noted and the onset of melting line plotted on the operating tables. Results from this work are presented in Chapter 5.

3.4.2 Modifications to the Finite Difference Model

3.4.2 (i) Creation of a Diagramatic Output

The first modification made to the finite difference model was to produce a program capable of giving easily interpreted output data. In order to do this the model was studied to ascertain the order in which data points were stored for each node so that the data could be correctly transferred to another file. A program was written to convert the nodal temperatures and co-ordinates for each of the 9000 elements into a Femview 5 database. This program is called GMESH2. In essence, the program reads the dimensions of the mesh, IX, IY, IZ and DELTA from a program run and generates a new database from the temperature array TEMP. Again, the code for GMESH2 is presented on microfiche inside the back cover. This gives output of the form shown in Fig. 3.4, compared to a large number of printed data sheets for each run by the old method. As shown, the data is easy to interpret and the onset of melting and case hardening lines can be clearly extracted if necessary. For the results discussed later, the colours were set to particular isotherms so that they could clearly be viewed. From the mesh generated in this way, it was also possible to determine the effect of the number of iterations on the model output and the temperature profile for any line chosen through the heat affected zone.

3.4.2 (ii) Modification of the Boundary Conditions

Engine valve stems are of finite width but comparatively infinitely long. Therefore, there is insufficient bulk material to accomodate adequate conductive cooling from the circumference of the stem during laser transformation hardening but conduction can occur along the length. Cooling occurs by convection and radiation from the sides of the valve stem. If the valve stem is considered on some cartesian axis then the x direction is the beam direction, along the length for most experiments, the y direction is the width of the stem and the z direction its thickness. The assumption made in the existing finite difference model is that the x and y boundaries allow conductive heat transfer and the z boundary allows convective and radiative heat transfer. In fact, real the situation would be more closely modelled if the y boundary were also cooled by convection and radiation.

Modification of the boundary conditions required a closer look at subroutine CALC - the main heat transfer calculations to understand how the boundary conditions are incorporated into the main structure. Six Fourier heat flows are calculated and stored in the variables DXEF, DXWF, DYNF, DYSF, DZUF and DZDF. The relationship of each of these surfaces to the substrate geometry is shown in Fig. 3.5.

Surface elements DZDF or DZUF - depending on whether the upper or lower surface is being considered - are calculated as having convective and radiative heat transfer. The model is symmetrical in the y direction and models outermost in the x and y directions are assumed to conduct into the material remaining at ambient temperature. The finite difference equations must allow for such boundary effects thus separate heat balance equations are derived for grid points lying on the boundary surfaces. The stability criterion (the limit imposed on the allowable time step in the solution process) is more stringent for surface nodes than for those in the interior. In reality, each point will have its own stability criterion, however in practice this is too wieldy and a single stability criterion is chosen for each iteration level, such that it satisfies the stability criterion for all grid points, preventing errors propagating through the solution.

A series of write statements have been incorporated into the code of the modified boundary condition model, GLAB3, to explain the calculations. The y boundary has been altered to allow for convection and radiation and a series of runs performed to establish the effect of this change and its relevance to the problem in hand. Essentially modifying the y boundary means that the temperature of nodes on the boundary face can rise above ambient where they were unable to do so previously. A modification to the output definitions was also needed so that these higher temperatures could be incorporated. The effect of increasing the beam diameter to the same width as the substrate has also been investigated as haave the effects of speed and power. Results have been used to compare with experimentally determined results and are discussed in Chapter 6.

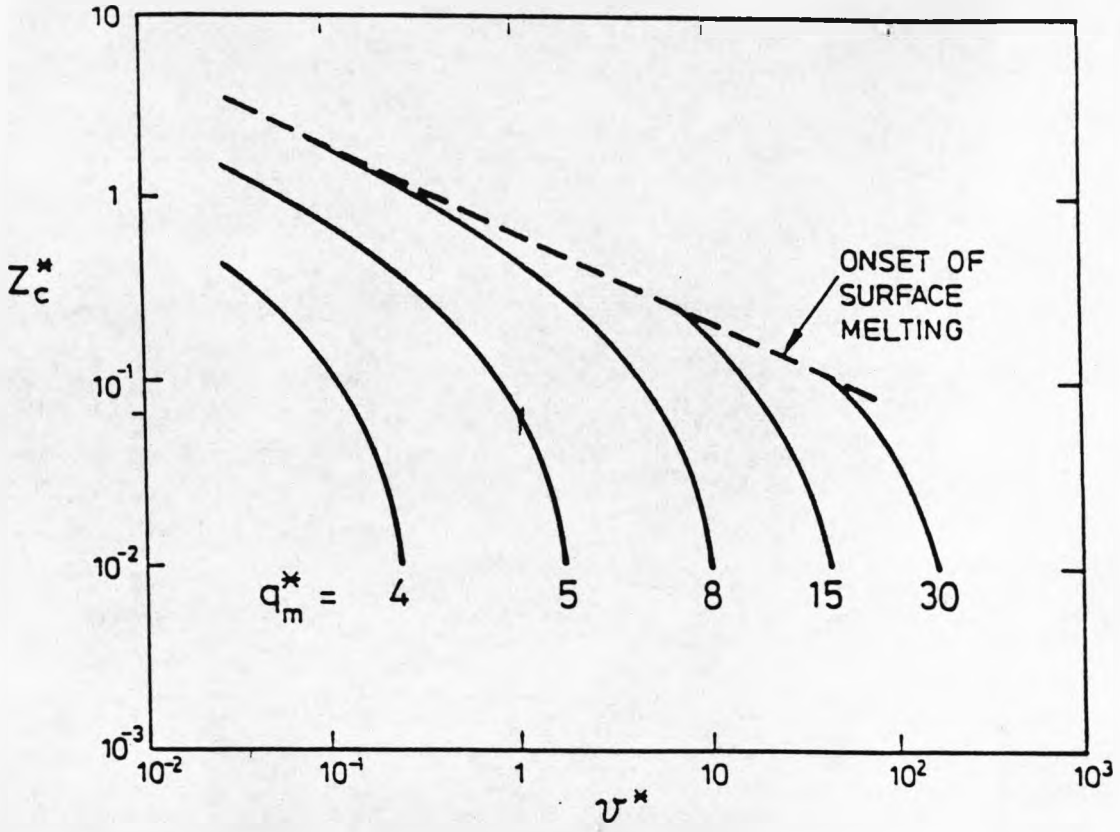

Fig. 3.1 Shercliff and Ashby (180) master plot for case depth prediction (log(base 10) scales)

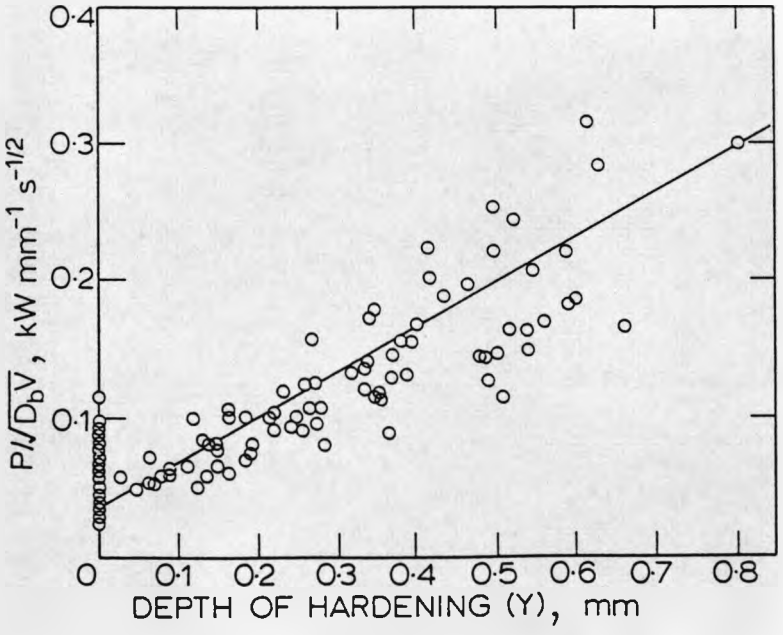

Fig.3.2 Hardened depth correlation according to Steen and Courtney (134)

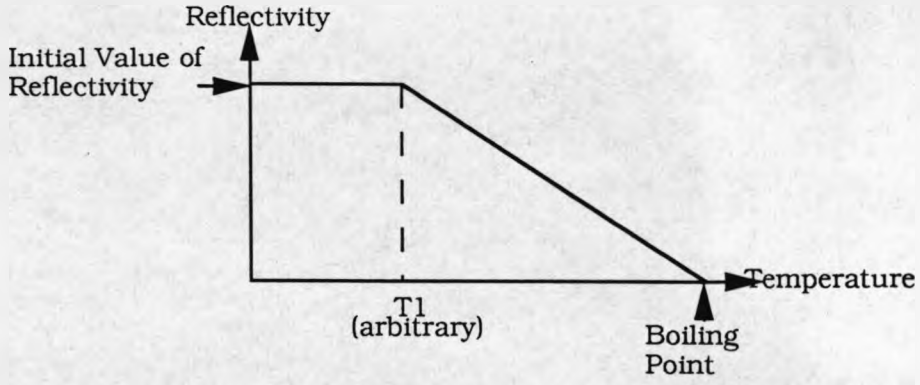

Fig. 3.3 Variation of Reflectivity with Temperature

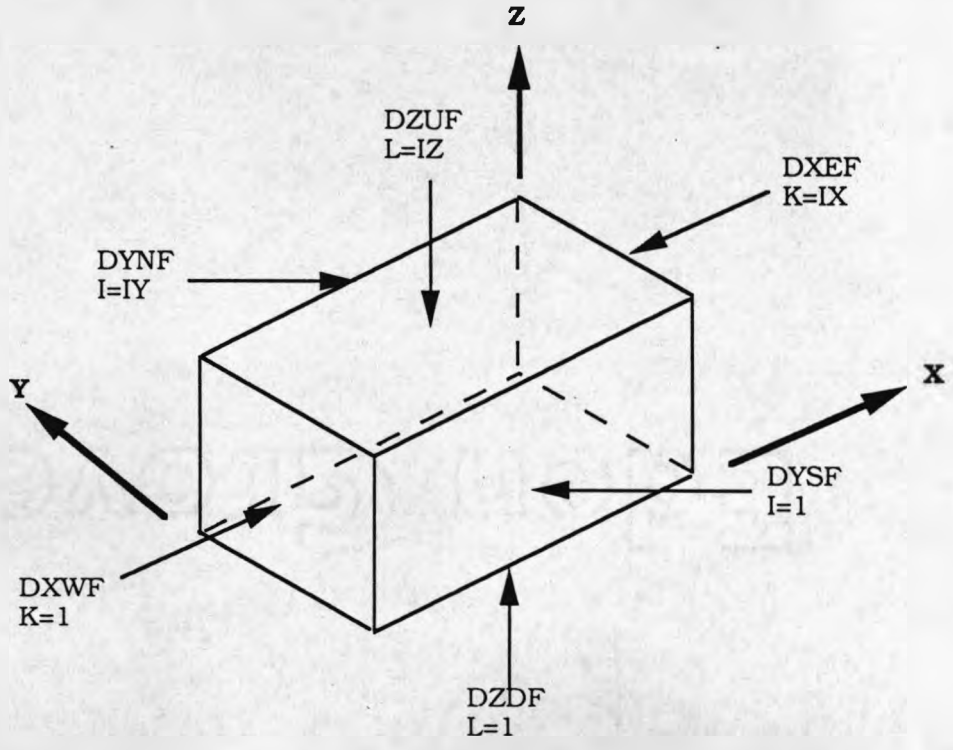

Fig. 3.5 Faces and Index Points for Subroutine CALC

Quantity	En24	En52
Specific heat per unit volume (s-1m-1K-1)	4.9x10 -6	6.9x10 -6
Thermal conductivity (Js-1m-1K-1)	33.89	18.83
Thermal Diffusivity (m2s-1)	6.9x10 -6	3.7x10 -6

Table 3.1 Thermal properties of En24 and En52 steels

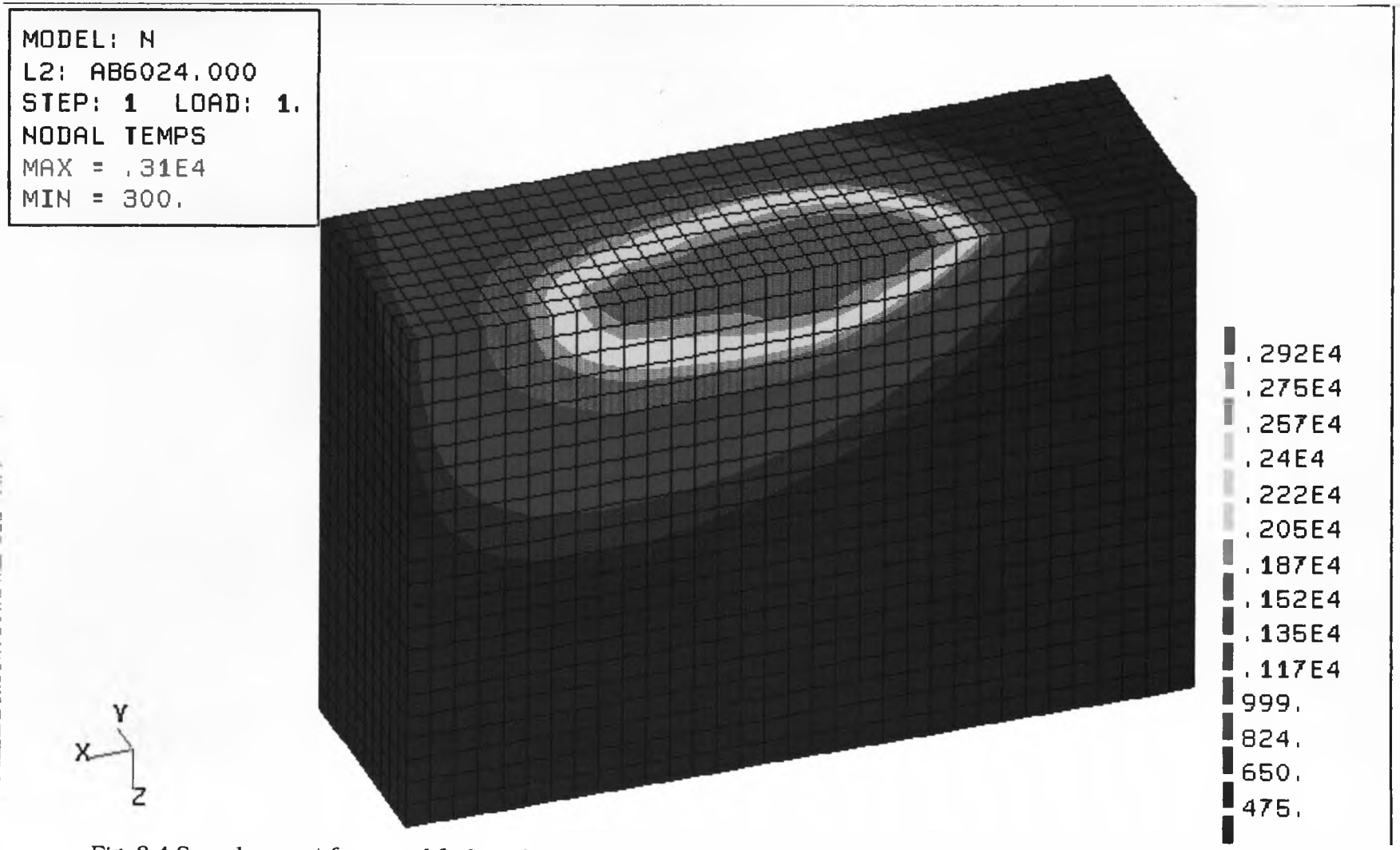

Fig. 3.4 Sample ouput from modified mathematical model illustrating temperature contours for moving Gaussian beam

CHAPTER 4

EXPERIMENTAL PROCEDURES

4.1 Equipment Used for Laser Treatment

4.1.1 Lasers Used

This section will describe briefly the different lasers used and what they were used for. Four carbon dioxide lasers and an excimer laser were used during the course of this work.

4.1.1 (i) BOC 2kW Control Laser

The BOC Control laser is a fast axial flow continuous wave CO_2 laser. It has four discharge tubes, which operate at low current (140mA) and high voltage (30kV). This high voltage discharge is used to excite a gas mixture of CO_2, He and N_2, to produce laser radiation at the 10.6 μm wavelength. The diameter of the raw beam is 22mm and is output via a cooled 35% reflectance zinc selenide window. The laser beam is directed to the workstation through aluminium flight tubes using a series of three gold coated, water-cooled copper mirrors. The cavity can be tuned using a 2-screw combination, aligning the back mirrors and output window of the laser cavity..

4.1.1 (ii) Electrox 1500W Laser

The Electrox CO_2 laser is also a fast axial flow laser similar to the BOC laser - in fact historically it is a smaller copy having some of the same designers - which has four discharge tubes. In this case, the output beam diameter is 18mm. A similar optical arrangement is used, the beam being reflected to the workstation by three mirrors,as above. This laser operates predominantly in the $TEM_{01}*$ mode.

4.1.1 (iii) Laser Ecosse (Ferranti) AF5 Laser

The AF5 laser is another fast axial flow high power CO_2 laser, with maximum output power of 4kW in continuous wave operation in TEM_{00} mode, 5kW in $TEM_{01}{}^*$ mode and 6kW in multimode. The limiting power is determined by the maximum thermal stress on the zinc selenide output window. The discharge tubes, of which there are twenty, are arranged in a series of four, the rows of tubes joining to form a zig-zag pattern. The raw beam diameter in this case is 20mm. Altering the deformation of the output mirrors allows the operator to modify the beam mode. This laser was mainly used for the laser cladding section of this work and the TEM_{01} mode was

chosen. Five gold coated, water cooled copper mirrors were used to deliver the beam to the work piece.

4.1.1 (iv) Laser Ecosse (Ferranti) MF400 Laser

The MF400 is a low power (400W) slow flow CO_2 laser with 12m of folded water cooled discharge tubes. It was used to experimentally determine the reflectivity of different surface coatings used for transformation hardening. A single gold coated copper mirror was used to deliver the beam to the work piece. The output beam was 15mm diameter with a Gaussian intensity distribution.

4.1.1 (v) Excimer Laser

A Lumonics HyperEx-460 SM laser was used for this study. This laser operates in pulse mode only. The gases used were krypton, neon and fluorine. With this mixture of gases, the laser operates at a wavelength of 248nm. A complete study of the output characteristics and power dependence of this laser is given by O'Neill (33). For the purposes of this work, it is sufficient to say that the composition of the gas mixture introduced to the laser chamber was 1.4% F_2, 1.9% Kr and 97.6% Ne, with total pressure 3100 torr. This corresponds to the manufacturers recommendations.

The laser was used to roughen the steel surfaces to improve absorptivity before CO_2 laser hardening. After a certain time period of operation, the laser power is reduced to a level which is unacceptable for this application. This is a direct result of a reduction in halogen content of the gas mixture (due to generation of impurities and dissociation products). Further injections of fluorine are possible to a limited degree, but a complete gas refill is required eventually. One gas fill was found to be sufficient to treat about 300mm of steel surface at the very slow speeds ($0.25mms^{-1}$) before halogen replenishment was necessary. After which, a change of gas was needed when a further 200mm had been treated. Treatment in this manner resulted in a track width of about 5mm. Two tracks were generally used to cover the surface area of a 100mm long sample with an 8mm ground flat. The resultant surface was blackened, with a rippled pattern which was visible to the naked eye on close inspection.

4.1.2 Beam Delivery System

The laser beams in all cases except the excimer laser were delivered to the workstation by a series of reflective gold coated copper mirrors, water cooled from the reverse side. Aluminium flight tubes were used to encase the beam as it travelled from the laser head. It is important to note that the ambient temperature and temperature fluctuations of the mirrors affect beam alignment and the alignment should be checked each time the laser is restarted.

4.1.3 Laser Beam Alignment

Since the alignment procedure is similar for all lasers, the principle will be illustrated for the Laser Ecosse AF5 laser only, as this was the laser most frequently used.

Alignment is facilitated using a visible helium-neon (HeNe) laser beam to map the path of the CO_2 beam. The operating arrangement of the AF5 laser is shown in Fig. 4.1.

Referring then to this diagram, the beam exits the laser horizontally at point A and is deflected vertically downwards by mirror M1 (All mirrors are gold coated copper mirrors which are water-cooled), to mirror M2 directly below it. The first stage in alignment is to check that the HeNe and CO_2 beams are aligned at this point. This is done by firing the CO_2 beam at a firebrick to produce a glassy indentation, the centre of which should be concurrent with the centre of the HeNe beam. If the two are not centred on the same spot, the position of the HeNe beam can be adjusted to suit using two micrometer screws situated on the laser head.

This procedure is then repeated at each mirror, so that the beams fall roughly centrally on each mirror, and the two beams are aligned at each stage.
It is therefore possible to align the CO_2 beam to the job without actually having to fire at the surface. After satisfactory alignment has been achieved to the final mirror M5, the beam can be directed into a focussing optic, which will be either a mirror or a lens, depending on the application. The two types of focussing arrangement have been used in the course of this work and are discussed below.

4.1.4 Lens Focussing assembly

The lens holding assembly is illustrated in Fig. 4.2. It basically consists of a holder for the potassium chloride lens (38mm diameter), whose height with respect to the substrate surface can be varied by means of spacers in the unit. The beam is focussed through a nozzle using adjustment screws on the lens assembly which moves the whole unit in relation to the laser beam. A 125mm focal length lens was used, the height set so that the beam focus was just below the end of the nozzle. A down draught of argon gas was used to protect the lens from dust particles which cause hot spots on the lens leading to cracking.

The lens focussing system was used for the early part of the work detailed here. However, alignment was found to be a very tedious process and the lens system was discarded in favour of a mirror focussing arrangement when it became available.
One further disadvantage of the lens system, especially for laser cladding was the geometry of the lens holder. It was extremely difficult to arrange the lens holder, powder feed tubes and substrate, and still maintain sufficient working distance to achieve the required beam diameters.

4.1.5 Mirror Focussing Assembly

Referring to Fig. 4.1, replacement of mirror M5 (or the final reflecting mirror for the other lasers) with an off-axis parabolic mirror allowed the beam to be focussed on the work piece without the use of a lens.

The mirror used was coated and cooled as before and had a 500mm focal length. The beam produced was a circular beam and allowed the operator more experimental freedom in terms of geometry. The working distance with respect to the beam focus was altered by changing the height of the workstation. In view of the replacement cost of KCl lenses, and their poor durability when compared with the mirrors, it is envisaged that the use of focussing mirrors will increase in the future.

4.1.6 Safety

Another important aspect of experimental work with lasers is safety. The lasers used are provided with interlocks to ensure operator safety from that point of view, but it is vital for the user to protect himself and others whilst working. During the alignment procedure, aluminium guard tubes are often removed to assist alignment. It is important that they are replaced before the laser is fired, to avoid an exposed beam travelling in the laboratory. As with all laser work,safety spectacles must be worn to protect the eyes from the intense and scattered radiation and the work must be shielded from on-lookers by means of protective perspex screens.

4.1.7 Determination of Process Variables

The process parameters which require measurement include focal point of the laser beam, beam power, beam diameter and mode structure, substrate velocity and surface reflectivity. A concise review of laser beam parameter measurements is given by Oakley (183). The following section details how each of these variables were determined experimentally. Surface reflectivity measurements were made only for the hardening experiments, where different coatings were used, the experimental details will therefore be discussed in section 4.2.1 (v).

4.1.7 (i) Focal Point of Laser Beam

Due to the difference in wavelength of the CO_2 and HeNe beams, they focus at slightly different positions after the lens or mirror. It is thus not adequate to choose the focal point of the visible HeNe beam as the actual focus of the CO_2 beam. Two methods were used to determine the focus of the CO_2 beam.

Method 1 - Blue Flash Test

This method was used with the lens focussing assembly. Argon gas applied as a lens shroud forms a bright blue plasma when the beam is fired at a steel surface in its presence. By moving the steel up and down around the focus, it was possible to

determine the focus as the point where the brightest flash was observed. This method could not be used with a mirror focussing optic as the argon shroud was neither powerful enough, nor in the vertical direction.

Method 2 - Perspex Print

This method was used with a mirror and also in conjunction with method 1 for lens focussing. A strip of perspex was held vertically so that its edge was just in the path of the beam, close to the focus. The beam was momentarily fired producing an imprint of its shape in the perspex, the convergent point of which represents the beam focal point. This determination was more difficult for the off-axis parabolic mirror due to the longer focal length and somewhat elongated focus.

4.1.7 (ii) Laser Beam Power

Three methods of power determination were employed:

Method 1 - Water Cooled Copper Calorimeter

The water cooled copper calorimeter is an integral part of the lasers and was used as a method of determining laser power at the laser head. The laser beam is deflected into the calorimeter when it is not being fired by a reflecting mirror which can switch the beam back to the workstation when the shutter is opened. The temperature of a known flow of water is measured by thermocouples, as shown, which is proportional to the beam power. This method of power determination is an integral part of the CO_2 lasers used, except the Electrox laser, and is usually connected to a LED display panel. The method has three major disadvantages:

(1) the calorimeter is not operational during firing
(2) the power recorded is critically dependent on the water flow rate and temperature, deviations in either result in changes in the recorded power which may not be representative of the laser power.
(3) the power measured is the output power of the laser and hence is not inclusive of power losses occurring at the optics. The power recorded at the laser is therefore not equivalent to the power incident on the work piece.

Method 2 - Laser Power Meter (Puck)

The power meter consists of a non-radiating black aluminium puck which is connected to a pressure gauge by a gas filled tube. The puck is held in the path of the laser beam and moved around while the beam fired for 10s, so that surface damage does not occur. The heat absorbed by the body causes expansion of the gas which produces a reading on the gauge, calibrated from 0-10kW, proportional to the incident beam power. The advantage of this method is that it can be used close to the work piece (although not after focussing the beam), and is a measurement of the beam power as it is being fired.

Method 3 - Copper Sphere

The experimental arrangement of power determination using a copper sphere is a

simple method of determining the laser power at the work piece. It therefore has the advantage of being a more accurate measurement of the incident power. i.e. after losses due to reflection/transmission of the beam at mirrors or lenses.
The focussed beam is fired into a small hole in the 'black body', a copper sphere of known mass with three supporting legs which made minimum contact with a firebrick to prevent heat loss by conduction. The sphere can be assumed to behave as a thermally isolated body, losing heat by convection and radiation only.
The focussed beam is scattered when it enters the body, and a heating rate is recorded via a K-type thermocouple placed in another hole in the sphere, as shown in the diagram. The thermocouple was connected to a chart recorder which allowed the heating and cooling cycles to be recorded.

The laser power (q) can be calculated from the trace produced using a simple energy balance equation, where;

$$q = m C_p[(\frac{dT}{dt})_H - (\frac{dT}{dt})_C] \qquad (4.1)$$

where q = laser beam energy (W)
m = mass of sphere (kg)
C_p = specific heat capacity of copper ($JK^{-1}kg^{-1}$)
$(dT/dt)_H$ = heating rate (Ks^{-1})
$(dT/dt)_C$ = cooling rate (Ks^{-1})

The heating and cooling rates were measured from the gradients of the trace as shown. In some cases the power measured in this way is as low as 69% of the output power. It is therefore important to measure the actual power at the work piece.

4.1.7 (iii) Beam Diameter

It is of particular importance for the materials processing specialist to have an accurate determination of the diameter of the defocussed laser beam incident on the work piece, as this parameter greatly affects the nature of the surface treatment. There are a number of methods for determining beam diameter, but these tend to be comparative rather than absolute. The various techniques have been discussed in Chapter 2. Two methods were used here.

Method 1 - Burn Print in Wood or Perspex
The beam was fired instantaneously, into a piece of wood or perspex at the working distance. For wood, a charred imprint of the beam was formed from which the diameter was measured. Perspex vaporises in the laser beam, leaving an indentation from which the diameter can be determined, using a vernier. This method has some limitations, in that the print size is dependent on both the interaction time and the mode structure of the beam.

Method 2 - Calculation of Diameter from Focal Length

The mathematical determination of beam diameter from a known focal length optic is illustrated in Fig. 4.3. The focal length must first be checked to ensure that the quoted value is correct. If the work piece is set a distance x below the optic (lens or mirror), and the diameter of the raw beam is known, then the beam diameter at the substrate can be calculated as follows:

$$\tan q = \frac{R_b}{f} = \frac{r_b}{f} \qquad (4.2)$$

And:

$$d = 2\, r_b \qquad (4.3)$$

Where R_b = raw beam radius
f = focal length of optic
x = distance of substrate below focus
d = beam diameter at work piece
r_b = beam radius at work piece

4.1.7 (iv) Beam Mode Structure

The mode structure of the laser beam is another very important parameter for laser surface treatment, as discussed in Chapter 2. A number of methods were used to determine the mode structure of the beam before treatment.

Method 1 - Raw Beam Print

The most elementary method of mode determination is to take a raw beam print (before the beam passes through the final lens or mirror) in wood or perspex, as detailed in the previous section. The imprint produce allows one to observe whether the power distribution is symmetrical and what form the mode is. For example, a Gaussian beam would produce a single indentation, whereas a TEM_{01} mode would produce a donut shaped indentation. Although relatively unsophisticated, this method was found to be effective.

Method 2 - Laser Beam Analyser (LBA)

The laser beam analyser (160) was used for more accurate mode tuning. This consists of a rotating reflective rod which passes through the raw beam reflecting a small proportion of the energy onto two pyroelectric detectors. These detectors record the intensity distribution of the beam in two orthogonal directions. The LBA was connected to a cathode ray oscilloscope (CRO) which showed amplified intensity distributions. The laser was tuned (where possible) to produce the required mode by observing changes in the intensity distribution on the CRO. When the facility for mode tuning was available (depending on the laser used) the mode chosen for surface treatment was TEM_{01}.

4.1.7 (v) Traverse Speed of Substrate

The substrate velocity was controlled by a computer numerically controlled (CNC) workstation. The software used was marketed by TRIO™ . The table is driven by DC motors connected to encoders, which control the distance moved by the table. The accuracy of the CNC table is quoted as +/- 0.05%. The velocity was verified by calculating the time taken for the table to travel a known distance.

4.1.8 Equipment Specific to Laser Hardening Experiments

Certain pieces of equipment were used for the transformation hardening section of this project only and will be discussed in this section.

4.1.8 (i) Rotating Jig for Hardening Circular Bars

A rotating jig was used for hardening valve stems. This is illustrated in Fig. 4.4. It consists of a 3-jaw chuck in which the rods were held, whose speed was controlled by a DC motor. The motor was calibrated before use as follows:

Calibration of Rotating Jig

The motor controller for this piece of equipment has two possible speed ranges, indicated by slow and fast. Each setting operates from 0 - 10, and is set using a rotating dial which can be locked into position. For each integer number on both the slow and fast settings, the time taken for twenty revolutions was measured with a stopwatch. For ease of measuring, a fiducial mark was attached to the jig, which was observed to click on the CNC table on each revolution. The time taken for one revolution was calculated in each case.

4.1.8 (ii) Design of Shrouding System for Valve Stem Hardening

The hardening of a significant length of valve stem for wear testing samples presented a problem regarding the maintenance of an adequate quench rate of the bar. In order to aid cooling and prevent substrate melting over a 100mm length, the jig illustrated in Fig. 4.5 was designed. The shroud nozzles were made of black coated copper and were positioned approximately 2mm behind the point of incidence of the laser beam. The shroud gas used was argon, at a pressure of 40 litres per minute. This system was found to be highly effective, the depth of hardness remaining essentially constant over the length of the valve stems.

4.1.9 Equipment Specific to Laser Cladding Experiments

In addition to the equipment already described, a number of additional items were used for laser cladding, which are described in detail below.

4.1.9 (i) Powder Feed System

For cladding with a single powder,a screw fed, pneumatic powder feeder was used to deliver the powder to the work piece. This was based on a design by Weerasinghe and Steen (24), and is illustrated in Fig. 4.6. The screw is a twist drill, whose edges aid powder flow by displacing it into the flutes. The screw pitch was chosen to allow uniform feeding of the powder at an argon flow rate of 2 l/minute. Initial trials using a larger pitch screw led to pulsing of the powder on exit from the feed tube. Weerasinghe, also investigated the effect of varying factors such as screw pitch, screw speed, particle size and hopper pressure on the flow rate (24). The powder was delivered to the melt pool via a copper tube (3mm internal diameter), positioned at a 40^{0} angle to the horizontal, and about 12mm from the melt pool. The geometry of the experimental arrangement is indicated in Fig. 4.7.
The range of motor speeds available was 0 - 2000 rpm. It was found that the powder feed rate varied in a linear fashion with screw speed upto about 1400 rpm, after which, the flow rate decreased due to many factors reported by Weerasinghe.
The powder flow rate was calibrated at regular intervals to ensure consistency. The calibration data for Stellite 35 and Stellite 6 is presented in Chapter 7.
The argon flow rate was minimised to reduce particle velocities to the lowest possible and thus aid deposition. It has been noted, (51), that increasing particle velocity has the effect of lowering the deposition of powder. This is due to a number of effects including, particles bouncing from the surface, unfavourable distribution of powder in the particle jet and increased convective cooling effects.

4.1.9 (ii) Three Hopper Powder Feed System

A system using three hoppers of the type described in the previous section was used for cladding with more than one powder. This variation was first suggested by Takeda and Steen (80), for in-situ alloying of powders. The design is illustrated in Fig. 4.8. It consists of three hoppers each having a separate argon supply with its own flow meter. This allows different gas flow rates to be used for different powders.
Since this system has been recently developed, a considerable amount of time has been spent establishing the desired gas flow rates and entry points for uniform powder flow. It was necessary to blank off the third powder feeder when not in use to avoid the creation of a back pressure of argon, by the empty hopper. Further development work into screw pitch size has also been done. The three hopper system is controlled by software developed by Jeng (79), which allows the composition of the powders to be varied over the length of a single clad. The system operates on mass flow rates, which are measured prior to use and entered as calibration data for the system. If the track length and traverse speed are then entered as input data, the composition can be varied, keeping the total mass flow rate of powder constant.

The system has been used in two configurations for the cladding of composites of Stellite 35 with different ceramics:

(1) cladding Stellite and ceramic powders using a single copper delivery tube - the two powders were conveyed through a single copper feed tube to the melt pool. This method of delivery allowed the gas flow rates to be set individually at the hopper. Mixing was facilitated by a perspex reservoir, to which each hopper was connected. The mixture of powders was then fed into a single delivery tube onto the substrate surface.

(2) cladding Stellite and ceramic powders using separate feed tubes - the powder feeders behaved as if single feeders for this arrangement. They were fed through separate delivery tubes to the interaction region, the effect of tube position was thoroughly investigated, including varying the height from the surface and which powder entered the melt pool first.

The effect of screw speed and argon flow rate was especially noticeable for the ceramic powders, due to their much lower density. At very low screw speeds (< 200rpm) the ceramic powders were observed to pulse, hence the minimum screw speed for these powders was 200 rpm. Also, the maximum powder flow rate before non-linear behaviour was seen was lower than that for metal alloy powders. Argon flow rate was kept to an absolute minimum for all experiments sing ceramic powder. At higher flow rates, the particles splayed out from the feed tube and very few actually entered the melt pool, they tended to spray the surrounding area.

4.1.9 (iii) Gas Shrouding Device

Since the work on laser cladding was done using an off-axis parabolic mirror as a focussing optic, shrouding of the interaction area was a problem. An argon shroud was designed to cross the clad immediately after it passed through the beam. The gas flow was positioned at 90^{o} to the direction of powder flow, and was set using an argon rotameter to 5 litres/minute. This was the maximum flow rate which would act as a shroud and cause no interference with the powder flow from the copper feed tube. The arrangement is illustrated in Fig. 4.9.

4.1.9 (iv) Rotating Jig for Valve Cladding

The rotating jig detailed in section 4.8.1 was modified for use in laser cladding experiments on engine valves, shown in Fig. 4.10. This allows the angle of the valve face with respect to the incident laser beam to be varied by a simple screw adjustment. The valve chuck was inclined at 40^{o} to the horizontal for this study.

4.2 Materials and Substrate Preparation

4.2.1 Transformation Hardening

The following section details the materials used and their preparation for laser

treatment. An investigation of surface coatings for improved absorptivity was undertaken in the initial stages of the work, the application of these coatings is also contained within this section.

4.2.1 (i) Materials

Samples of En24 and En52 steels were supplied by Valve Technics™ (Northampton), in the form of circular rods, 120mm in length and 8.025mm diameter.
En24 was supplied in the annealed condition, whilst En52 was quenched and tempered. The nominal composition of the as-recieved steels is given in Table 4.1.

4.2.1 (ii) Sample Preparation

All substrates,whether they had been surface ground for use or in the condition in which they were supplied, were ultrasonically cleaned before treatment using a solution of 'Decon' (1 part) and water (9 parts). Each sample was then thoroughly washed, with water and then alcohol to remove the solution. The samples were then used for laser processing experiments or surface coated.

4.2.1 (iii) Surface Coating Techniques Employed

The following surface coating techniques were used in an attempt to decrease the reflectivity of the steel surfaces to 10.6 μm radiation. Each coating was applied to degreased specimens with a 7mm surface ground flat.

Spray Paint Coated Surface
Specimens were sprayed using an aerosol canister of matt black automobile paint held ~ 300mm from the surface. The coating was formed in a single pass to ensure an approximately uniform surface coverage.
Graphite Coated Surface
The flame of an oxy-acetylene torch was used to deposit a thin layer of graphite on the substrate surface. The coating was produced by dragging the 'smoky' part of the flame slowly across the surface. The coating had a velvety black appearance. Use of this coating posed two disadvantages, (a) uniform thickness is difficult to achieve, especially if more than a single pass is required, and (b) the coating is easily dislodged by touching or knocking.
Residual Graphite Coated Surface
A series of experiments were conducted using the graphite coating technique above then wiping off the loose graphite with a tissue. This resulted in a thin, uniform coating of soot which did not completely blacken the surface.
Grit Blasted Surface
Sample surfaces were shot blasted at T&N Technology Ltd. using a sand blasting unit, to a surface roughness of R_A=7. The surface finish in this case was highly uniform.

DAG Colloidal Graphite Coated Surface

A thin layer of DAG colloidal graphite (a suspension of graphite in water) was applied to the surface using a paint brush. A deep grey coloured layer was produced which appeared to be uniform.

Excimer Laser Roughened Surface

The excimer laser discussed in section 4.1.1.5 was used to pretreat the steel surface. In general two passes over the length of the bar were required for complete coverage of the ground flat. A range of velocities for excimer from 0.25 - 1.5s^{-1} pretreatment was chosen, using laser power of 90W.

4.2.1 (iv) Characterisation of Coated Surfaces

A 3-D surface characterisation rig developed by Dr.D.R.Bury of T&N Technology Ltd. was used to measure the sample surfaces both before and after coating. This method of measurement eliminates problems induced by a highly directional surface by measuring the surface as a whole. A schematic diagram of the apparatus is shown in Fig. 4.11. It consists of a stylus which is driven across a pre-defined area of the surface by stepping motors. The signals produced are converted to digital and used to plot colour contour maps of the surface, or alternatively, an isometric projection. Information relating to the usual 2-D surface parameters is also calculated.

4.2.1 (v) Experimental Determination of Absorptivity

A mounting jig designed by O'Neill (33) was used to experimentally determine the absorptivity values of the coated steel surfaces.The jig is illustrated in Fig. 4.12. It has been designed to minimise conductive heat losses, by the use of insulating ceramic material, and effect good thermal contact between the sample and the thermocouple. Three ceramic locating brackets hold the sample in place and the thermocouple is pushed against the back surface by a spring loaded ceramic plunger. The determinations have been repeated using spot welded to the back of the steel samples, to check the accuracy of this technique, but O'Neill found measured values of absorptivity for copper and aluminium were indicative of the validity of this method of determination. A chrome-alumel, K-type, thermocouple was used (Specification: grounded junction, mineral insulated, diameter of leads 100 μm, diameter of sheath 250 μm), connected to a calibrated K-type thermocouple amplifier (RS AD595AQ thermocouple cold junction compensator, linearised output 10 mV/^{o}C), to a Siemens 4-channel chart recorder. The accuracy of the system in terms of temperature was +/- 5% over the range 0-1200^{o}C. The experimental set-up , as shown in Fig. 4.12, samples of known mass, 12mm diameter and ~1mm thick were used. The samples were surface coated in the same manner as the bars, described in section 4.2.3. The laser power on the MF400 was set to 90W (power was checked using an independent calorimeter at the work piece) and the laser was fired for 5s at the sample, an electronic timer was used to ensure consistency between

samples. The rise and fall in temperature of the sample was recorded on the chart recorder. The maximum temperature was also recorded using a Comark digital thermometer attached to the thermocouple

Determination of Absorptivity from Output Produced

The absorption determination is based on an energy balance technique (34), and relies on the sample being heated uniformly. If one examines the total heat flux entering and leaving the system, then:

Heat flux entering system during heating is given by:

$$Q_h = m C_p \frac{dT_h}{dt} = A P_o - P_{Lh} \qquad (4.4)$$

And heat flux leaving system during cooling is given by:

$$Q_c = m C_p \frac{dT_c}{dt} = P_{Lc} \qquad (4.5)$$

The power losses on heating and cooling are assumed to be equal as the conductive losses remain equal. Radiation losses (proportional to sample area which is constant, temperature to the fourth power which is equal for heating and cooling and sample emissivity which changes on heating and cooling, but whose effect is considered to be negligible as the area of damage on the surface is very small) are negligible, and convective losses (a function of sample area, temperature difference with surroundings and convective heat transfer coefficient which are all constant for the course of an individual experiment) are considered to be equal for the heating and cooling phases.

Hence:

$$Q_h - Q_c = m C_p = A P_o - P_{Lh} + P_{Lc} \qquad (4.6)$$

Now, since $P_{Lh} = P_{Lc}$, an expression for the absorption of the sample can be written as:

$$A = \frac{m C_p}{P_o} \qquad (4.7)$$

Where m is the sample mass, Q the energy, P_o the incident laser power, P_L the power loss by the sample and T the temperature. Subscripts h and c represent the heating and cooling cycles respectively.

This method allows the absorption to be calculated at any point within the heating phase for a known incident power, if the heating and cooling rates are known.This is very useful as the time dependence of the absorptivity can be observed.The sample

heating and cooling curves allow the heat retained by the sample and the combined heat losses at any temperature T. An example of the trace produced for a determination is given in Fig. 4.13. At any temperature, T, the heating and cooling rates can be determined by measuring the gradients of the tangents to the curve at that point. Substitution of these values into Equation (4.7) enables one to calculate the absorption of the specimen.
The results from these determinations are presented in Chapter 5.

4.2.2 Laser Cladding

The details given in this section refer to the supplied substrate and powder materials used in the cladding section of this work.

4.2.2 (i) Substrate Materials

Initial experiments were done using En3b bright mild steel (supplied by Mersey Metals Ltd.) substrates to establish the general operating regime for the Stellite powders. The substrates were in the form of rectangular slabs, 100 x 50 x 10mm. Each piece of steel was ultrasonically cleaned to degrease the surface.

Further cladding experiments were performed on 21-4N valve steel substrates. These were supplied by TIW Valves Limited, in the form of bars, 5 metres long and 31mm in diameter. The bars were cut into manageable sections, 450mm in length using an abrasive wheel. The outer diameter of each bar were then surface ground to produce an octagonal cross section, each of the eight flats being about 11mm wide. This allowed maximum usage of the surface area of the substrate. Although these specimens were a difficult size to work with, for metallographic purposes, the steel was extremely difficult to cut, and surface grinding was the only option for the production of flats. Each substrate was carefully degreased using alcohol before use.
The composition of the substrate steels are given in Table 1.1.

Diesel engine exhaust valves of 21-4N steel were supplied by A.E. Valves Division of Asseng Automotive, Natal, South Africa. The groove was machined prior to receipt and is designed for the plasma spray process, currently in use for hard facing. Figure 4.14 illustrates the dimensions of the valves. The groove for cladding has a 3mm radius.

4.2.2 (ii) Powders

Various powders were used for laser cladding. these included three different types of Stellite powder and various ceramic powders, as indicated below:

<u>Stellite Powders</u>
Stellite powders were supplied by Deloro Stellite Ltd. Types 6'W', 35, and 21 were used. These had all been produced by the gas atomisation process and were spherical

in shape.

Ceramic Powders

Four types of ceramic powder have been used. These are as follows:

Silicon carbide (SiC) - supplied by Electro Minerals Co. Limited.

Silicon nitride (SiN) - supplied by T&N Technology.

Alumina (Al_2O_3) - supplied by William Rowland Ltd. Particle size range

Chromia (Cr_2O_3) - also supplied by William Rowland, particle size range

The chemical analyses and technical data for all of the powders is given in Table 4.1. The distribution in particle size of the ceramic powders was determined by sieve analysis at T&N Technology Ltd. and the results are given in Table 4.2.

4.3 Experimental Procedures

4.3.1 Laser Transformation Hardening

4.3.1 (i) Single Pass Experiments on Untreated Circular Bars

Samples of En24 and En52 in the as-recieved condition were treated using the BOC 2kW laser and a lens focussing arrangement. Single passes of the beam were made as the substrate was rotated under the defocussed beam using the rotating jig described in section 4.1.8.1. The laser output power was fixed at 1.6 kW, and a beam diameter of 5mm was used. The speed of rotation was varied to establish the operating window for transformation hardening. A series of runs, 10mm apart were made on each bar, the bar was allowed to cool to room temperature before successive tracks were made.

4.3.1 (ii) Single Pass Experiments Across Ground Bars

A 7mm wide flat was surface ground onto each bar. so that the samples could be easily sectioned for analysis and eventually wear tested. The samples were mounted in the jig as above, and held stationary. A dial test indicator was used to ensure that the flat was level with respect to the workstation, so that the angle of incidence of the laser beam on the surface remained constant at 90^{o}. The sample was moved under a stationary beam, using the BOC laser and lens as above, such that a single track was produced across the bar. In order to effect treatment at constant velocity, the sample was moved about 30 to the side of the beam and traversed a distance of around 80mm in total so that it reached uniform velocity before passing under the laser beam. The laser was fired as the substrate passed, a sheet of waste steel being placed beneath the specimen to protect the workstation from the beam, should it overrun at either side of the specimen. A series of tracks at different processing conditions were made at 10mm intervals along each bar. The bar was allowed to cool to ambient temperature between each run so that a cumulative increase in temperature was avoided. Samples with spray paint, graphite, wiped graphite coatings and untreated surfaces were treated in this way, at a range of different

velocities and beam diameters. To eliminate edge effects due to the finite width of the bars, further tracks were made along the length of the bars.

4.3.1. (iii) Single Pass Experiments Along the Length of Bars

Runs along the length of bars with various surface coatings were made in the same manner as the tracks described above. Each run was 30 in length, so that edge effects were not a contributory factor. Experiments in this configuration were conducted using three different lasers, BOC 2kW, Ferranti AF5L and Electrox 1.5kW lasers, so that the effect of beam mode structure could be studied. An off-axis parabolic mirror (500mm focal length was used to focus the beam in all cases except those tracks made using the BOC laser. The laser and method of focussing used are stated with the tables of operating parameters, in Chapter 5.

As a result of preliminary experiments, it was decided that DAG colloidal graphite and shot-blasting offered the most practical and effective methods of surface absorptivity improvement, thus extensive experimental trials have been made using each of these coatings.

4.3.1 (iv) Use of Thermocouples to Determine Penetration Depth

A series of hardening trials were done across bars which had previously been drilled to accommodate thermocouples. The dimensions of the holes are shown in Fig. 4.15. Successive holes, 1mm below the substrate surface, were drilled at 10mm intervals along the bars. Thermocouples were made to size with very fine wire to minimise the time delay in recording the temperature changes.
The K-type thermocouples were made by fusing a 300mm piece of both NiCr and NiAl wire (0.1mm diameter) together using a small oxy-acetylene torch, to form a bead. The wires were then threaded through either side of a piece of twin bore (Internal diameter 0.2mm) alumina tube which was chosen to be a tight push fit for the drilled holes. The thermocouple was connected to a chart recorder via a cold junction, so that temperature changes could be recorded as the laser beam passed over the sample, above the thermocouple. With the chart recorder on, the BOC 2kW laser beam (with the lens assembly) was fired as the bar passed beneath it. The temperature rise in the sample was recorded, and the maximum temperature indicated on a digital thermocouple device also connected to the thermocouple.

A second series of measurements were made with the thermocouple placed in the hole adjacent to the one over which the laser was scanned. This produced measurements of the temperature rise induced in the bar at a distance 10mm away from the impingement position of the beam.

4.3.1 (v) Multiple Pass Experiments on Valve Stems - Initial Trials

Using DAG colloidal graphite as a surface coating, a series of experiments were

performed to establish the operating parameters necessary to transformation harden an area of the valve stem. The area to be treated was around 80mm in length. In order to treat such an area, the valve stems were placed in the rotating jig, and the required speed of rotation and traverse speed were calculated so that a spiral track of different pitch could be produced on each sample, when the motion was effected and the laser fired. The shroud described in section 4.1.8.2 was used to aid cooling of the stems. These experiments were done with the AF5 laser using an off-axis parabolic mirror (f = 500mm) to focus the laser beam.

The required rotation and traverse speeds were calculated from the parameters established in previous experiments which produce transformation hardening to a sufficient depth. Having set the parameters to suit, the samples were rotated under the beam as it was fired for sufficient time to treat a 30mm length of valve stem. Varying the speeds allowed the distance of overlap (or gap between successive loops of the spiral) to be controlled and varied. A range of tracks were produced from 50% overlap to 50% gap between loops.

e.g for a 3 track width, 50% overlap corresponds to a 1.5 overlap of successive loops of the spiral, whereas 50% gap between loops corresponds to a 1.5 gap between successive loops.

4.3.1 (vi) Multiple Pass Experiments to Produce Hardened Stems for Wear Tests

The experiments detailed in section 4.3.1.5 were used as a guide to the operating window suitable for the production of hardened valve stems to be used for wear evaluation. The length of valve stem to be treated was 100mm. Since the bar becomes hotter as the stem is traversed, an external cooling agent was deemed essential for this series of runs. The shroud was used as above with an argon pressure of 40 litres/minute supplied to the inlet. This prevented surface melting along the whole length of the stem. A series of stems of En24 and En52 were treated with a range of overlaps, as shown in the operating tables at the end of this chapter.

4.3.2 Laser Cladding and Particle Injection

All cladding runs were made using the Ferranti AF5 laser with an off-axis 500mm focal length mirror to focus the beam. In each case, a defocussed beam of 5-8mm diameter was employed.

4.3.2 (i) Laser Cladding with Single Powder

Laser clads of Stellite 6'W' and Stellite 35 were made on both mild steel plates and 21-4n substrates using a single powder feeder. The feed tube was angled at ~40^{0} to the horizontal, and held in position 15mm above the work piece and 12mm behind the

laser spot. The substrate was mounted on a protective steel plate on the CNC table. The powder flow and table motion were effected simultaneously and the laser was fired. Tracks 50mm long were produced, as detailed in Chapter 5.

4.3.2 (ii) Stellite/Ceramic Cladding with Twin Feed Tubes

The geometry of the system used is shown in Fig. 4.16. The feed tubes were angled at 40^{o} to the horizontal and each was directed so that the powder was blown into the laser generated melt pool. Various combinations were investigated i.e. whether the ceramic should be fed directly into the melt pool or slightly ahead/behind to allow its inclusion in the clad without causing melting. Clads of varying percentage by weight of each ceramic were made over a 400mm length.

4.3.2 (iii) Stellite/Ceramic Cladding with Reservoir Mixing

The geometry of this system is comparatively simple, one feed tube angled at 40^{o} to the horizontal conveyed the two powders to the melt pool. Powders were mixed in the reservoir before reaching the substrate. Clads of varying composition were made as above.

4.3.2 (iv) Cladding with Premixed Powders

Stellite 35 was mixed with either SiC, Cr_2O_3 or Al_2O_3, and used to clad 21-4N substrates via a single hopper and feed tube system. Mixtures containing 5, 10 and 20% by weight of each ceramic were investigated, the geometry used was as follows: distance of feed tube from spot, 15mm, height above work piece, 17mm.

4.3.2 (v) Cladding on Substrate Inclined at 45^{o} Relative to Incident Beam

A series of experiments in which the substrate was angled at 45^{o} to the incoming laser beam were conducted, in each of two directions. The first, the conventional cladding direction, and the second, where the powder was fed tangentially to the direction of traverse. The same operating distances as above were used.

4.3.2 (vi) Cladding of Poppet Valves

The valves were ultrasonically cleaned to remove dust and grease. The valve surfaces were slightly tarnished as a result of oxidation during the hot forging stage of manufacture. This was advantageous in terms of absorptivity. Stellite 6'W' was used for the valve cladding experiments. The valve was positioned (see Fig. 4.10) so that the point of incidence of the laser beam was at the top, slightly off centre, with the chuck at an angle of about 40^{o} to the horizontal. The powder feed tube was positioned ~8 above and ~17.5 to the side of the laser spot. The shrouding nozzle, supplying

argon, was set at 90° to the melt pool, as shown to give maximum coverage without disrupting the powder flow. The Stellite powder was fed through a single copper tube to the melt pool and the laser fired whilst the valve was rotated.

4.3.3 Wear Tests

Wear studies of hardened and clad samples were performed using two different testing rigs.

4.3.3 (i) Wear Testing LTH Samples - The Boundary Lubrication Wear Rig

Laser hardened samples were tested using a boundary lubrication wear rig. This is a high frequency, short stroke machine which is illustrated in Fig. 4.17 (a) and (b). The sample was held in an isothermal heated bath and a counterface silver steel pin was held in a moving holder and mechanically oscillated. The frequency was determined using a strobe. The parameters for the tests were as follows:

Load = 2kg
Frequency = 1500RPM
Time = 4hr test
Stroke = +/-0.25mm
Temperature = 200°C
Lubrication = none
Reciprocating pin = Silver steel (6.4 diam, 12.7mm radius ground tip)

Each sample/pin was ultrasonically cleaned before and after testing and weighed to determine the weight loss of material. Samples with a shot blasted surface were ground flat to the same finish as the other samples, before testing.

4.3.3 (ii) Wear testing of Hardened Valve Stems

Hardened valve stems were tested for wear resistance using a rig similar to the boundary wear rig above but with a long stroke length. These tests were performed at Brico Engineering Limited, Coventry (acknowledgements to Helen Brownlie for preforming this series of tests). A cast iron valve guide was used to provide the reciprocating motion. The results from these tests provide a direct comparison with existing wear data for chromium plated valve stems, previously tested on the same rig under comparable conditions. The test conditions were as follows:

Test type = scuff
No. of data points = 500
Speed = 750rpm
Duration = 4hours

Temperature=20^{o}C

Load = 8kg

Lubrication = none

4.3.3 (iii) Wear Testing of Laser Clad Samples - The Hammer Drill Rig

A hammer drill rig at Liverpool University was used to wear test the samples produced by laser cladding. The rig is illustrated in Fig. 4.18. It consists of a hammer drill, mounted on a supporting stand. A silver steel pin, as described in section 4.3.3 (i), was mounted in the drill chuck and the sample clamped firmly beneath the pin. The hammer action drill was switched on for a period of 30s for each sample/pin combination and the extent of wear examined. Each sample was ultrasonically cleaned both before and after testing then weighed and examined to determine the extent of wear.

4.3.4 Metallographic Examination and Analysis

4.3.4 (i) Surface Appearance

The surface condition of each specimen was examined both by eye and optically. For the hardened specimens, it is necessary to determine whether or not surface melting has occurred, the effect of laser treatment on the surface coating (if any) and the width of the heat affected zone (HAZ) on the surface. For the laser clads, one is interested in the surface finish, is the clad smooth, is there a scale - if so is it loose or adhered to the clad, does the clad appear to be of uniform thickness and height?

4.3.4 (ii) Surface Hardness Measurements

Initial surface hardness measurements were made using a Rockwell hardness tester (scale C). Samples were mounted in a V-block vice and levelled with a miniature spirit level. Although quick, the accuracy of these tests were is questionable as in some cases where the HAZ is shallow, the indenter may actually penetrate into the base metal giving an erroneous reading. The initial tests and all subsequent surface hardness determinations were made using a Vickers hardness tester with a load of 10kg.

4.3.4 (iii) Specimen Preparation For Metallurgical Analysis

Laser hardened specimens - sections of hardened bars were cut using a Metaserv cut-off machine either transverse or longitudinal to the direction of traverse during processing. Specimens were mounted in conductive Bakelite resin, ground to 1200 grit with SiC paper and polished on diamond polishing wheels to a 1μm finish. The etchant used for En24 was 2% nital and for En52, Marble's reagent..

Laser clad specimens - octagonal bars and flat plate clads were sectioned

transversely to the clad track and prepared as above. It is worth noting that those samples containing clads composed of a mixture of Stellite 35'W' and chromia were extremely difficult to cut. Laser clad poppet valves - sections of clad valve seats were cut using a band saw and prepared for examination in the manner described above.

4.3.4 (iv) Microstructural Characterisation

Samples were examined using a variety of techniques and magnifications. In order to understand the effect on microstructure of laser treatment, the initial microstructures of the valve stem steels were characterised. Similarly, to determine the effect of ceramic additions on the microstructure of as-clad Stellite 35'W', clads made purely from the Stellite alloy were characterised.

Optical Microscopy

Optical microscopy at a range of magnifications upto 1000x was carried out using a Nikon 'Epiphot' and Leitz 'Metalloplan' microscope. This allowed detailed examination of the microstructure.

Measurement of HAZ, Clad Dimensions and Dendrite Spacing

The dimensions of the HAZ were measured using a Leitz microscope to image etched transverse sections on a screen at 50x magnification. The dimensions were measured with an ordinary ruler and scaled down. This method was also used to measure the aspect ratio and level of dilution of the clads. At higher magnification (1000x) the same technique was also employed to measure the secondary dendrite arm spacings of the clads where possible.

Scanning Electron Microscopy (SEM)

Scanning electron microscopy was for a closer examination of microstructures. With this technique, it was possible to view ferrite grain boundaries in the stem steels which are not visible optically. Energy dispersive X-ray analysis (EDX) was used to determine the composition of the matrix constituents in as-recieved and heat-treated steels. The phases present in clad samples were also investigated using EDX analysis, as were areas of dissolved or partially dissolved ceramic inclusions.

Transmission Electron Microscopy (TEM)

In order to identify the precipitates present in En24 and En52 steel, the precipitates were extracted onto carbon replicas from polished and etched metallographic sections. Qualitative and quantitative analysis of the particles was obtained using EDX analysis on the TEM. The replicas were produced by carbon coating the specimens under high vacuum conditions. The carbon film was cut into 2mm squares with a scalpel and lifted from the surface in a solution of 5% nitric acid in water. The squares were cleaned in alcohol and water, floated onto gold grids and dried. The specimens were suitably imaged and photographed using a Phillips 400 TEM. (Standard conditions of a 70μm condenser aperture, probe size 20nm, window size 20eV and 15,000 counts in the iron window or 100s were employed). For qualitative analysis, peak areas were ratioed to iron whilst quantitative analysis was obtained using the RTS2 programme (supplied by LINK Software). Convergent beam and selected area diffraction analyses were also carried out for the two types of

precipitate. The patterns were analysed and compared with standard patterns and known values of interplanar spacings.

X-Ray Diffractometry

X-ray diffractometry of polished, electro-polished and powdered samples of En24/52 steels was used to further elucidate the composition of the precipitates present. Lines for different phases at characteristic scattering angle values (2 θ) were used to compare the spectra produced with published data (184). The possible phases present, from the Fe-C-Cr phase diagram are MC, M_3C, M_7C_3 and $M_{23}C_6$, where M represents Fe, Cr or a combination of both. The conditions used were as follows: Cr k-alpha radiation was used as iron fluoresces the more usual Cu radiation,

Electron Probe Micro-Analysis

The electron probe was manipulated to image polished and etched clad samples. EDX analysis was then utilised to determine the clad composition. A 50μm window was selected and analyses taken for 100s at various positions within the clad. Wavelength dispersive analysis (WDS) was used to scan through the clads and interface region into the base material to determine the level of homogeneity and dilution present. In addition, dot mapping was carried out on selected areas of each clad for the major elements (Fe, Cr, Si, Ni) to further examine partitioning of elements between phases within the clad. Dot mapping for carbon was also carried out in some cases but was not on the whole successful - this is discussed in the results section for cladding, Chapter 7.

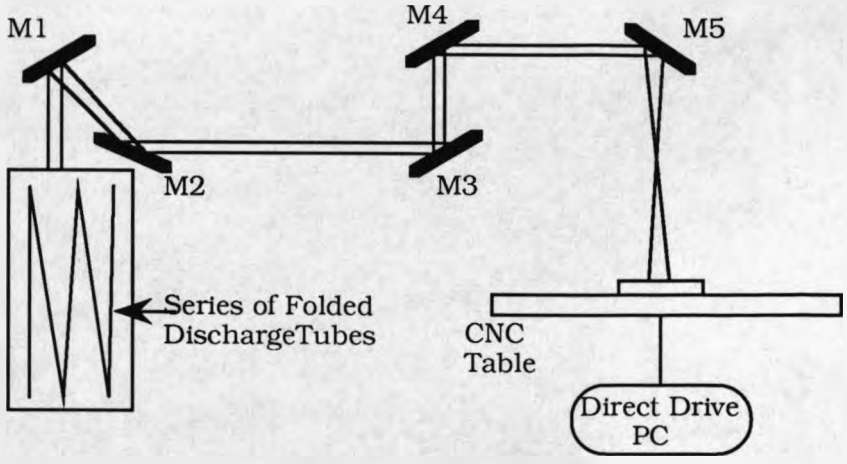

Fig. 4.1 Alignment path and operating arrangement for Laser Ecosse AF5L, M1-M5 represent water cooled, gold coated copper mirrors

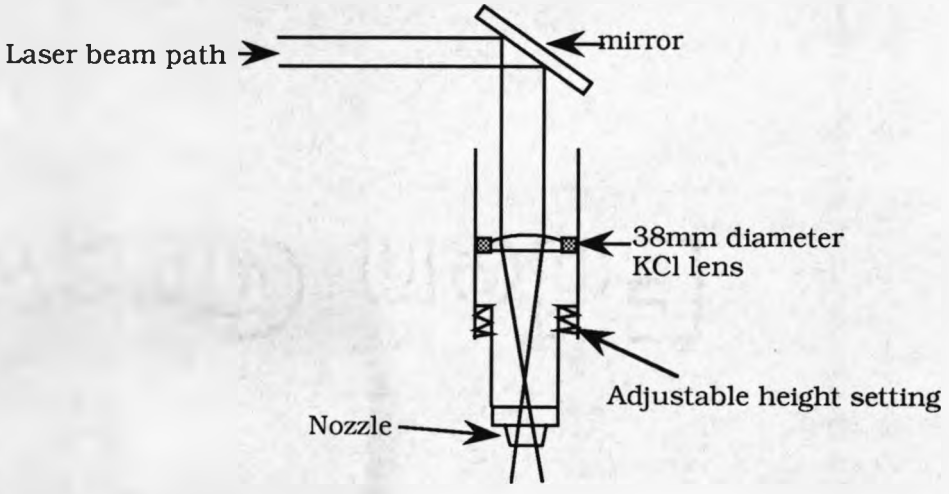

Fig. 4.2 Lens holding assembly used for initial hardening trials

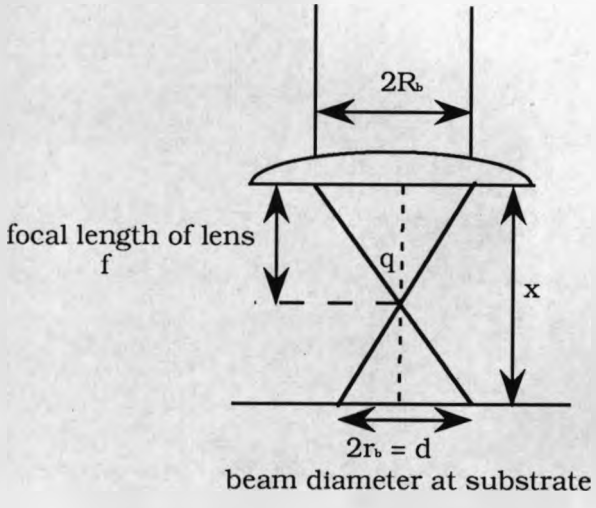

Fig. 4.3 2-D schematic for calculation of beam diameter using raw beam diameter and focal length of lens

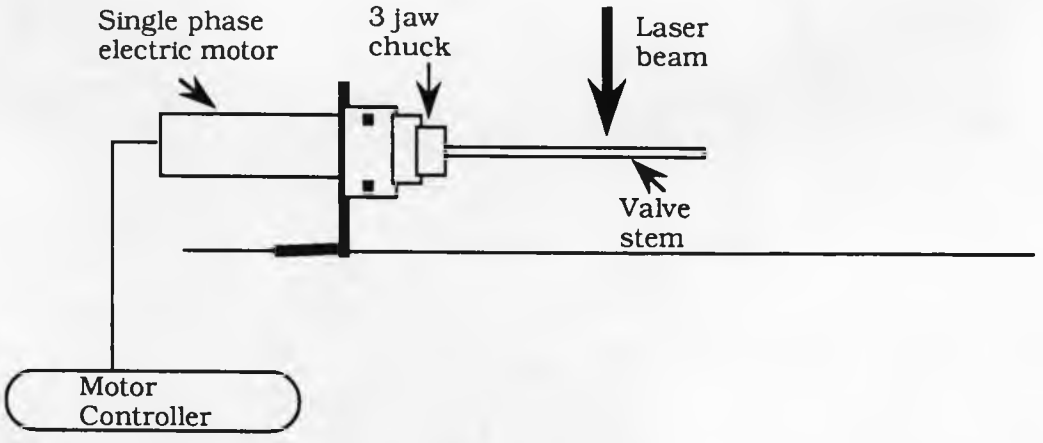

Fig. 4.4 Rotating jig used for valve stem hardening

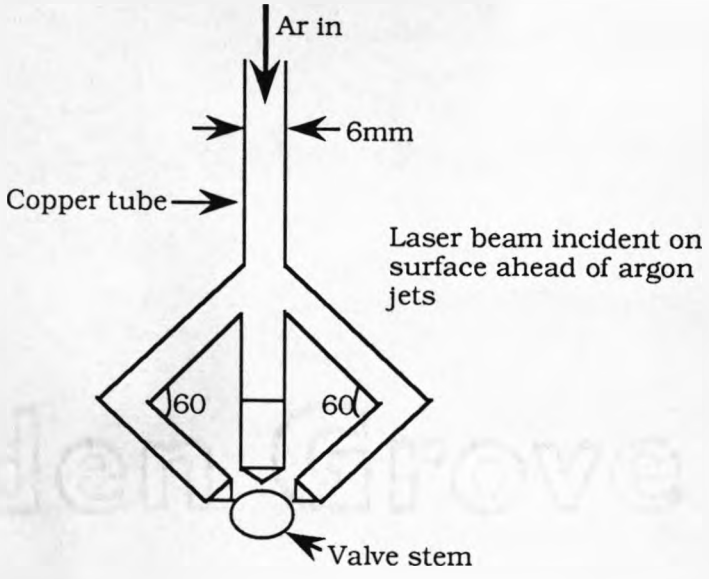

Fig. 4.5 Argon cooling assist device designed for valve stem hardening

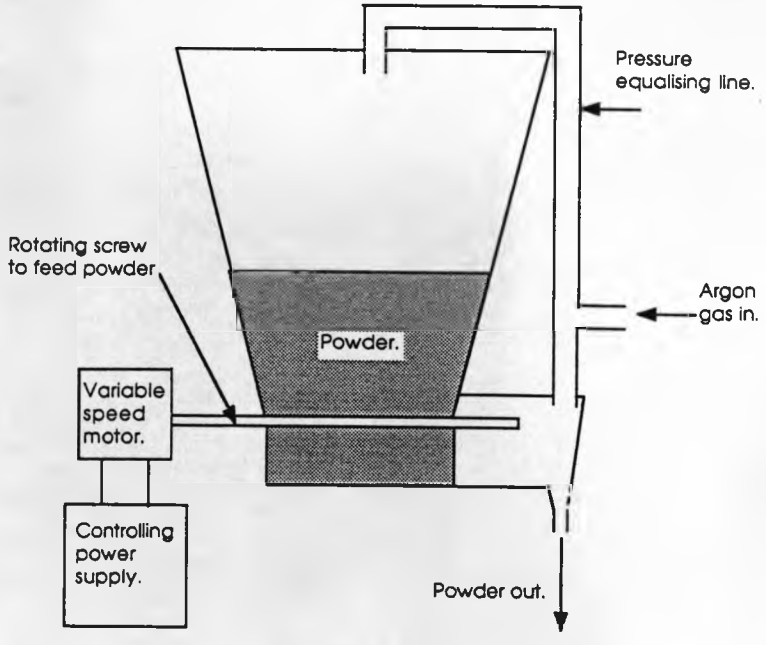

Fig. 4.6 Powder feed hopper device (24)

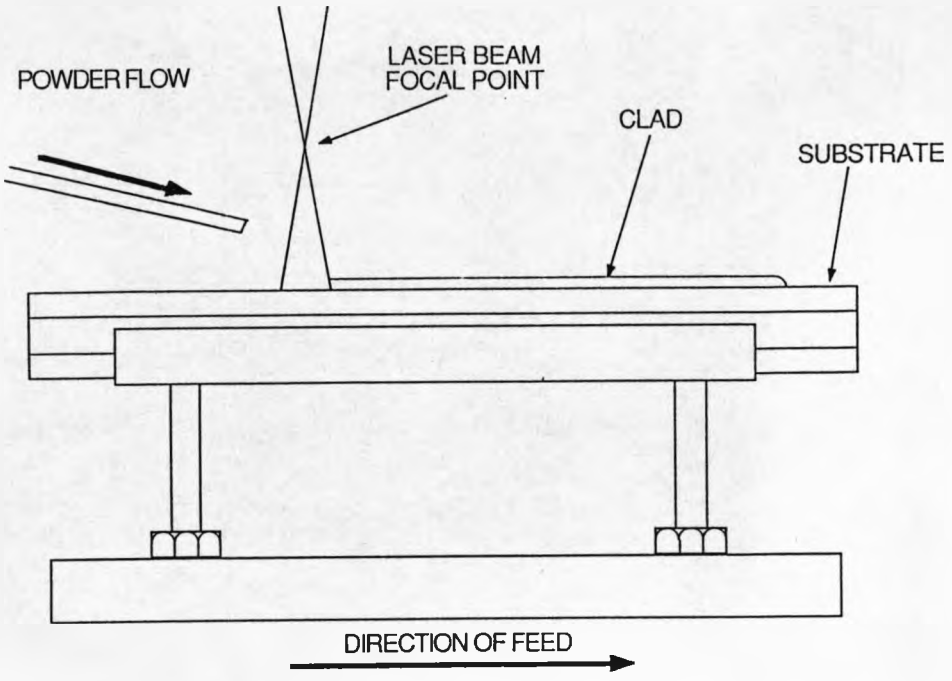

Fig. 4.7 Experimental arrangement for laser cladding

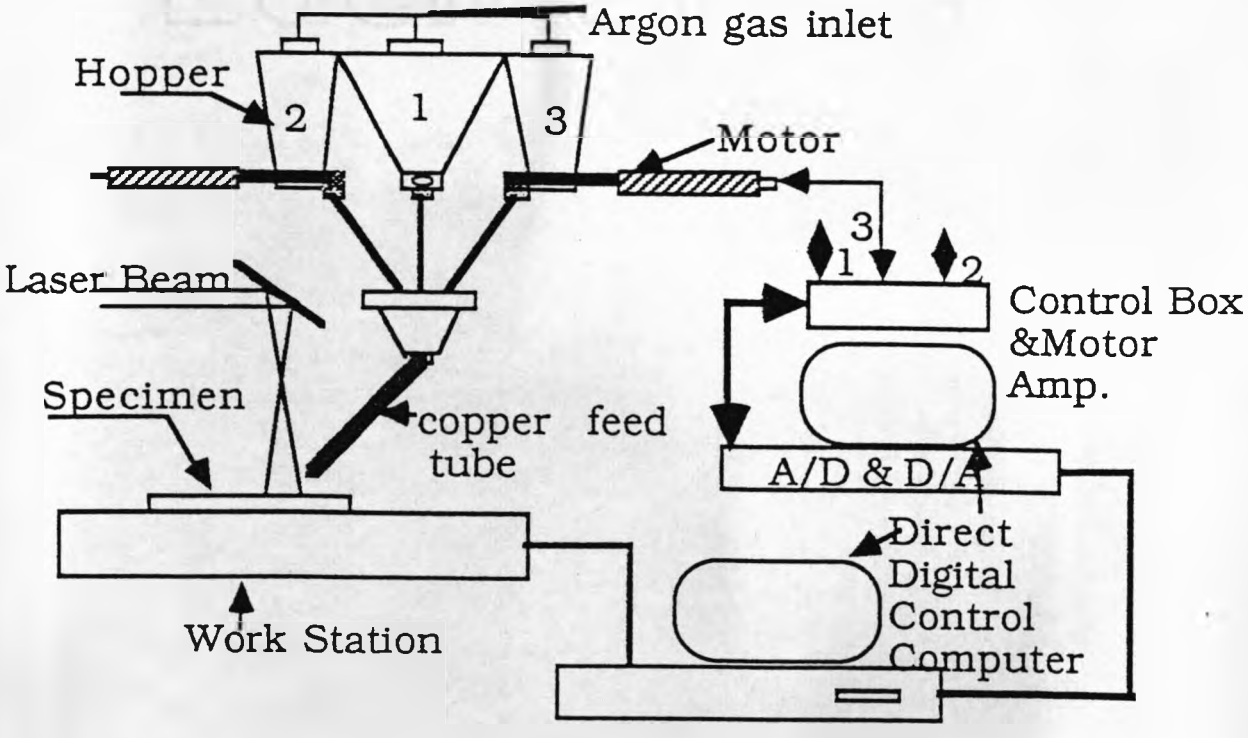

Fig. 4.8 Tripple hopper powder feed system (79)

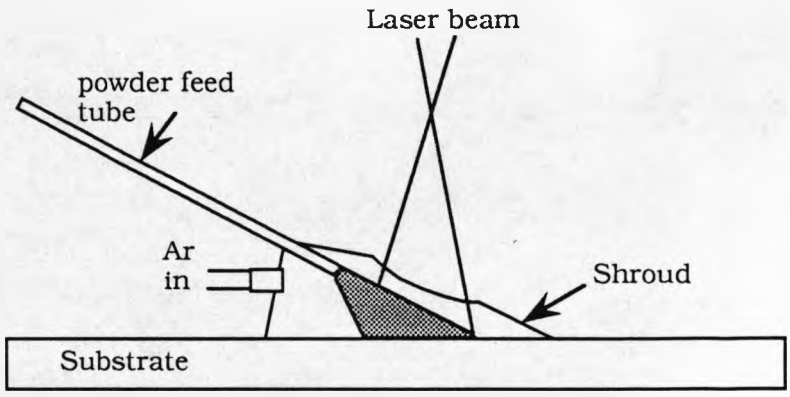

Fig. 4.9 Shrouding device designed for laser cladding

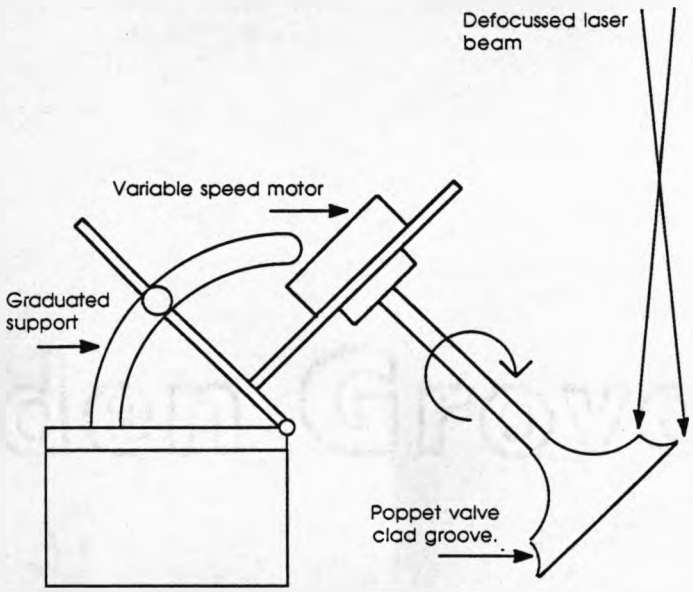

Fig. 4.10 Rotating jig for cladding of poppet valves

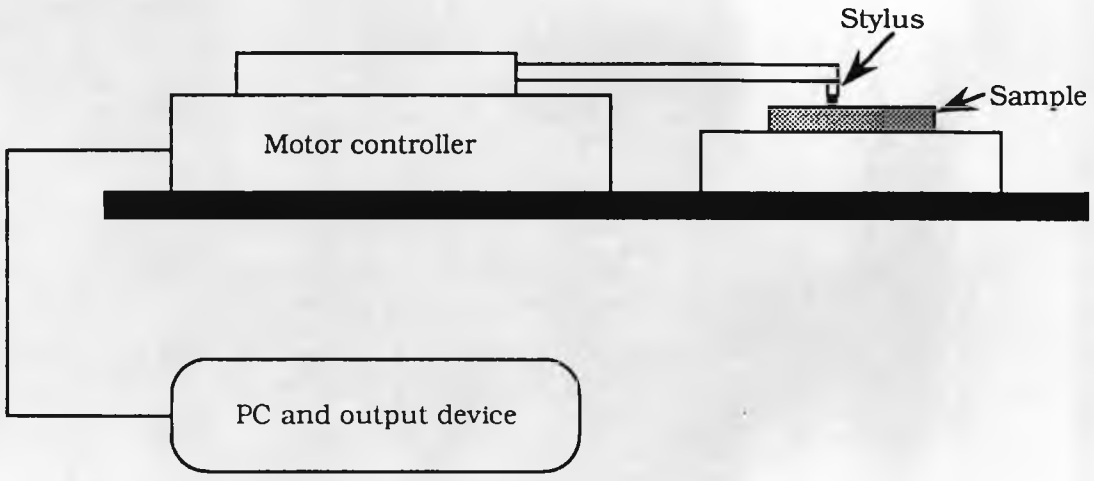

Fig. 4.11 Schematic showing 3-D surface profiling rig (T&N Technology)

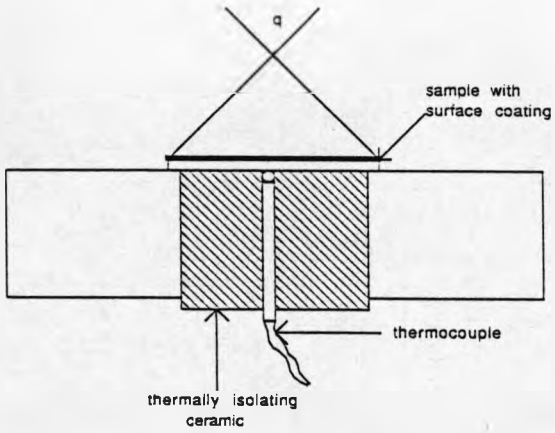

Fig. 4.12 Mounting jig and experimental set-up for absorptivity determination

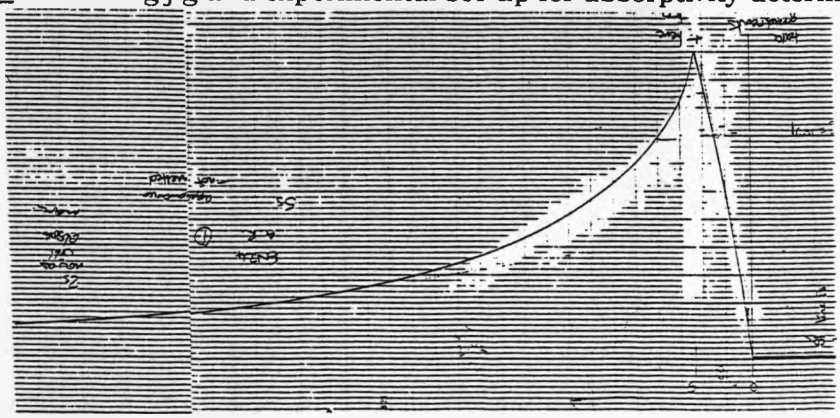

Fig. 4.13 Example of trace produced from experiments to determine absorptivity (En24, graphite (oxy-acetylene coated), 90W incident laser power)

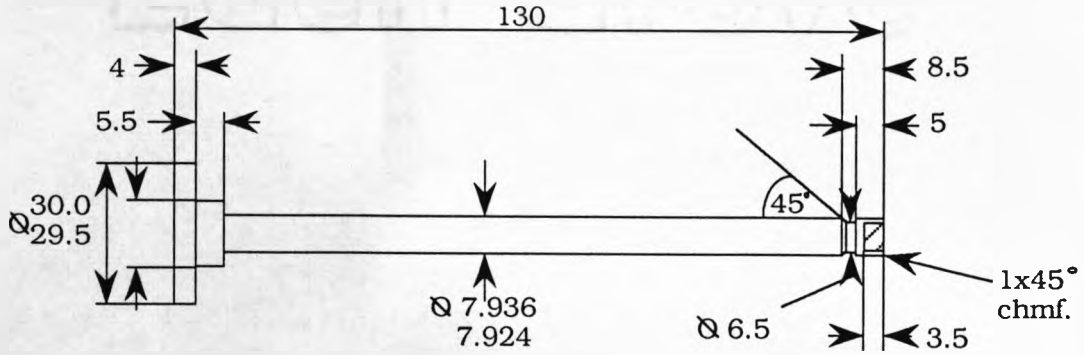

All corners chamfer 0.5x45
Unless otherwise stated

Fig. 4.14 Dimensions of poppet valves used in the study

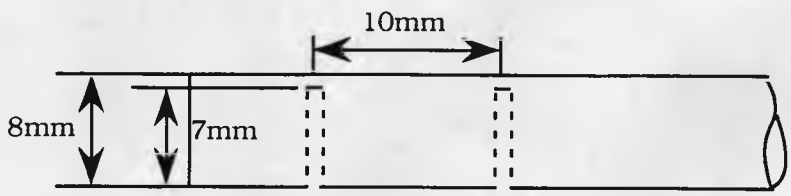

Fig. 4.15 Holes drilled in valve stems for temperature determination using thermocouples

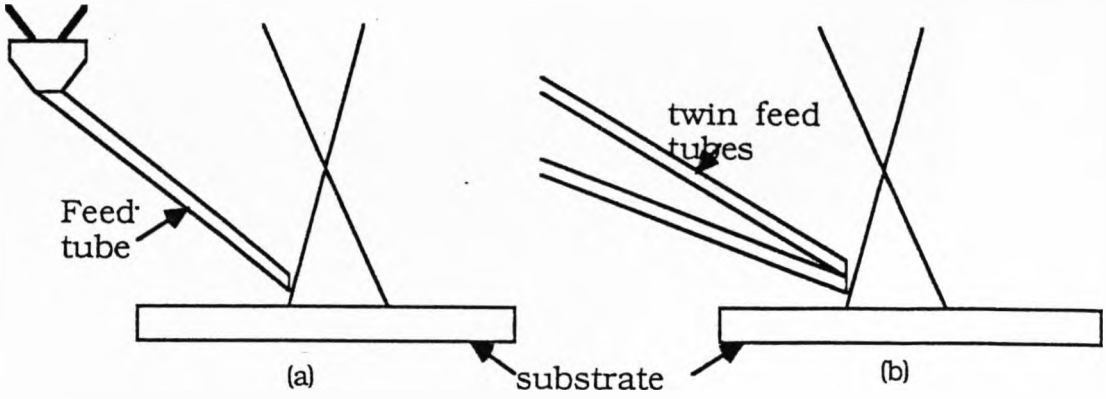

Fig. 4.16 Geometry of laser cladding systems, (a) single and (b) twin feed tubes

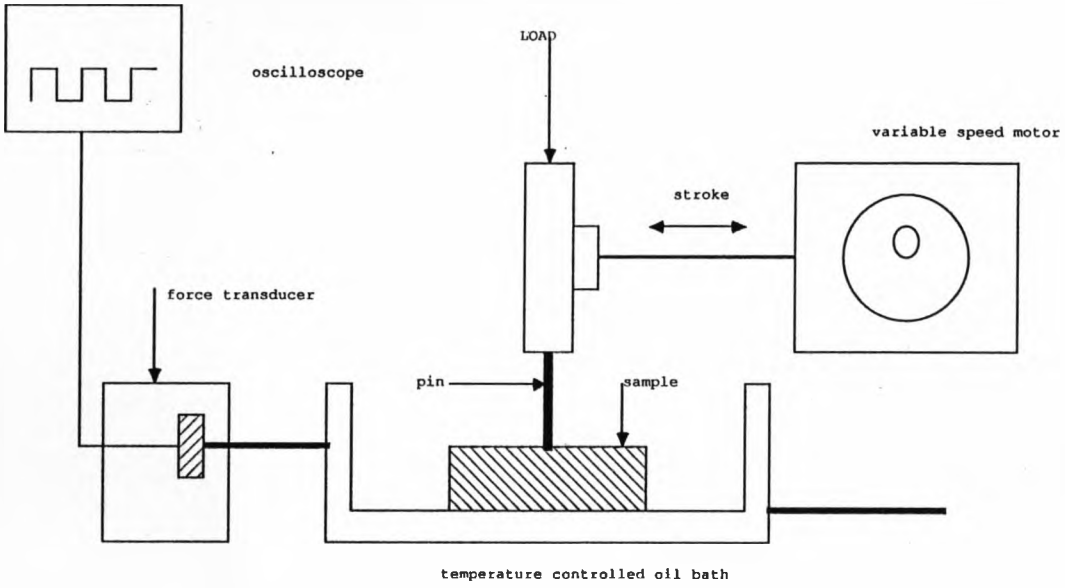

Fig. 4.17(a) Boundary lubrication wear rig used for wear testing laser hardened samples

Fig. 4.17 (b) Photograph showing boundary lubrication wear rig

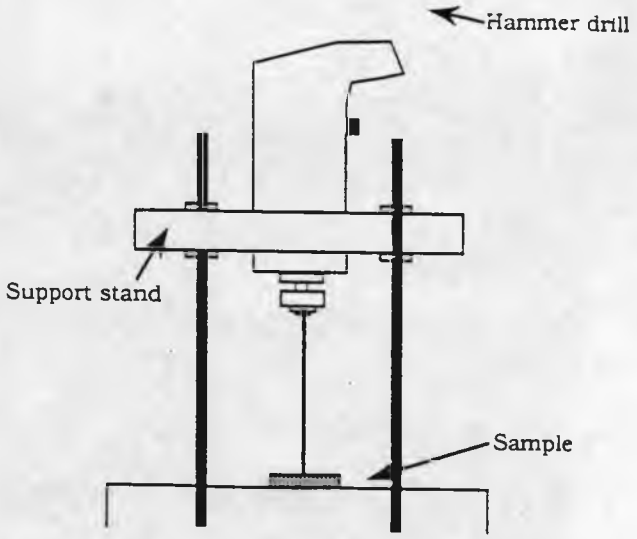

Fig. 4.18 Hammer drill rig for wear testing of clad samples

Element	En24	En52
C	0.41	0.47
Si	0.23	3.45
Mn	0.51	0.61
Cr	0.69	9.22
Ni	1.32	0.37
Fe	Balance	Balance
S	0.025	0.02
P	0.02	0.028

Table 4.2 Compositional analysis of En24/52 steels (Wt%)

Property	Alumina	Silicon carbide	Chromia
Hardness	2100 knoop(100)	2480 knoop(100)	Not available
Melting Point	2051 C	dissociates >2250C	Not available
Chemical Analysis	Not available	SiC 98.73 SiO2 0.48 Si 0.30 Fe 0.09 Al 0.10 C 0.30	SiO2 0.08 TiO2 0.06 Fe2O3 0.06 Cr 0.09 balance = Cr2O3
Other Information Available	SGR=1819	Pour density=3.20g/cm2	SGR=1818

Table 4.1 Manufacturers data for ceramic powders

Mesh	Aperture (μm)	% under	% in sieve	Mesh	Aperture	% under	% in sieve
10	2000.0	100.0	0.0	60	250.0	94.2	5.8
12	1700.0	100.0	0.0	70	212.0	78.5	15.7
14	1400.0	100.0	0.0	80	180.0	57.6	21.0
16	1180.0	100.0	0.0	100	150.0	30.4	27.1
18	1000.0	100.0	0.0	120	125.0	7.6	22.8
20	850.0	100.0	0.0	140	106.0	2.5	5.1
25	710.0	100.0	0.0	170	90.0	2.0	0.5
30	600.0	100.0	0.0	200	75.0	1.8	0.2
35	500.0	100.0	0.0	230	63.0	1.7	0.1
40	425.0	100.0	0.0	270	53.0	0.4	1.3
45	355.0	100.0	0.0	325	45.0	0.1	0.3
50	300.0	100.0	0.0	400	38.0	0.0	0.1

SiC

Mesh	Aperture (μm)	% under	% in sieve	Mesh	Aperture	% under	% in sieve
10	2000.0	100.0	0.0	60	250.0	100.0	0.0
12	1700.0	100.0	0.0	70	212.0	100.0	0.0
14	1400.0	100.0	0.0	80	180.0	100.0	0.0
16	1180.0	100.0	0.0	100	150.0	99.9	0.1
18	1000.0	100.0	0.0	120	125.0	99.5	0.4
20	850.0	100.0	0.0	140	106.0	99.3	0.1
25	710.0	100.0	0.0	170	90.0	96.8	2.6
30	600.0	100.0	0.0	200	75.0	75.5	21.2
35	500.0	100.0	0.0	230	63.0	44.0	31.5
40	425.0	100.0	0.0	270	53.0	19.8	24.2
45	355.0	100.0	0.0	325	45.0	8.6	11.2
50	300.0	100.0	0.0	400	38.0	4.8	3.8

Cr2O3

Mesh	Aperture (μm)	% under	% in sieve	Mesh	Aperture	% under	% in sieve
10	2000.0	100.0	0.0	60	250.0	100.0	0.0
12	1700.0	100.0	0.0	70	212.0	100.0	0.0
14	1400.0	100.0	0.0	80	180.0	100.0	0.0
16	1180.0	100.0	0.0	100	150.0	92.4	7.6
18	1000.0	100.0	0.0	120	125.0	75.1	17.3
20	850.0	100.0	0.0	140	106.0	52.2	22.9
25	710.0	100.0	0.0	170	90.0	27.4	24.8
30	600.0	100.0	0.0	200	75.0	8.6	18.8
35	500.0	100.0	0.0	230	63.0	3.6	5.0
40	425.0	100.0	0.0	270	53.0	3.3	0.2
45	355.0	100.0	0.0	325	45.0	2.5	0.9
50	300.0	100.0	0.0	400	38.0	1.2	1.3

Al2O3 sph

Table 4.2 Sieve analysis for ceramic powders used

CHAPTER 5

EXPERIMENTAL RESULTS - LASER TRANSFORMATION HARDENING

5.1 Introduction

This chapter details the results obtained from experiments to surface harden the exhaust valve steels En24 and En52 using a high power CO_2 laser. The first series of results presented are operating charts calculated using the Shercliff and Ashby model (see Chapter 3) to define the required window of parameters to be used and experimentally determined values for the absorptivity of the surface coatings used. Tables of operating parameters, measured depths of hardness, surface hardness and parametric relationships are presented in the second section followed by the results of microstructural analysis. The final section of this chapter details the results obtained from wear testing the hardened steel samples.

5.2 Results of Calculations to Define the Operating Window for LTH

The Shercliff and Ashby model (180) discussed in Chapter 3 was used to calculate the operating window for hardening En24 and En52 steels using a laser. The use of such a model allowed the laser parameters needed for successful hardening to be estimated therefore eliminating trial and error techniques.

The dimensionless equation was manipulated and a computer programme in basic written (Appendix A) to calculate the velocity required to produce a 0.5mm case depth over a range of powers, beam diameters and absorptivities.

Obviously, certain combinations of parameters will lead to surface temperatures in excess of the melting point. Therefore, a second series of calculations have been performed using another Basic programme, to calculate the surface temperature for each set of conditions. Those combinations of parameters leading to surface melting were noted and the onset of melting line plotted on the operating tables. For ease of reference, the operating parameters are presented graphically. Fig. 5.1-5.3 show plots of absorbed power against traverse speed for a series of beam diameters, for producing a 0.5mm case depth in En24 steel. These plots are representative of the data calculated. On each plot, a series of lines of Aq versus traverse speed for a number of different beam diameters is shown, none of the conditions shown would be sufficient to cause melting hence the plots define the operating window for LTH.

5.2.1 Temperature Determination Using Thermocouples

Experiments to determine penetration depth (section 4.3.1 (iv)) using thermocouples

embedded 1mm below the substrate surface produced the results given in Table 5.1.

5.3 Results of Absorptivity Determinations for Different Surface Coatings

The experimentally determined values of surface absorptivity calculated using the energy balance method (outlined in section 4.2.1 (v)) for the various types of surface pretreatment, are presented in Table 5.2. The effect of the incident laser energy on the coating condition is also indicated. Table 5.2 indicates that the highest improvement in absorptivity was provided by the excimer laser treatment followed by the DAG colloidal graphite coating. Poor improvements were noticed with etched and wiped graphite surfaces.

An important factor in absorptivity is the surface roughness of the steel. The degree of roughness of an as-ground steel sample is illustrated in the form of a 3-D plot in Fig. 5.4(a). The average value of Ra for the 0.5mm area scanned was 0.89 perpendicular to the grinding direction and 0.35 parallel to it. Similar plots for an excimer laser pretreated specimen (0.75mms^{-1} traverse speed) and a grit blasted surface are presented in Fig. 5.4(b) and (c) with average values for Ra of 1.28 and 7.07 respectively.

Similar effects on coating condition after laser firing were observed for both En24 and En52 steels. For as ground (uncoated) surfaces, charring was noticed in the area surrounding the point of impact of the beam as a result of surface oxide formation. Spray painted, DAG coated and graphite coated (oxy-acetylene) coatings remained in place in most cases, after irradiation but were all visibly changed in some way. There was a tendency for the graphite coatings to burn with increasing power density. Spray paint blistered over a large area compared to the beam diameter, the graphite (oxy-acetylene) coating was observed to burn slightly on firing the laser but remained intact, except at high intensities, whilst the DAG coating was slightly dulled but not removed.

Grit-blasted, etched and wiped graphite coated samples again exhibited surface charring directly beneath the beam. There was no visible alteration in the surface condition of excimer laser pretreated samples. It is worth noting that under higher intensity radiation (i.e. sufficient energy to cause surface melting) spray painting the surface or coating with one of the graphite coatings can lead to an increased concentration of carbon at the surface.

The highest increase in absorptivity compared to the ground base material was obtained using DAG colloidal graphite coating, which gave approximately a 65% higher value than for the ground steel surface. The value quoted for the excimer pretreated surface was for a pretreat speed at 0.75mms^{-1}.

5.4 Results of Transformation Hardening En52 and En24 Valve Steels

The operating tables for transformation hardening of En24/52 steels are presented in Appendix B. In each case, the coating used, the experimental configuration and the measured values for case depth and surface hardness are shown. The cross section of a typical hardened layer in En24 is shown in Fig. 5.5.

5.4.1 Transverse Tracks Across Substrates

Significant edge effects were noted for tracks made across the width of the ground bars, for substrates in the untreated, spray paint, graphite or wiped graphite coated condition. The maximum surface hardness value was obtained in the centre of each track, decreasing both towards the edges of the bar, and at the sides of the track where the incident intensity is much lower. This is an edge effect. The interaction time of the laser beam is not sufficient to transform a uniform thickness of material before the edge of the bar is encountered. The variation of hardness across the surface of a typical track is shown in Fig. 5.6.
A reduction in surface hardness was noted for certain runs on the untreated substrates. This is thought to be due to annealing of the material by the scanning laser beam. The surface hardness of treated specimens correlates reasonably well with the interaction time, except for samples which were untreated. Examples of the data are shown in Fig. 5.7 and 5.8 for En24 and En52 with spray paint coatings respectively. As expected, increases in power lead to higher hardnesses upto the melting point. At that point, the curve flattens off and further increases in power or interaction time serve only to melt the surface. At low power (800W), the interaction time is insufficient to produce fully hardened surfaces. Increasing the power leads to high hardness, but once this is achieved, further increases in the power level do not improve the hardness. This data was representative of the results.

5.4.2 Variation of Hardness - Longitudinal Tracks

Longitudinal tracks were made to eliminate edge effects. Among other things, the uniformity of the hardened profile depends upon whether the start of the track (start of firing laser) corresponds with the start of motion of the CNC table, or whether the laser is fired whilst the table is already in motion. A more uniform profile is observed when the table is already in motion before the laser is fired, and continues to move after firing. This prevents the appearance of a deeper region at the start of the track thus reducing the possibility of surface melting by maintaining constant dwell time of the beam on the surface.

Plots of hardened depth versus interaction time for a series of samples of En24 treated at different conditions are shown in Fig. 5.8 and 5.9, for grit blasted and DAG coated surfaces. Again, there seems to be an increase in depth with interaction time, although the correlation was found to be non-linear for both of the steels. Again, these plots are representative of the data collected.

Fig. 5.10-5.12 show a number of hardness profiles for En24 and En52 samples hardened at different traverse speeds (power and beam diameter constant) i.e. different interaction times. The effect of increasing the velocity clearly decreases the depth of hardness and also generally decreases the surface hardness, but to a lesser degree.

5.4.3 Variation of Hardness - spiral tracks

Spiral tracks on DAG coated valve stems produced uniform case depths along the lengths treated. The appearance of stems after treatment is shown in Fig. 5.5 (c). Rotation speeds using the motorised jig were measured and are presented in Table 5.3, Fig. 5.14. By selecting the correct traverse and rotational speeds, the degree of overlap of the tracks was varied. The hardness profiles of three different samples of each steel are shown in Fig. 5.15 (a)-(c) show three track profiles for the hardened valve stems. In Fig. 5.15 (a), the motor settings were such that there was no overlap of the heated zones. Fig. 5.15 (b) and (c) correspond to an increasing degree of overlap. The consequence of this was that there was an unhardened spiral track in the sample represented by (a), whereas for the samples represented by (b) and (c), the overlap region, between the fully hardened track was partially hardened. This partially hardened region was caused by a backtempering effect on passing the laser beam over an already hardened layer in the overlap zone. In all cases, the effect of this backtempering reduced the hardness more substantially for En24 than for En52.

5.5 Microstructural Evolution During the Heating and Cooling Cycles

The microstructural changes accompanying the rapid heating and cooling cycles will be presented in this section. In order to appreciate the changes, it is necessary to first examine the initial microstructure of the two steels examined in this study.

5.5.1 As-received Steels

5.5.1 (i) En52

Optical microscopy of En52 steel, in the as-received condition, revealed a microstructure which consisted of very fine precipitates, in a ferritic matrix, as shown in Fig. 5.16. Scanning electron microscopy indicated that these precipitates were situated at the ferrite grain boundaries, Fig. 5.17. A corresponding chromium dot map of this area, shown as an overlay demonstrated that these precipitates were chromium rich with respect to the matrix.
Higher magnification microscopy using TEM carbon extraction replicas revealed a network of intra-granular precipitates which were somewhat smaller than those situated at grain boundaries (Fig. 5.18). An enlarged micrograph of these intra-granular precipitates is shown in Fig. 5.19. Stereographic pairs taken using the TEM show that most of the precipitates are shaped something like a bar of soap.

The sizes of these large grain boundary precipitates range from 0.3μm to 3μm in length and the intra-granular precipitates are between 0.1 and 0.01μm. Typical grain sizes for En52 in the as received condition lie in the range 2-10μm.

Statistical EDX analysis of both types of precipitate to determine the respective compositions, yielded the results given in Table 5.4 (results grouped into five groups of 20 and averaged for each type of precipitate). The composition of both types of precipitate was found to be identical. Analysis of the matrix composition, also determined by EDX analysis, is given in the same table. It can be seen that the carbide phase contains approximately a 2:1 ratio of Cr:Fe. From the known composition, these precipitates are presumably $(Cr,Fe)_{23}C_6$ in type. The matrix of En52 was ferritic and therefore the Cr depletion, with respect to the bulk composition, was to be expected.

To verify that these precipitates were indeed $(Cr,Fe)_{23}C_6$ in type, selected area and convergent beam diffraction patterns for the carbides were obtained. Fig. 5.20 ,5.21 show the patterns obtained and the precipitate from which they were taken in each case. Fig. 5.20 also shows the corresponding EDX analysis for the precipitate indicated, which is typical of the precipitates present in this steel.

The following section briefly describes the procedure used to analyse the diffraction pattern to calculate the lattice parameter for the precipitate indicated in Fig. 5.20.

Experimental Data:

Indicated camera length, l (mm) = 800mm
Measured camera length, l (mm) = 826mm (determined from EM400t calibration using [011] Si pole SAD pattern)
Electron wavelength, λ (nm) = 0.037×10^{-10}m (at 100kV)

Now:

$$R\,d = l\,\lambda \qquad (5.1)$$

And R is measured from the negative of the SAD pattern. As the distances of all nearest neighbours from the central spot are equal then the beam direction is presumably [111].

From Fig. 5.20, R = 8.2mm.
Therefore the interplanar spacing, d, is given by:

$$d = \frac{3.7 \times 10^{-12} \times 826 \times 10^{-3}}{8.2 \times 10^{-3}} = 3.73 \times 10^{-10} m \qquad (5.2)$$

And for a cubic crystal, the interplanar spacing of the (hkl) plane is given by:

$$\frac{1}{d^2} = \frac{1}{a^2}(h^2 + k^2 + l^2) \qquad (5.3)$$

Thus for (hkl) = (220), i.e. beam direction [111], nearest neighbours represent (220), the lattice parameter, a, is given by:

$$a = \sqrt{8\,d^2} = \sqrt{8\,(3.73 \times 10^{-10})^2} = 10.56\ A \qquad (5.4)$$

This compares favourably with the literature value (102) of 10.589A for the face centred cubic $(Cr,Fe)_{23}C_6$. It was therefore concluded that the En52 precipitates were $(Fe, Cr)_{23}C_6$ in type. Similar analysis of the pattern illustrated in Fig. 5.21 gave the value of a= 10.54A. The selected area diffraction pattern for this structure - plotted using MacDiffract.^{TM} with atom positions taken from Westgren (185) - is illustrated in Fig. 5.22. This is indeed similar to the pattern obtained experimentally, Fig. 5.20.

Attempts to determine the composition of the precipitates using XRD proved very difficult. Powdered samples of En52 yielded no peaks other than those found in a standard sample of α-Fe. Similarly, a sample of 0.8%C steel chosen for its high cementite content yielded only the pure iron peaks. A second series of samples were prepared by spark machining (to prevent work-hardening during cutting) and electro-polishing in 70% phosphoric, 10% sulphuric acid solution. This sample of En52 revealed the peaks shown in Table 5.5, with the corresponding peaks for the α-Fe and 0.8%C steels also shown. This is in agreement with structures determined from the diffraction patterns.
The measured macro-hardness value for En52 was 263 HV_{10}.

5.5.1 (ii) En24

The initial microstructure of En24 valve steel is indicated in Fig. 5.23. As shown, the structure was found to consist of a fine dispersion of spheroidal precipitates in an iron matrix. The precipitates smaller than those found in En52 steel, ranging in size from 0.1-1μm. A scanning electron micrograph of En24 steel, shown in Fig. 5.24 indicated that these precipitates are mainly situated at grain boundaries. TEM of carbon extraction replicas indicated that the precipitates were in fact elongated

spheroids, mainly arranged parallel to the rolling direction with some perpendicular to it, as shown in Fig. 5.25 (a) and (b). From the known steel composition and a knowledge of the phase diagram, one would expect these precipitates to be cementite in a ferritic matrix.

The results of EDX analysis of a representative selection of various sizes of precipitate using both SEM and carbon replica TEM analysis revealed that the precipitates contained only iron (Fe) and chromium (Cr), as shown in Table 5.4. (However, elements of atomic number <11 are not detected by these methods (unless more sophisticated detectors are employed). It can be concluded therefore, that the particles are almost certainly $(Fe,Cr)_3C$. The matrix composition - also determined from analyses taken randomly within the samples - indicated a much lower chromium content, also shown in Table 5.4. En24 steel in the as-recieved condition was also found to contain a small number of manganese sulphide inclusions in the form of stringers, elongated in the rolling direction.

Difficulty was encountered in trying to obtain a diffraction pattern from the carbide particles as they tended to be too thick for electron transmission. However, suitable particles were eventually found and the selected area and convergent beam diffraction patterns illustrated in Fig. 5.26, 5.27 obtained. Also included in these figures are photographs of the precipitates from which the patterns were obtained and a typical EDX trace from one such precipitate, indicating the levels of Fe and Cr present. The peaks detected by XRD analysis are shown in Table 5.5 and further support the structure of the carbides as being $(Fe,Cr)_3C$. It was noted that during diffraction analysis of En24 that the unit cell was large, as would be expected for the M_3C type structure.
The measured Vickers hardness value of the as-recieved En24 steel was 237 HV_{10}.

5.5.2 Microstructure of Laser Hardened Steels

Changes in the microstructure of the two steels were observed after laser transformation hardening. This section details only the microstructural changes occurring without a phase change, i.e. surface hardening without melting, the microstructural changes observed as a result of melting are somewhat different and are addressed in the subsequent section, Section 5.6.

5.5.2 (i) Laser Treated En52

Surface transformation hardening of En52 generally resulted in heat affected zones (HAZ) having two distinct layers. The two zone microstructure is illustrated in Fig. 5.28. The upper layer consisted of martensite and undissolved carbides and the lower layer contained undissolved carbides, martensite and untransformed ferrite regions. Fig. 5.29 and 5.30 show the upper and lower layers observed. In some cases, where complete austenitisation had not occurred, a single layer was observed of similar constitution to the lower layer described above. In the case of En52, all of the

carbides probably do not dissolve during the heating cycle.
Closer examination of TEM carbon extraction replicas for the heat treated samples indicated that the intra-granular precipitates had dissolved, whilst those at the grain boundaries appeared to have grown somewhat in size, this is illustrated in Fig. 5.31. The structure of the carbides was the same as in the untreated steel.

5.5.2 (ii) Laser Treated En24

Laser hardening of En24 steel produced the near-surface microstructure illustrated in Fig. 5.32. The micrograph, shows a fully martensitic surface, and complete dissolution of the carbide phase. Moving away from the surface, towards the bulk, gradual reappearance of the carbide precipitates was observed. These precipitates were somewhat smaller than those seen in the initial structure, suggesting that partial dissolution had occurred during laser treatment to some distance below the surface.

In some instances the treatment was sufficient to cause a decrease in the size and number of the precipitates present, but not sufficient to produce a fully martensitic surface layer. This effect is illustrated in Fig. 5.33. It would appear that the carbides become unstable at temperatures below A_1. The presence of a greater number of smaller precipitates in En24 was probably a result of too low a quench rate, $(Fe,Cr)_3C$ precipitating out in the form of small spheroidal precipitates on cooling. The heat affected region in En24 steel - assuming that hardening had occurred - again consisted of two clearly defined zones. The structure gradually reverted back to the base structure i.e. a gradual increase in the size and number of precipitates moving away from the surface. The Cr:Fe ratio of the precipitates after heat treatment was found to be identical to that of the precipitates in the as-recieved material. Hardness values in the region of 700 HV_{10} were noted, for fully martensitic regions.

5.6 The Effect of Surface Melting

Surface melting of En24 and En52 steels occurred in some instances. The microstructure produced being different to that seen previously for surface hardened tracks.

The microstructure obtained on surface melting of En52 is illustrated in Fig. 5.34. The heat affected region consists of four distinct zones. The composition of each phase within the zones has been analysed using EDX analysis on the scanning electron microscope.

Examination of the microstructure from the base surface through to the surface, reveals the initial change in microstructure shown in Fig. 5.35. Areas appear around the carbides. The chromium content in these areas was measured slightly above that of the base matrix (8.4% Cr cf 7.5% Cr in matrix), in addition, the Cr

content of the carbides seems to have decreased slightly, suggested that chromium is diffusing out. Moving up through the structure a region containing white particles (Fig. 5.36) can be seen. These larger particles are thought to be retained austenite, since the Cr content was determined at 18.1%, the silicon content of these white lumps was also less than that of the original carbides but close to the matrix Si content. The darker areas present in this region were also analysed for composition and were similar to the base matrix in both Si and Fe content but slightly higher in chromium.

The presence of carbides is apparent all of the way upto the martensitic zone which is lower in Cr than the matrix (a function of the lower solubility of Cr in martensite), see Fig. 5.37. However, the chromium in the martensitic region is thought to be contained in the small somewhat fuzzy white particles.
The final zone of the heat affected region is shown in Fig. 5.38 and has a dendritic microstructure because of surface melting.

5.7 Effect of Mode Structure on Hardened Track Profile

The intensity distribution (mode structure) of the laser beam can have a significant effect on both the geometry and the microstructure of the transformed layer, as discussed in Chapter 2. The cross-sectional profile of two laser hardened tracks on En24 substrates, treated with beams having the TEM_{00}, TEM_{01^*} mode structure are shown in Fig. 5.39.

Tracks produced using a Gaussian beam, under the same conditions used with a TEM_{01^*} mode structure tended to exhibit surface melting in the track centres more readily. The effect was quite substantial, for example, a speed of $100mms^{-1}$ with the Gaussian mode structure was sufficient to cause deep melting of the surface whereas with the donut mode, only shallow melting was observed at speeds of $35mms^{-1}$.

5.8 Reproducibility

Reproducibility of results was relatively good. For runs at the same power, speed and beam diameter conducted 1 hour apart, the depth of hardness was found to vary by <5% This must be viewed in the light of earlier discussions relating to the power measurement technique. Fluctuations could also be a function of the laser system warming up, resulting in slight variations in focussing mirror deformation and therefore beam focal point, or alternatively, the degree of uniformity of the coating could have been variable.

5.9 Wear Test Results

5.9.1 Single track tests (T&N Technology)

Wear test results of single track hardened zones, measured using the boundary lubrication wear rig (BLWR) at 200^{o}C, are presented in Fig. 5.40-5.49. The results are plotted as bar charts showing the weight loss of the pin, the weight loss of the substrate and the total weight loss of the system in each case. In most case, the factor of interest to the automobile manufacturer is the total weight loss of the system, i.e. certain combinations of pin/substrate hardness will be more compatible than others and it is this compatibility which ensures a system with the greatest durability. However, in addition to the total loss, the weight loss of the substrate was also considered as a means of assessing the effect of microstructure due to LTH on wear performance.

The results show that in general, laser treated substrates of both types of steel show superior wear performance to those which have been hardened by conventional induction hardening. Also shown for comparison, Fig. 5.40 is the data for the as-received base materials and conventionally heat treated materials. The first point to make is that En52 in the as-received condition exhibited lower wear resistance than did En24 (total loss 3.7mg compared to 2.9mg). On heat treating the steel samples by conventional methods (induction hardening), En24 showed a significant improvement in wear performance, the total loss falling to <1.5mg. However, no such improvement was observed with En52 where the substrates performed slightly betteress after treatment but the total wear loss did not decreases, showing a 4-5mg weight loss in the system. This indicates that En52 does not respond well to conventional heat treatment. In fact, on metallurgical examination, the induction hardened samples showed no significant microstructural changes.

Laser treatment of the two steels showed improvements in the wear performance of both types of steel, the level of improvement varying with the type of coating or pretreatment employed and the processing parameters. Perhaps the most noticeable improvements were those provided by grit-blasted samples, where for En24 the weight loss of the system in a number of cases was below 1mg and for En52, <2mg.Similarly, En24 responded favourably in terms of wear resistance to treatments where oxy-acetylene applied graphite coatings were used and where spray painting was employed. It is therefore fair to conclude that if the power density/interaction time is sufficient to harden the steel there is a resultant improvement in the wear characteristics.

The nature of the grit blasted surface would make processing more complicated as extra steps would have to be employed. Therefore, DAG colloidal graphite was deemed to be a more practical coating. Again, significant improvements in wear performance was observed with these samples. En24 showed losses of <2mg in total

for almost all specimens, as did En52 in a number of cases.

The test results presented in Fig. 5.48-5.49 (samples P1D1 etc), were made to verify the above results, and to further investigate the DAG coating method. Again,in many instances both steels showed total weight losses of <2mg. A relationship was not identifiable between treatment conditions and performance, but there seems to be a minimum level of treatment necessary to improve performance. This is acceptable since the optimum depth of hardening necessary to improve lifetime will depend on the likely amount of wear (<20μm on a stem diameter) and as long as the depth is adequate to allow for this then the depth of hardening would not seem important. However, the mechanism of wear may be such that the softer layer underneath the HAZ cracks and this could depend on the depth of the HAZ. Further work is necessary to elucidate whether this is an important factor. Also, further work to develop a test which is sensitive to nuances in microstructure is needed. One further point worthy of note is that even a more sensitive wear test would not be representative of an engine test and ultimately endurance would have to be measured under the exact loading conditions faced in service. The boundary lubrication wear rig is a ranking test used in industry to examine the bulk properties of a material.

In general, increasing the onteraction time increased the wear performance, however, this was a general trend and not always the case.

Examination of the wear scars resulting from the BLWR tests, using the SEM revealed almost circular wear scars on both pin and substrate, an example of which is given in Fig. 5.50. Higher magnification examination showed surfaces from which large flakes seem to have been pulled, Fig. 5.51 (a)-(d). Similar surfaces wear noted for both steels. It can therefore be assumed that the wear mechanism was the same in both cases. Elemental analysis was confined to a brief look at the surfaces of each steel, and revealed a surface representative in composition of the bulk material, the wear debris was found to contain Fe_2O_3. This type of debris is characteristic of reciprocating wear when fretting has occurred. It seems that the surface of the steel formed an oxide film which flaked off during the test. Conditions of 200^{o}C for 4hours could cause an enhanced rate of oxidation, accounting for this observation.

The substrate surface of a sample of En24 and En52 was scanned using the 3-D surface profiling rig at T&N Technology and the "before and after" test traces are presented in Fig. 5.52. As shown, the surface asperities before testing were at most 11μm deep. After testing, the surfaces resembled a flat-bottomed crater was found to range from 14-50μm, depending on the severity of wear.

The surface roughness (R_A) of the surfaces before testing tended to be around 0.3 and after testing, the value of R_A was found to increase to >1.8.

5.9.2 Valve stem tests (Brico Engineering)

The data from wear tests performed on fully treated valve stems at Brico Engineering is presented in Table 5.6. The friction value quoted was a measure of the resistance of the specimen to sliding but was not a measure of the friction coefficient of the material since the pieces tested were of circular section. Samples which pass this test usually have a friction value of 0.3-0.4 but the surface roughness is usually much lower than the values of these test pieces. It must be emphasised that Brico use this test as a rough guide as to whether the material might be suitable for valve stem application and that further testing is done in terms of engine validation. The scope of this project did not cover engine testing and these results are therefore qualitative only.

All of the samples tested passed the test i.e. no sample failed by welding as would normally be the case. In general failure would occur by particles from the valve guide adhering to the stem and being torn away from the guide. Some samples were observed to gain weight during the test. This was due to material transfer from the guide in most cases. Another important feature of the test was whether the friction value remained smooth to the end of the test, if so this would be deemed a 'pass'. In all cases, the friction coefficient remained fairly constant over the duration of the test.

All of the valve stems showed a marked improvement in wear resistance compared to the untreated steels and another valve stem material, 21-4N. Another point was the similar wear performance noted from a Cr plated stem. The chromium plating operation is very expensive and surfaces showing similar wear resistance produced by LTH possibly offer an equally resistant, lower cost component.

5.10 Summary

A number of conclusions can be drawn from this chapter. It was possible to harden both En24 and En52 steels to differing degrees. The depth of laser treatment depends upon the treatment conditions. The surface hardness obtained is constant above a certain interaction time and further increases in the dwell time do not significantly improve either hardness or wear resistance. Laser hardened steels show excellent wear performance although surface melting diminishes the wear resistance. In terms of surface coatings, DAG colloidal graphite offers significant improvement in absorptivity with ease of use, although excimer roughening is also fast , effective and clean and probably offers a higher and more controllable degree of uniformity.

5.1

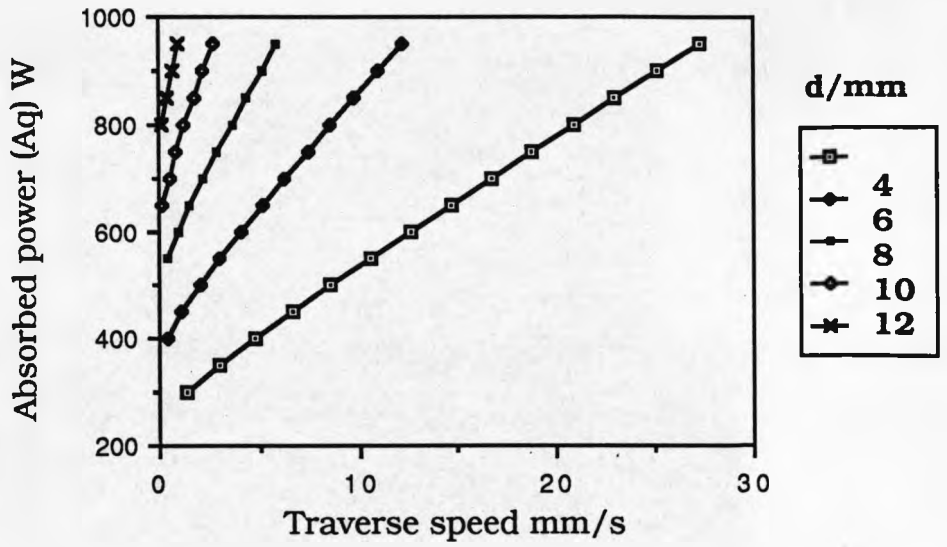

5.2

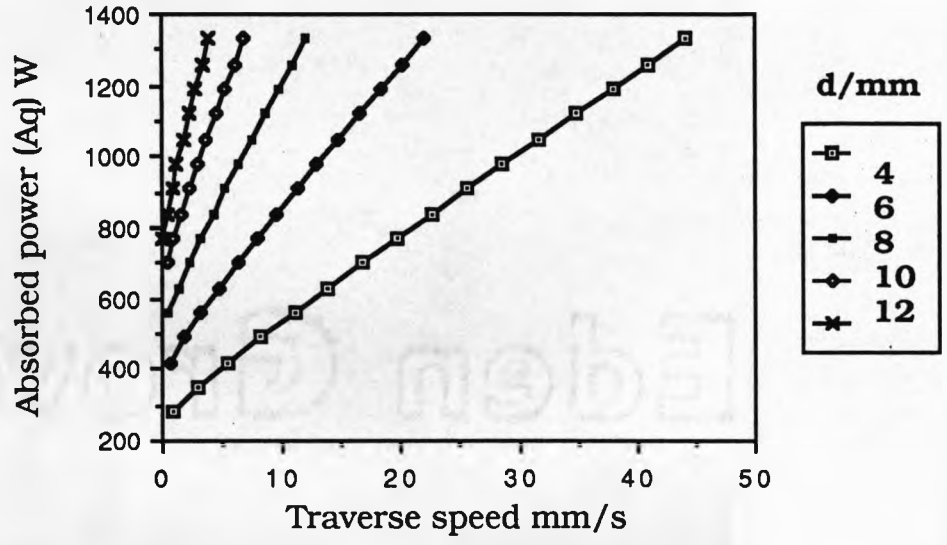

5.3

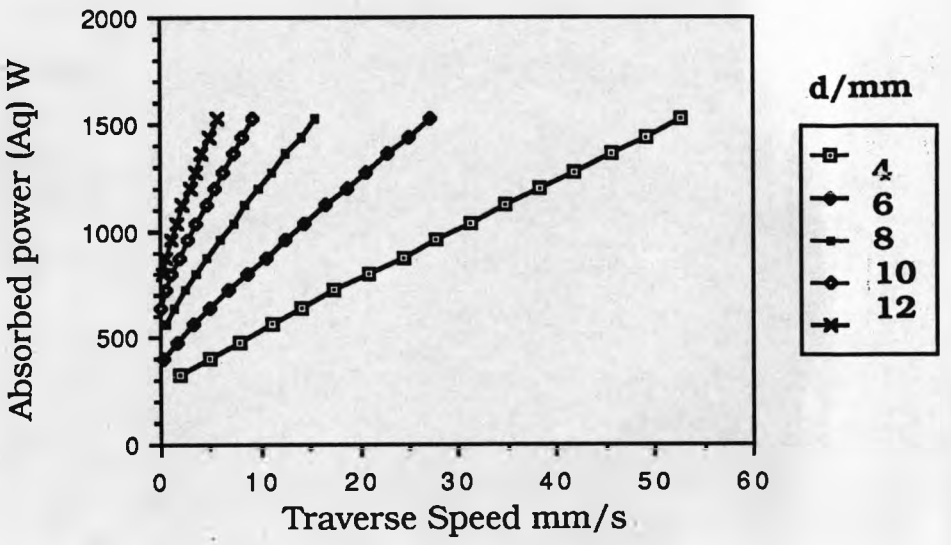

Fig. 5.1-5.3 Plots of required absorbed power versus traverse speed for a 0.5mm case depth in En24 steel

(a) ground surface

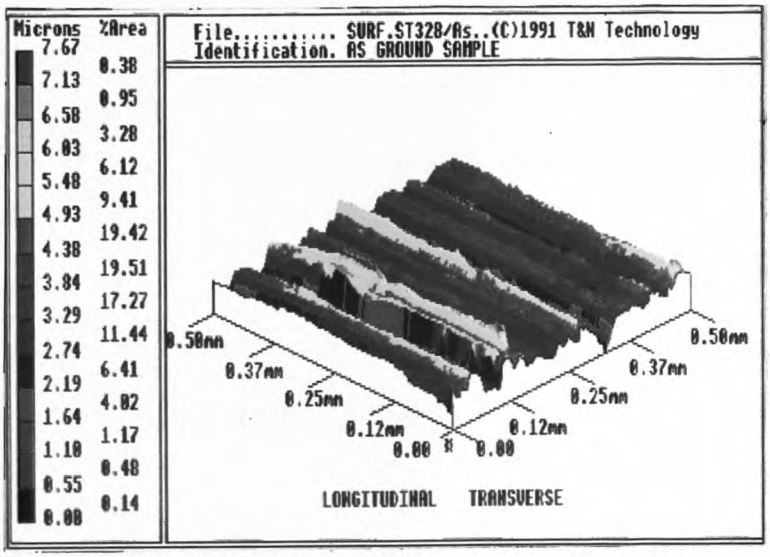

(b) excimer pre-treated surface (0.75mm/s)

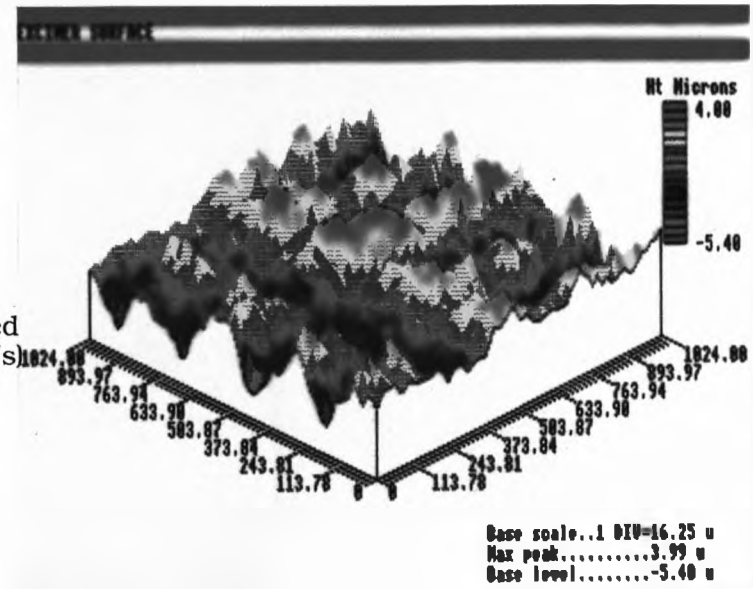

(c) grit blasted surface

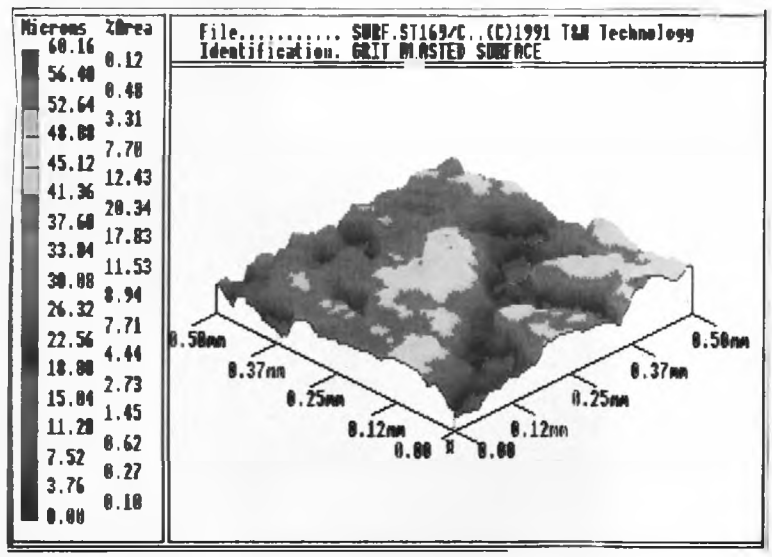

Fig. 5.4 3-D surface profiles of En24 steel surfaces, (a) ground, (b) excimer treated, (c) grit blasted

Sample	Power (kW)	Speed (mm/s)	Spot size (mm)	Peak T (K)
1	1.07	2.0	6.0	343.0
2	1.07	4.0	6.0	290.2
3	1.06	6.0	6.0	224.0
4	1.04	8.0	6.0	180.3
5	1.06	10.0	6.0	107.4

Profiles

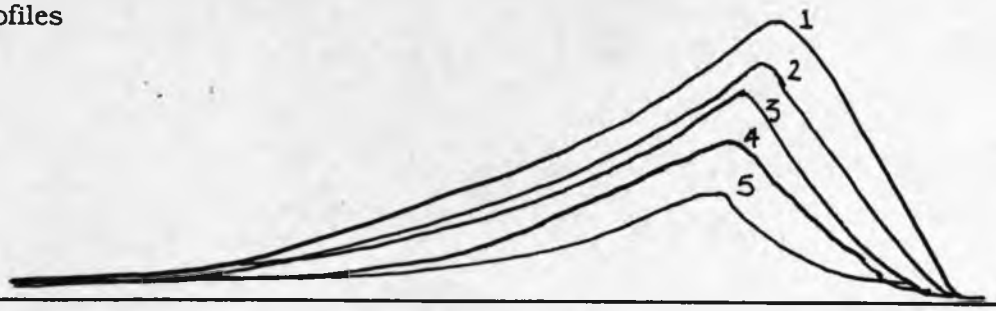

Table 5.1 Temperatures recorded 1mm below surface for En52 graphite (oxy-acetylene) coated

Surface Coating	Absorptivity at 100 C	
	EN24	EN52
Grit blasted	67.8	69.2
Etched (picral 60s)	37.4	33.5
Grit blasted and etched (picral 60s)	67.4	69.3
Graphite coating	54.4	54.0
Wiped graphite coating	9.1	8.1
Excimer pre-treated (0.75mm/s)	96.8	90.3
DAG colloidal graphite coating	74.4	72.4
Untreated ground metal surface	6.8	8.0

Table 5.2 Absorptivities of various surface coatings

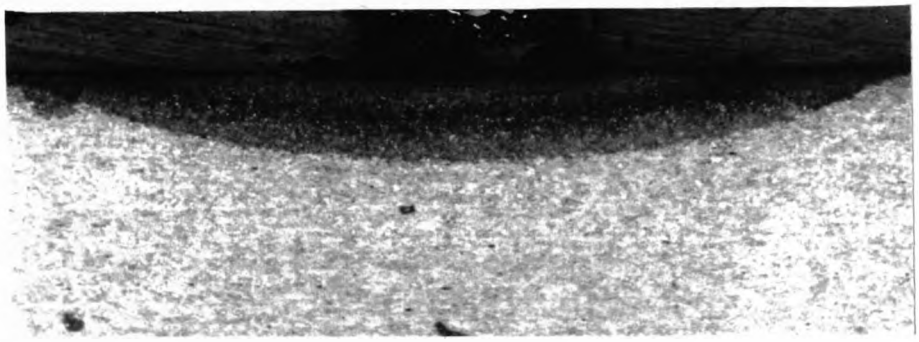

Fig. 5.5(a) Typical cross-section of LTH zone in En24 (q=1.6kW, v=16mm/s, d=6mm

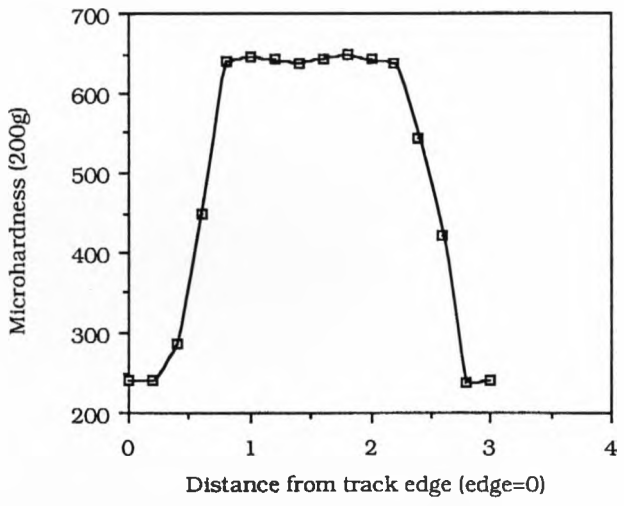

q=1610W, v=40mm/s, d=5mm, coat=DAG

Fig. 5.5 (b) Plot showing variation in hardness across surface of typical transverse track

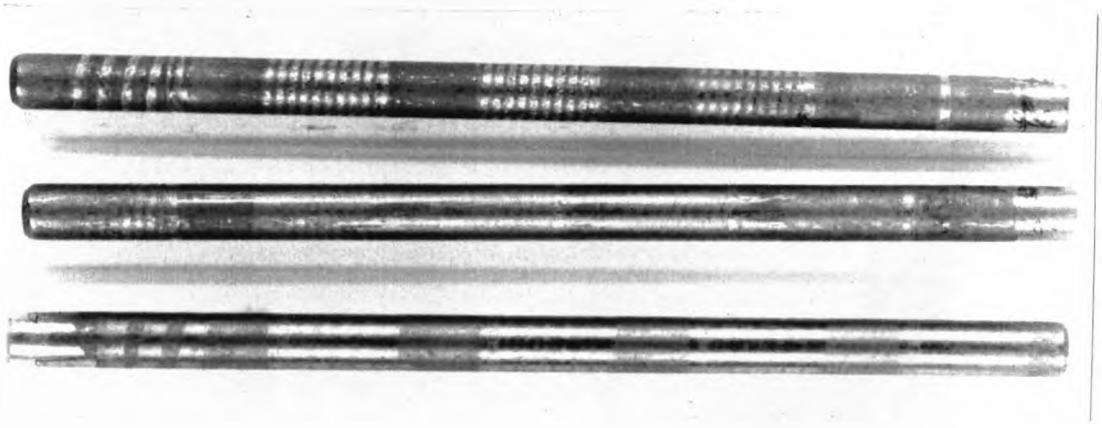

Fig. 5.5(c) Illustration of spiral hardened valve stems pre-coated with DAG colloidal graphite, different spiral pitches shown

Slow/Fast Setting (S/F)	Motor Setting	Speed rev/s	Surface Speed mm/s
S	0.00	0.040	1.01
S	1.00	0.045	1.13
S	2.00	0.049	1.24
S	3.00	0.056	1.41
S	4.00	0.063	1.59
S	5.00	0.072	1.82
S	6.00	0.085	2.14
S	7.00	0.105	2.65
S	8.00	0.125	3.15
S	9.00	0.185	4.66
S	10.00	0.313	7.89
F	0.00	0.429	10.82
F	1.00	0.476	12.00
F	2.00	0.532	13.41
F	3.00	0.602	15.18
F	4.00	0.694	17.50
F	5.00	0.820	20.67
F	6.00	1.010	25.46
F	7.00	1.266	31.92
F	8.00	1.724	43.46
F	9.00	2.703	68.15
F	10.00	5.000	126.06

Table 5.3 Motor Calibration Data

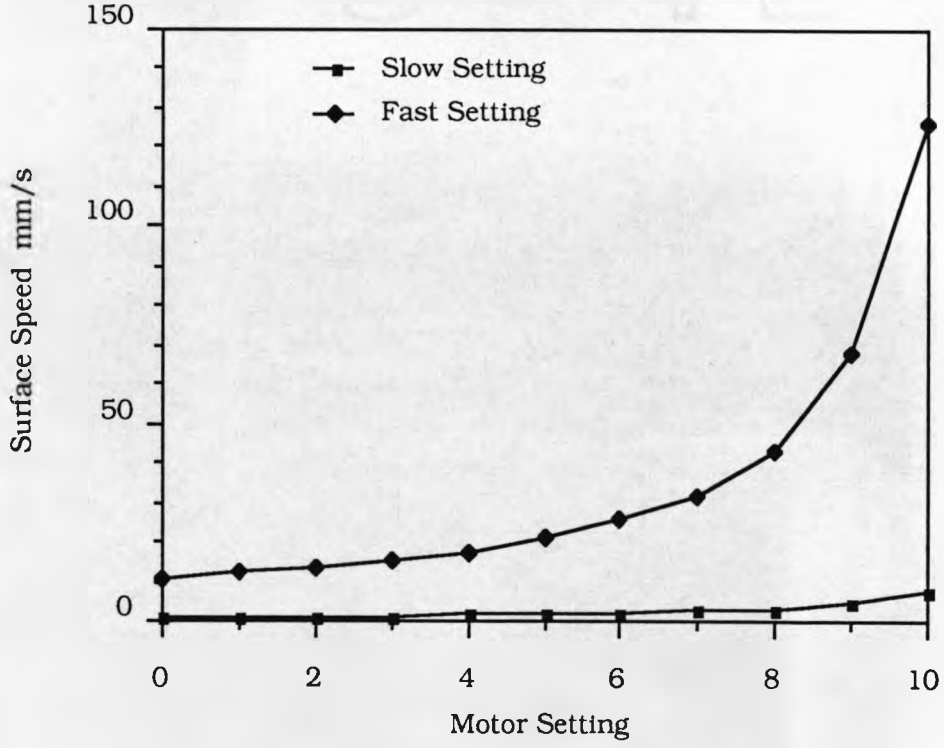

Fig. 5.14 Motor Calibration Curves

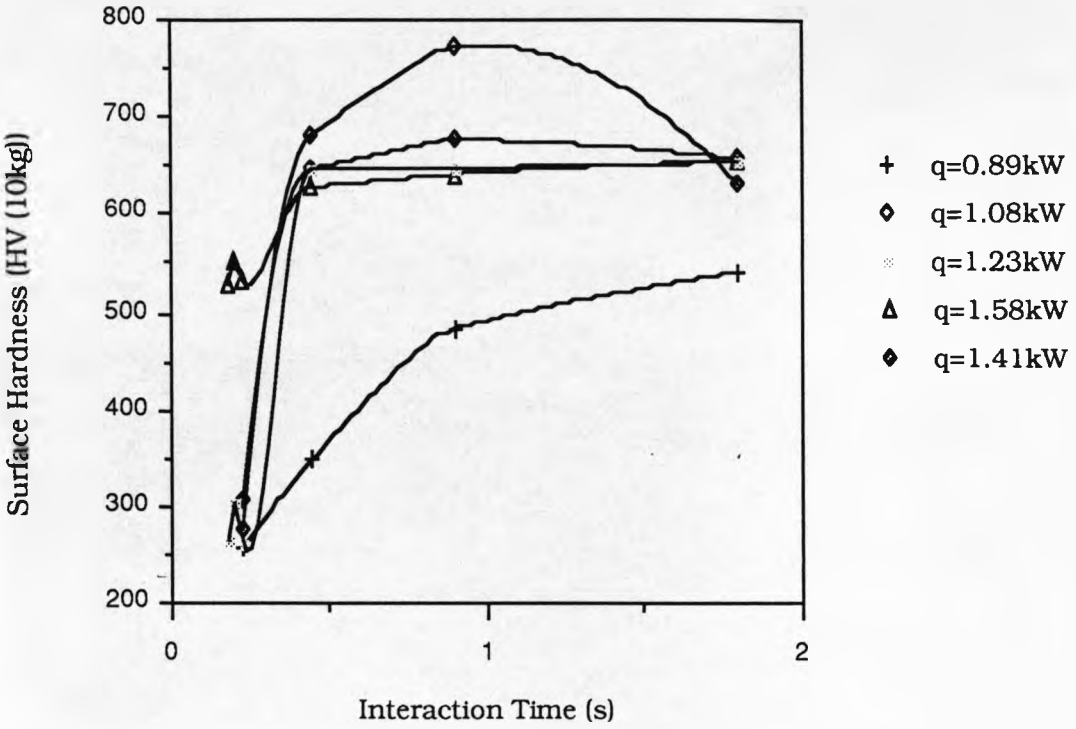

Fig. 5.6 Relationship between Surface Hardness and Interaction Time for En24 (spray paint coating)

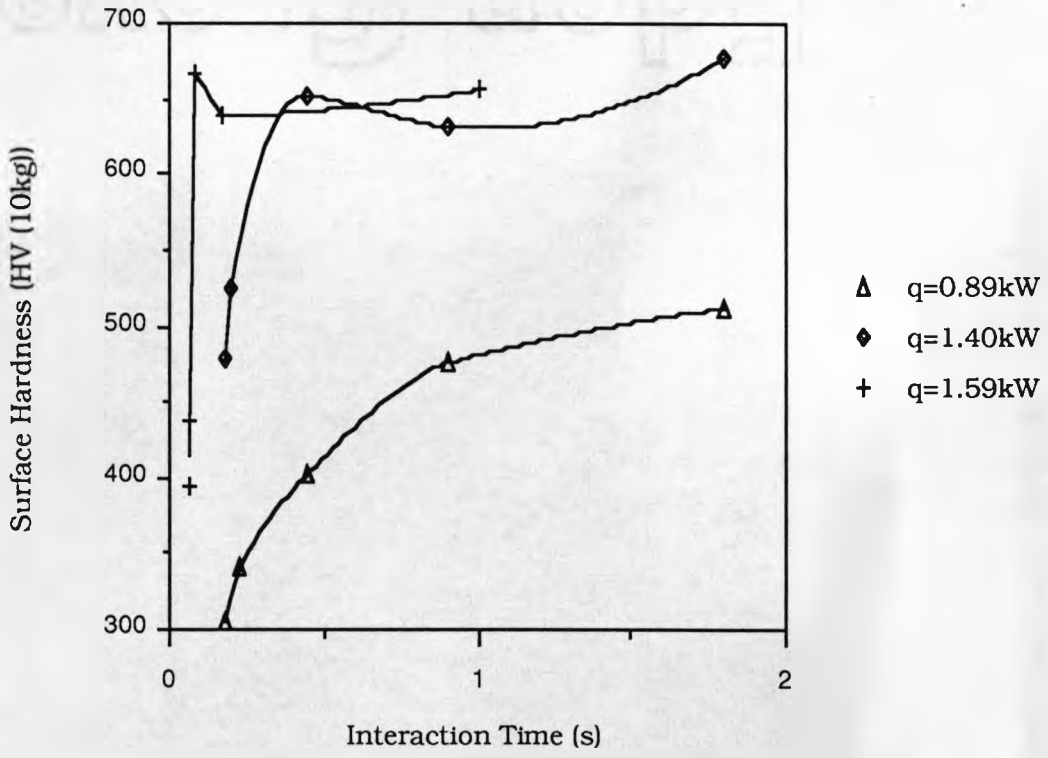

Fig. 5.7 Relationship between Surface Hardness and Interaction Time for En52 (spray paint coating)

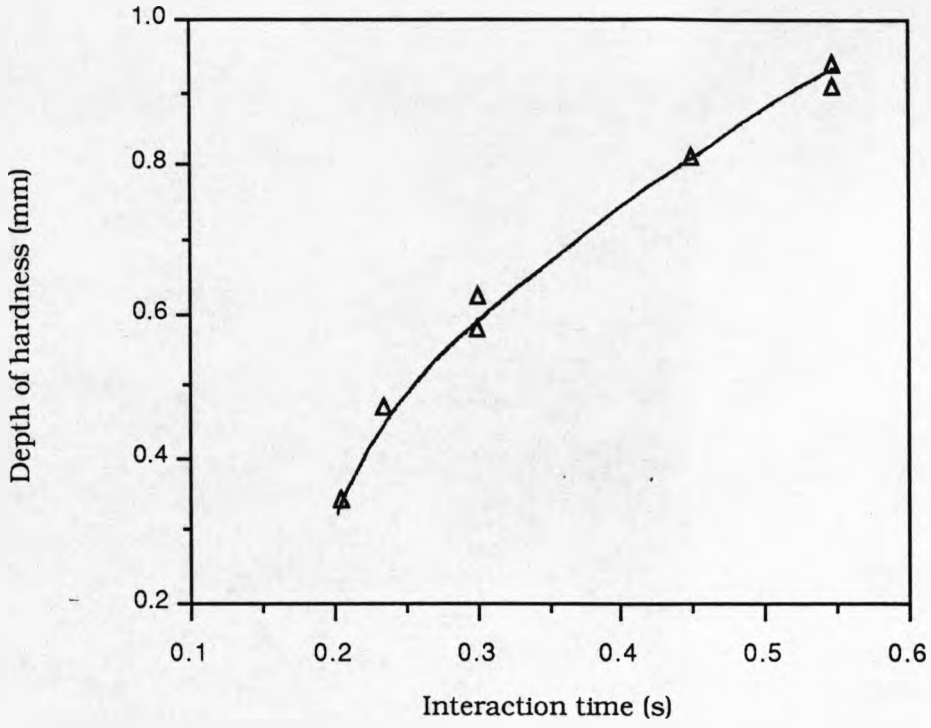

Fig. 5.8 Plot of Case depth vs Interaction Time for En24 (grit blasted surface)

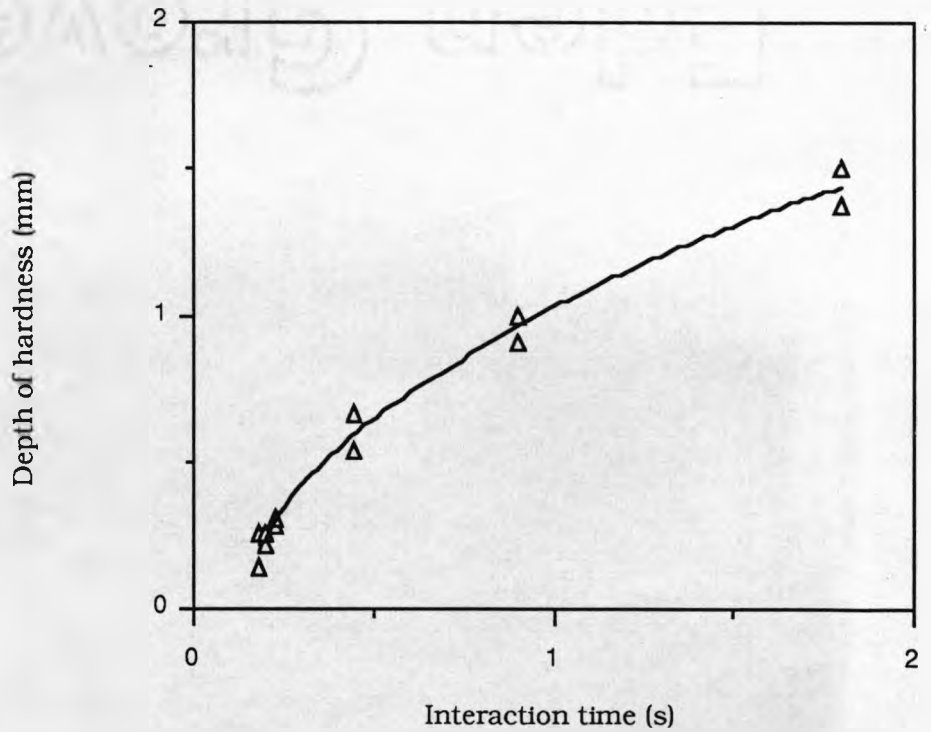

Fig. 5.9 Plot of Case depth vs Interaction Time for En52 (grit blasted surface)

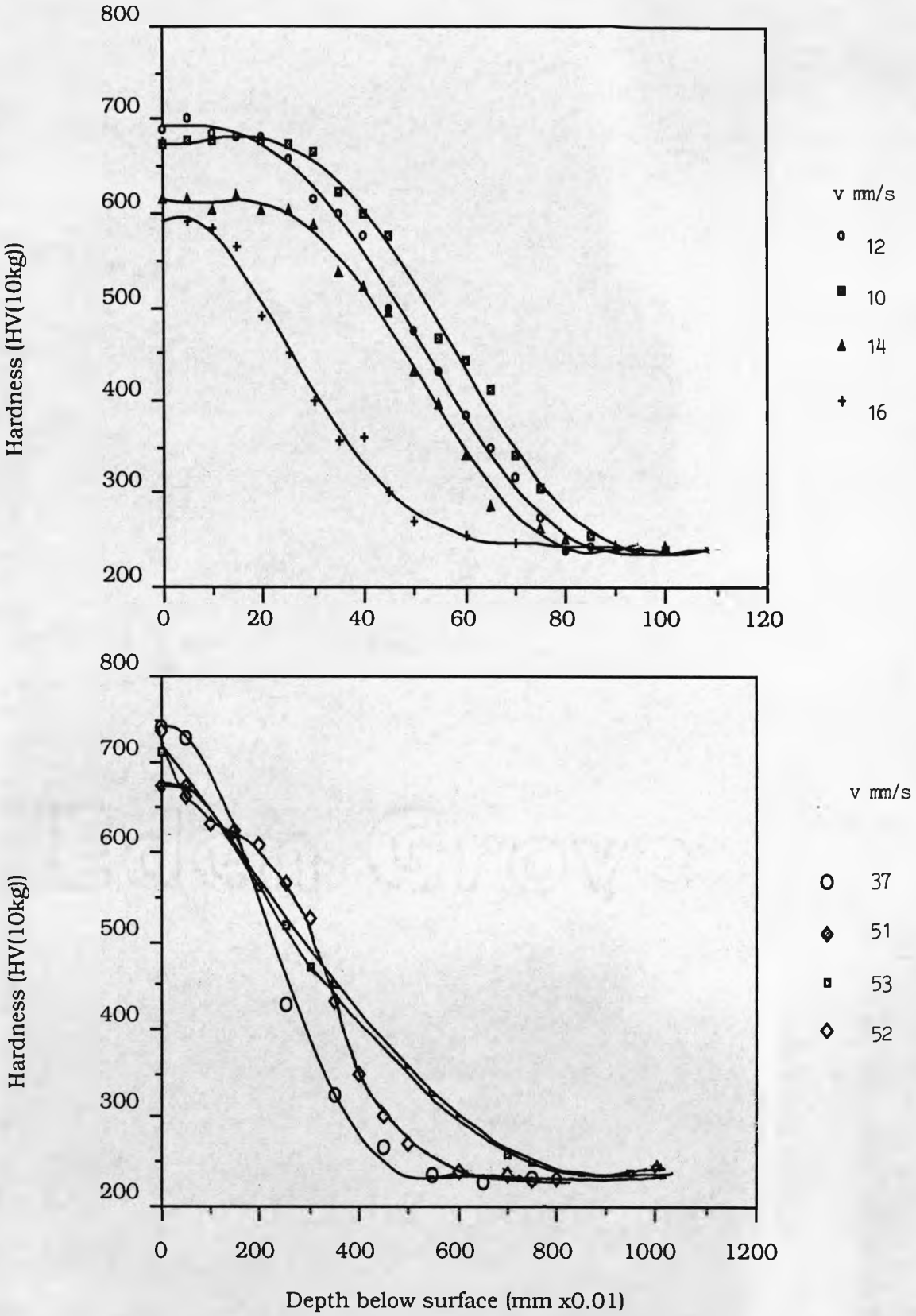

Fig. 5.10, 5.11 Plot of hardness vs depth below surface for 5.10 (top) grit blast and 5.11 (bottom) graphite (oxy-acetylene) coated En24

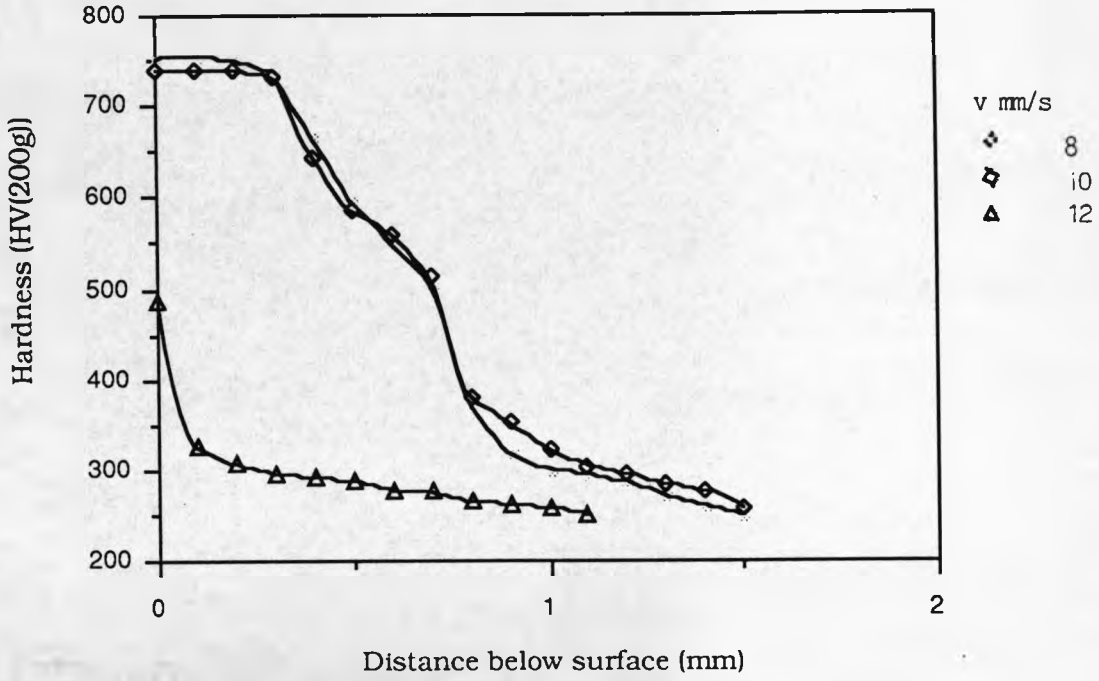

Fig. 5.12 Plot of Hardness vs distance below surface for En52, carbon coated surface
(q = 1600 W, d = 6 mm)

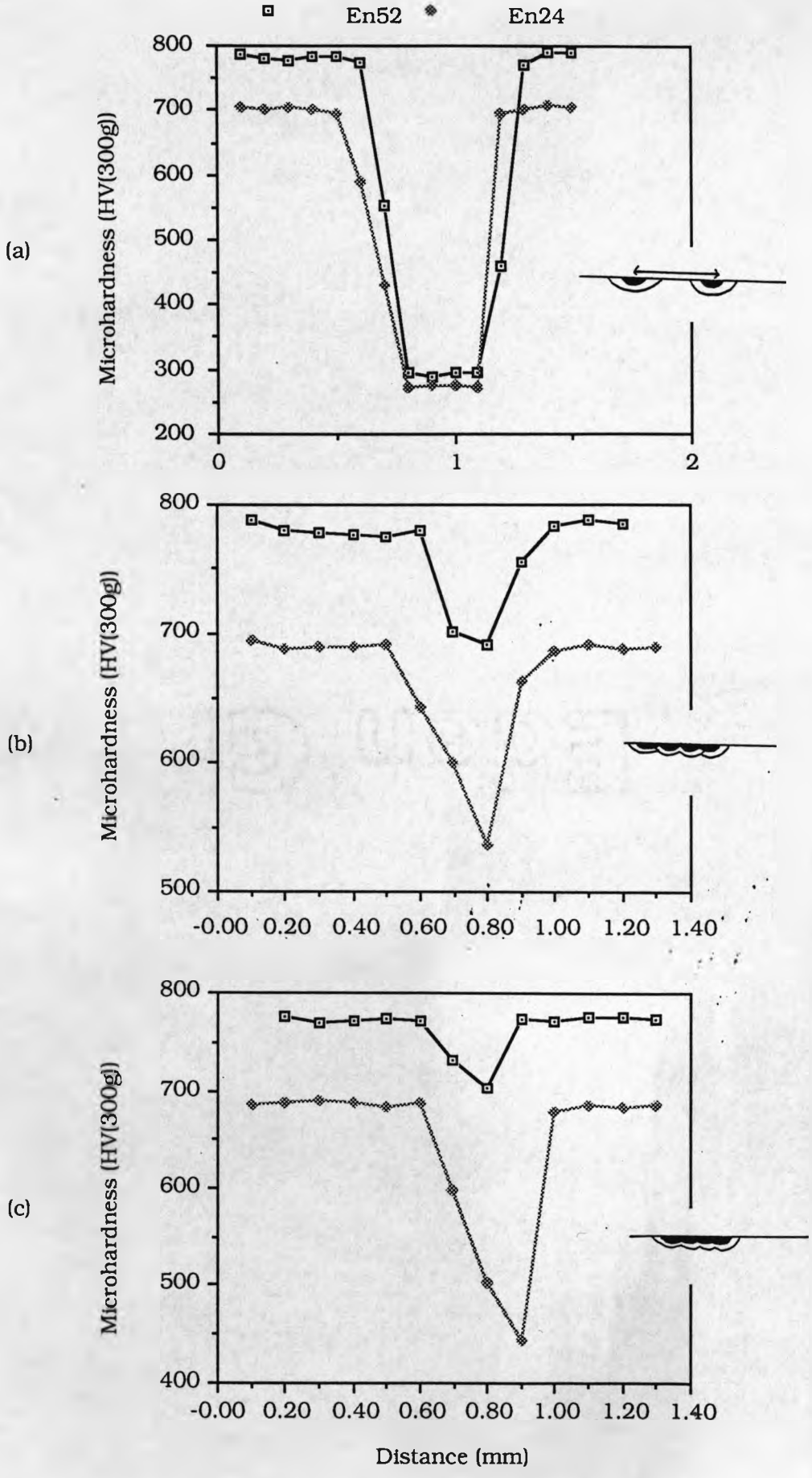

Fig. 5.15 (a)-(c) Hardness profiles for spiral tracks
N.B Scale limits vary

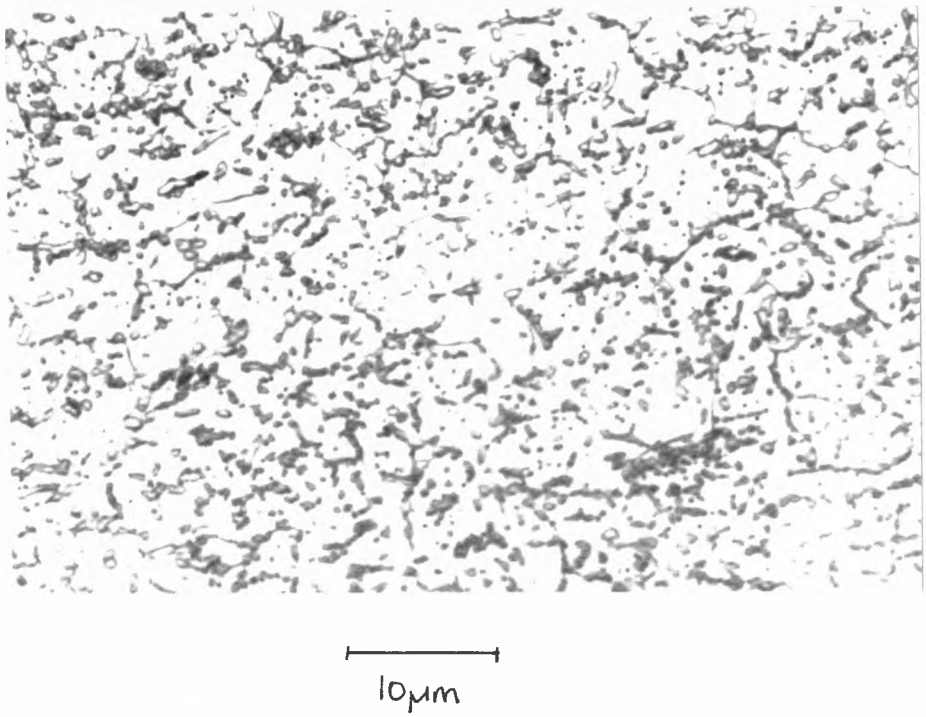

Fig. 5.16 Optical Micrograph Showing Spheroidised Structure of As-Recieved En52 Steel

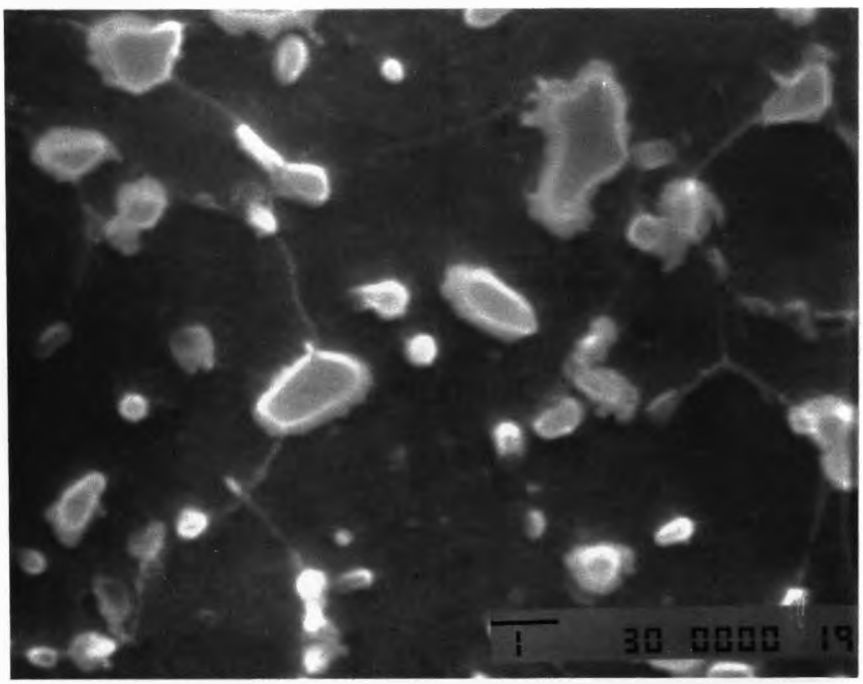

Fig. 5.17 Scanning Electron Micrograph Showing Grain Boundary Precipitates in As-Recieved En52 Steel (overlay showing Cr dot map, dark areas high Cr content)

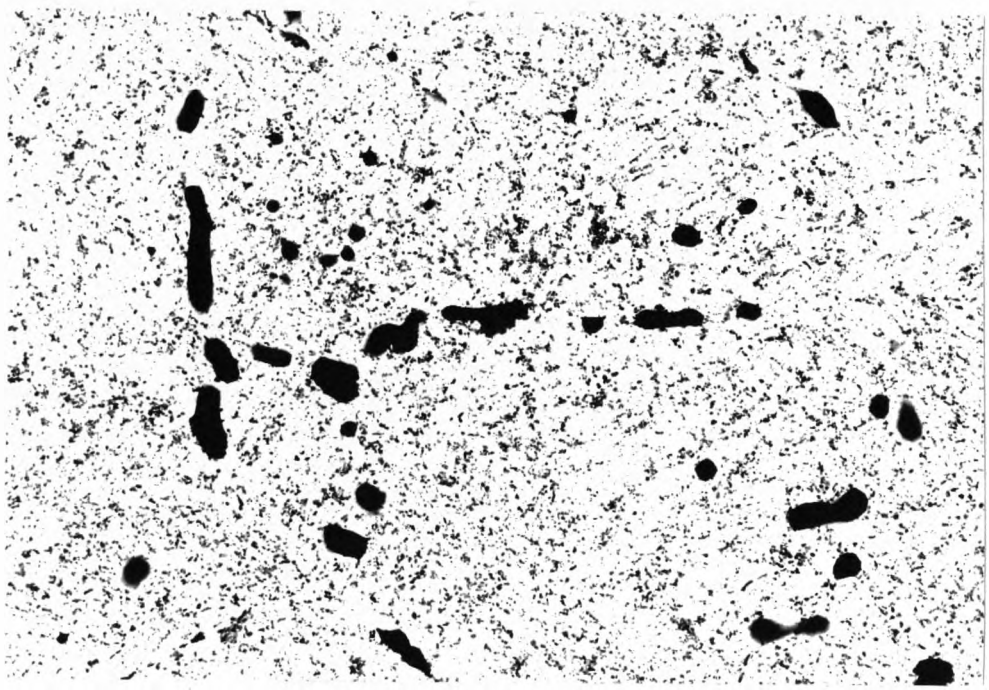

Fig. 5.18 Transmission Electron Micrograph Showing Network of Intra-Granular Precipitates in As-Recieved En52 Steel

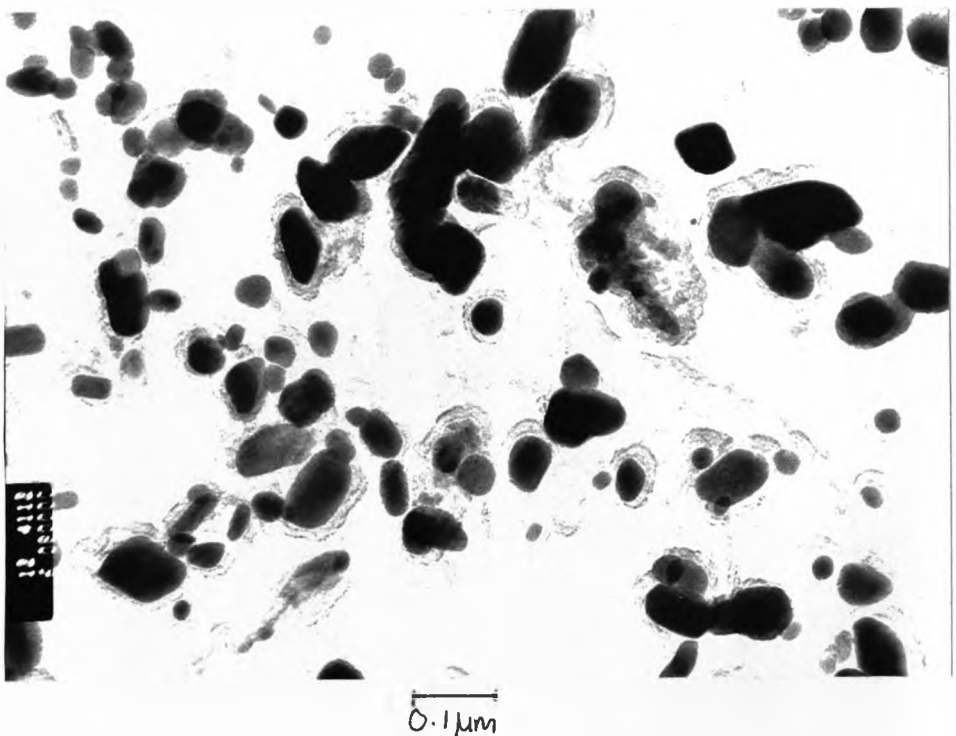

Fig. 5.19 Transmission Electron Micrograph Showing Intra-Granular Precipitates Iin En52 Steel

Fig. 5.20 Transmission Electron Micrograph Showing SAD pattern and Carbide from which it was taken, En52 Steel As-Recieved. Also shown is aa EDX Spectrum from the same precipitate.

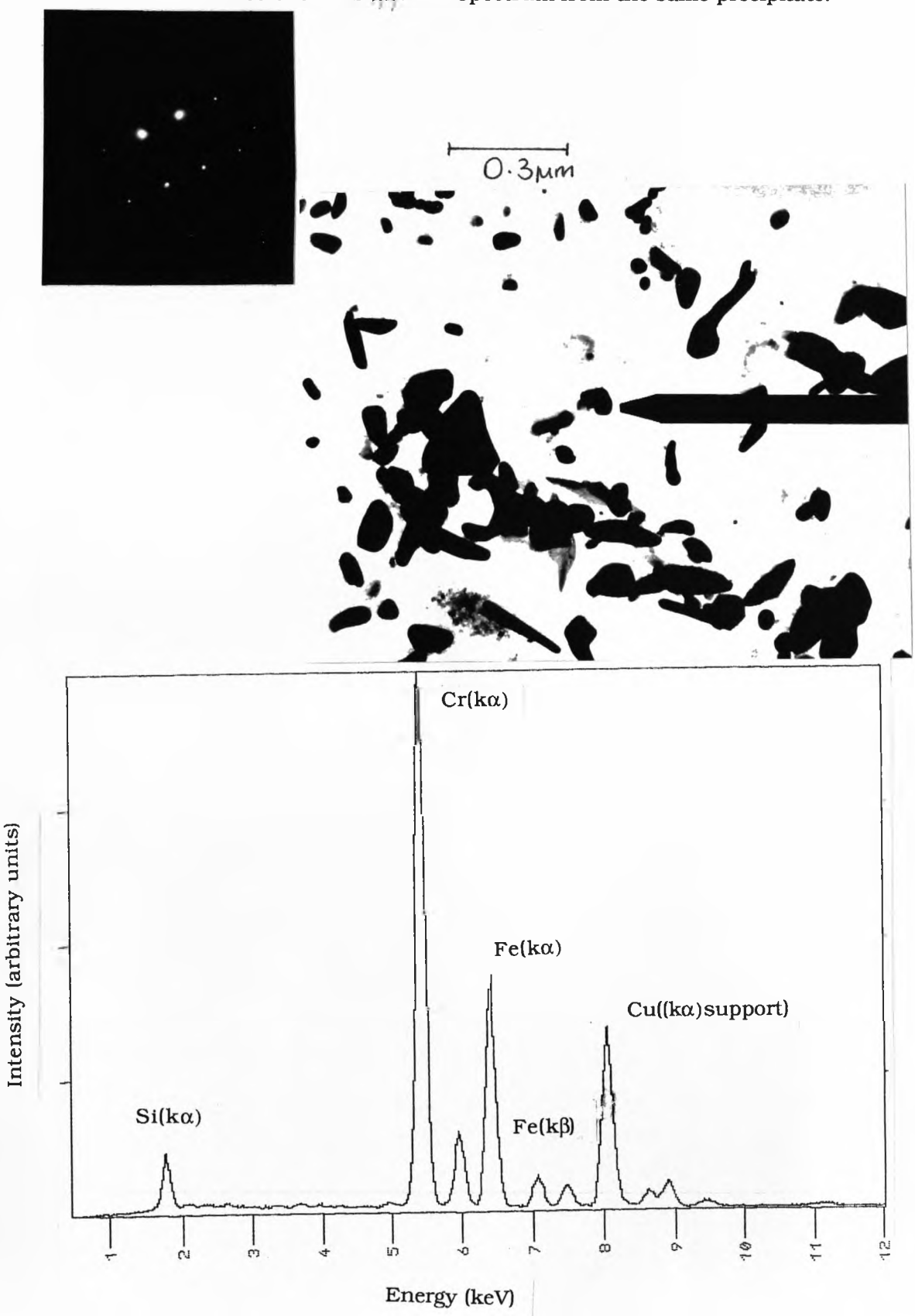

Fig. 5.21 Transmission Electron Micrograph Showing CBED Pattern and Precipitae from En52 Steel, As-Recieved

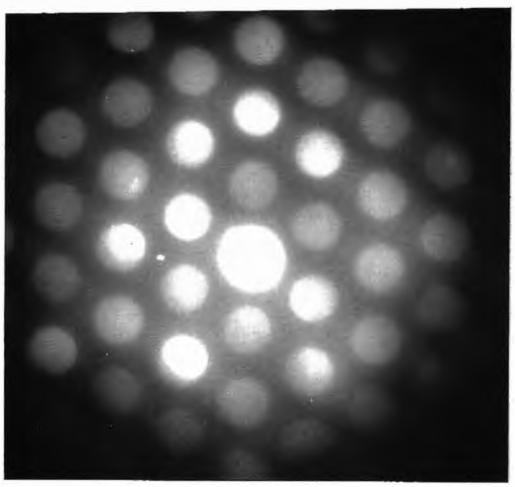

Constituent	Si (wt.%)	Cr (wt.%)	Fe (wt.%)
En24 Matrix	-	1.1	98.4
En24 Precipitate	-	17.3	82.7
En52 Matrix	3.8	7.5	88.7
En52 Precipitate	2.8	22.1	75.0

Table 5.3 Composition of phases for En24/52 steels, determined by EDX

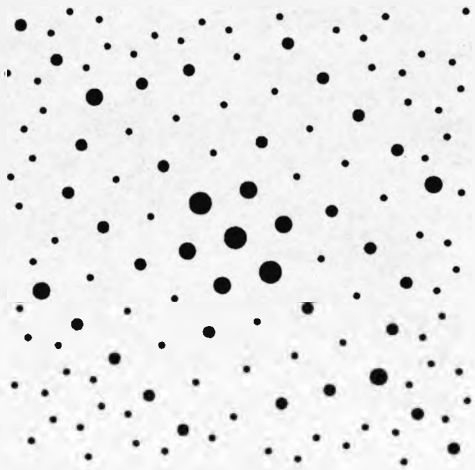

Fig. 5.22 SAD pattern [111] (Cr,Fe)23C6 (atom positions from Westgren (REF)

Reflection		alpha-Fe	0.8% C	En24	En52
alpha-Fe	110	2.0221	2.0236	2.0218	2.0263
	200	1.4314	1.4315	1.4315	1.4351
	211	1.1677	1.1676	1.1689	1.1679
	220	1.0136	1.0140	1.0138	1.0128
	310	0.9035	0.9049	0.8921	-
	222	0.8271	0.8273	0.8268	-
Fe3C	121	-	2.1031	2.1016	-
	210	-	2.0604	2.0631	-
	211	-	1.9722	1.9698	-
	113	-	1.8794	1.8801	-
(Cr,Fe)23C6	420	-	-	-	2.3581
	422	-	-	-	2.1664
	100	-	-	-	2.0589
	440	-	-	-	1.8890

Table 5.4 XRD Data for steel specimens

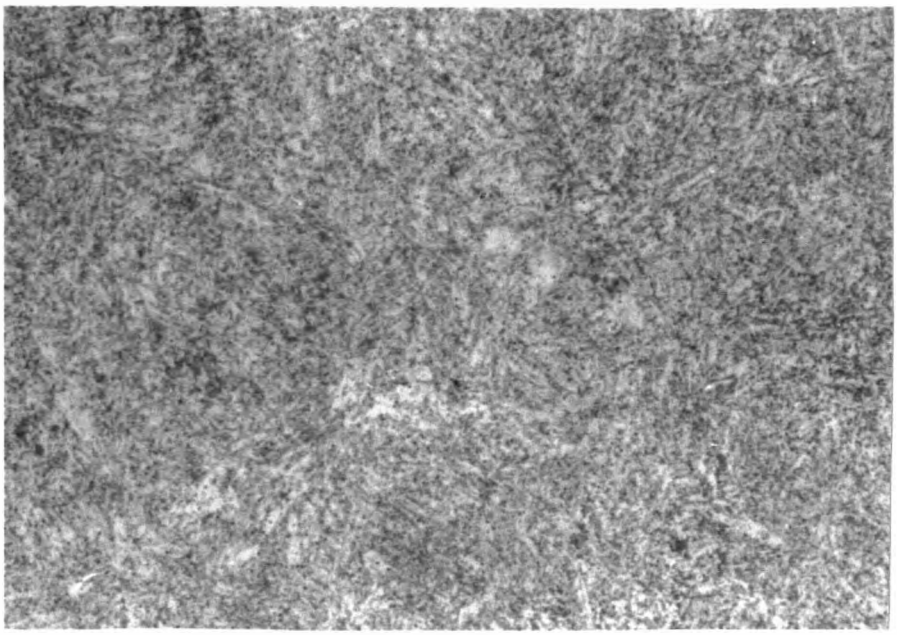

Fig. 5.23 Optical Micrograph Showing Spheroidised Structure of As-Recieved En24 Steel

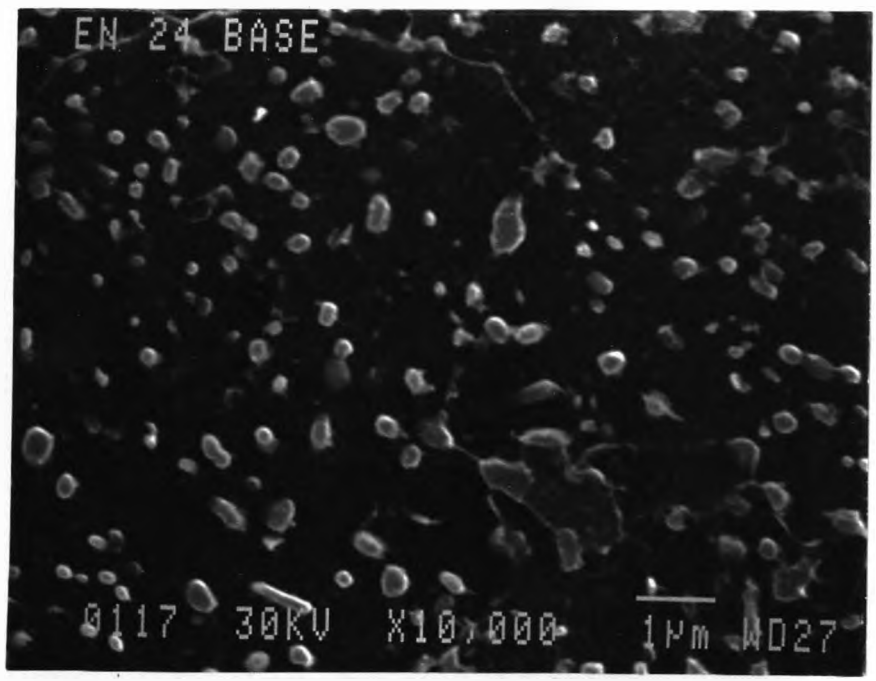

Fig. 5.24 Scanning Electron Micrograph Showing Grain Boundary Precipitates in As-Recieved En24 Steel

Fig. 5.25 Transmission electron micrographs showing elongated spheroids in En24 steel, A.R.

(a)

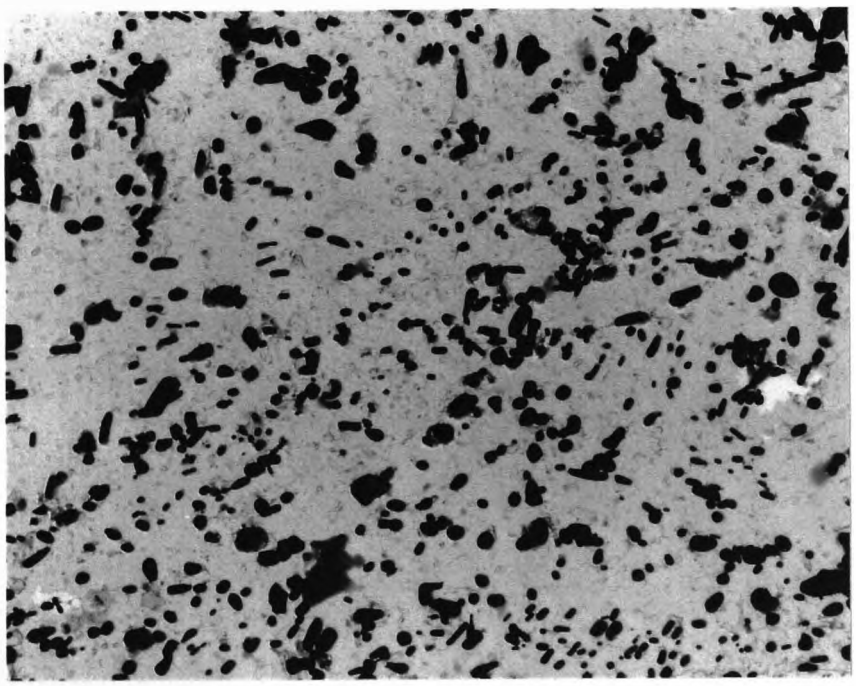

5 μm

(b)

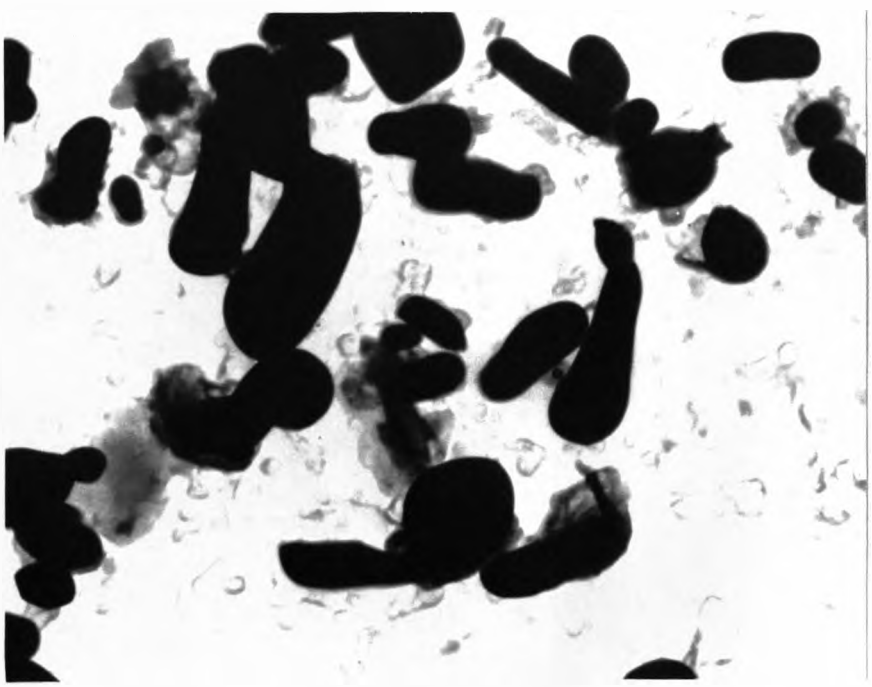

0·6μm

Fig. 5.26 Transmission electron micrograph showing SAD pattern from carbide indicated and corresponding EDX trace

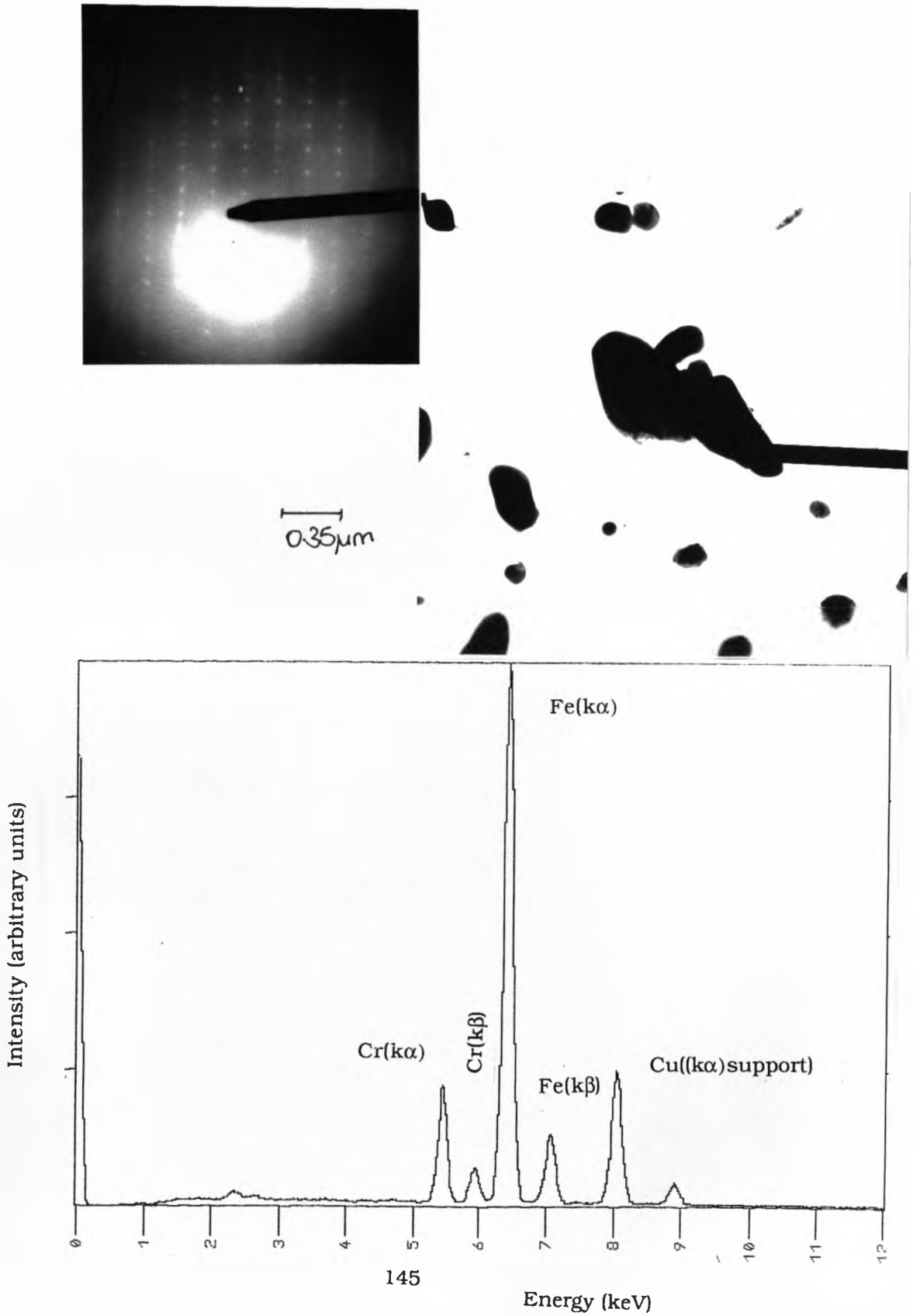

Fig. 5.27 Transmission electron micrograph showing CBED pattern from carbide indicated, En24 steel, as-received

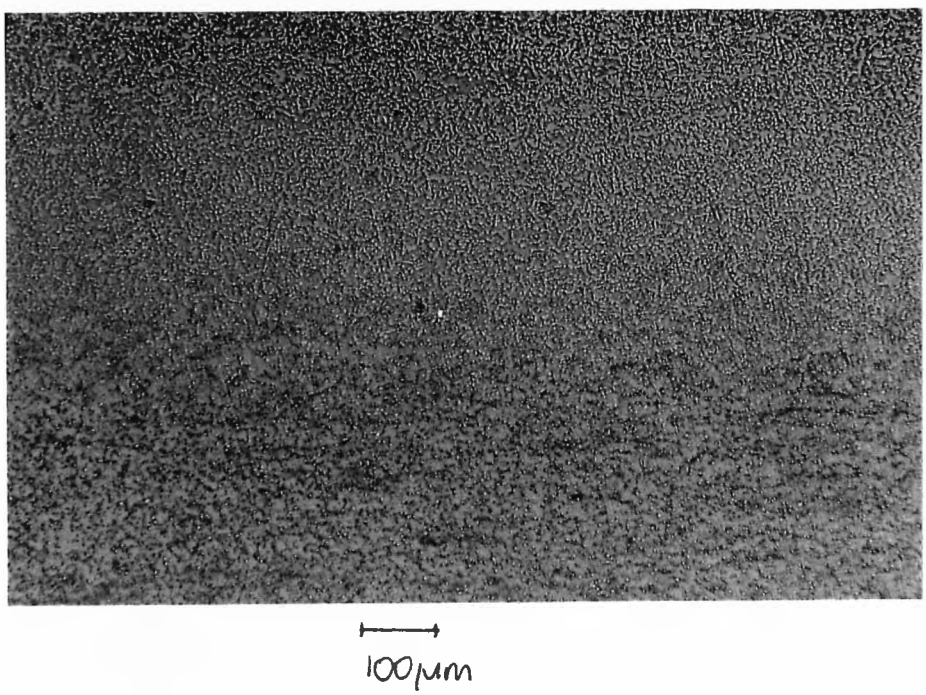

Fig. 5.28 Optical micrograph showing two zone microstructure of LTH En52, q= kW, v= mm/s, d= mm

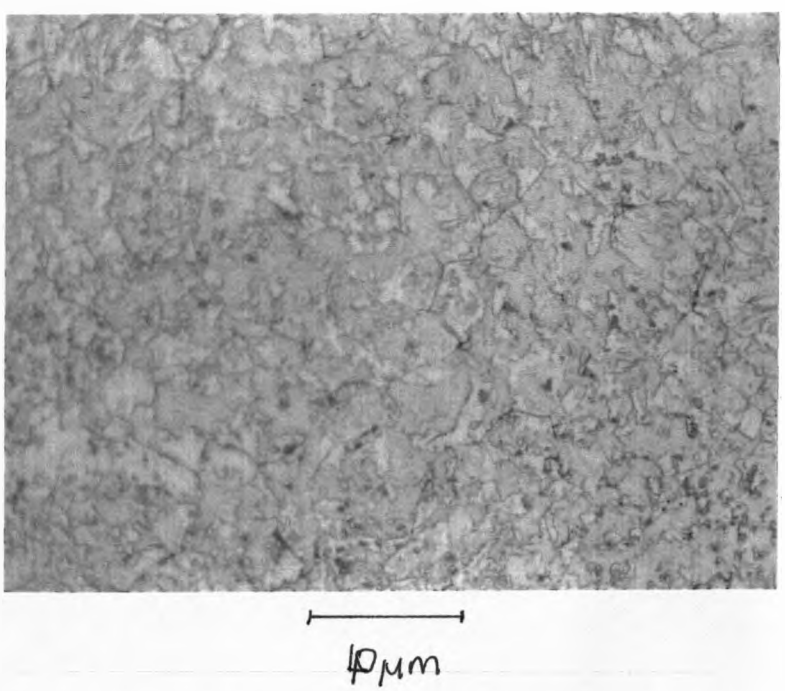

Fig. 5.29 Upper layer of HAZ in En52, processed as above

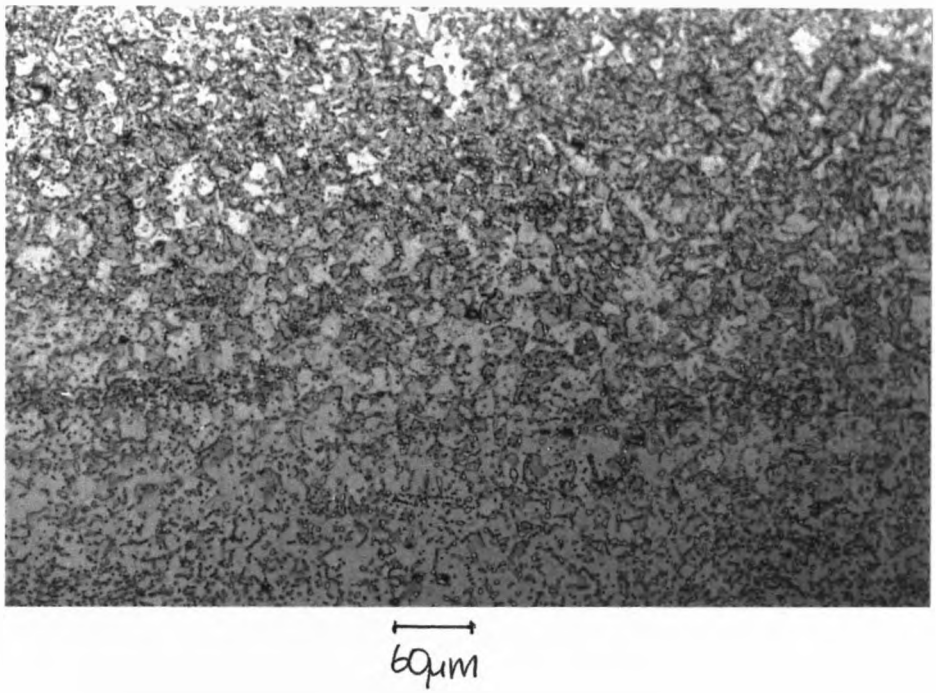

Fig. 5.30 Lower layer of HAZ in En52, processed as above

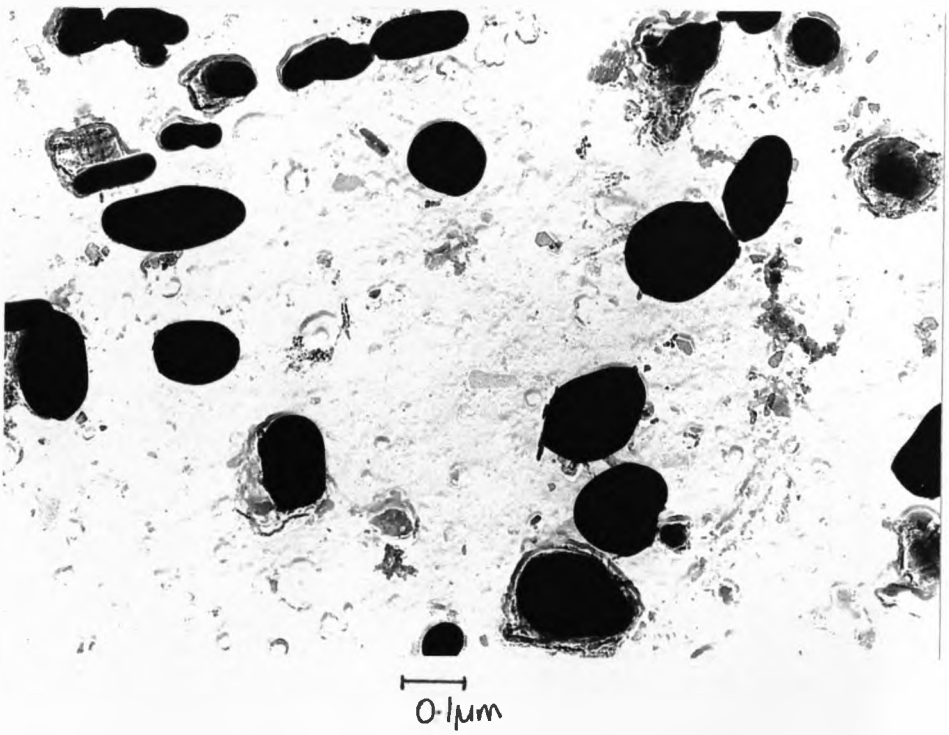

Fig. 5.31 Transmission electron micrograph showing coarsening of grain boundary precipitates

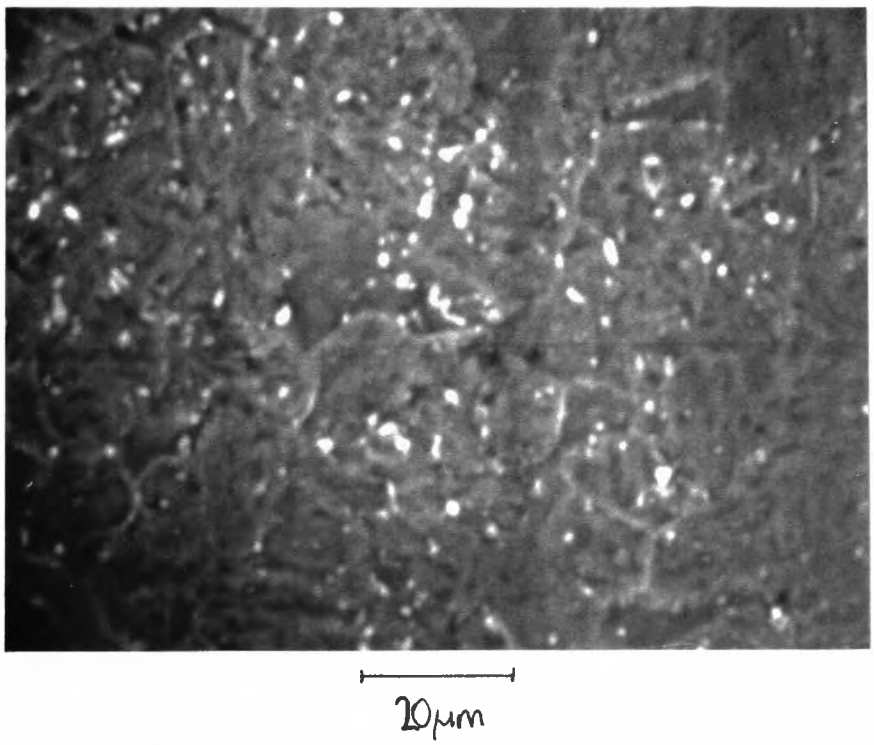

Fig. 5.32 Scanning electron micrograph showing martensitic surface of LTH En24 (q= kW, v= mm/s, d= mm)

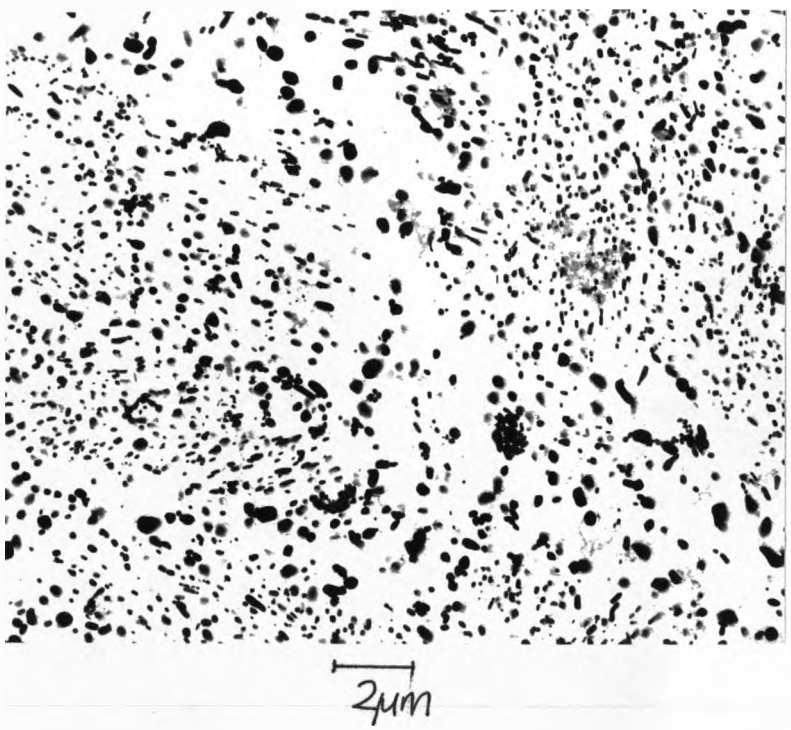

Fig. 5.33 Transmission electron micrograph showing precipitates after LTH, as above, note they are fewer in number and smaller

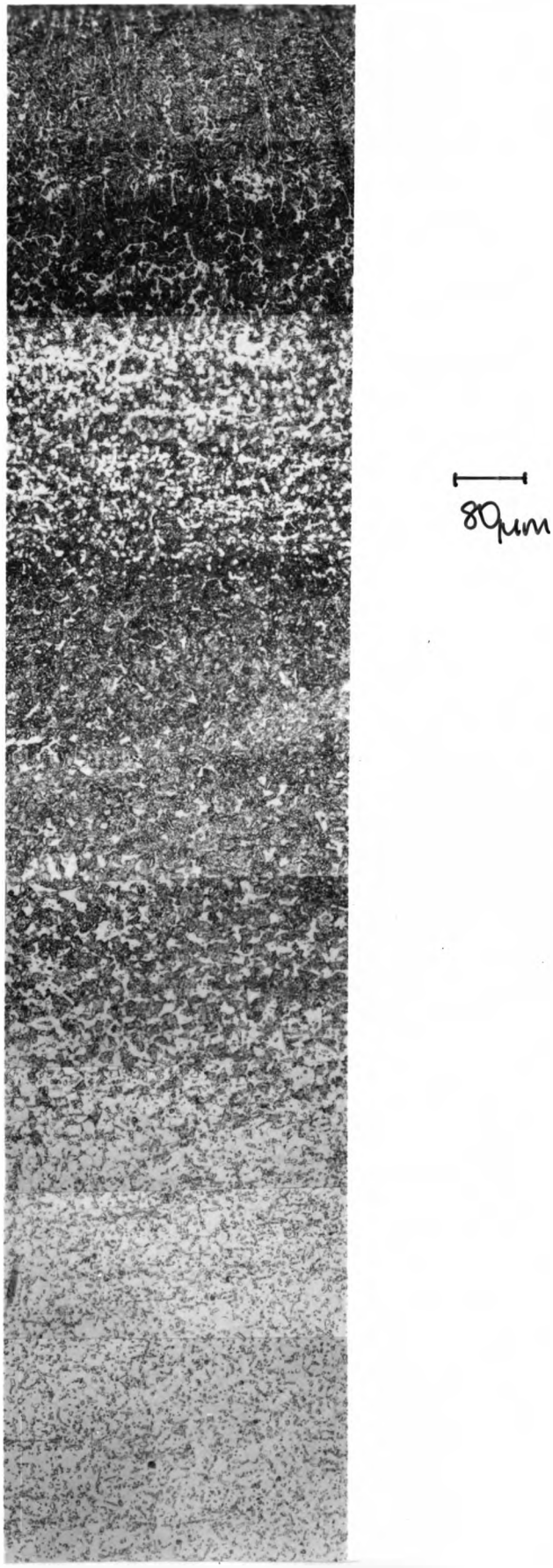

Fig. 5.35 Optical micrograph showing structures observed after surface melting of DAG coated En52

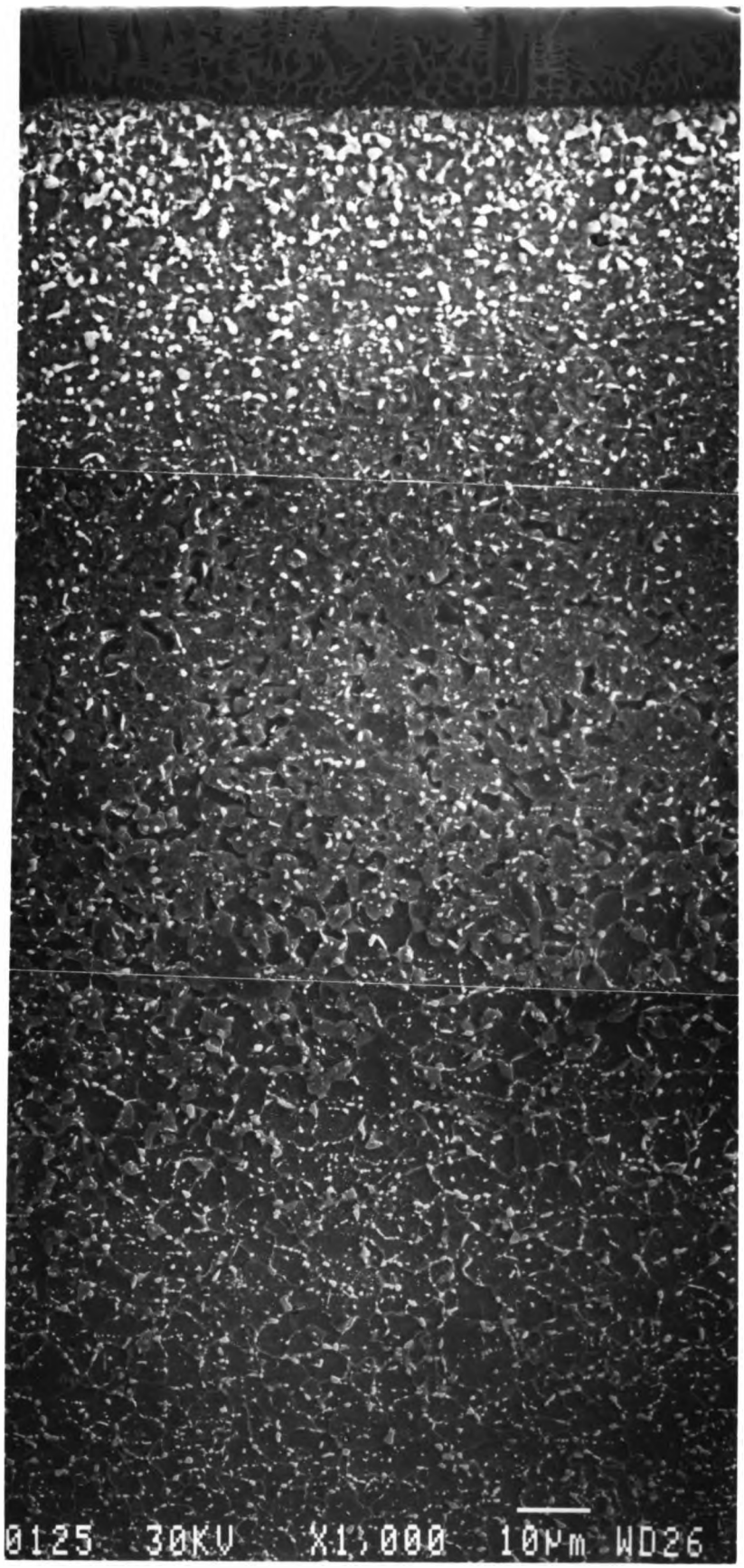

Fig. 5.35 SEM micrograph showing microstructural changes in En52 steel

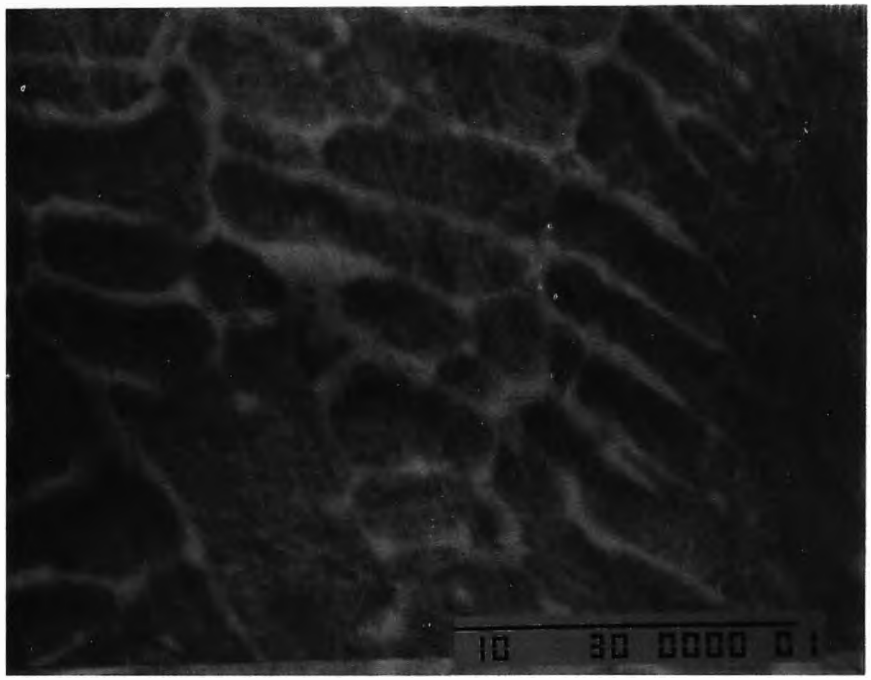

Fig. 5.36 (a) Scanning electron micrograph showing dendritic zone in surface melted En52 steel

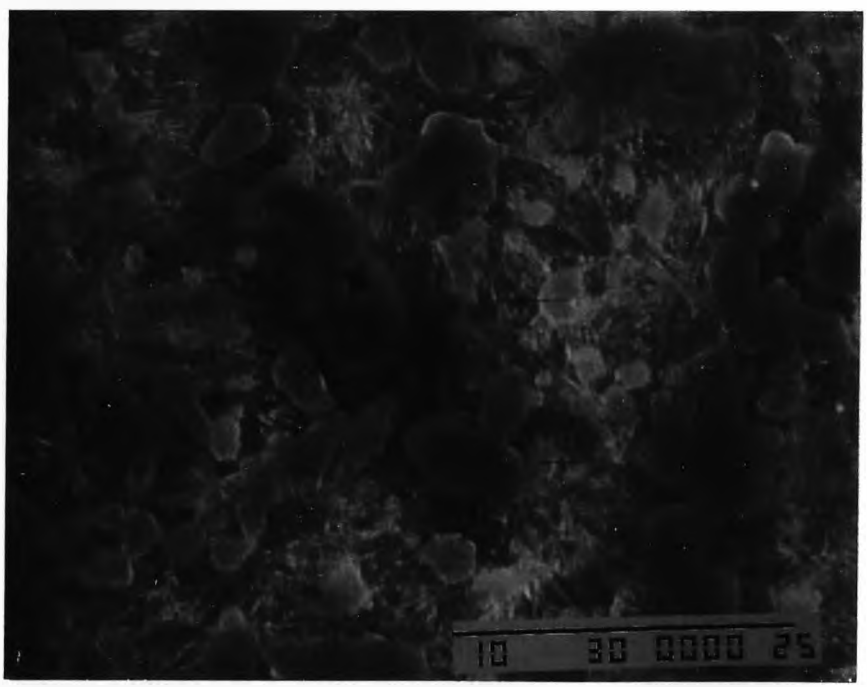

Fig. 5.36 (b) Scanning electron micrograph showing 'white' zone in surface melted En52 steel

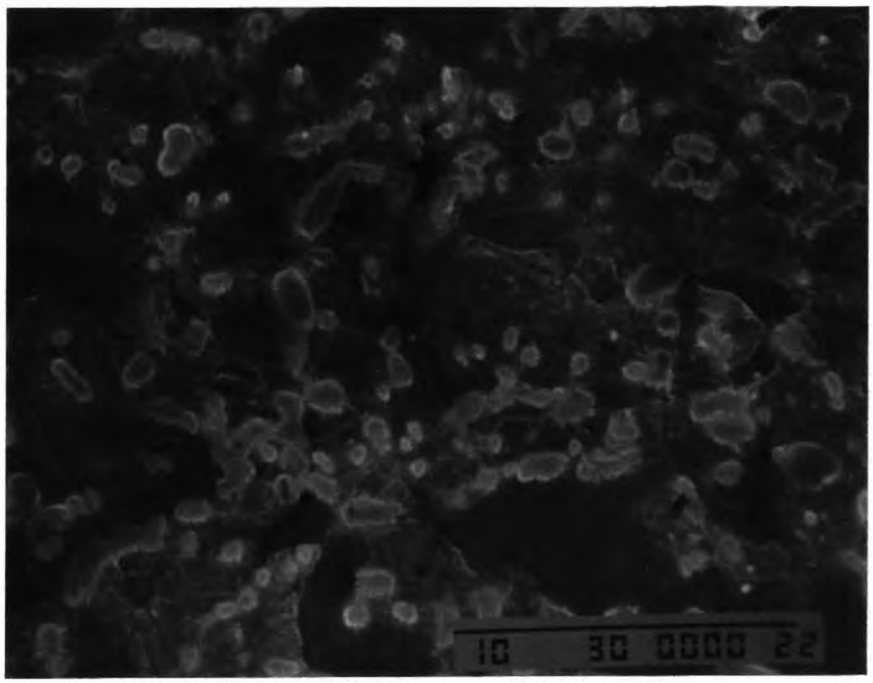

Fig. 5.37 Scanning electron micrograph showing partially transformed zone, surface melted En52

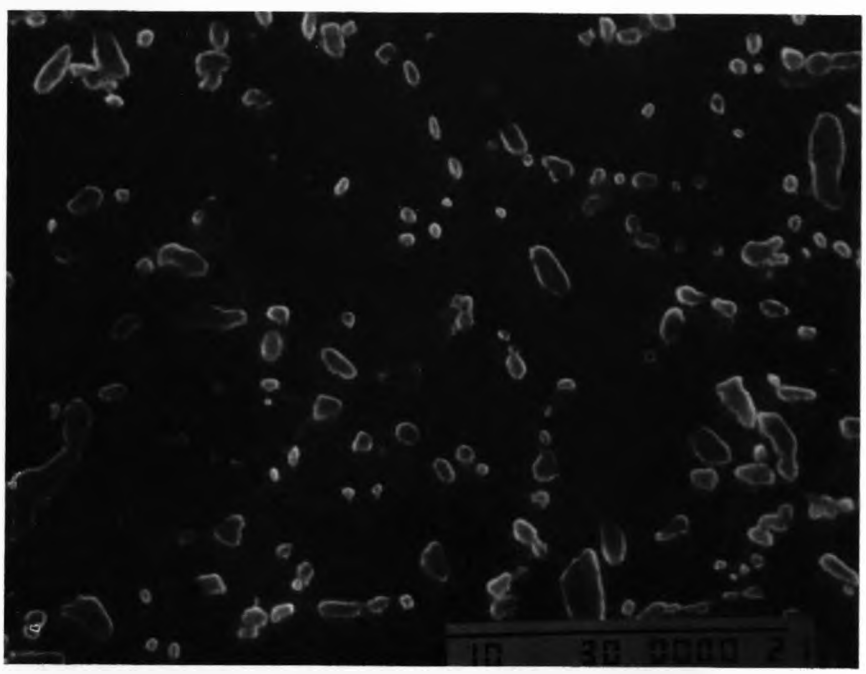

Fig. 5.38 Scanning electron micrograph showing partially transformed zone, surface melted En52

Wear Test Results - En24/AR & Conventional HT

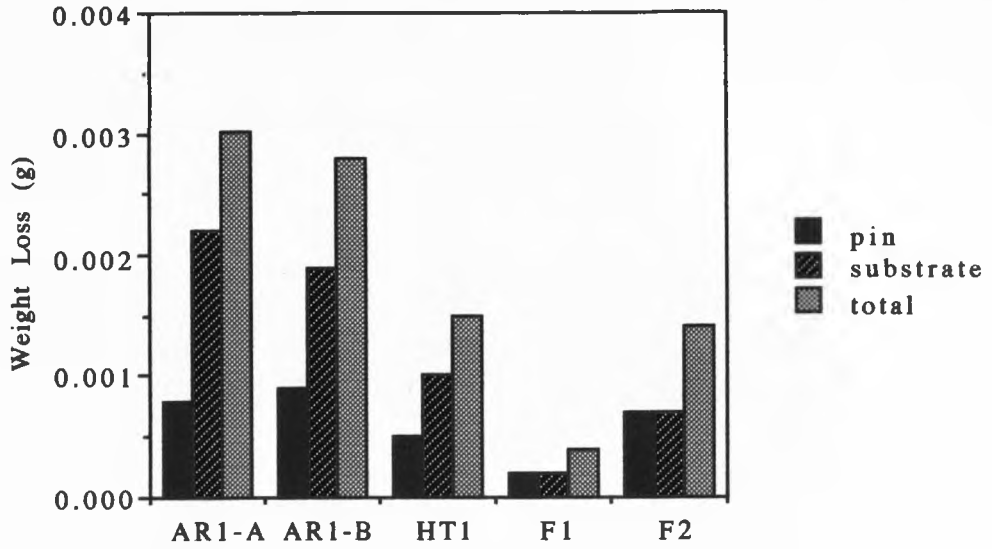

Wear Test Results - En24/Grit Blasted

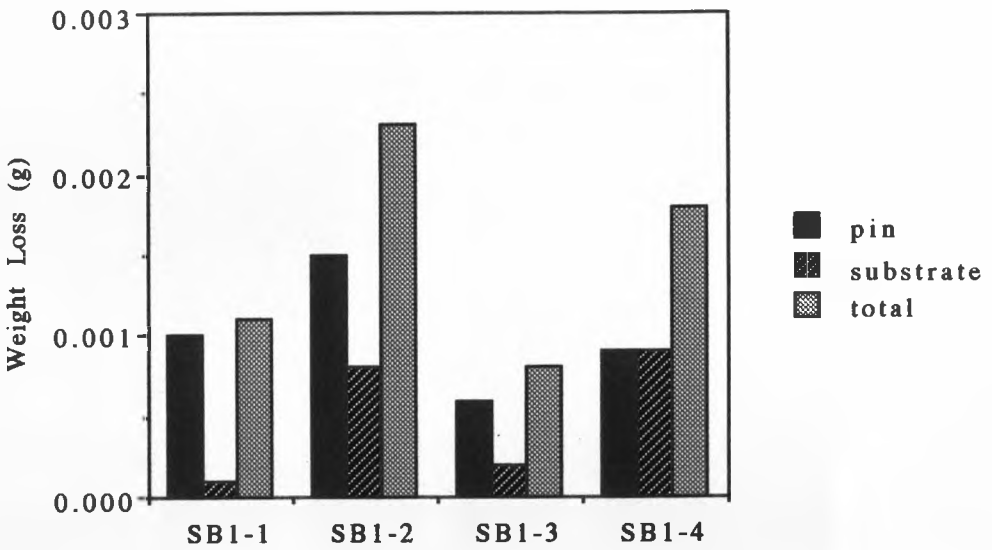

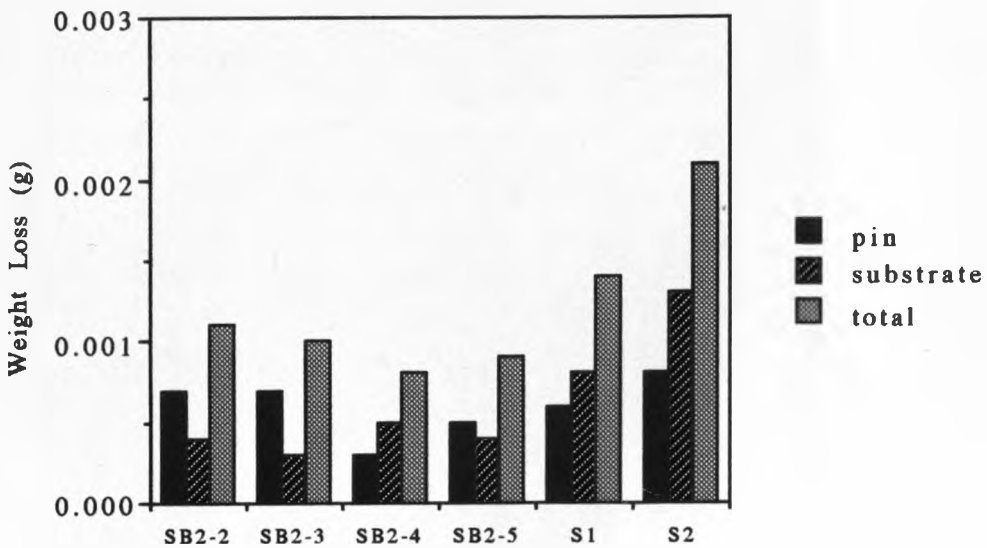

Wear Test Results - En24/DAG Coated 1

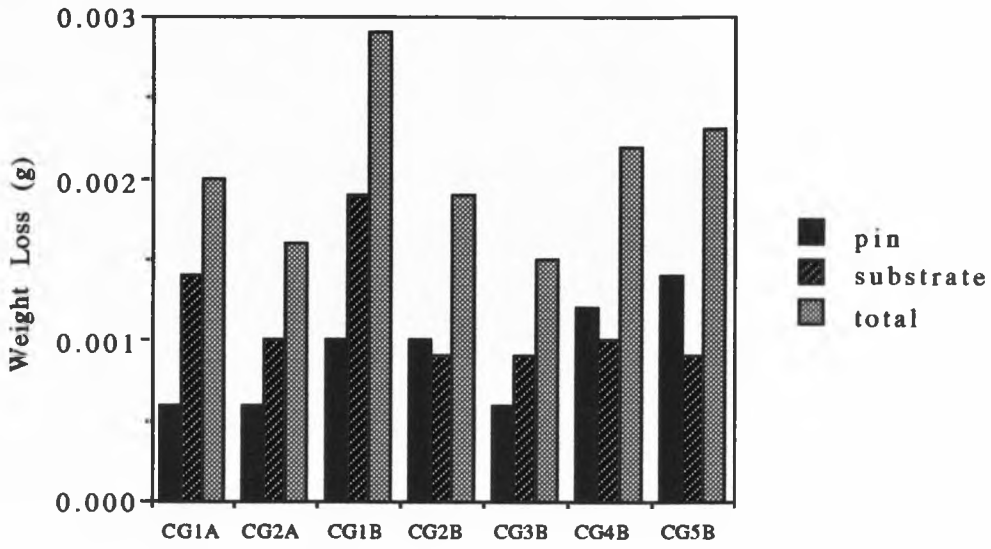

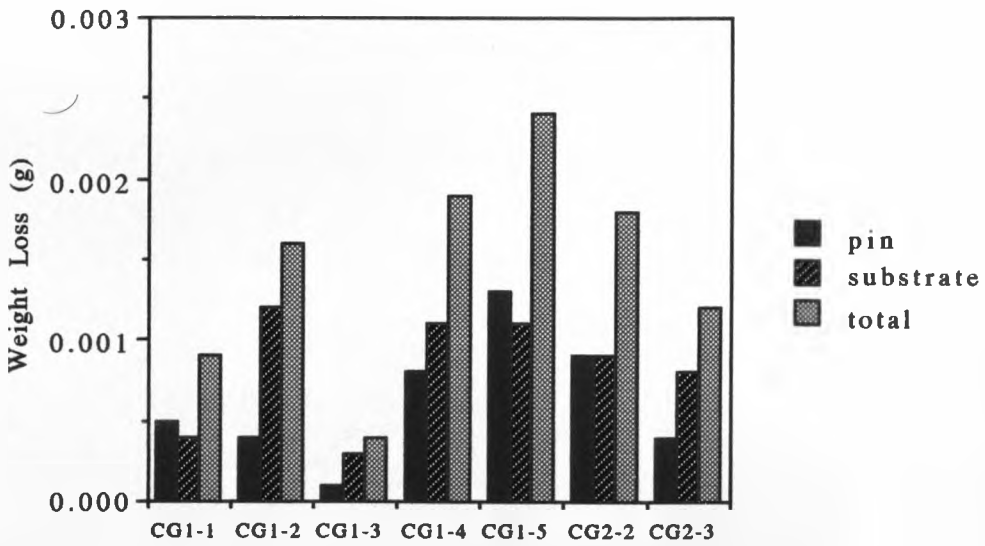

Wear Test Results - En24/Spray Painted

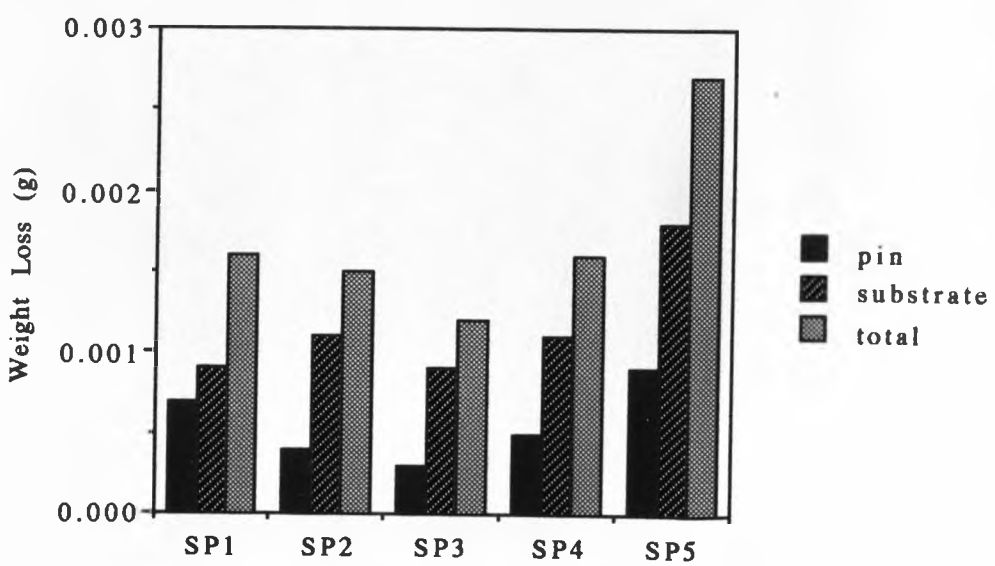

Wear Test Results - En24/1

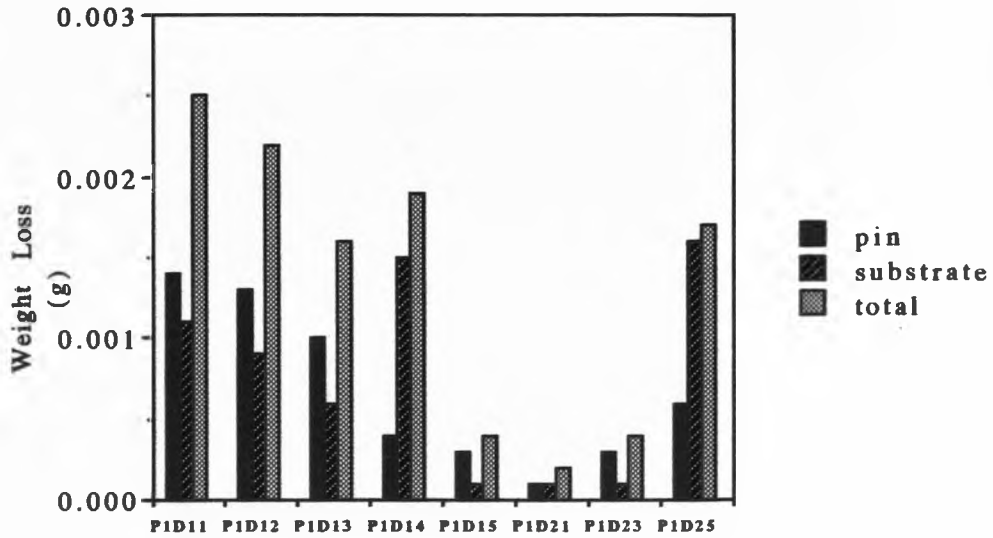

Wear Test Results - En24/2

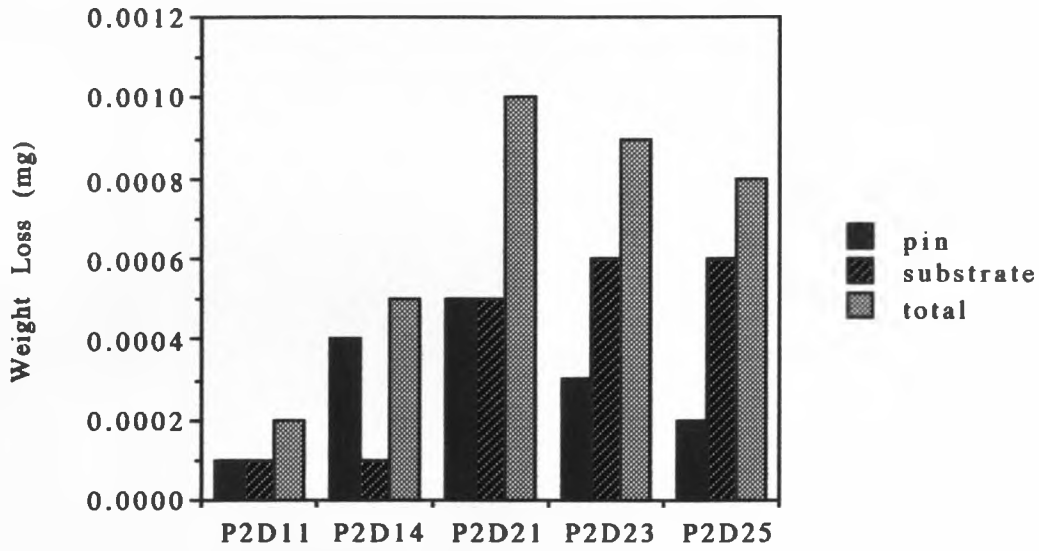

Wear Test Results - En24/3

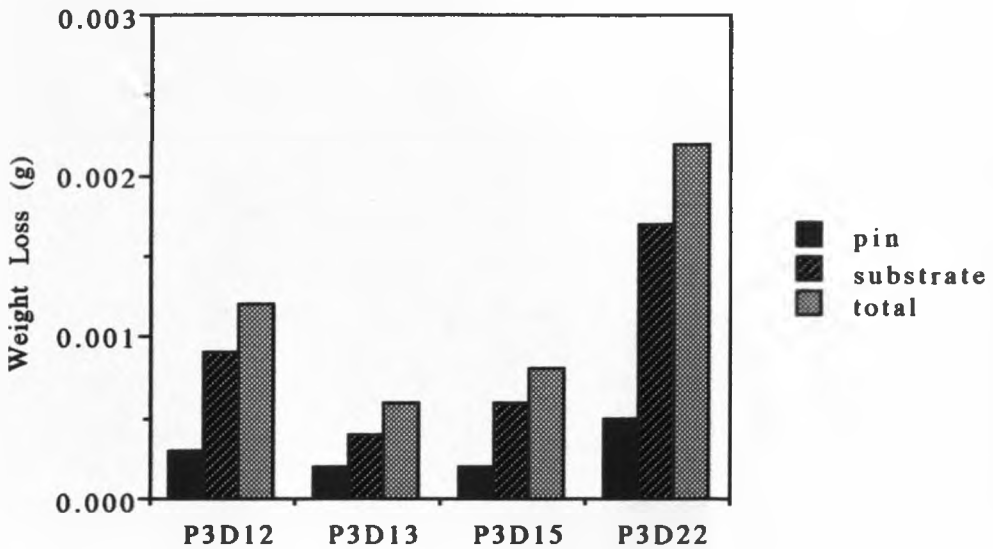

Wear Test Results - En24/Excimer Pre-treated

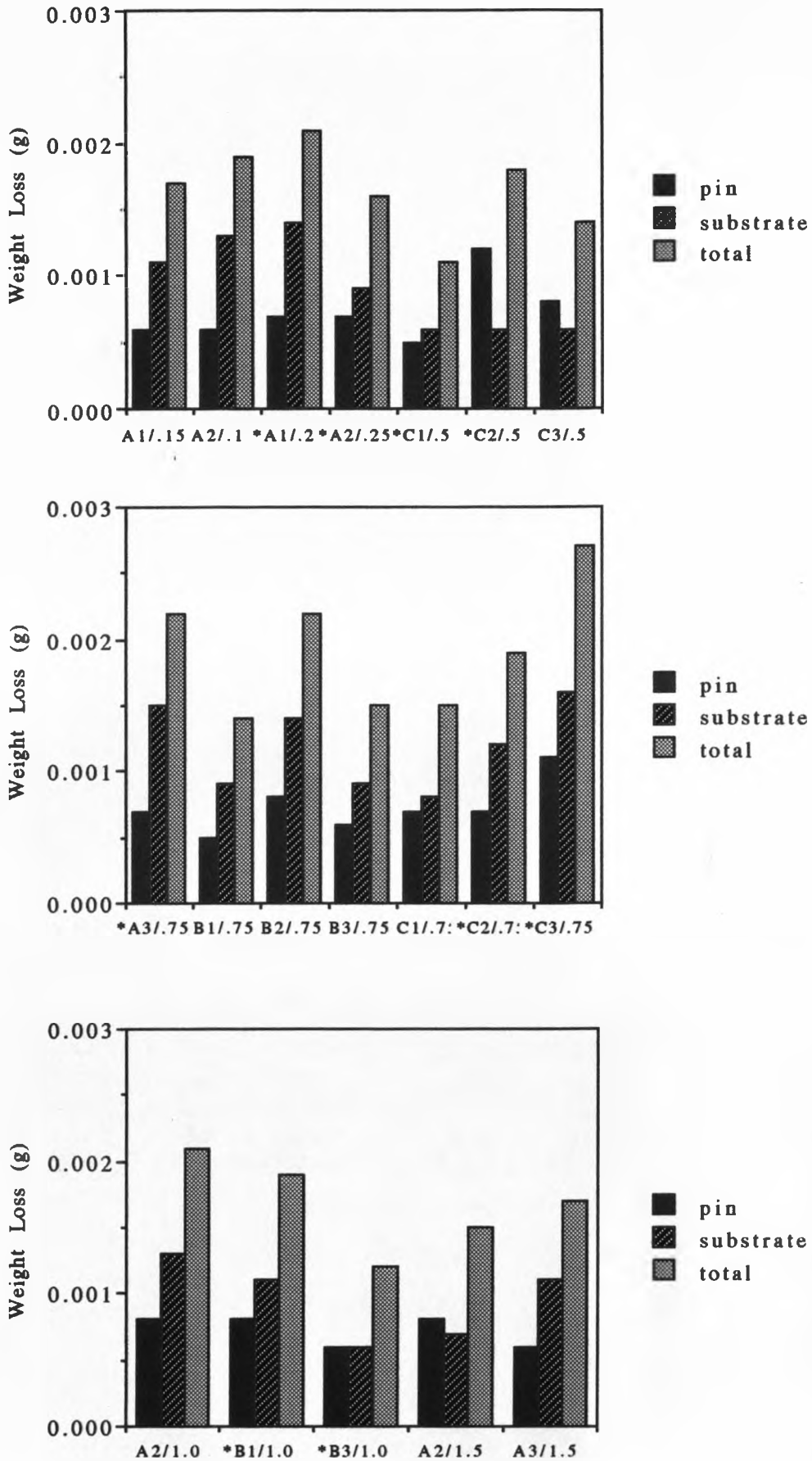

Wear Test Results - En52/AR & Conventional HT

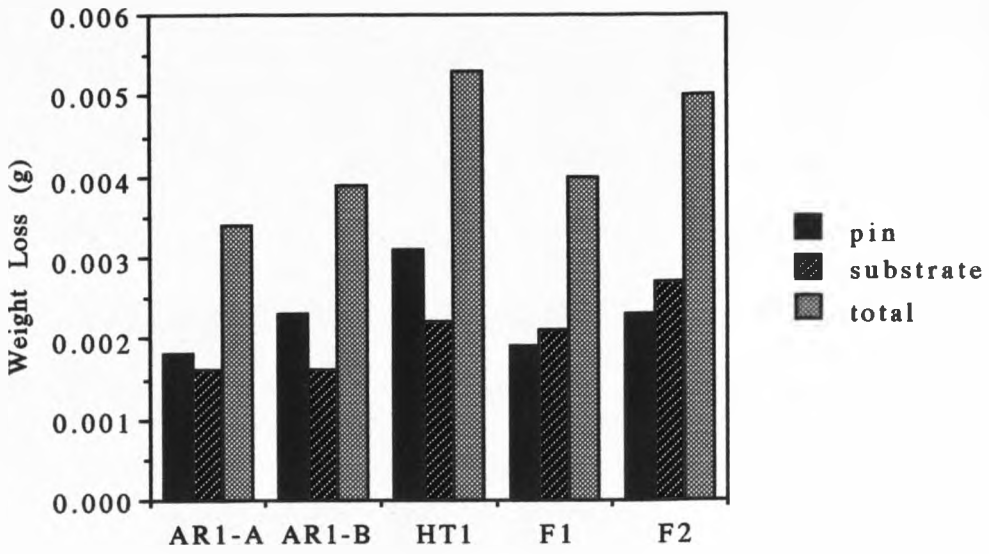

Wear test Results - En52/Grit blasted

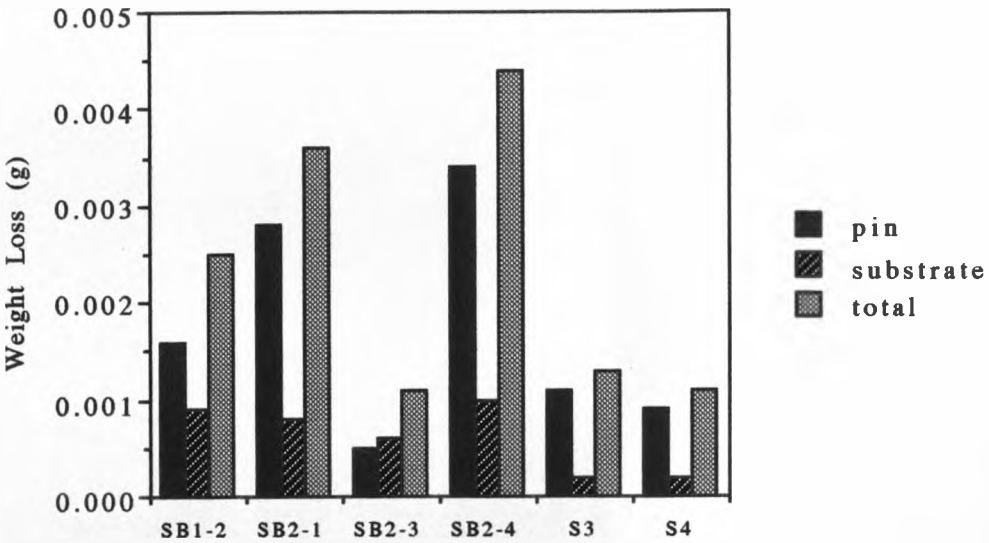

Wear Test Results - En52/DAG Coated

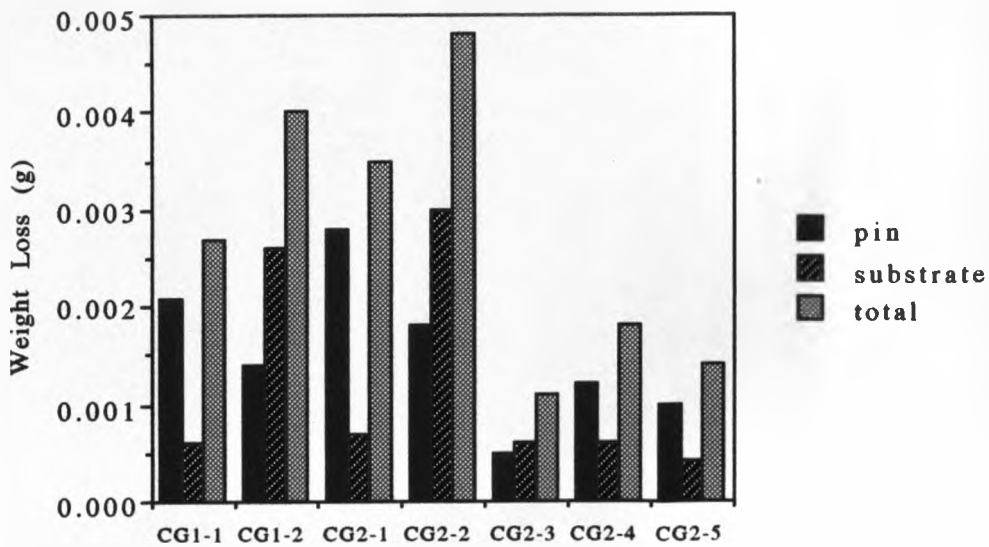

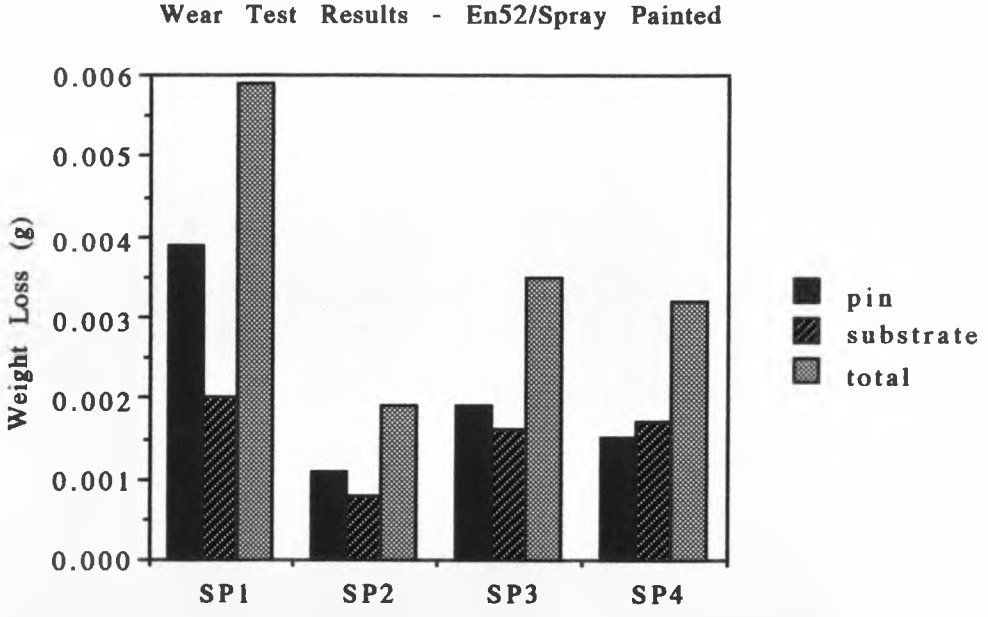
Wear Test Results - En52/Spray Painted
Weight Loss (g)
0.006
0.005
0.004
0.003
0.002
0.001
0.000
SP1
SP2
SP3
SP4
pin
substrate
total

Wear Test Results - En52/Excimer pre-treated

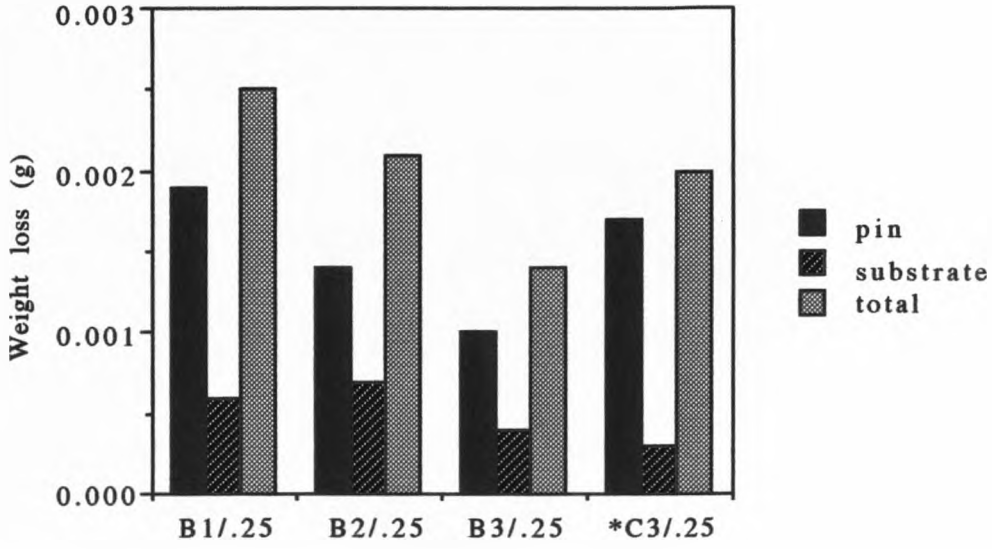

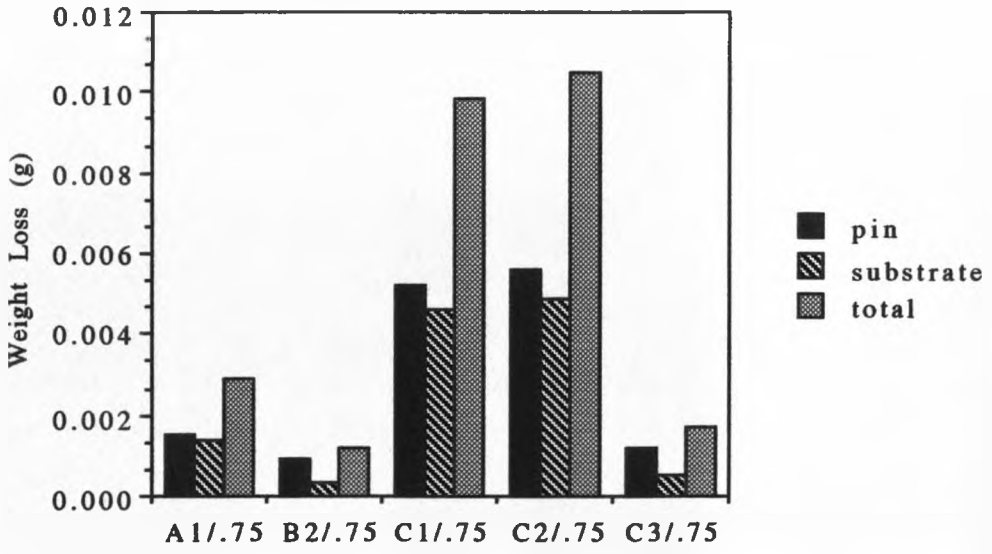

Wear Test Results - En52/Excimer Pre-treated

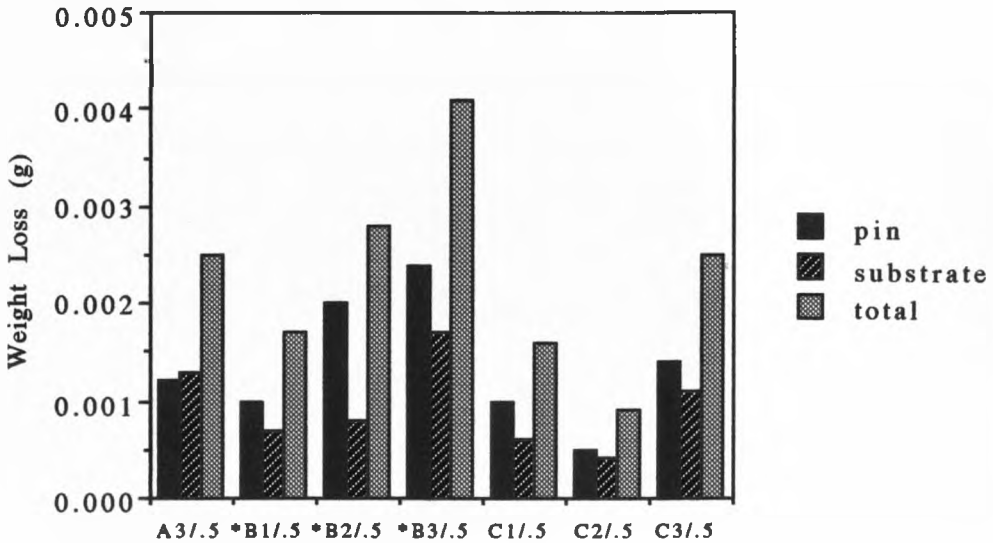

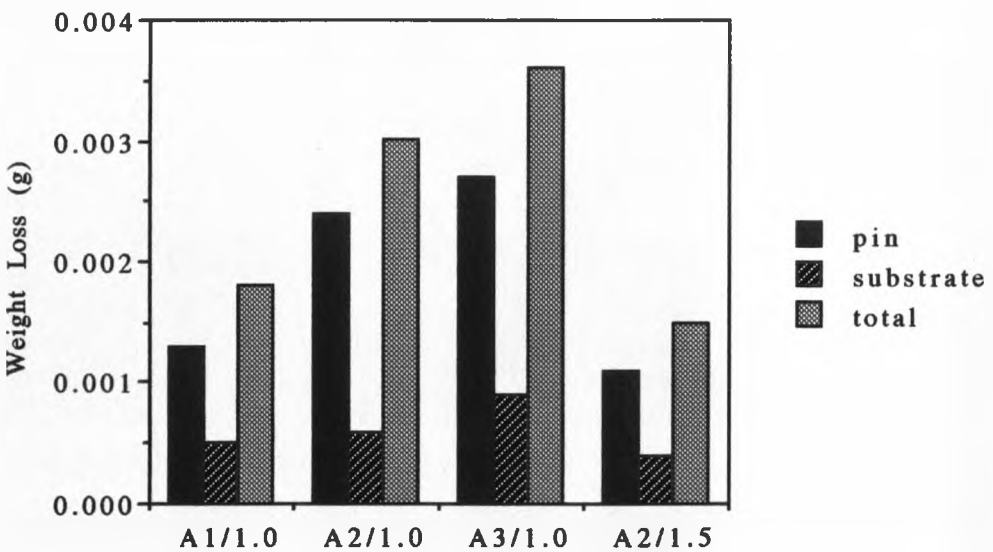

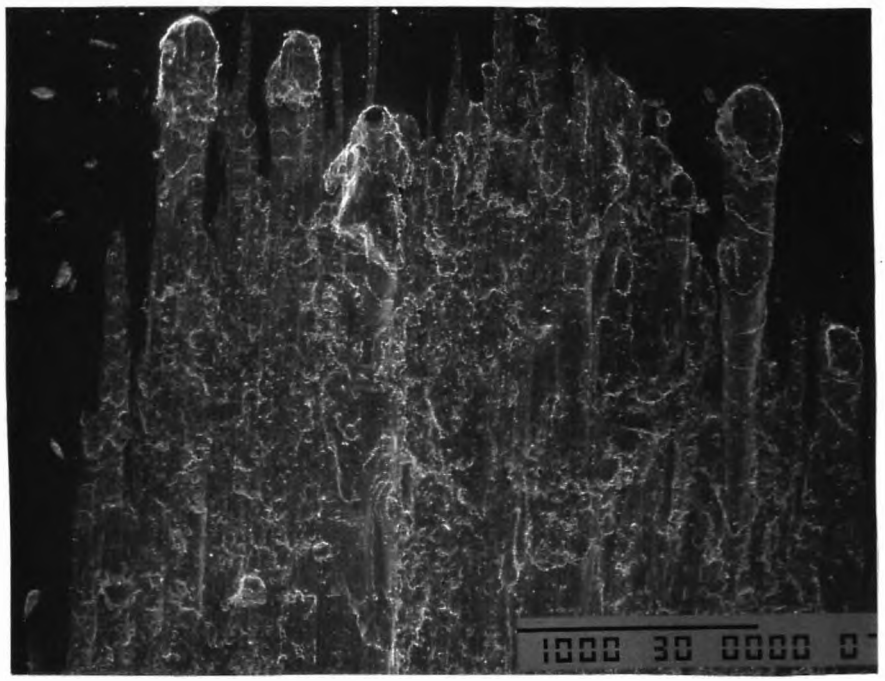

Fig. 5.50(a) Wear scar on substrate after only 2mins., stroke length 10mm
Sample=En24SB2-1

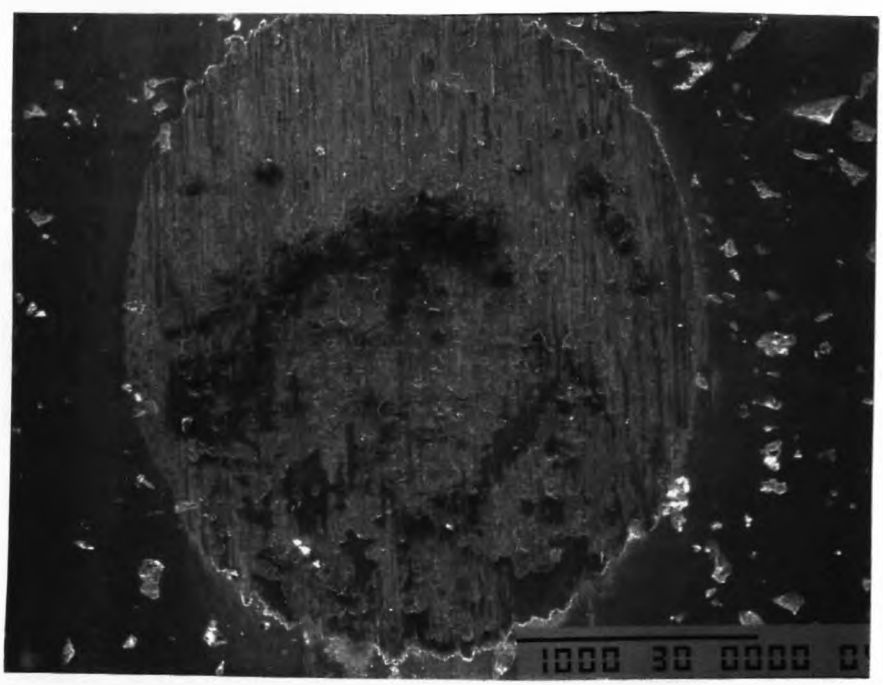

Fig. 5.50(b) Wear scar on substrate after BLWR test (2 hours).
Sample=En52SB1-1

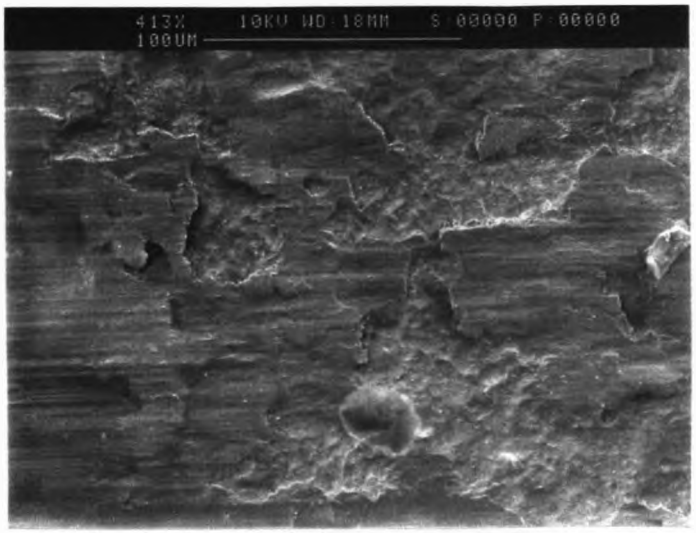

(a) En52
.5EX B3

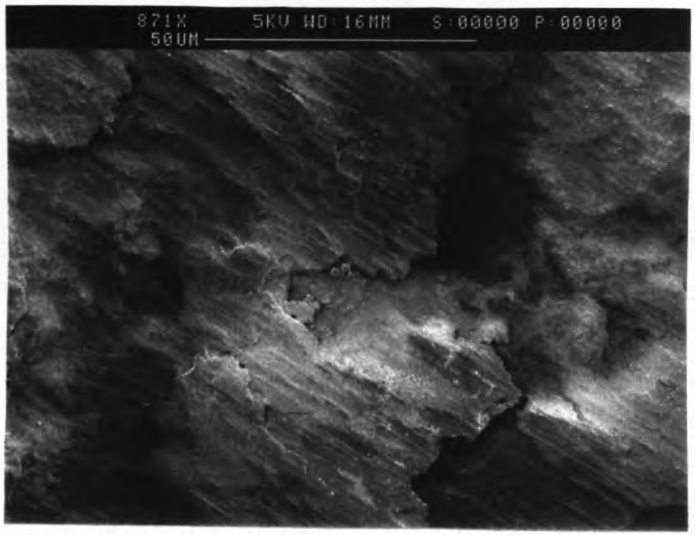

(b) En24
.25EX A2

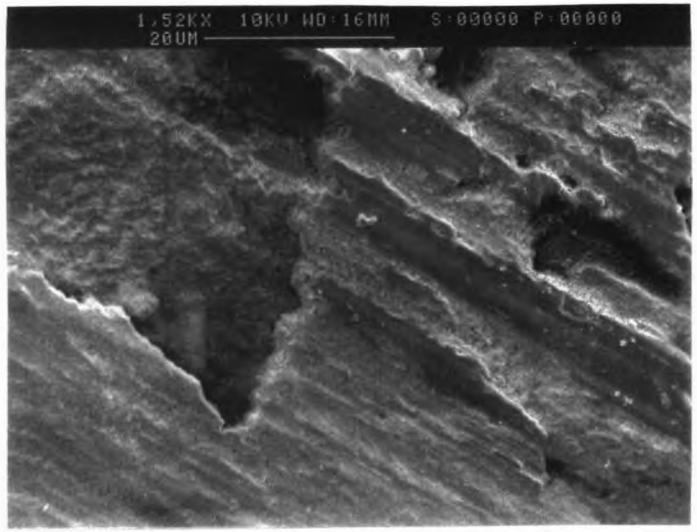

(c) En24
.25EX A2

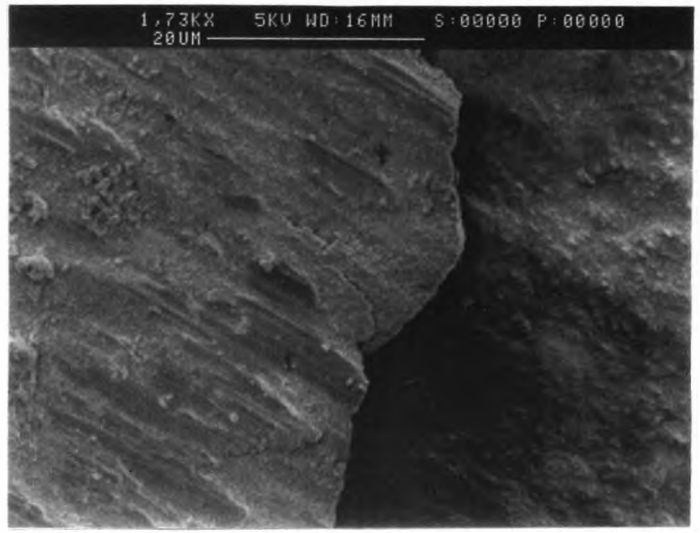

(d) En24
.25EX A2

Fig. 5.51(a)-(d) SEM micrographs showing wear scars observed on samples of En24/52 after BLWR testing

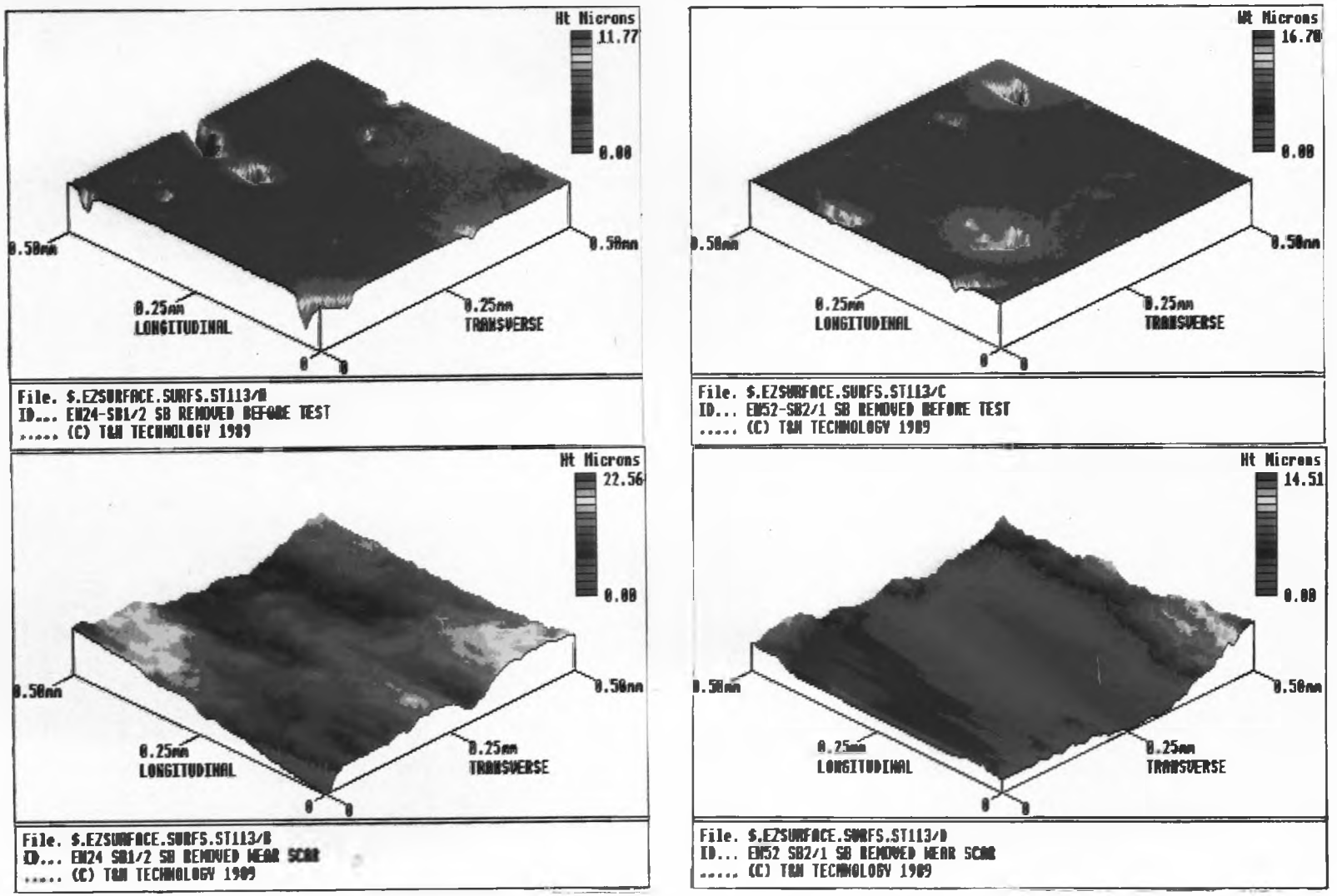

Fig. 5.52 (a)-(d) 3-D surface traces for samples En24 SB1-2 and En52 SB2-1 before and after BLWR testing, Ra values shown in brackets (a) En24 SB1-2 before test (0.29), (b) En24 SB1-2 after test (2.46), (c) En52 SB2-1 (0.31) and (d) En52 SB2-1 (1.91).

Scuff type test, duration=1440mins, temp.=15 C, speed=750rpm, load=8kg, gain=50, no lubrication. No. data points=500. Valve guide matl.=Alloy 48.					
	Valve Guide			Valve Stem	
Sample	Wt.Change (g)	Surface Finish (b/a)	Bore Diam. change/mm	Wt.Change (g)	Surface Finish
En24 En52	-0.018 -0.020	1.60/2.32 1.58/2.31	0.058 0.061	-0.014 -0.016	0.14/0.15 0.16/0.15
21-4N	-0.017	2.80/3.50	0.056	-0.014	0.13/0.14
Chrome plated	-0.006	2.80/3.20	0.001	0.000	0.16/0.15
En24 B	-0.003	1.580/1.175	0.002	-0.006	0.738/0.733
En24 C	-0.003	1.555/1.430	0.001	-0.005	0.757/0.781
En24 D	-0.002	1.482/1.048	0.000	-0.004	0.751/0.808
En24 E	-0.003	1.363/1.383	0.001	-0.004	0.907/0.840
En24 F	-0.001	1.412/1.127	0.000	-0.005	0.736/0.800
En24 G	-0.002	1.027/1.239	0.001	-0.006	1.031/0.784
En24 H	-0.004	1.293/1.497	0.001	-0.007	1.030/0.882
En24 I	-0.003	1.265/1.306	0.002	-0.006	0.834/0.750
En24 J	-0.002	1.849/1.591	0.001	-0.006	0.836/0.905
En52 3	-0.003	1.093/0.988	0.000	-0.007	0.473/0.388
En52 4	-0.001	1.404/1.327	0.002	+0.005	0.404/0.435
En52 5	-0.001	1.575/1.335	0.001	-0.004	0.456/0.481
En52 6	0.000	1.807/1.497	0.001	-0.006	0.550/0.652
En52 7	-0.001	1.337/1.453	0.000	-0.005	0.476/0.430
En52 8	-0.002	1.512/1.099	0.000	+0.006	0.550/0.430
En52 9	0.000	1.384/1.274	0.001	-0.006	0.451/0.575
En52 10	-0.001	1.396/1.271	0.001	-0.005	0.572/0.408
En52 11	-0.002	1.050/0.576	0.002	-0.002	0.428/0.393

Table 5.6 Wear test results - valve stem tests

CHAPTER 6

DISCUSSION

LASER TRANSFORMATION HARDENING

At first sight, the process of localised transformation hardening appears to be simply a matter of heating to the correct temperature to austenitise the steel without causing surface melting. However, on closer inspection, there are three inter-related conditions which must be met to achieve optimised successful hardening to a depth z:

(1) the penetration of the hardening isotherm must be deep enough to form austenite to the required depth z (and surface temperature must be $<T_m$)
(2) the cooling rate of the austenitised zone must be large enough to allow martensite formation
(3) the time spent above the austenitising temperature must be long enough to allow diffusion of carbon and/or alloying elements through the structure

Assuming that the temperature reached is sufficient for austenite formation, a certain critical cooling rate must be met (which depends upon the thermal properties of the steel in question). The effect of the cooling rate condition becomes more dominant with increasing interaction times as the bulk substrate tends to become hotter and therefore the thermal gradient decreases, decreasing the cooling rate. On the other hand, the time spent above the A_1 temperature becomes greater with decreasing interaction times which is advantageous for austenitisation. This factor is especially important in view of the high heating rates involved, and assumes even greater significance for coarse metallurgical microstructures where carbon has a longer molecular distance to travel.

Rapid heating rates, as are found in laser surface hardening are known to elevate the critical temperatures of a metal. The degree of elevation is not accurately known and a number of authors have conducted studies into this phenomenon (189) with various conclusions. However, the general opinion is that the A_3 line is displaced by at least 50-60K. The system then is far from equilibrium and conventionally determined CCT diagrams can be used as a guide only. The consequence of this critical temperature elevation is that a higher surface temperature is required to form austenite, with the melting temperature still acting as the physical limit.

Looking at this in respect of En24/52 steels, the critical cooling rate decreases with decreasing presence of carbide forming elements. Therefore, the cooling rate condition has a greater effect on En24. Similarly, the time spent above the A_1 temperature dominates for high alloy contents as a result of the slower rates of

diffusion of the carbide formers compared to carbon. This will be the limiting condition for En52.

The as-recieved microstructures of both En24 and En52 steels consist of spheroidised precipitates in a ferritic matrix. The structure in each case is very fine with the average distance between neighbouring precipitates lying in the range 0.1-10μm. This limits the molecular distances over which diffusing elements have to travel. Results of EDX, diffraction pattern analysis and XRD analysis show En24 precipitates are of the type $(Fe,Cr)_3C$ whilst those in En52 are $(Fe,Cr)_{23}C_6$. These results correspond with the predicted structures, found by Lundberg *et al* (100) and illustrated in the isothermal section of the Fe-C-Cr phase system at 873K, Fig. 6.1. A second section, Fig.6.2 shows that at 1273K, both steels should lie fully in the γ phase field.

The results presented illustrate the change in microstructure occurring as a result of laser transformation hardening. It is possible in the case of En24 to fully transform the surface layer of the steel to the harder and more wear resistant martensitic structure. However, for En52, the relatively high chromium content makes complete transformation to martensite very difficult. Complete dissolution of the carbide phase - and hence 100% transformation - requires a longer time at high temperature, i.e. a long interaction time (slow traverse speed) as a result of the slower diffusion rate of chromium in austenite compared with that of carbon. In the case of En52, the intra-granular precipitates tend to dissolve whilst those at grain boundaries are observed to coarsen initially, probably due to agglomeration. Successful hardening does occur but usually without complete carbide dissolution, i.e. a martensitic layer containing undissolved carbides. The effect of increasing chromium content on the steel is to increase the A_1 temperature and to decrease the eutectoid carbon content (see Fig. 6.3 (187). Therefore, the hardness of the martensite formed should be lower for En52, according to Fig. 6.4. The experimental results indicate that very similar maximum hardness values for the two steels. However, under the same treatment cycle, En24 attains a level of hardness of the order of 50 units greater than En52 on the Vickers scale.

In order to fully understand the microstructural changes taking place in the steels, it is necessary to examine the thermal cycles of the samples with a knowledge of their respective phase and CCT diagrams.

As reported in Chapter 5, the laser heated area consists of two distinct zones. The depths of hardness quoted refer to the depth to which the microstructure has been affected by the treatment (depth of lower zone). This corresponds to that point on the hardness/depth curve where the hardness value returns to that of the base material. The upper zone represents the depth to which complete austenitisation occurs and this region generally transforms to a fully martensitic structure on cooling. The microstructures noted are similar in character to those observed by Mulot and Badeau (188,135).

One can understand the nature of the phase changes occurring by looking at the temperature/time profiles of heat treated samples and comparing the calculated temperature history of a particular point with the microstructure observed. For the purposes of such calculations, the following equation has been used to calculate the temperature at depth z, below the centre of the beam as a function of time (180, 182):

$$T(z,t) = \frac{\frac{A\,q}{v}}{2\,\pi\,\lambda\,[t(t + t_o)]^{0.5}} \cdot \exp - \left[\frac{(z + z_o)^2}{4\,a\,t}\right] \qquad (6.1)$$

As previously explained (Chapter 3), z_o is the distance over which heat diffuses during the interaction time and t_o is the time taken for the heat to diffuse over a distance equivalent to the beam radius. z_o was estimated using the Shercliff and Ashby near-field solution ($z<r_B$). For each steel, the depth of the two measured zones in the heat affected layer produced under similar conditions were calculated. The calculations were based on the measured values of absorptivity given in Table 5.2. The resultant temperature profiles are plotted in Fig. 6.5-6.7.

For En52, Fig. 6.5 illustrates the critical thermal cycle for a specimen of En52 steel treated at 20mm/s. The measured depths of the upper and lower zones are 0.28mm and 0.63mm repectively. One would expect therefore that all of the area above 0.63mm depth was heated above the austenitisation temperature of the steel. The peak temperature calculated at this depth was 800^{o}C. At a distance 0.28mm below the surface the peak temperature reached was 1220^{o}C. All of the material above this depth had transformed to martensite with some undissolved grain boundary carbides. In the lower zone, the microstructure consisted of untransformed ferrite and undissolved carbides surrounded by martensite. Similarly, Fig. 6.6 shows a second sample of En52 treated with a longer interaction time (v=14mm/s). In this case the calculated temperature 0.31mm below the surface was >2000^{o}C and was around 900^{o}C 0.81mm below the surface. This corresponds with experimentally determined depths, but the depths are slightly larger in all cases than one would expect from the thermal cycles calculated (see below).

For En24, Fig.6.7, the observed depth of the upper zone at 0.3mm corresponds to the temperature 1120^{o}C, which is in accordance with the expected elevation in the A_1 temperature of the steel. Also, the depth of the lower zone of the HAZ in this case is recorded at 0.75mm. This is deeper than suggested by the calculated thermal profila since the peak temperature reached at this depth is around 660^{o}C. This is probably an effect of the finite specimen size which tends to increase the case depths possible for a given treatment, assuming conditions are such that self-quenching can still occur.

The thermal cycle produces structural changes, as discussed in Chapter 2. Certain of which are controlled by diffusion. Transformation of ferrite/carbide structures to austenite occurs by heterogeneous nucleation, initiated at carbide particles within the structure according to the literature (111, 113, 118). The fact that this is indeed the case is borne out by Fig. 6.8, which illustrates the transformed regions 120μm below the surface in a laser treated sample of En52. It is obvious from this micrograph that the regions immediately surrounding the carbide particles have begun to transform whilst regions clearly within the grains have not. There is no evidence to suggest that nucleation sites occur on the network of smaller intragranular precipitates in En52 steel, an observation which is in agreement with Paxton (109) who also found that these carbides had little effect as austenite nuclei. The constituents of this region are untransformed ferrite and undissolved carbides surrounded by austenitised regions which have transformed to martensite on cooling. These grain boundary carbide nucleation sites are the sites which increase the free energy of the material to a greater extent and which are therefore preferred. The free energy change for heterogeneous nucleation is given by equation (6.1) (190):

$$\Delta G_{het} = - V (\Delta G_v - \Delta G_s) + A_\gamma - \Delta G_d \qquad (6.2)$$

Where ΔG_d is the free energy released on creation of a nucleus. This free energy is able to reduce or possibly remove the activation energy barrier. The shape of the resulting embryo will be such that it minimises the total interfacial energy. In the case of En24/52, the structure of spheroidal precipitates in a matrix of α means that the minimum interfacial energy is observed when the austenite embryo forms a shell around the precipitates (109). These observations are substantiated by this work. In the case of the two steels studied, the distance between the carbide particles is small and an austenite shell formed around a particular carbide tends to engulf other particles before the central carbide has fully dissolved, this can also be seen in Fig. 6.8 (previous). The austenite region then proceeds to grow until it impinges upon another austenite region. For spheroidal cementite steels, the following equilibrium probably exists (118):

$$\alpha + \text{cementite} \rightarrow \gamma(\text{equil.}\alpha) + \text{cementite}$$

Where at some distance from the α/γ interface, a second reaction occurs as the remainder of the precipitates dissolve:

$$\gamma(\text{equil.}\alpha) + \text{cementite} \rightarrow \gamma(\text{high C})$$

Similarly, if the temperature is raised sufficiently (as one might expect in LTH), the α phase may transform without simultaneous precipitate dissolution and dissolution will then occur in a γ matrix. i.e.

$$\gamma(\text{low C}) + \text{cementite} \rightarrow \gamma(\text{high C})$$

Whereby the decrease in size of the precipitates and the corresponding increase in carbon content of the matrix is a measure of the progression of the reaction. Obviously, since the phase transformation is diffusion controlled, the subsequent growth of the austenite nuclei is determined by the diffusion distances and rates involved. The above equations may apply equally well to the two steels, although the precipitates in En52 are $(Cr, Fe)_{23}C_6$ rather than cementite. A full analysis of austenite nucleation and growth in spheroidised cementite/ferrite steels was performed by Hillert (118) who showed that the rate of reaction is governed by the rate of diffusion of carbon. The presence of alloying elements is known both to inhibit the nucleation of austenite (116) and to cause diffusion of the carbide forming element (Cr in this case) to become rate controlling, an effect which is much larger for En52 than for En24. The rate of diffusion of Cr in austenite much slower than for carbon, which partly explains the observed need for longer interaction times for En52, to dissolve the precipitates. In addition, Beswick (121) also noted that the ferrite-austenite transformation required higher temperatures in the presence of chromium as an alloying element.

That En52 is much more resistant to 100% transformation to martensite than En24 (complete carbide dissolution) can therefore be explained by the increased chromium content. The rate of diffusion for chromium containing steels is thought to be dependent upon the rate of chromium diffusion from the carbide-matrix interface.(109, 121). The experiments reported in this work further support the theory that the increased chromium content slows down the dissolution rate of the carbide phase significantly. En24 becomes fully martensitic at much lower interaction times than does En52. The rate of diffusion of Cr in austenite is slow compared to carbon and this is another important factor in the transformation. The presence of undissolved carbides in the martensitic zone indicates that the martensite formed is lower in carbon and will possibly be less hard than expected. The characteristic high heating rates encountered with LTH can causes problems in this respect. Krauss (104) reports lower strength and hardness in this mixed layer of martensite and partially dissolved carbides. Plots of hardness versus depth for En24/52 steels however, do not indicate any decrease in the surface hardness of treated En52 where values >700HV_{10} were noted.

The above outlines the transformation to austenite occurring during rapid heating. The other important factor in terms of rapid heating is the cooling cycle and the effect of chromium on the formation of martensite. The martensite reaction is a diffusionless shear process. The hardness of the martensitic layer is dependent upon the cooling rate. Relating the experimental conditions to the CCT diagrams for En52/24, as shown in Fig. 6.9 (a) and (b), one observes that the critical cooling rate for martensite formation in En24 must exceed 300^{o}C/min whilst for En52 the rate must exceed 100^{o}C/min. This verifies the observation that the optimum conditions

for LTH of En24 are high power density and high traverse speed which provide this enhanced thermal gradient for rapid self-quenching. Cooling rates below those stated will lead to the formation of phases other than martensite and will limit the strength and wear resistance of the layer. Experimental determination of the cooling rate in samples of each steel were conducted at a distance 1mm below the surface. The rates are representative of the near-surface region since the cooling rates in the critical cooling period decrease only marginally with depth (23). Another effect of the increased chromium content in En52 is the lowering of the martensite start temperature (180^{o}C in En52 cf 300^{o}C in En24) such that it is easier to self-quench to martensite for En24.

Relating the cooling rate information from Fig. 6.5-6.7 and from calculated peak temperatures at 1mm below the surface (section 5.2.2), at the surface of En52, the cooling rates are >2500^{o}C/s, even at depths up to 0.8mm below the surface and for longer interaction times, the cooling rate remains high enough to enable martensite formation. In the case of En24, the cooling rate 0.75mm below the surface (Fig. 6.7) is around 800^{o}C/s and this is a fairly average interaction time. So, for the interaction times studied for the two steels , none are such that self-quenching is prohibitive to the formation of martensite.

In cases where surface melting occurs, the four zone microstructure outlined in Chapter 5 exists, this is illustrated schematically in Fig.6.10. Occurrence of retained austenite in laser hardened zones is common, especially as the peak processing temperature is increased (187). However, it is possible that the occurrence of the 'white' layers in En52, when surface melting occurs is due to the formation of a configurationally frozen metastable structure. Similar areas were seen by Bury (191), Ramous *et al* (192) and Turnbull (193). The presence of such a phase is due to the formation of metastable states on quenching, in which, mobility is high. The structure then becomes frozen into the intermediate state. Ramous *et al* (192) report high hardness of this layer. This was found in the case of En52, however, the microstructural scale was too fine to allow accurate resolution of the phase. SEM micrographs in Fig. 6.11 (a) and (b) illustrate the occurrence of the white layer in a surface melted sample of En52. One further possibility is that such layers contain retained austenite which is softer than the surrounding zones and may be detrimental to the overall mechanical properties.The mechanism of formation of such layers is thought to be a result of carbon diffusion from the melt to stabilise austenite and the high thermal gradients encountered. However, a full investigation of surface melting is not the subject of this study. The results in this case only show occurrence of the white phase when surface melting does not occur for a limited number of samples which have been processed at high energy density. Palombarini *et al* (125) found that the retained austenite layers are stabilised by diffusion of carbon into the melt zone from coatings applied to improve absorptivity. This does not seem to be the case here since such 'white' layers are present in grit-blasted samples as well as the samples coated with carbon rich layers. In summary, for the

DAG coatings, the specific energy must be <30J/mm^2 to prevent melting in En52 and must be <20J/mm^2 for En24. Interaction times for hardening also vary with the surface characteristics, but in general, En24 requires about 2/3 the interaction time for hardening that En52 does.

An important consequence of the starting structures studied here, which have previously not been fully investigated, is the uniformity of hardness of the laser hardened surface which is far superior to that obtained from the more coarse ferrite/pearlite starting structures investigated by Bradley and Kim (122, 123) and numerous others. This is advantageous in terms of the wear resistance of the surface and indicates a high degree of homogeneity. The variation in microhardness across a typical surface hardened layer in En24 was <5HV (200g) and for En52 slightly higher at <10HV (200g). This is somewhat more even than the layers observed in ferrite/pearlite steels and is thought to be due to the more uniform distribution of small carbide particles, which limits the diffusion distances. Other authors (194) have found that initial microstructure has minimal effect on the case depth but does change the homogeneity of the HAZ, as discussed above. The dependence of case depth on interaction time is similar to that observed by Ruiz *et al* and Bell (18).

The results of LTH of En24/52 valve steels confirm that ground steel surfaces exhibit extremely poor absorption characteristics to 10.6μm radiation, as observed by numerous authors. Tracks made on untreated steel surfaces were very narrow and non-uniform with unsatisfactory results. As the results indicate, substantial improvements were brought about by the use of surface coatings, certain of which are more practical than others. Grit blasting the surface improved the absorptivity from <10% to >50% and resulted in a highly uniform coating and thus consistent experimental results. However, in practice the use of such a pretreatment would probably negate some of the major advantages offered by laser hardening. Two additional steps in the manufacturing process are necessary, firstly to apply the treatment and secondly to remove it to leave a smooth surface. Excimer roughening of the surface is similarly complicated although the results are very encouraging. In situ roughening followed by LTH is an attractive proposition which should be explored. Of the remaining coatings investigated, DAG colloidal graphite offers the best solution. It is easy to apply, effective in improving absorptivity, repeatable and durable - as opposed to oxy-acetylene applied coatings which are easily dislodged during experimental set-up.

Multiple pass experiments to produce patterned hardness along valve stems were extremely successful. The jig designed to provide gas-assisted cooling and therefore limit the cumulative temperature rise during processing proved highly effective, preventing melting in all cases. Highly uniform hardened zones were produced along the bars with the exception of the first rotation whilst uniform traverse speed was reached. The hardness profiles of the two steels indicate that backtempering does occur with multiple pass treatment, in agreement with Bell, Steen and

Sandven. This phenomenon occurs via lateral heat flow from the laser beam which raises the temperature of the previously hardened region causing backtempering. This effect increases with decreasing traverse speed for both En24 and En52 as might be expected. Sandven found that this problem could never be entirely eliminated, even with external heat sinks and cooling. The backtempering effect is much worse for En24 (hardness decreasing by around 200HV_{10} in the overlap zone). Again, this is a function of the alloy content, the presence of chromium retarding the rate of softening by carbide formation (88). En52 exhibits a very minor degree of backtempering, the hardness decreasing in the overlap zone by around 30HV_{10}. This is clearly indicated in Fig. 5.15, where the respective hardness profiles for the two steels are shown. This suggests that by changing the alloy composition of the steel used, the extent of backtempering can be changed, to minimise the effect to something of the order of a 10% variation in hardness. This result is of importance and may be helpful criterion for materials engineers selecting steels for a heat treatment process.

The backtempering effect may be used to the advantage of the manufacturer in cases where patterned hardening is beneficial. This may indeed be the case for the diesel engine exhaust valve if third bodies are part of the reciprocating system. The soft zones on the surface may form a place where the third body particles can become embedded preventing further abrasion.

Comparison of experimental results with the models discussed in chapter 3 shows that the Courtney (34) empirical model is a poor fit for the experimental data, as shown in Fig. 6.12. This is in agreement with Sharp's (24) observations on this model.

However, the results for LTH using grit-blasted and DAG colloidal graphite coatings do fit fairly well with the Shercliff and Ashby (180) model for predicting case depths. Fig. 6.13 (a)-(d) shows the comparison of measured case depth and that calculated theoretically for samples of each steel with grit-blasted and DAG colloidal graphite coated surfaces. The scatter observed in the results is greater for the DAG coated specimens in each case. Furthermore, there is generally better agreement between the results for grit blasted samples and the model calculations. To determine why this might be so, one must examine the assumptions on which the model is based. These are as follows:

(1) Surface absorptivity is constant
(2) All absorbed energy goes into raising the temperature of the material with negligible latent heat of transformation
(3) Thermal conductivity and diffusivity are constant
(4) Eutectoid transformation, A_1, is as given by phase diagram
(5) Solid is large enough that its bulk temperature is unchanged

It should be noted that in the Shercliff and Ashby model (180), experimentally determined absorptivities were used. Assumptions (2) and (3) are believed to be true for the situation in question, as the effects are small enough to be considered negligible. Surface absorptivity is known to change with time and the assumption of constant absorptivity is likely to be less applicable for the DAG coated specimens where the coating is sometimes observed to burn under the laser beam - this is thought to account for both the increased scatter in the results. In addition, the beam is never truly Gaussian and the uniformity of the coating thickness cannot be guaranteed which further exacerbates the problem of assuming a constant value for absorptivity. The assumption that the eutectoid temperature, as given by the phase diagram, corresponds to the transformation onset is not correct. The elevation of such a critical temperature has already been discussed, but this is likely to have only a minor effect on the reliability of the model. Finally, and probably of greatest significance for the components in this study, is the assumption that the solid is large enough that its bulk temperature is unchanged. This assumption cannot be regarded as accurate as the bulk samples do not remain at ambient temperature during the treatment cycle, a condition which is worsened with increasing interaction times. Even the presence of external heat sinks such as a contacting metallic bed and external gas cooling jet do not prevent the samples from heating up.

When one considers the finite difference model, similar assumptions apply. Absorptivity is assumed to be constant up to the melting point and again a semi-infinite substrate is assumed. An important point to note is the large difference in thermal properties of the two steels under consideration. The thermal conductivity of En52 is half that of En24 (see Table 3.1), useful data can be generated from the model for the different steels as this property affects the resultant temperature profiles significantly, thereby indicating that the model is applicable and sensitive to changes in the material properties and therefore its compostion. The results of the model compare very favourably with experiment, in terms of depth of hardening and depth of penetration of the A_1 isotherm. The modifications to the model to provide colour 3-D plots of the heat flow is extremely useful for interpretation and allows the depth of treatment, depth of penetration of a particular isotherm and size of the HAZ to be read at a glance. Using this type of output, one finds that the model does not reach steady state until 2000 iterations are requested. This value is used for all subsequent plots.

A plot of the data generated from the model overlayed onto the Shercliff and Ashby master plot (Fig. 6.14) shows that the values calculated for constant power do lie along the predicted isotherm shapes for q*, although the values of q* and the onset of melting line are slightly shifted due to the fact that actual En24 parameters were used in the F.D. model. The typical heat flow pattern in the x-axis of the bar is illustrated in Fig. 6.15 for the surface of the plot shown and at a distance 1mm below the surface. The effect of changing the boundary in the y-direction, from conductive to convective/radiative heat transfer on the heat flow pattern is illustrated in Fig.

6.16, for the same parameters as in the semi-infinite case. As shown, the peak temperatures reached at the surface are almost identical. However, 1mm below the surface, the penetration of the 1000K isotherm is shorter in the x-direction. Examining the 3-D figures, for the semi-infinite case, the back face (y-boundary) remains close to ambient temperature whilst for the convective boundary condition (CBCC) it reaches 1000K. The heat flow in the sample changes markedly when the boundary condition is altered. This observation fits more closely with the experimental observations whereby the sample becomes too hot too touch for a number of seconds after treatment and will emphasise the need for a rapid quench to form martensite at the surface as the bulk sample is much less effective as a heat sink than one might expect. The results from model runs at the same conditions plotted in Fig. 6.14 using the CBCC model show increases in the value of z^*, the dimensionless case depth, as shown. This means that for conditions which the model predicts a surface temperature >1800K (e.g. Fig.6.17(a)), where surface hardening without melting would be expected, the heat flow pattern is such that the temperature of the bulk sample rises, heat dissipation by conduction is less efficient, and a much larger region under the beam spot reaches the peak temperature. Although this is desirable in terms of uniform hardening, the finite sample size lowers the thermal gradient within the heated region making rapid quenching more difficult (Fig. 6.17(b)).

To summarise then, the mathematical models examined here represent the experimental conditions to a greater or lesser degree. The simple empirical Courtney model, although reasonably representative at low power (large d) becomes less accurate with increasing magnitude of $q/\sqrt{(dv)}$. The Shercliff master plot shows the correct shapes of lines for z^* vs v^* for constant values of q^* but the onset of melting line is shifted for En24 and the whole plot is effectively transposed to the right (higher q^*) compared to the master plot. The numerical model also gives a rough estimate of the predicted case depth which is slightly closer to the real case than the analytical model. However, the effect of having a small sample size means that the results could be more accurately represented by changing the boundary conditions of the model to allow for convection and radiation in the y-direction, as opposed to conduction. This limits the thermal gradients set up in the material making self-quenching more difficult. However, assuming that this effect is not large enough as to completely prohibit martensite formation, then the case depths potentially possible are much greater than would first be predicted.

An important consequence of this work is that the model has been shown to have the power to have its boundary condition changed to suit experiment and that it is indeed a very flexible tool. The modified model produced in this project allows for the finite size in the valve samples and can be expected to apply similarly well to other substrate geometries. The work has led to the production of a versatile model accounting for finite sample size in both y and z coordinates with user friendly output allowing direct reading of thermal gradients in any chosen direction or at any depth below the surface.

Wear tests of untreated and induction hardened samples of En24 shows a clear benefit in terms of substrate wear due to the heat treatment. For En52, there seems to be a slight increase in the performance of the substrate but the advantages of conventional heat treatment are not immediately obvious.

Wear test results for laser hardened En24/52 steels are extremely promising. Significant improvements in the wear performance of both steels under pin on disc testing are effected by laser treatment. The relative improvement for En24 is impressive and is also noted for a fairly wide range of laser processing conditions. En24 is less dependent on slight variations in laser processing conditions, a fact which is borne out by the noticeable reduction in wear of the system over a wide range of samples.

In similar manner, En52, not normally heat treatable shows great improvements in wear resistance for laser treatments. This is all the more apparent when viewed in the light of conventionally hardened and tested samples where the weight loss for the system is reduced to half in many instances.

In summary, wear resistance for grit blast and laser treated steel surfaces increases as long as the power density is sufficient to promote hardening. A direct relationship between treatment conditions and wear performance was not identified. The application of a coating to decrease this power density required to cause hardening seeme to be a physical effect which is not quantifiable from the data presented. However, there may be some minimum level of coating below which, the efficiency of the coating may decrease dramatically. It has been suggested (33) that the surface finish be of the order of the wavelength of the CO_2 laser light (10.6μm).

The use of the excimer laser for surface roughening was highly successful, in terms of increasing the surface absorptivity, facilitating LTH and also improving wear performance. One can easily see the possibilities for using the excimer laser and CO_2 laser in combination. A rapid, clean simultaneous process would be possible, whereby pretreatment for surface oxidation would preceed LTH but the whole operation could be carried out in-situ. This would also be clean and requires less steps and component transfer than conventional methods.

A number of authors (116) have found correlations between the surface hardness of laser treated steels and the interaction time (d/v). If this were the case, one might expect the interaction time to have some influence on the material loss of the substrate during wear testing. The results for different samples (different surface coatings and therefore different levels of absorbed power for the same interaction time) show loose correlations, the wear loss generally increasing with decreasing interaction time. However, examination of the microstructures does not point to any physical reason for this observation.

The actual lfetime of an engine valve is >100,000 miles. At a wear rate of 1mg/4hours the valve would lose around 300μm of its diameter during its lifetime. This is a very small fıgure. In view of this, it becomes apparent that once the stem surface is hardened then its wear resistance is adequate for the service requirements and there is no necessity to correlate microstructure with wear resistance. However, there is the possibility of a correlation but the tests used in this study were not sensitive enough to detect nuances in microstructure. The tests are merely a ranking system for industry. One further point to note is the increase in weight loss during testing of surface melted samples due to the non-martensitic surface structure.

The wear mechanism in these tests is fretting, substantiated by analysis of the wear debris which contains Fe_2O_3. Examination of the worn surfaces reveals on first assessment craters from which pieces of material appear to have been torn this would suggest sub-surface cracking due to the hardened layer with a softer layer underneath. However, closer examination reveals no cracking. SEM analysis reveals very little chromium in the scale from the worn surface, suggesting that Cr depletion occurs during testing.

Valve stem wear test also show encouraging results. None of the samples tested failed the standard test for valve stems at Brico Engineering. Correlation of the test results with processing parameters do not provide any rigid guidelines as to the optimum treatment for this type of component. However, the samples exhibiting the lowest and most consistent friction coefficient over the test duration are those in which the overlap zones overlap very slightly or not at all. In general, En52 samples perform better than En24 under the valve stem test conditions. This could be due to the observed backtempering effect in the steels when overlapping tracks are made. This effect is greater for En24 as the higher alloy content in En52 limits the backtempering and therefore allows the hardness of the surface to remain almost constant in the overlap zone. All laser hardened stems showed improved wear resistance over the untreated steel stems. Again, this acts only as a method of ranking the components and further, more rigorous and sensitive testing is needed to correlate wear properties with near-surface microstructure.

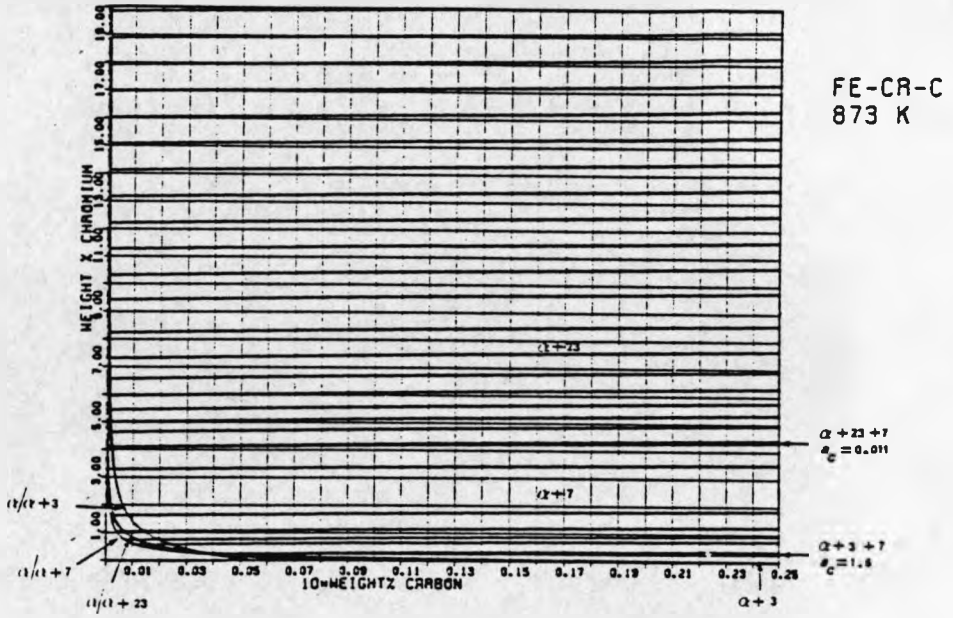

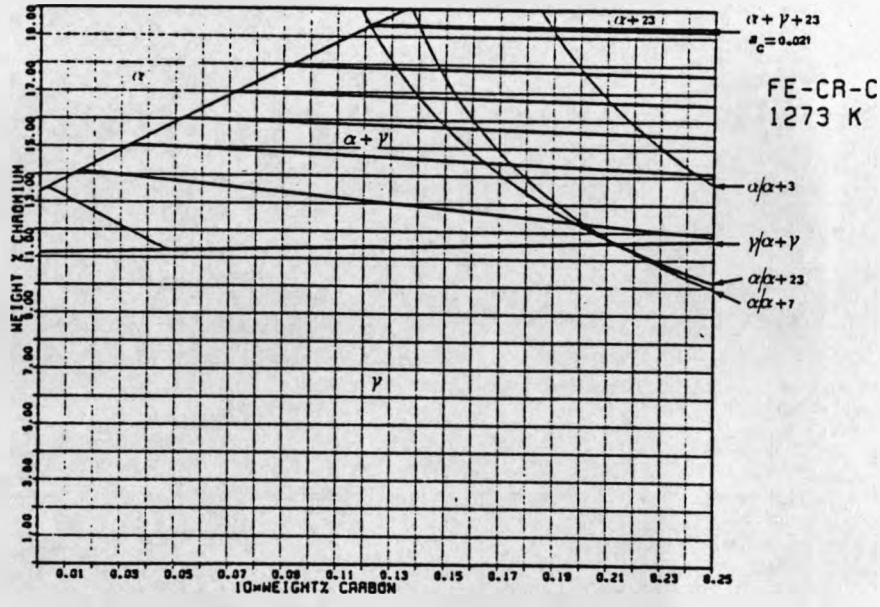

Fig. 6.1.6.2 Isothermal sections of the Fe-C-Cr phase diagram at 873°K and 1173°K respectively

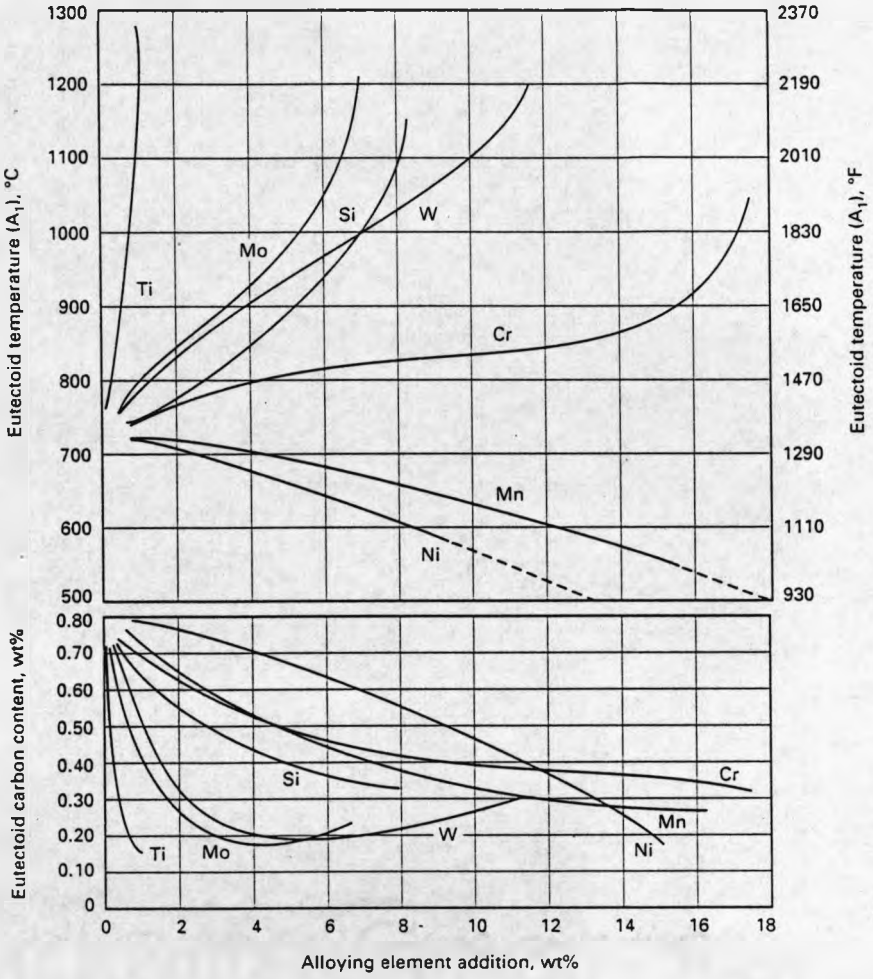

Fig. 6.3 Influence of alloying element additions on eutectoid temperature and eutectoid carbon content (186)

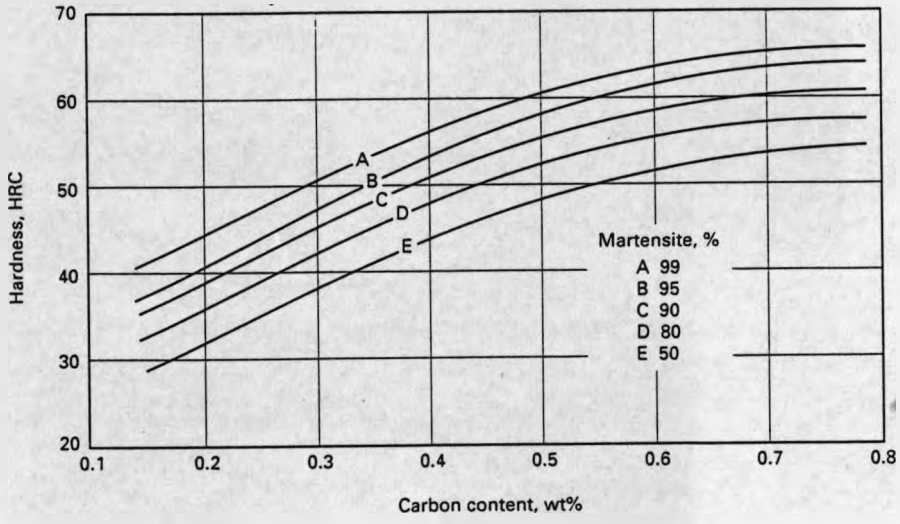

Fig. 6.4 Relationship between hardness, carbon content and amount of martensite (186)

Calculated critical thermal cycles sample 52sp1, v=20mm/s, q=1615w, d=6mm

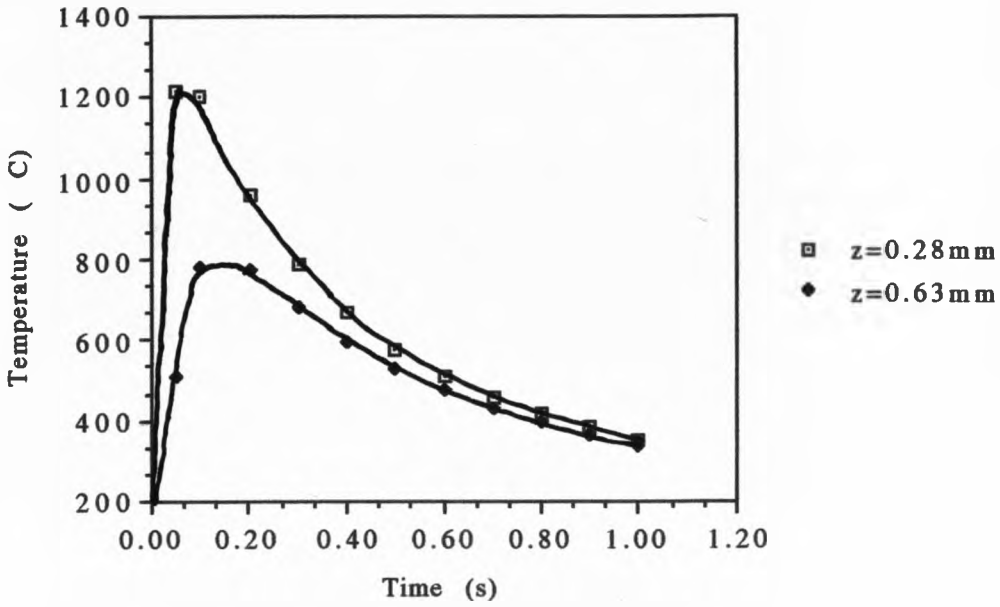

Fig. 6.5

Calculated critical thermal cycle sample 52sp4, v=14mm/s, q=1615w, d=6mm

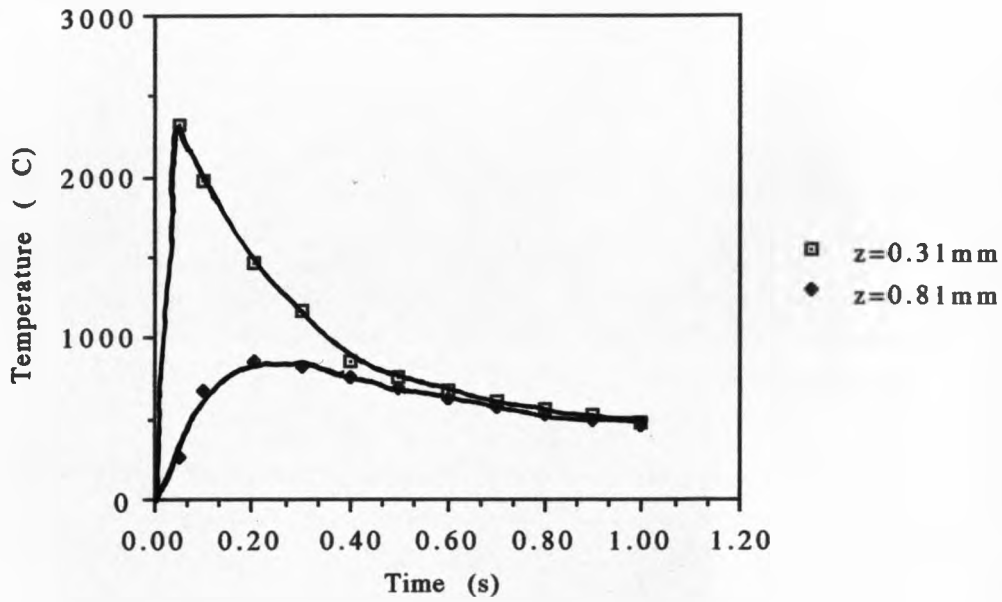

Fig. 6.6

Calculated critical thermal cycles for 24s3, v=24mm/s, q=2039w, d=6mm

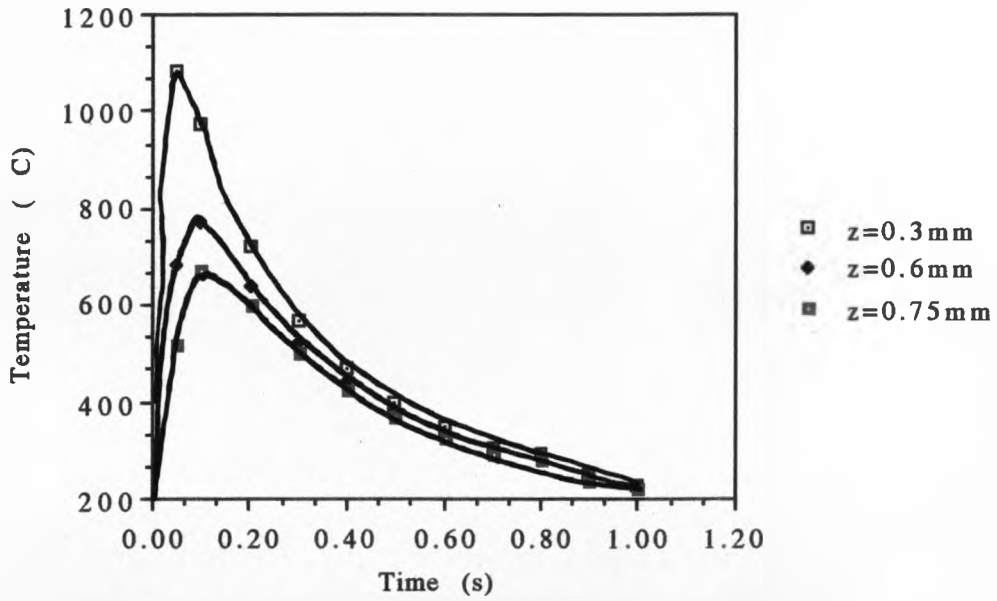

Fig. 6.7

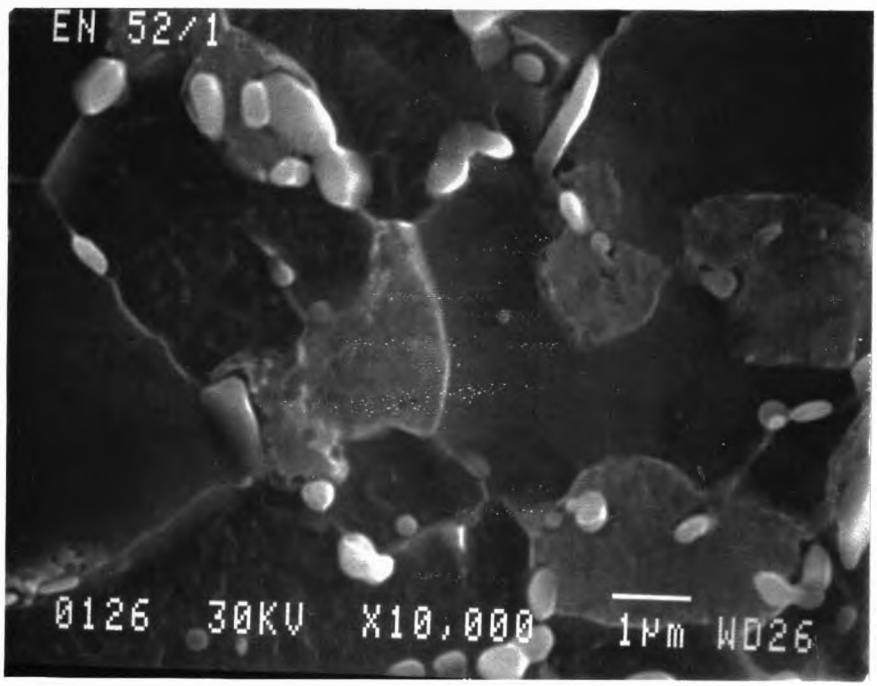

Fig. 6.8 SEM micrograph showing Initiation of austenite transformation at carbide particles in En52

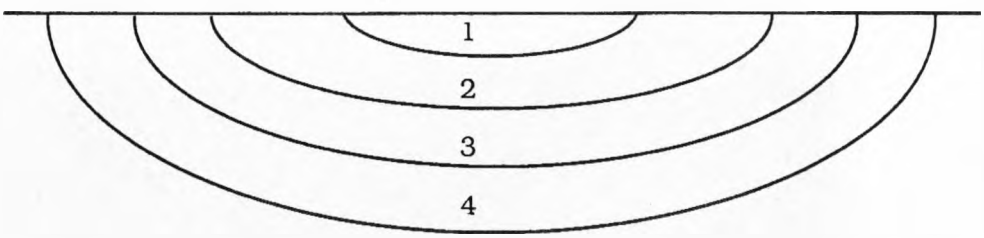

Zone 1 = dendritic
Zone 2 = martensite
Zone 3 = martensite + retained austenite/metastable phase + carbide
Zone 4 = retained austenite/metastable phase + ferrite + carbide

Fig. 6.10 Schematic representing four zone microstrusture in En52

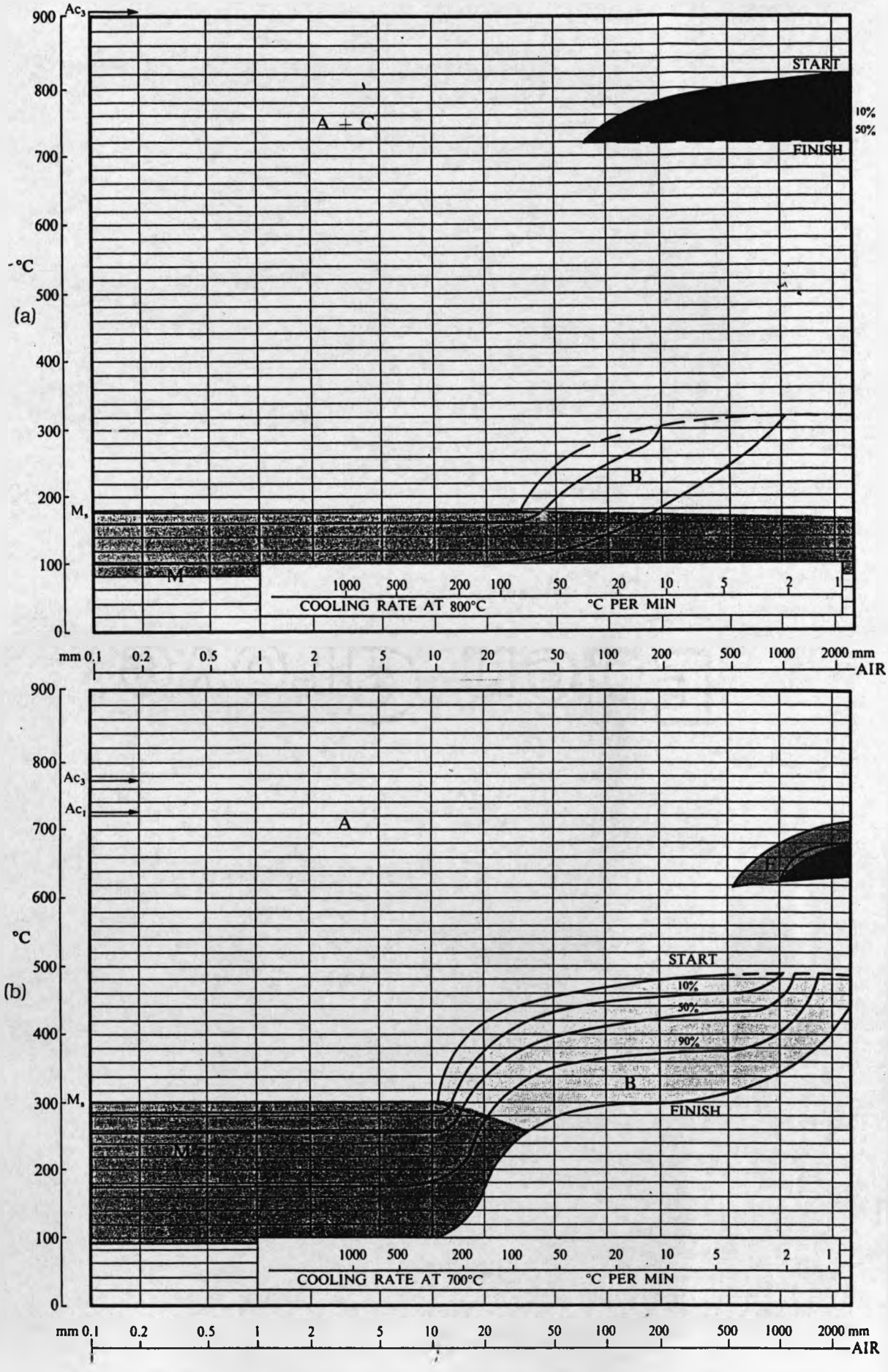

Fig. 6.9 (a) and (b) CCT diagrams for En52/24 steels

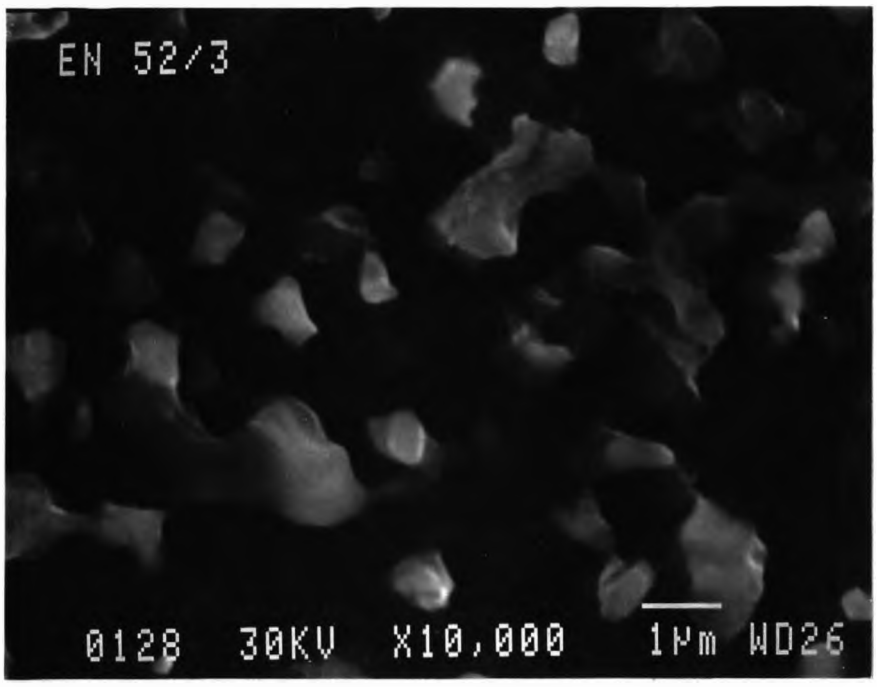

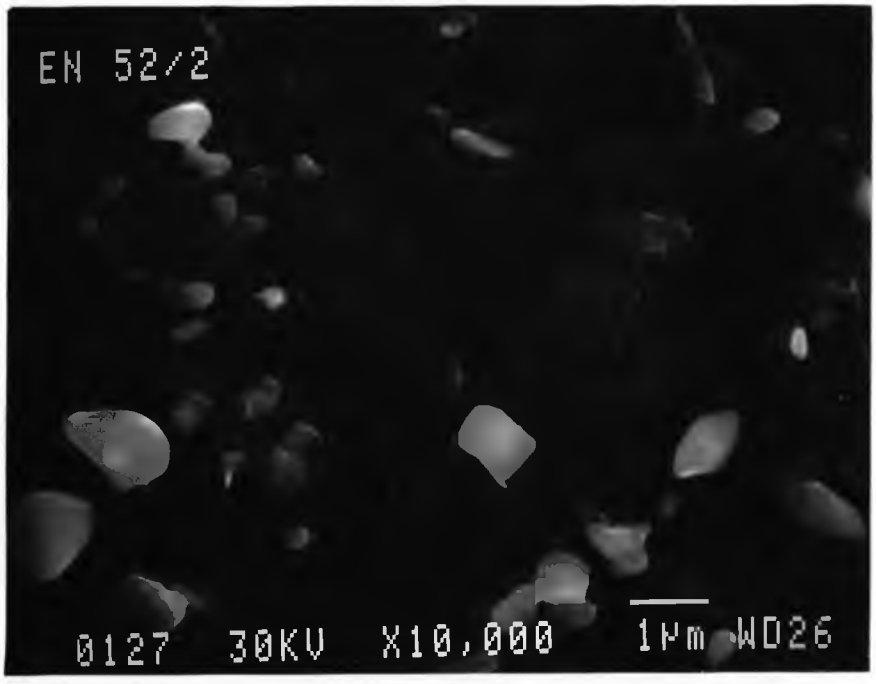

Fig. 6.11 (a) and (b) SEM micrographs showing partially transformed zones in En52

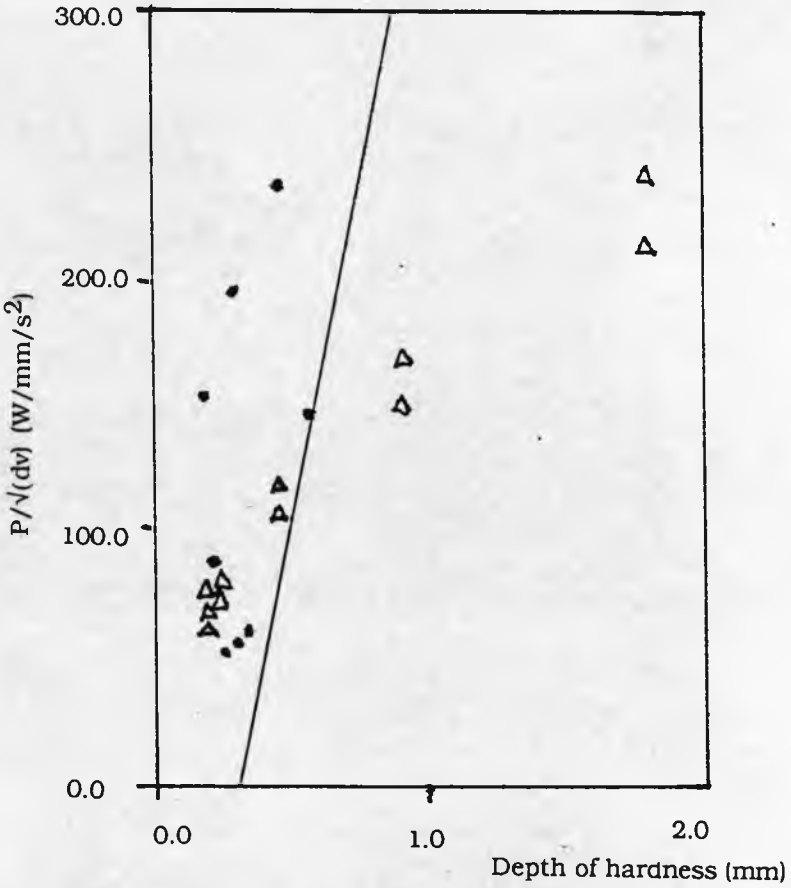

Fig. 6.12 Plot of $P/\sqrt{(dv)}$ against depth of hardness for En24/52 steels, spray paint coated, Courtney and Steen correlation marked by straight line

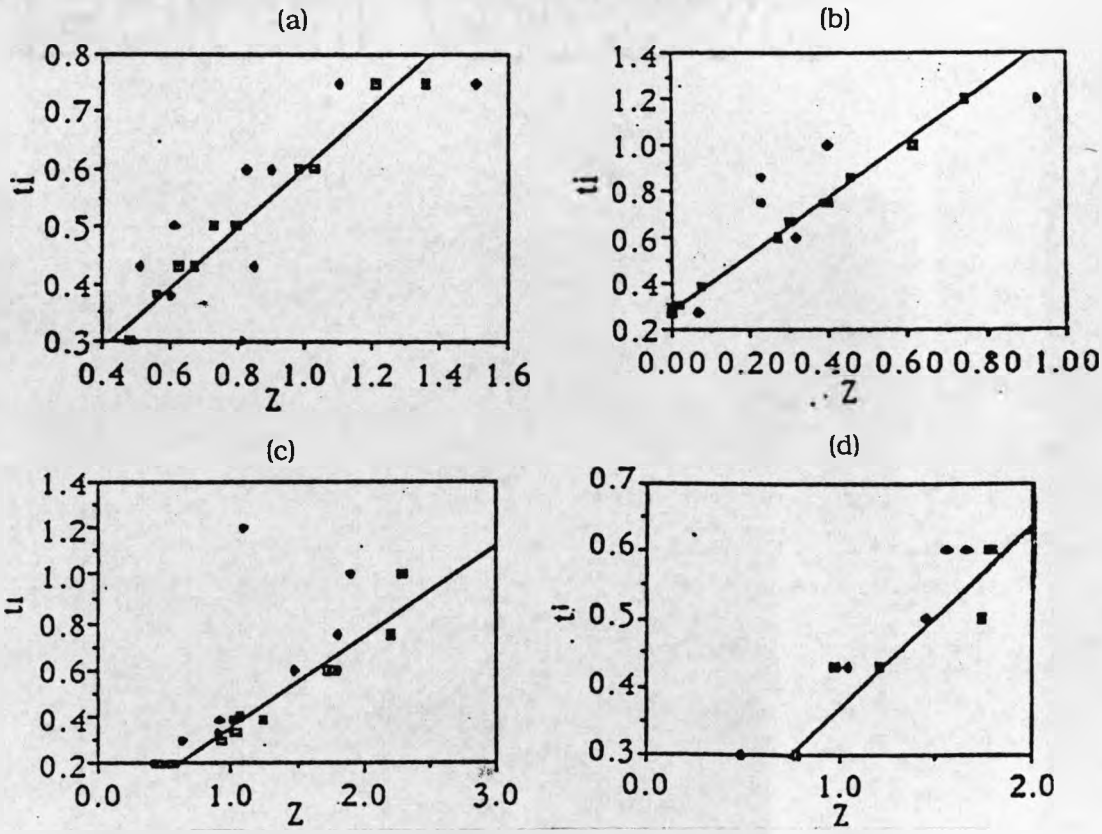

Fig. 6.13 Plots of theoretical (square symbols) and experimentally determined (round symbols) case depths against interaction time. (a) (a) En52 S (b) En24 S (c) En24 CG (d) En52 CG

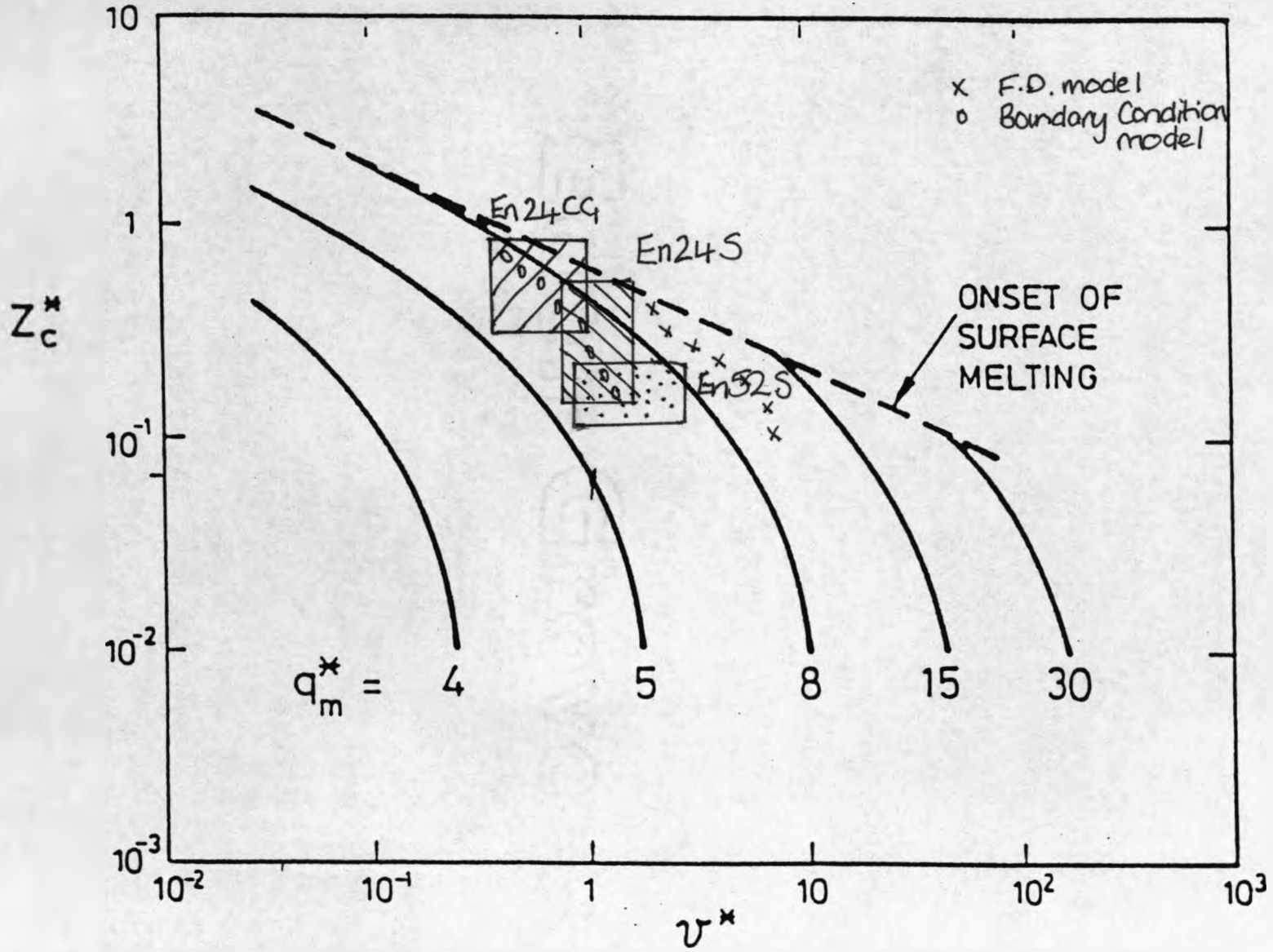

Fig. 6.14 Shercliff and Ashby master plot with experimental values and values derived from finite difference model and modified boundary condition model.

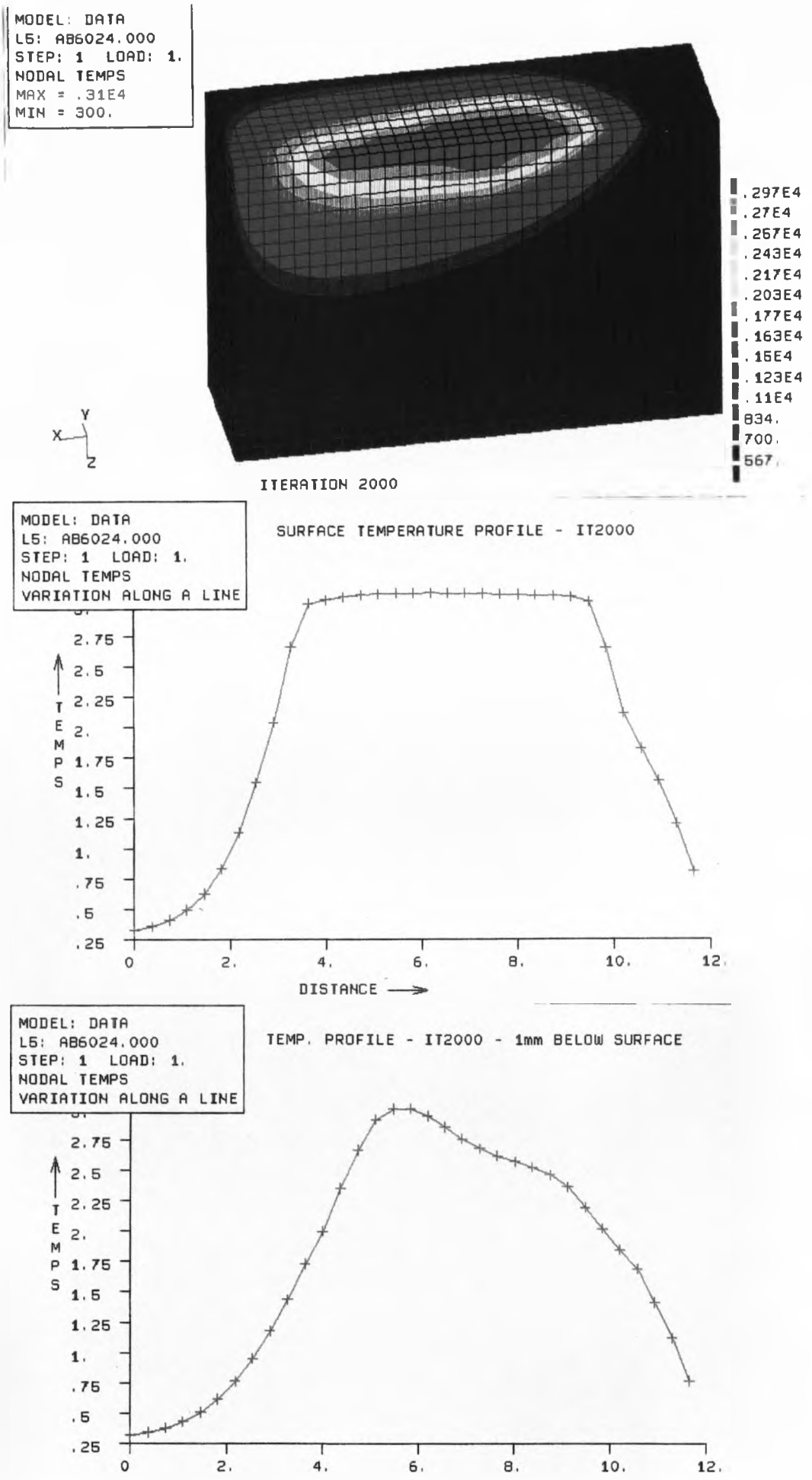

Fig. 6.15 Heat flow pattern (3-D) calculated using original F.D. model also shown are temperature profiles along the x-axis at the surface and 1mm below (En24)

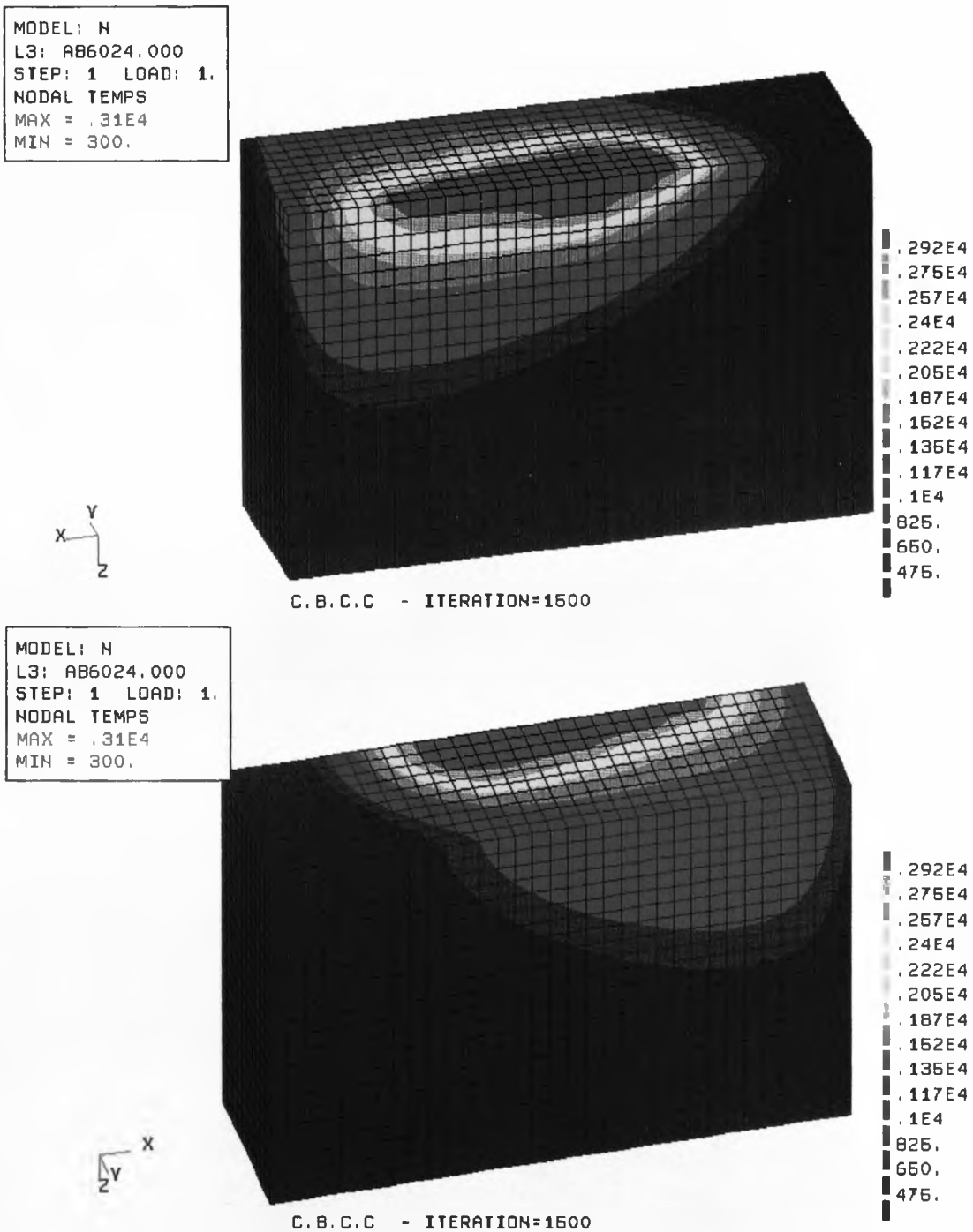

Fig. 6.16 3-D heat flow pattern for En24 calculated using modified boundary conditions

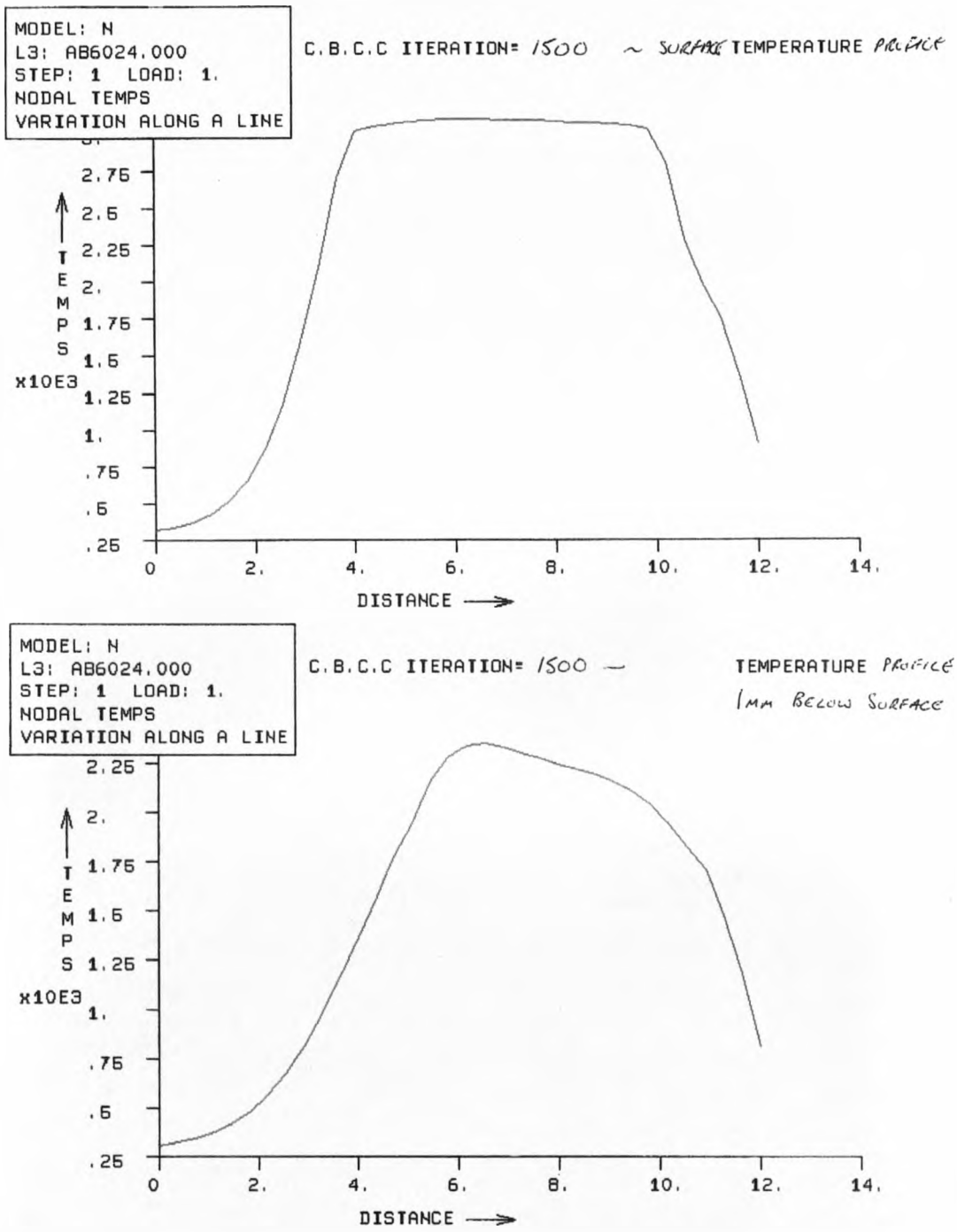

Fig. 6.16 x-axis temperature profiles at surface and 1mm below for modified boundary condition model

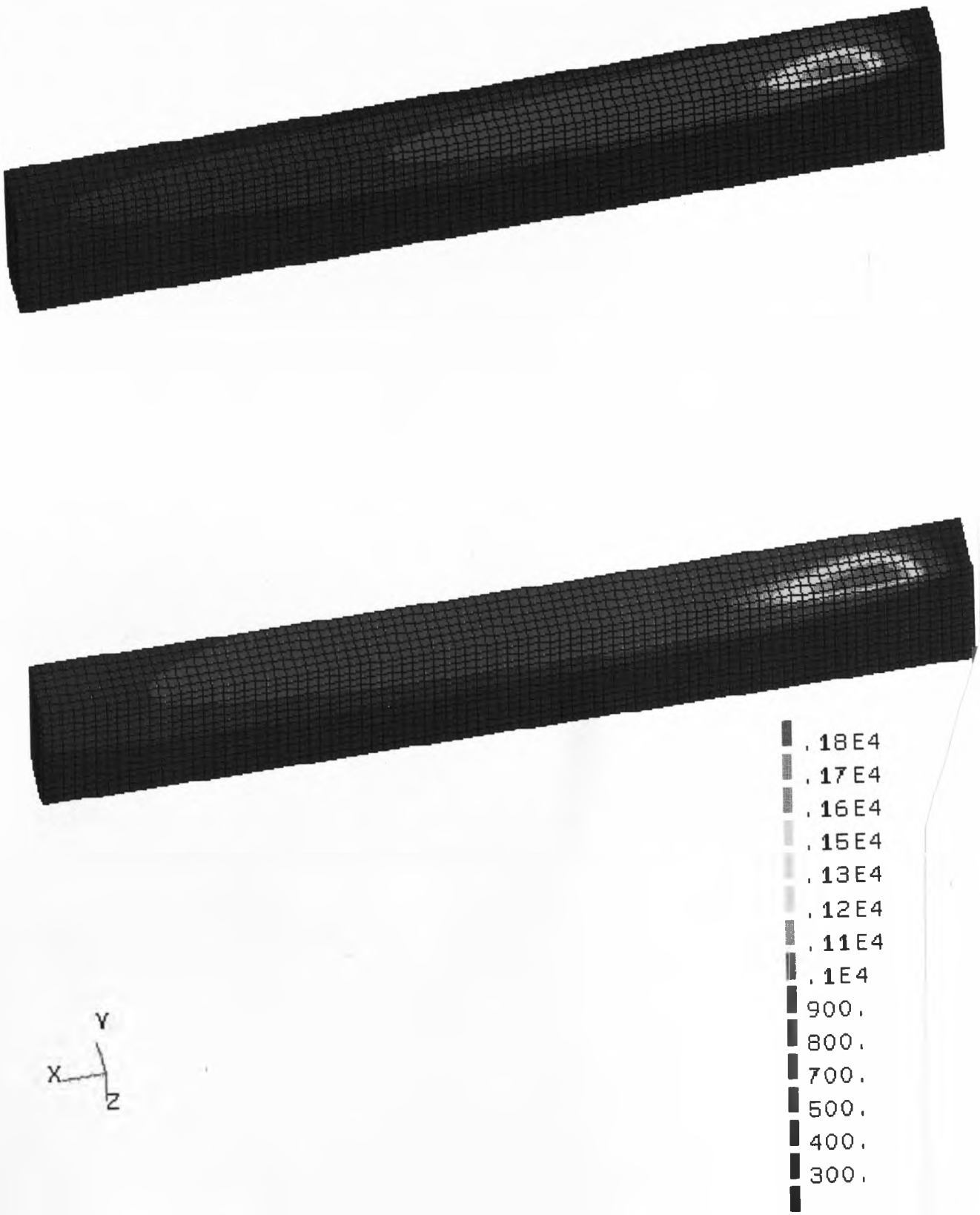

Fig. 6.17 (a) and (b) Comparison of heat flow induced in valve stem modelled using original (a), and convective boundary conditions (b)

CHAPTER 7

RESULTS - LASER CLADDING EXPERIMENTS

7.1 Introduction

The diesel valve seat is of considerable importance to the automotive industry. The aggressive environment in which it operates presents a challenge to the materials engineer and corrosion specialist alike. Valve seat faces have been hardfaced for many years, Judge (2) reports Stelliting of valves as early as 1938. Suitable hardfacing deposits for the component require high hot hardness, creep and fatigue strength, wear resistance, corrosion resistance (especially to lead compounds, SO_2, sulphates and vanadates) and will also be thermally insulating to protect the valve face from distortion. Conventional methods for hardfacing the seat face use the plasma transferred arc, TIG welding and spray techniques. However, any method which can give deposits having the above properties economically would be acceptable. The aim of this work was:

(1) to assess the feasibility of cladding valve seat faces with Stellite 6 using a high power CO_2 laser,
(2) to investigate the use of Stellite 35 as a cladding material, compared with the more traditional Stellite 6,
(3) to determine the optimum processing parameters
(4) to establish the wear resistance and microstructures of the layers produced. In addition,
(5) to investigate the effect of introducing a second phase into the Stellite layer.

The technique used is particle injection whereby a ceramic powder is injected into the melt pool. A series of experiments using four different ceramic powders are reported. In each case, a number of experimental geometries were investigated. Testing the weldability of Stellite 35 is important as it is hoped that Stellite 35 will provide enhanced corrosion resistance over previous alloys. This becomes increasingly important with the advent of new fuels as the valve environment will reach higher temperatures together with higher speeds. Coupled with this is the drive towards lower exhaust emissions, adding to the need for improved materials.

A number of factors are important in assessing clad quality, as follows, height and width of the bead, appearance of the clad, level of dilution, presence of porosity, deposit cracking and surface oxidation. In the case of the poppet valve, it is especially important that dilution and distortion of the workpiece be avoided, since the thickness of the valve seat where the clad is deposited is very small and critical in terms of performance. For the purposes of this chapter, the measurements made on clad beads refer to those indicated in Fig. 7.1.

7.1.1 Development of Optimum Gas Flow System for Powder Feed System

The triple hopper feed system (THS) developed by Jeng (79) at Liverpool University was used for this work. The gas delivery configuration normally used with this system did not provide uniform powder flow at speeds <500rpm for the ceramic powders. The system finally used consisted of argon gas exiting the bottle at 1bar pressure after which it was split three ways to supply the top and side gas entry points of each feeder. Each feeder was fitted with its own argon rotameter to control the gas flow to the powder and a needle valve to finely tune the gas pressure acting above the powder. When only one or two of the hoppers were in use, the empty hopper(s) were blanked off to prevent back flow of gas. Pressure control was especially important when the reservoir was in use. The combined gas pressures were set so that the powders did not exit the feed tube with excessive velocity and the flow showed the correct pattern.

7.2 Cladding of Stellite 6 'W'

7.2.1 Flat Plate Clads

Results for flat plate cladding of Stellite 6 'W' on En3a mild steel are shown in Table 7.1. These clads were made for the purpose of fixing alignment, testing procedures and determining the optimum speed/power conditions.

7.2.2 Valve Cladding with Stellite 6'W'

The valve cladding results of Stellite 6 'W' on alloy 21-4N valve heads are shown in Tables 7.2 and 7.3. The best result in terms of surface finish and zero distortion of the valve was obtained at 2kW laser power, 6.5mm beam diameter, valve rotation time 13.9s/rev. and powder flow rate 0.32g/s. This clad is shown in Fig. 7.2 (a), alongside photographs illustrating an unclad valve, (b), a poor quality or 'baubled' clad, (c), and a finished article, (d), which has been filled by plasma arc deposition and subsequently machined. The friction welded joint between the head and stem, discussed in Chapter 1 can also be seen in these figures. Fig.7.2 (a) represents a clad with a smooth surface finish, negligible oxidation and complete filling of the groove with a flattened surface profile.

Fig. 7.3 illustrates the dendritic microstructure obtained within the clad. The dendrites are observed to coarsen slightly moving away from the interface due to the decreasing effect of quenching from the bulk substrate. The interface region of the clad is shown in Fig. 7.4, illustrating a region of planar solidification at the interface. Fig. 7.5 shows incomplete mixing in the clad layer. Turbulent mixing patterns in the region have been effectively frozen on solidification.

Fig. 7.6 illustrates the Vickers hardness values for samples K3, R16 and W7 moving from the surface of the clad layer, through the interface and into the base material.

Hardness values upto $800HV_{10}$ were observed for sample W7.

7.3 Cladding of Stellite 35

7.3.1 Stellite 35 on mild steel

An initial series of Stellite 35 clads were made on mild steel substrates to define the operating window. This also allowed determination of whether the powder could be blown into the focus of the laser beam (1-2cm above the surface) and dropped onto the surface molten, in a similar fashion to the bithermal technique described by Fellowes (186). The operating parameters and observations are presented in Table 7.4. Examination of clads 3.1 and 3.2 using the SEM revealed highly dense, uniform clads showing minimal dilution. The surface of the clads was smooth and no cracking or porosity was observed. The microstructure of laser clad Stellite 35 on mild steel is illustrated in Fig. 7.7. The structure was dendritic with a two phase eutectic. Compositional analysis (EDX) of the clad compared to the starting composition of the powder at various depths within the clad indicated that the compositions were effectively the same (no increase in Fe content of the clad) and therefore the clads are representative of the starting material and no dilution occurs during processing.

7.3.2 Stellite 35 on 21-4N

Single tracks of Stellite 35 were made on 21-4N to assess the weldability of the Ni-base alloy compared to that of Stellite 6. The operating parameters for this combination of overlay and substrate and the effect of various parameters on clad dimensions and properties were also assessed. Optimisation of the processing parameters aimed to produce a dense, well-bonded and homogeneous layer with minimum dilution. The most influential parameter on clad dimensions and quality was the traverse speed, the effect of varying speed on clad height and hardness was investigated over the range 5-20mm/s and is plotted in Fig. 7.7 (b) and (c). As shown, the effect of increasing traverse speed increases clad hardness as a result of the increasing rate of solidification and therefore increasingly finer microstructural scale. On the other hand, increasing the speed decreases the height of clad. Optimised clads in terms of coverage rate, clad dimensions and hardness were achieved at 2kW laser power, 12mm/s and beam diameter 6mm. The powder flow rate for producing such clads was 0.26g/s with an argon carrier gas flow rate of 1l/min.. Increasing the powder flow rate beyond this yielded good quality clads but there was a considerable amount of overspray and therefore powder wastage. In the above experiments, the level of dilution was <5% in all cases. This is further indicated by EPMA results of a typical clad of Stellite 35 on 21-4N (Fig. 7.8 (a) and (b)) analysed for Fe, Cr, Ni, Si and C. As shown, the interface region is defined by the sharp changes in composition of the elements, there is no prolonged diffusion zone, the diffusion zone shown in Fig. 7.8 (b) is representative of the maximum level observed and is about 20μm. The averaged elemental analysis for the standard clads

of Stellite 35 on 21-4N are presented in Table 7.5. Corresponding dot maps of the clad are presented in Fig. 7.9, and show that the eutectic phase is chromium rich.

7.4 Cladding of Stellite 35 and SiN

The particle size of the silicon nitride powder supplied by T&N Technology was too small for use with the triple hopper feed system (<25μm). Attempts to clad using this powder resulted in the screw feed blocking and the nylon bearings of the feeder seizing. To overcome this problem, the SiN powder was mixed to a slurry with water and pasted onto the 21-4N samples with a paint brush. Although a series of 20 clads of Stellite 35 was made on top of the dried slurry mixture, no SiN was detected during analysis. It is possible that the SiN was volatilised by the laser beam on impingement, or that there was simply too little SiN present to be detected. No peculiarities were observed in the microstructure at the interface, nor was there any appreciable difference in the hardness of the clads compared with those made from Stellite 35 alone. It was concluded that SiN, at least in the form available was not suitable for blown powder laser cladding.

7.5 Cladding of Stellite 35 and alumina

As reported in Chapter 4, the particle size range of the alumina powder used was 63-150μm. Tracks were produced using a single feed tube (separate hoppers with reservoir mixing), premixed Stellite + alumina and separate feed tubes for the two powders. In all cases, the plume occurring during cladding was observed to increase in intensity and size with increasing addition of alumina, suggesting that rather than being deposited as solid particles, the alumina was in fact melting in the beam path. Similarly, for all modes of cladding, the appearance of the resultant clad changed with addition of alumina from shiny and metallic (100% Stellite) to a scaly two layer structure, the top layer of which was black and became thicker with increasing proportion of alumina. This upper blackened layer sloughed off on cooling whereas the layer underneath showed a smooth surface finish and was securely bonded to the substrate. The presence of this two layer structure was only noticed when alumina was added to the melt pool, an effect which was observed to increase with increasing amount of ceramic.

Using two separate feed tubes, the geometry was changed slightly to try to introduce the alumina into the melt pool underneath the jet of Stellite powder, thereby shielding the alumina particles from direct radiation and also trapping the alumina underneath the Stellite layer as it solidified. This geometry is illustrated in the photograph shown in Fig. 7.10. EDX analysis of typical sloughed layers detected the presence of only aluminium on both the upper and lower surfaces (although elements with atomic number <11 are not detected). There was no evidence to indicate that any mixing between the two powders had taken place. The upper surface appeared to contain undissolved spheroidal alumina particles whilst the lower surface was mostly smooth, the alumina obviously having melted and

resolidified. SEM micrographs of the upper and lower surfaces of the sloughed layer are shown in Fig. 7.11 (a) and (b). The processing parameters for producing good clads of Stellite 35 + alumina were as follows: q=2.00kW, v=5-7mm/s and d=5.5mm, total powder flow rate=0.24g/s, however, this produced good Stellite clads with the over layer as above. The addition of alumina to Stellite clads affected the geometry, porosity and dilution of the clad as illustrated in Fig. 7.12 (a)-(e) (points plotted for two clads, SAD/2/2 and SAD/2/1 processed). The height and total thickness of the clads decreased with increasing additions of alumina so much so that by the time 20 wt.% addition was reached, both had been halved. The width of the clad increased marginally (1mm in total over the range 0-20 wt.% alumina) with increasing alumina addition. On the negative side, the percentage porosity and dilution were both observed to increase slightly as more alumina was added to the clad although the maximum level of dilution recorded in this series was ~6%. There was no correlation between clad hardness and amount of alumina added, presumably due to the problem in incorporating the alumina into the matrix. The change in shape of a typical clad with addition of alumina is illustrated in Fig. 7.13.

A subsequent idea for incorporating alumina into the Stellite 35 clads was to make one clad layer of alumina on the substrate surface and to overlay a second clad of Stellite 35 on top of this. The method used was similar to that described by Fellowes (186), whereby the alumina powder was blown into the beam focus around 18mm above the surface of the valve steel substrate. The ceramic was melted in the beam in this manner and dropped down onto the substrate whilst still molten. The results of these experiments indicated that the alumina underwent some reaction with the surface of the 21-4N. A red deposit was observed on the surface of the substrate, which was attacked quite considerably by the molten alumina. This massive oxidation was also noted by Fellowes (186) and was probably a function of inadequate inert gas shrouding at such high temperatures (>2000^{o}C) or incompatibility of the materials. The appearance of some tracks prepared in this way is shown in Fig. 7.14. Changing the processing speed served only to alter the amount of substrate damage, as indicated, but did not prevent the oxidation reaction occurring, as shown.

7.6 Cladding of Stellite 35 and SiC

The particle size range of the SiC powder used in this study was determined in the range 106-250μm (see Table 4.2). Clads were made in each of three geometries, premixed, reservoir mixing and twin feed tubes. Again, the feed positions of the Stellite 35 and alumina tubes were varied to assess the best combination for incorporation of the ceramic into the alloy matrix on solidification.

A similar problem in powder flow was noted. At very low flow rates (<200rpm motor settings for feeders), the powder flow becomes non-uniform. Pulsing tends to occur and the result is a fluctuation in the size and intensity of the melt pool as the clad is made. This also affects the clad dimensions, since the ceramic powder flow induces

non-uniformity in the Stellite flow pattern and the deposits become uneven in a regular pattern corresponding to the pulsing of the powder, an example of a deposit exhibiting this problem is shown in Fig. 7.15. Addition of SiC to the Stellite cladding system tends to produce a surface crust, as does alumina. However, this crust is not as thick or brittle as the alumina crust and tends to adhere to the clad. The surface appearance of a clad covered with adherent SiC particles (detection of only Si on the surface via EDX analysis on the SEM) is shown in Fig. 7.16.

The results of EPMA analysis of clads containing 5, 10 and 20 Wt.% addition of SiC in the premixed configuration are presented in Fig.7.17. As shown, the Si content of each of the deposits with SiC addition increases towards the surface, indicating that the SiC particles are either not reaching the depth of the Stellite molten pool, or that they are floating towards the surface due to their comparatively low density. The high near-surface variation in Si content is due to porosity observed in each of the samples made with Stellite 35 + SiC (N.B. standard deviation of Si scans higher than previous scans for the other elements). The samples were analysed for Si, Fe, Cr, Ni and C using the dot mapping technique. The results are shown in Fig. 7.18. Carbon analysis was particularly difficult to carry out, however, as shown, the chromium rich areas correspond to the carbon rich areas very well indicating the presence of Cr carbides in the eutectic. In addition, the Ni, Si and Fe dot maps correspond very well showing that these elements are primarily contained within the dendrites. To further elucidate the segregation in the clad and determine whether SiC had indeed dissolved and the carbon combined with chromium, a second WDS scan for Si and C was done. The areas rich in carbon were found to coincide with a drop in the Si content (and a rise in the Cr content) suggesting that there is no detectable presence of silicon carbides.

As stated above, most of the ceramic particles undergo partial or complete dissolution in the molten Stellite 35. This accounts for the observed increase in silicon content of clads made using this system. Those SiC particles which did not dissolve tended to be situated towards the upper surface of the clad or trapped in the interface layer. The results of compositional analyses are presented in Table 7.5.

Therefore, it is understandable that the measured compositions did not wholly represent the amount of SiC added. A series of micrographs indicating the occurrence of undissolved and partially dissolved SiC particles are given in Fig. 7.19. Also shown is the observed microstructure of the clad layers. The different geometries of the cladding experiments resulted in slightly different levels of Si detected in the layers for a given composition set on the powder feed system, the twin feed system was tried using a number of different injection points for the ceramic, some of which are shown in Fig. 7.20. The addition of the ceramic into the melt pool seems to give a higher level of incorporation. On the whole, the systems produce similar levels of Si for a given weight percent addition of SiC. However, one noticeable exception is the twin feed set up where the ceramic is blown into the beam focus (17mm above surface). In this case, most of the SiC does not enter the clad but

simply solidifies on the surface and does not dissolve to any significant extent. A system of cladding with the substrate angled at 45^{o} to the incoming beam was also tried. Although this did produce some nice clads, there was a problem with back reflection of the CO_2 radiation so this technique was not pursued. In the case of SiC + Stellite 35, the effect of adding an increasing amount of SiC by weight acts to change the nature of the deposit by increasing it in height. This is due to an increasing degree of deposit porosity with addition of SiC. The porosity is restricted to the surface layer as might be expected, as this is where most of the ceramic is retained. One further consequence of such additions is to improve the hardness of the clad substantially from around 450 HV(10kg) to >700 HV(10kg) for 18 Wt.% SiC addition. This is plotted in Fig. 7.21. However, further increases in the addition of SiC serve only to deteriorate both the quality of the clad and its hardness as the deposits become brittle, poorly bonded and smash under hardness testing.

7.7 Cladding of Stellite 35 and Chromia

Sieve analysis of chromia indicated that the size range of the powders used was 38-90μm, as shown in Table 4.2. The results presented in Fig. 7.22, 7.23 show the WDS traces for two clads made with Cr_2O_3 + Stellite 35, analysed for Ni, Fe, Cr and Si. Fig. 7.22 is the analysis for a clad made using 10Wt.% Cr_2O_3 + Stellite, premixed and deposited at 8mm/s, 2kW laser power (d=5mm). In this case there is a noticeable variation in the detected level of Cr across the sample. No increase in the level of chromium towards the clad surface was observed and the interface is defined by a sharp fall in the levels of iron and chromium, indicating minimal dilution. There does not seem to be a correlation between the peaks and troughs in the chromium trace with any of the other elements detected. For the second sample illustrated, made from 4.5 Wt.% Cr_2O_3 + Stellite, variations in the Cr level across the deposit are much less dramatic. A slightly higher level of dilution is noted, but this remains at <20μm. Again, no increase in the level of chromium occurs towards the surface of the deposit, as was the case for SiC. Dot mapping of the 10% by weight Cr_2O_3 in Stellite 35 gave the results presented in Fig. 7.24. Again, Cr is present in the eutectic phase. Also shown is a micrograph illustrating the fine scale dendritic microstrucuture common to laser clad layers.

In general, slagging of chromia from the upper level of the clad was less of a problem, occurring only with two feed tubes. Premixing or reservoir mixing of the powders allowed the chromia to dissolve. That which did not dissolve was found as overspray in the area surrounding the work piece. Injection of chromia to the Stellite 35 was highly effective in improving the hardness of the deposits, as shown in Fig. 7.25. Hardness values >700 HV (10kg) were noted for additions of chromia above 10 weight percent. Undissolved particles of chromia (Examples in Fig. 7.26) were situated at the upper edges of the clad beads. A typical clad of Stellite 35 with 5Wt% chromia (premixed) is also shown in Fig. 7.26.

7.8 Wear Testing of clad samples using hammer drill rig

As reported in Chapter 4, clad samples were evaluated for wear resistance using the hammer drill rig described. This test was intended to provide qualitative information regarding the resistance to abrasive wear (i.e. it is a ranking test rather than a quantitative test). Samples were tested for 60s under a 1.5kg load. The results are presented in plots 7.27 and 7.28.

Although complete analysis of the wear mechanism and resultant surfaces was not within the scope of this work, the appearance of the wear scars was examined using the SEM. Typical scars from the sample and silver steel wear pin are given in Fig. 7.29 (a)-(c). The wear resistance of Stellite 35 clads was found to improve markedly on addition of SiC and chromia to the clad. However, no improvement in wear resistance was noted from additions of alumina, which corresponds with the failure to detect any significant aluminium content in the layers or any microstructural changes. The wear resistance of the clads tested as a function of weight percent ceramic addition is shown in Fig. 7.27. The improvement in wear characteristics is a result of increasing the content of silicon, chromium or carbon in the clad. For Stellite 35 clads alone, the wear resistance increases with increasing velocity during processing, in line with the hardness values noted for the clads, this is illustrated in Fig. 7.28. For the Stellite + SiC clads, the wear resistance also follows the same trend as the macrohardness of the clads.

The most significant improvements in clad wear resistance were observed in the Stellite 35 + Cr_2O_3 deposits. One obvious verification of this is the extreme difficulty noted when trying to section the clads with high chromium content.

No significant differences were observed for clads of similar composition made using different experimental configurations, assuming that the clads were of good quality.

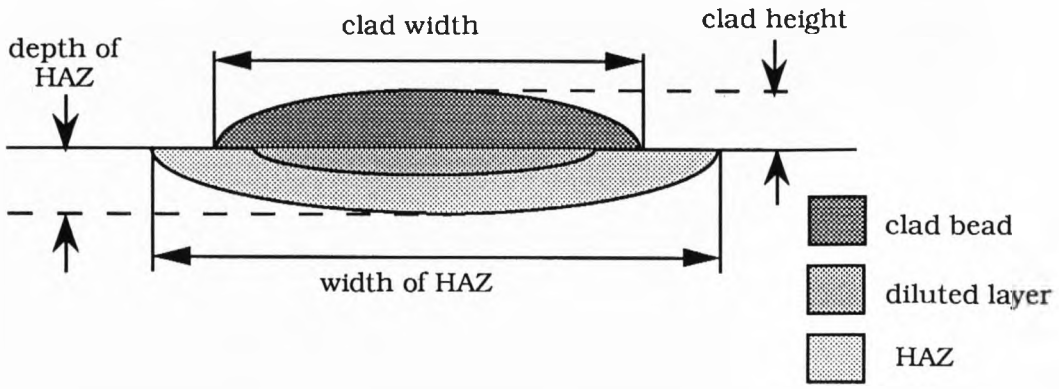

Fig. 7.1 Dimensions of laser deposited tracks

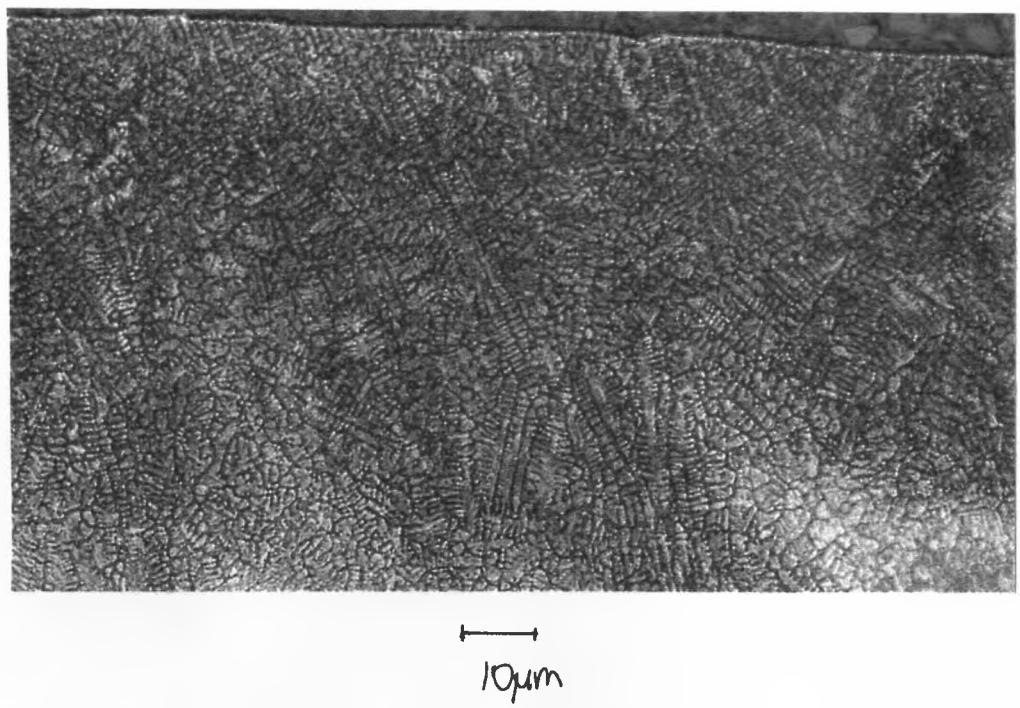

Fig. 7.3 Showing dendritic nature of laser clad track of Stellite 6'W' - 21-4N valve steel (q=2kW, time/revolution=13.9s, flow rate=0.32g/s)

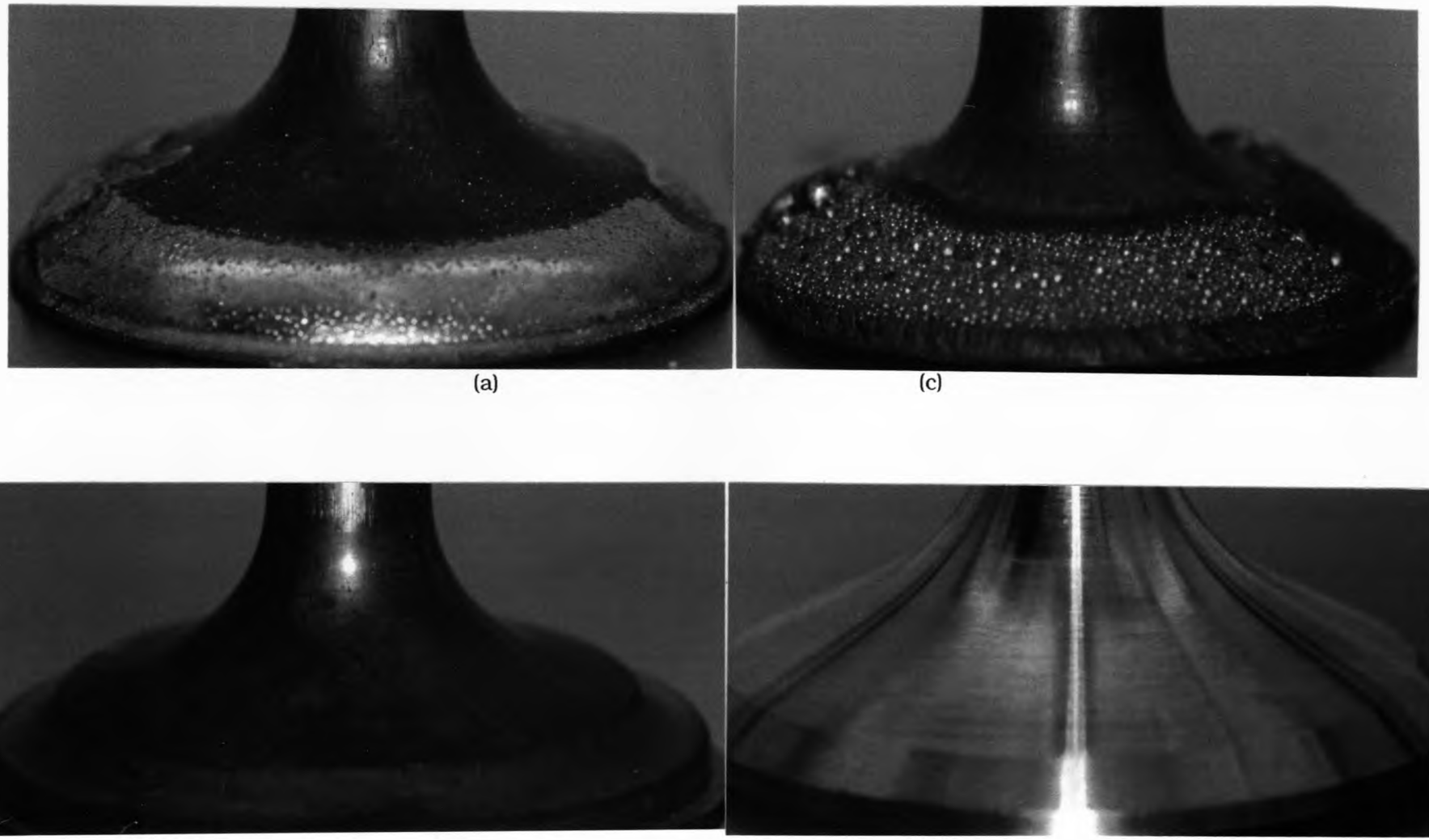

Fig. 7.2 (a)-(d) Illustrating laser clad valve (a) of good finish and quality, unclad valve groove (b), poor quality (baubled) laser clad valve (c) and production finished valve (d)

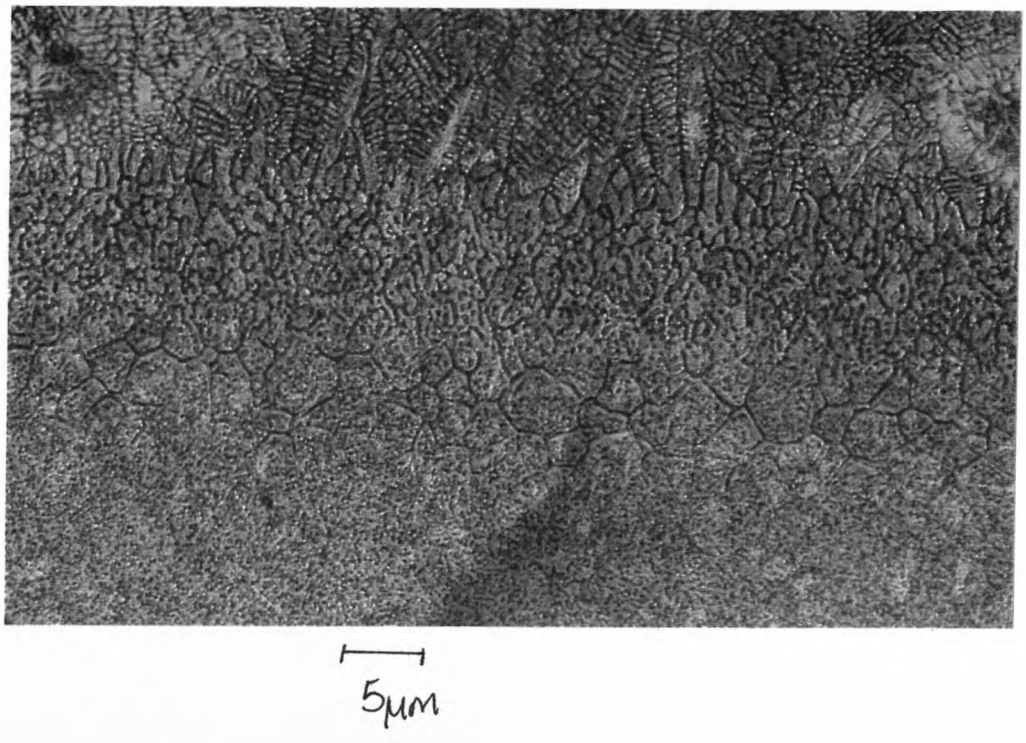

Fig. 7.4 Interface region of Stellite 6'W' laser clad on 21-4N, showing region of planar solidification and formation of dendrites

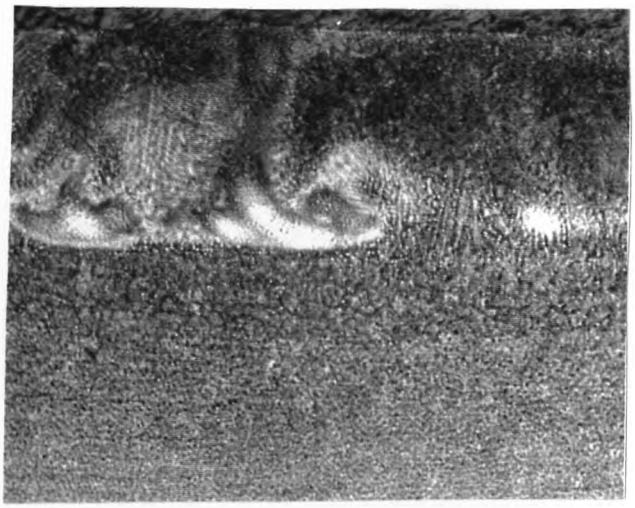

Fig. 7.5 Incomplete mixing in clad, turbulent mixing pattern frozen in

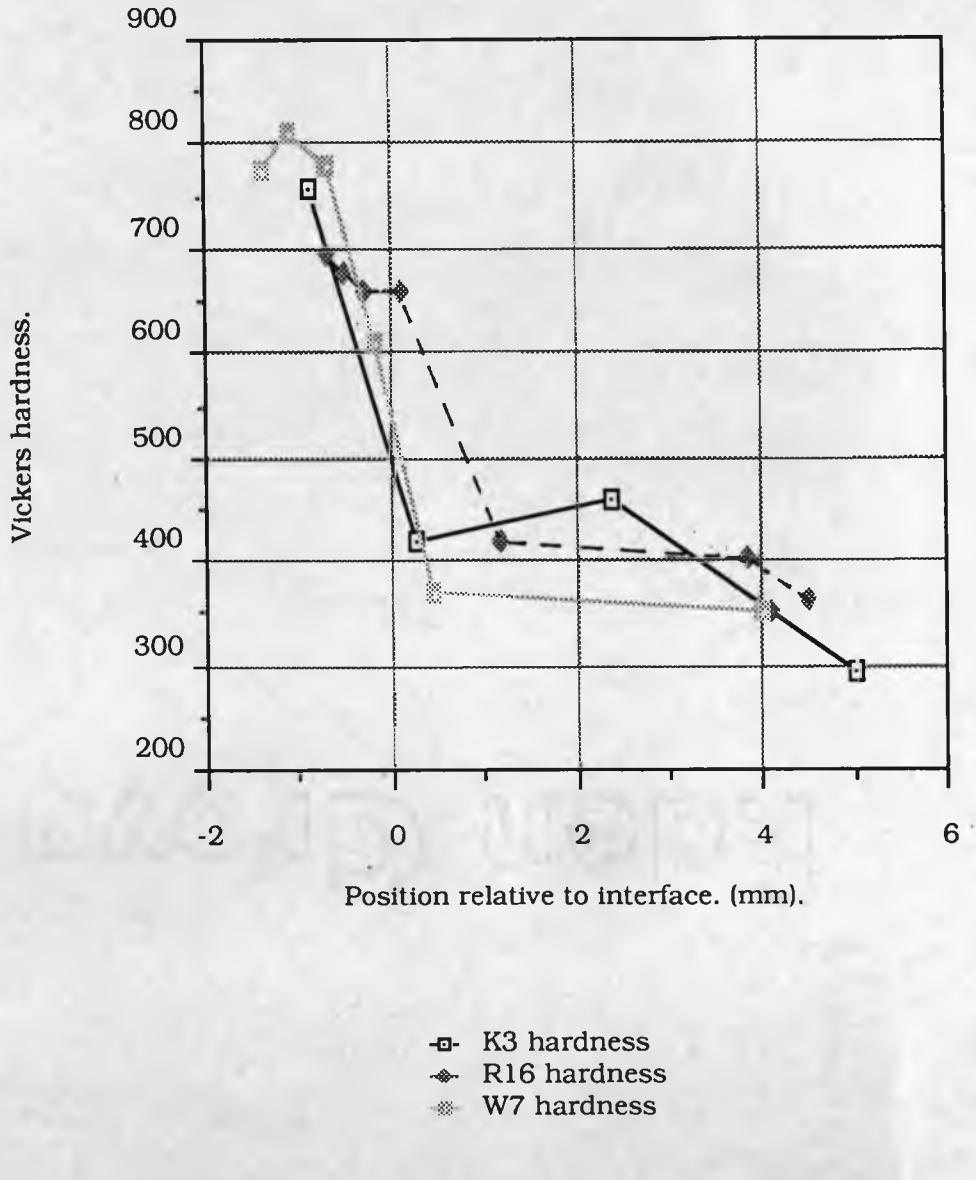

Fig. 7.6 Hardness of clad layers of Stellite 35 on valve seat faces

Fig. 7.7 (a) Microstructure of Stellite 35 clad on mild steel substrate, v=12mm/s, q=2kW, d=6mm

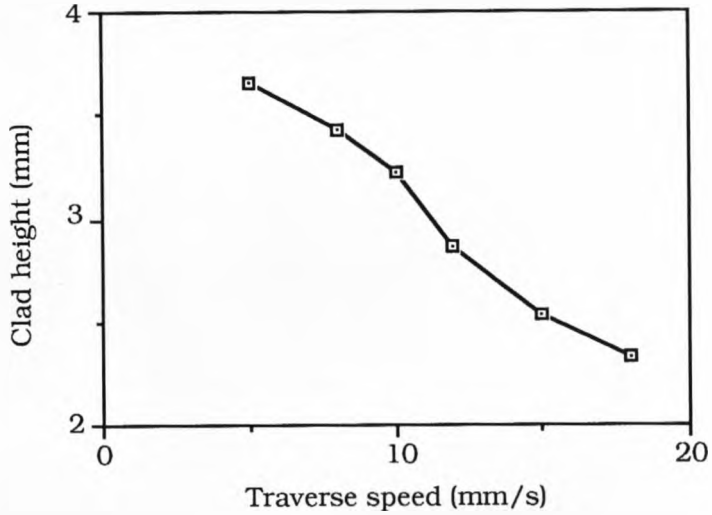

Fig. 7.7 (b) Effect of traverse speed on clad height for Stellite 35 on 21-4N substrate

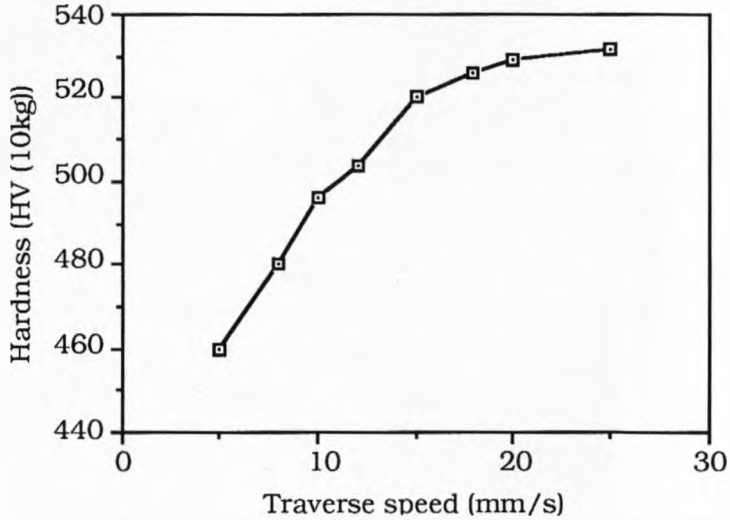

Fig. 7.7 (c) Effect of traverse speed on hardness of clad for Stellite 35 on 21-4N substrate

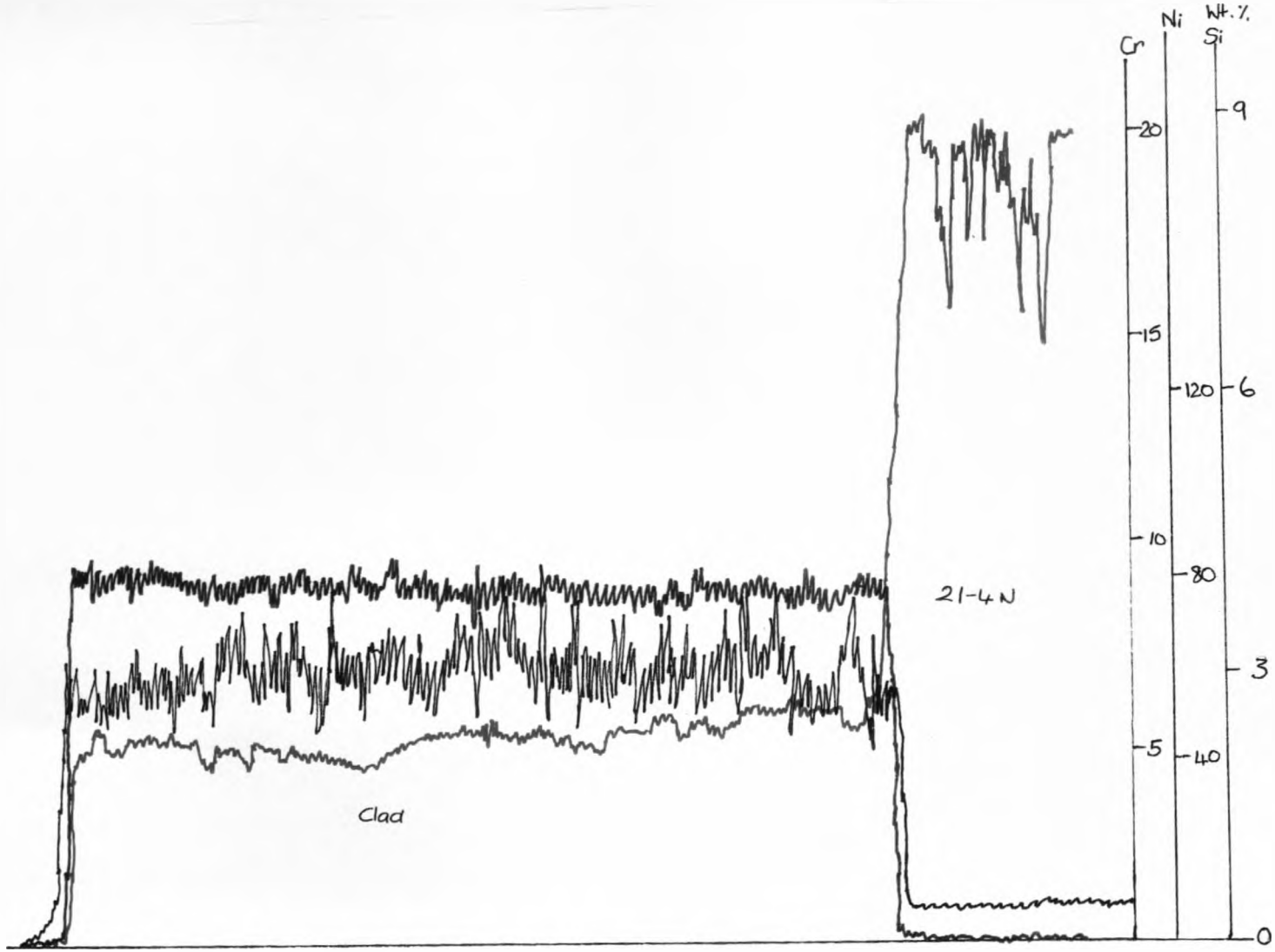

Fig. 7.8 (a) EPMA traces for Stellite 35 clad on 21-4N substrate, q=2kW, d=5mm, v=15mm/s

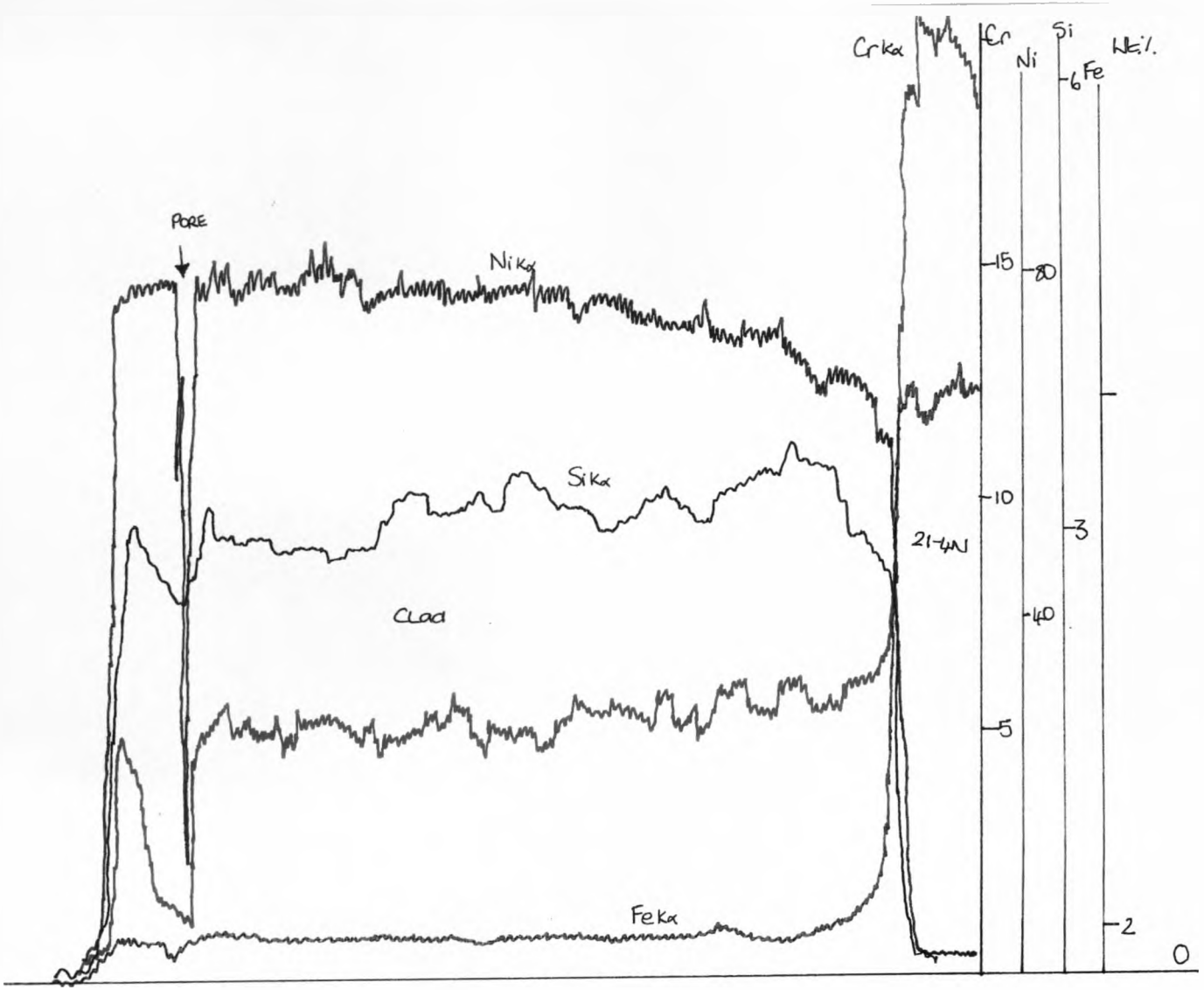

Fig. 7.8 (b) EPMA traces for Stellite 35 clad on 21-4N substrate, q=2kW, d=5mm, v=7mm/s

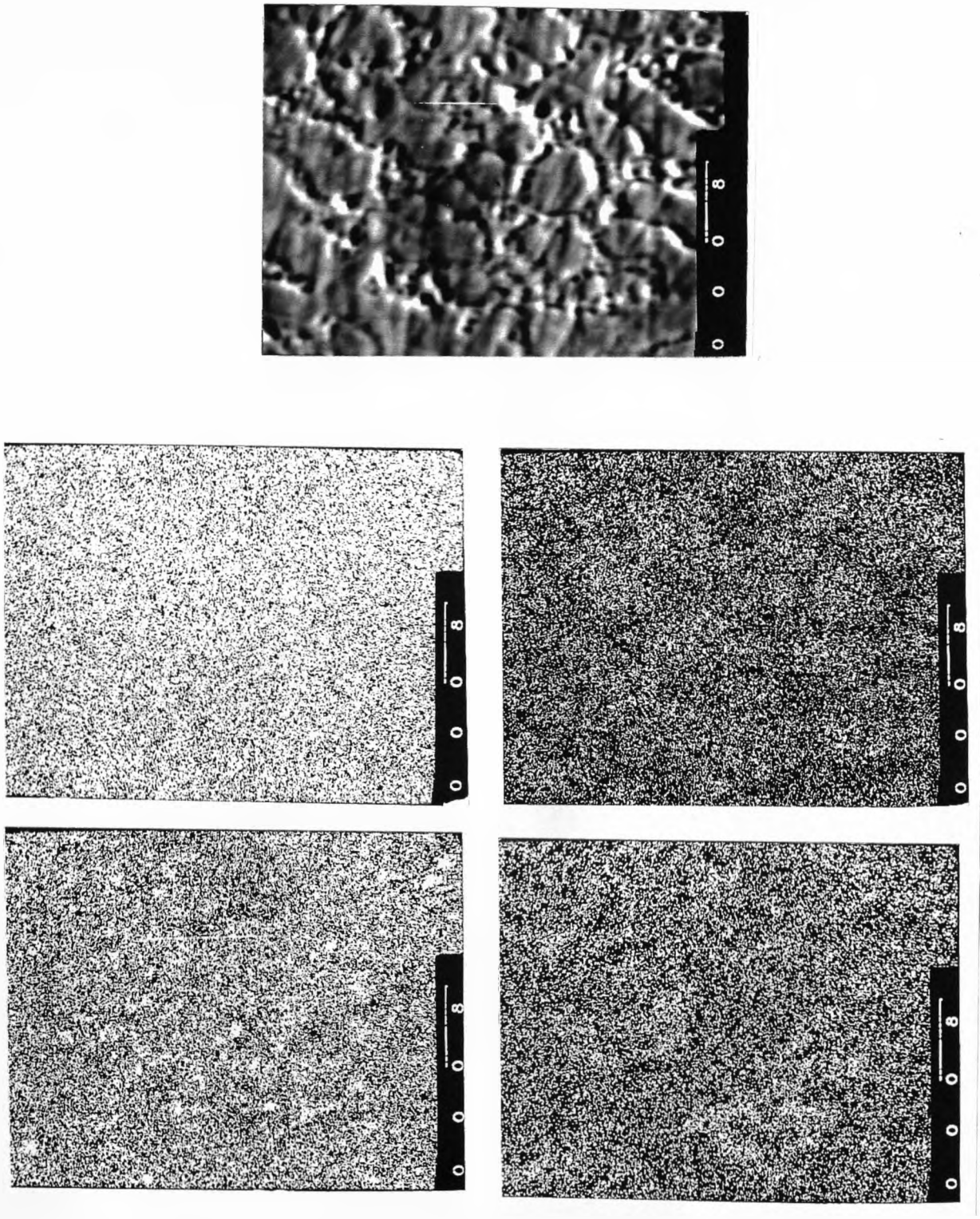

Fig. 7.9 Dot mapping micrographs of standard Stellite 35 clad on 21-4N

Fig. 7.10 Geometry using twin feed tubes for cladding Stellite 35 + alumina

Fig. 7.14 Attack of alumina on 21-4N surface for laser cladding at 2kW, d=5mm and speeds 15, 10 and 5mm/s

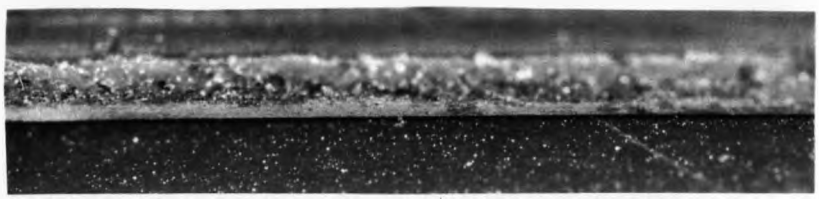

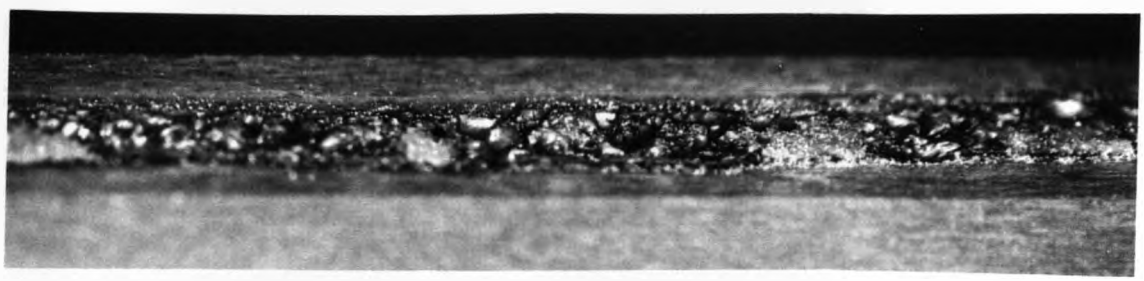

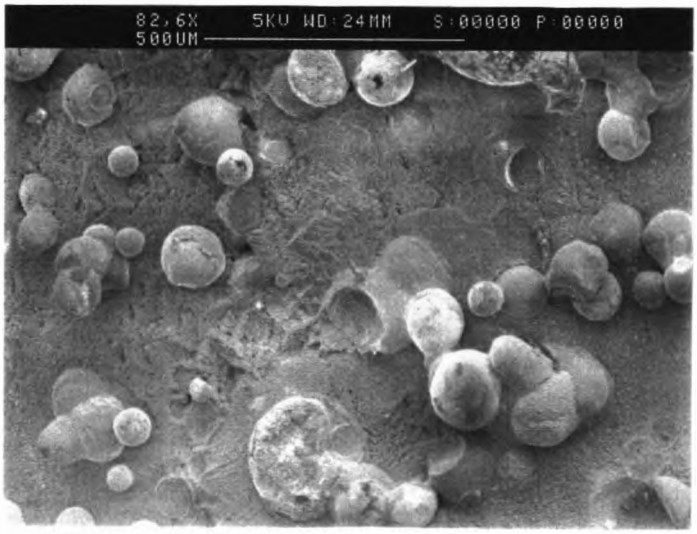

Fig. 7.11 (a) and (b) Above, (a) showing upper surface of sloughed alumina layer, and (b), below showing lower surface, alumina has clearly melted and resolidified

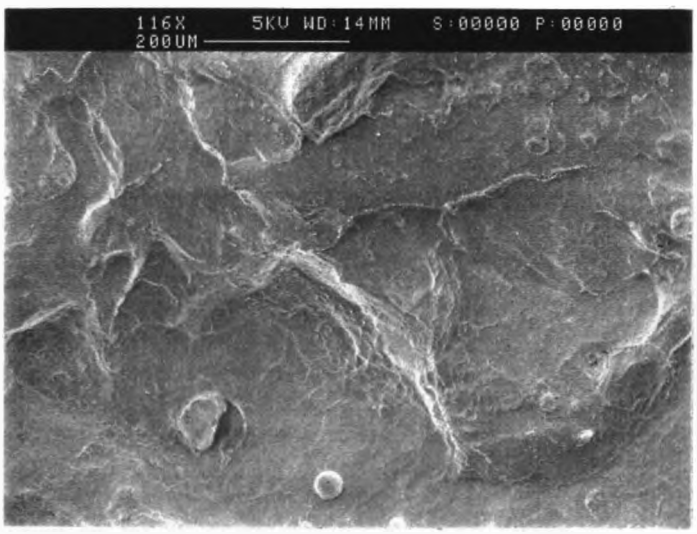

(a)

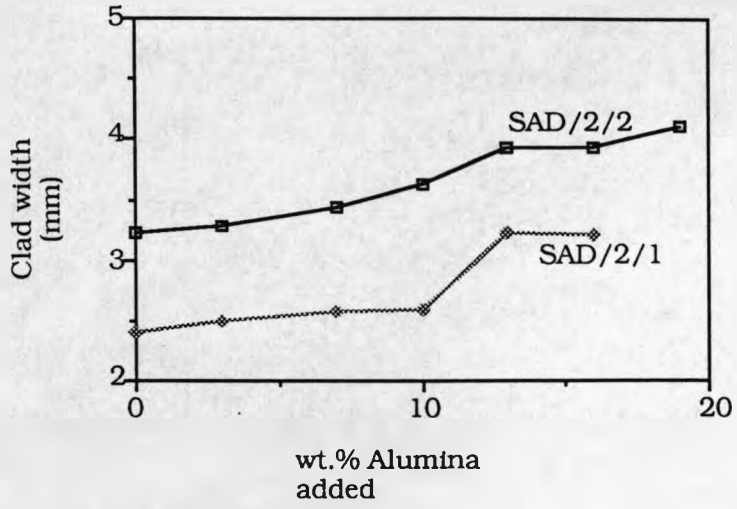

(b)

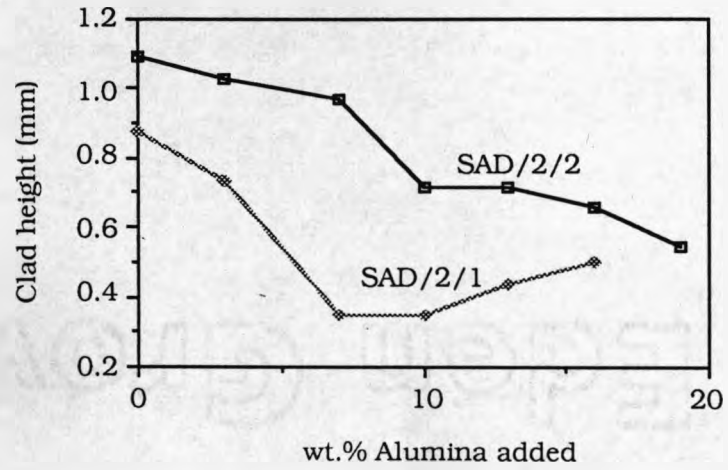

(c)

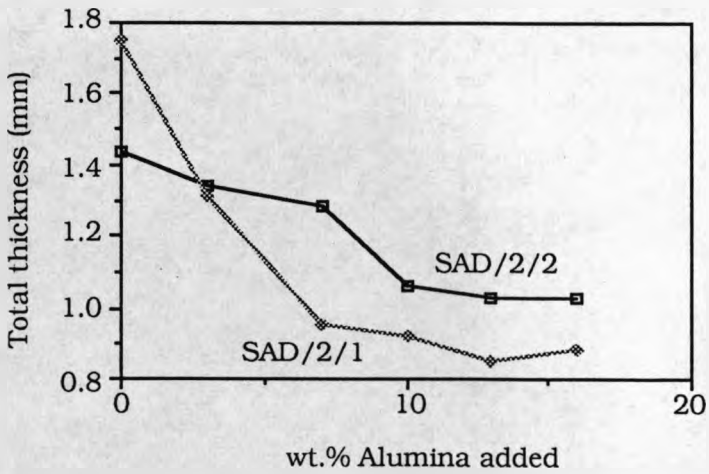

Fig. 7.12 (a)-(c) Dimensional relationships of Stellite + alumina clads with wt.% alumina added

(d)

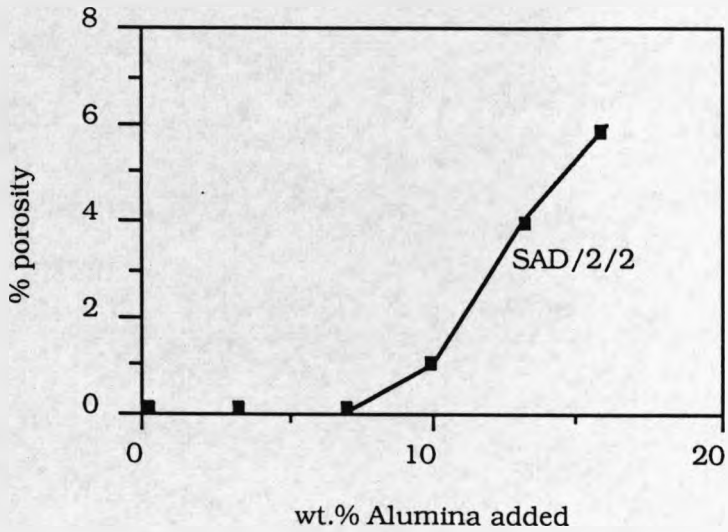

(e)

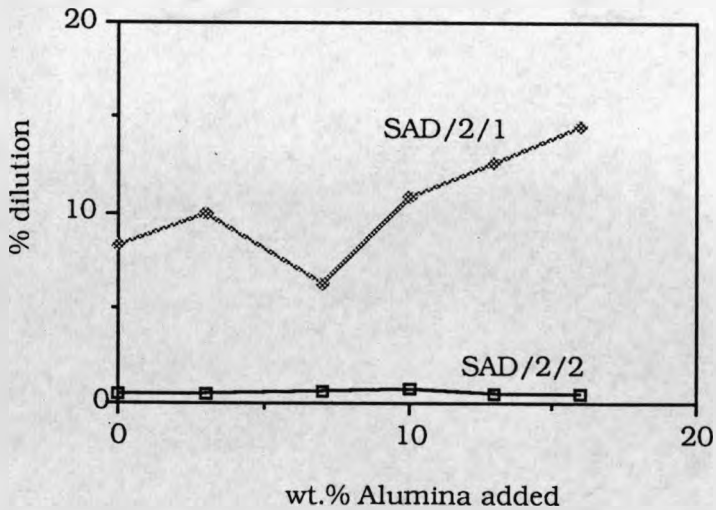

Fig. 7.12 (d) and (e), Variation of Hardness and Dilution for Stellite 35+alumina clads with wt.% alumina added

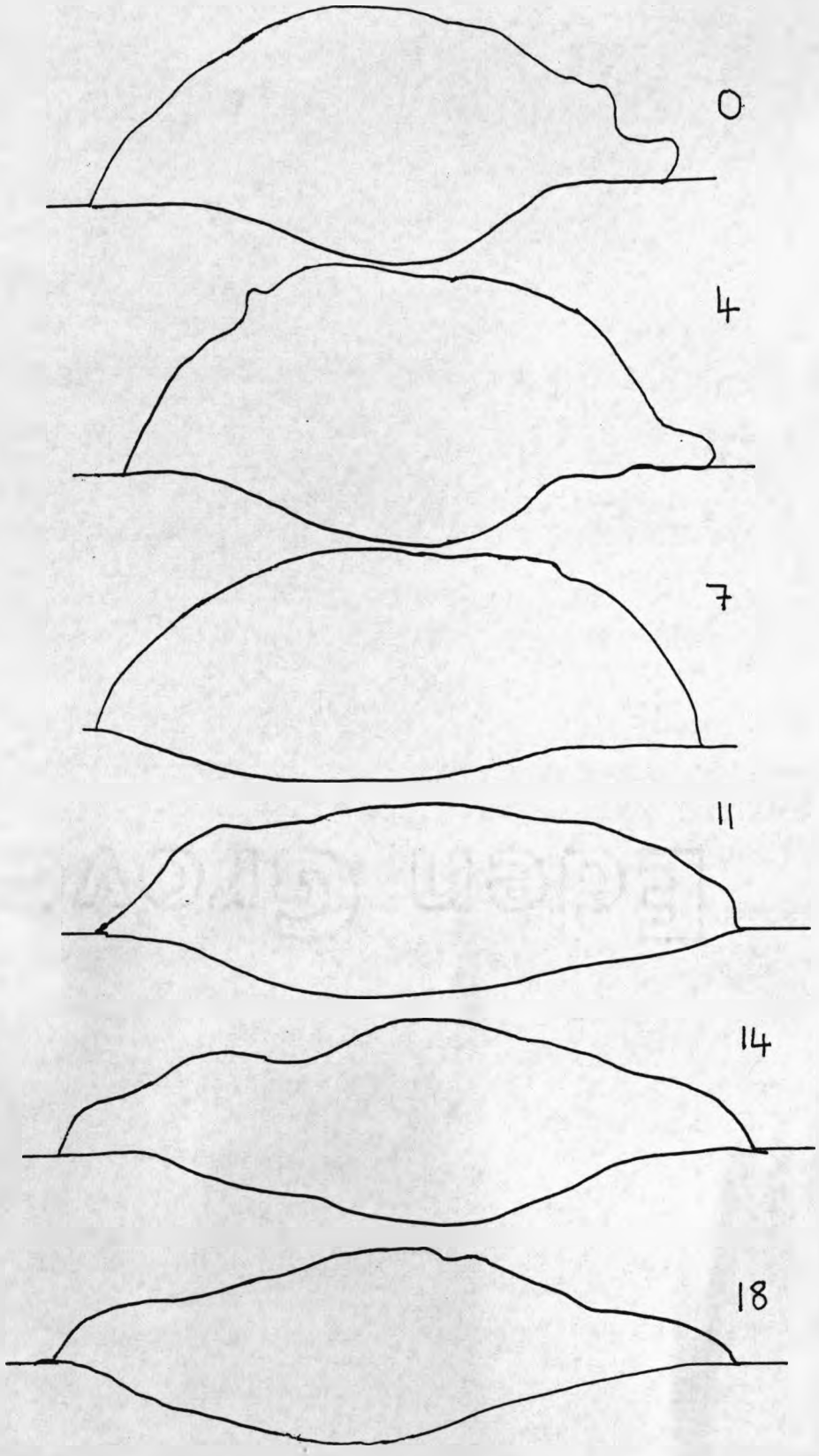

Fig. 7.13 Change in shape of clad with increasing wt.% alumina added

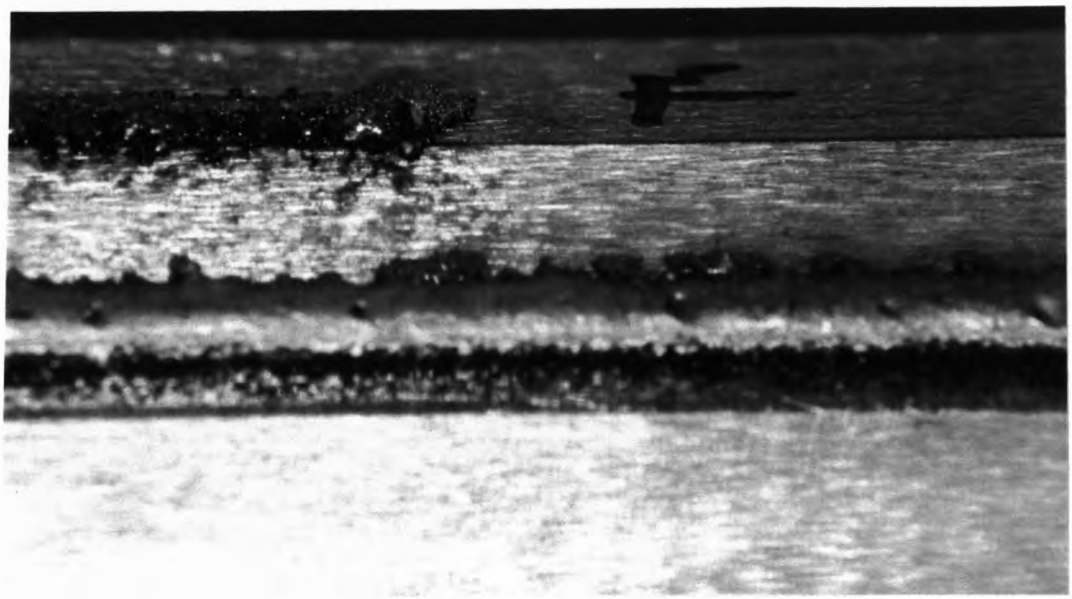

Fig. 7.15 Example of 'pulsed' deposit due to irregular flow of ceramic powder at low motor speeds (<200rpm)

Fig. 7.16 SiC particles covering clad surface (upper) and embedded in upper part of clad (lower)

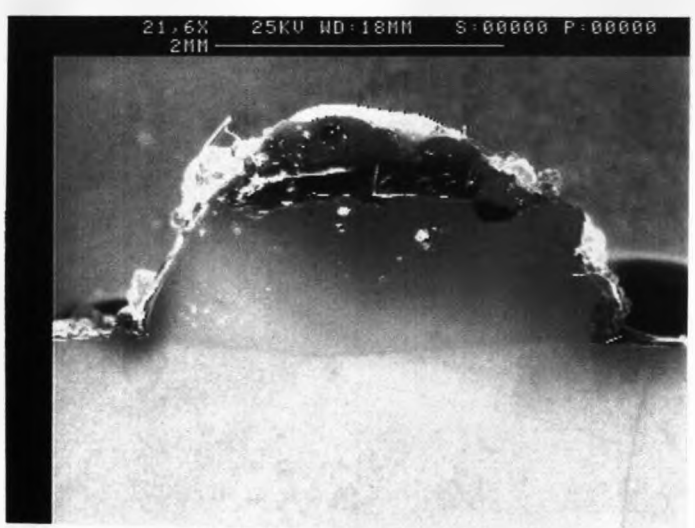

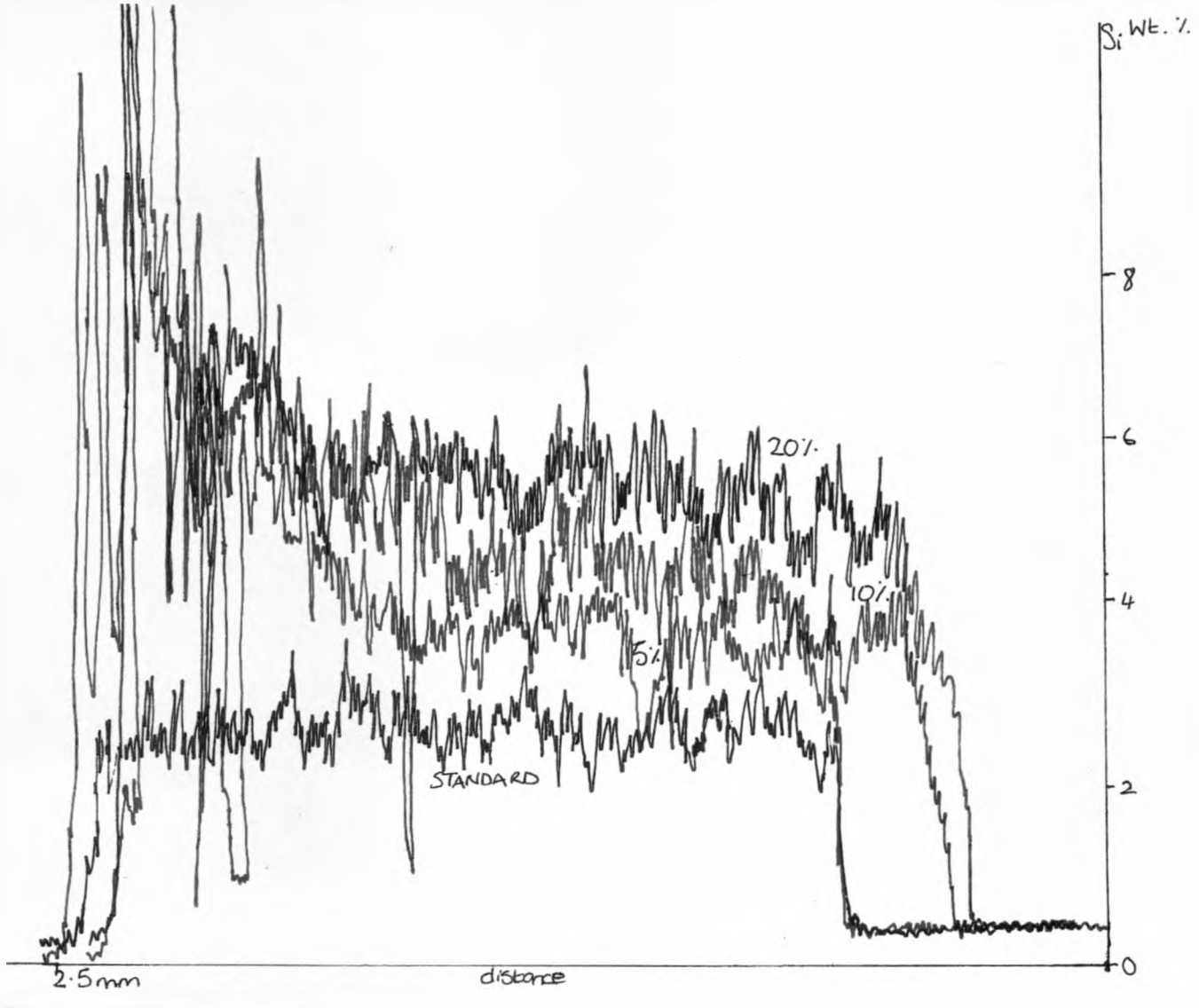

Fig. 7.17 EPMA traces for 5, 10 and 20 % by weight SiC premixed with Stellite 35

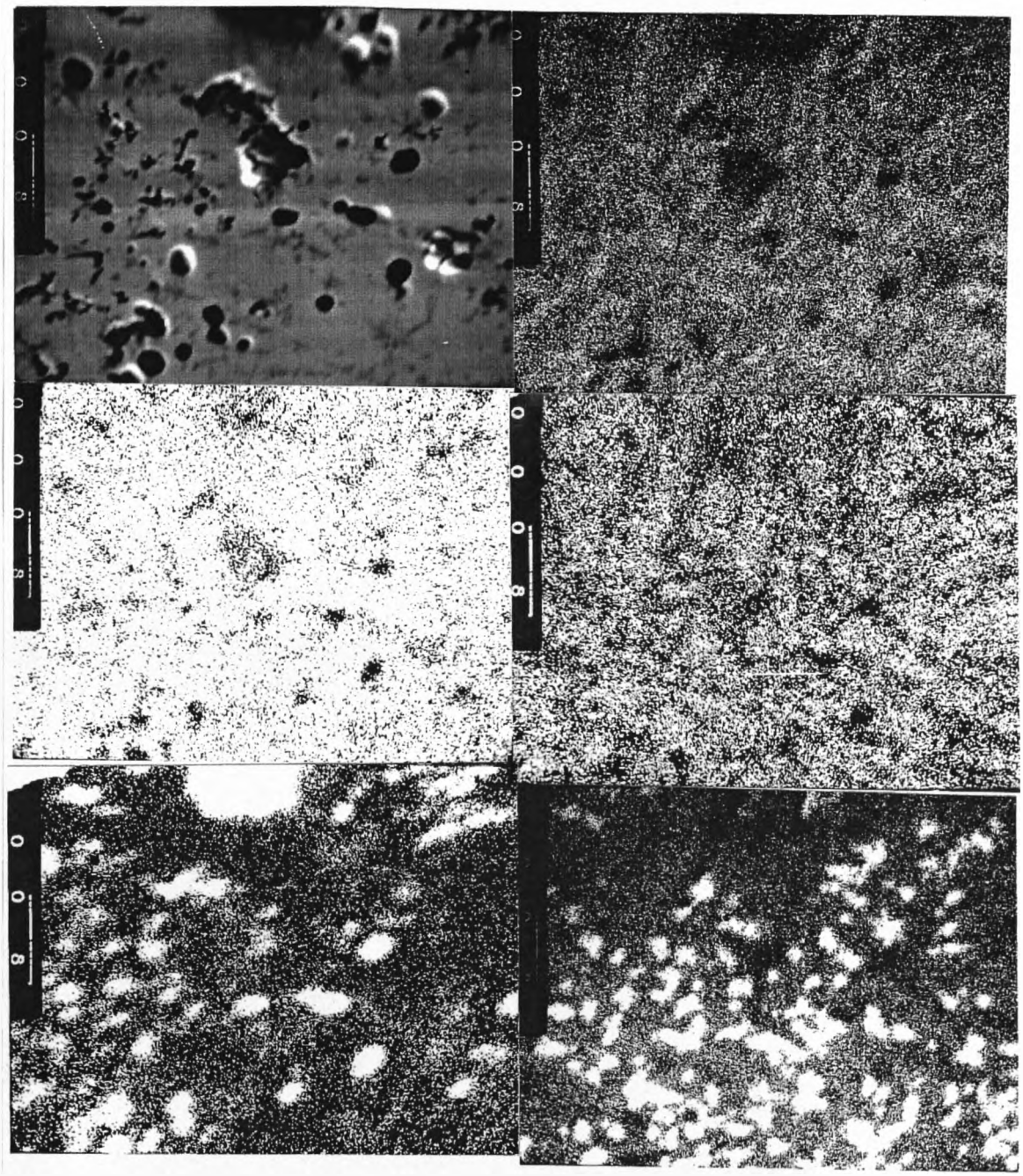

Fig. 7.18 Dot maps for 5 % by weight SiC premixed with Stellite 35

Scanning electron micrograph showing dimensions of a typical clad

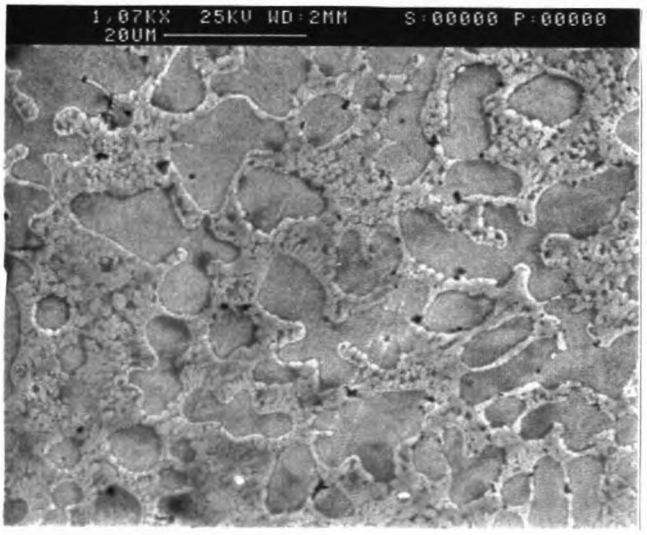

Scanning electron micrograph illustrating dendritic microstructure

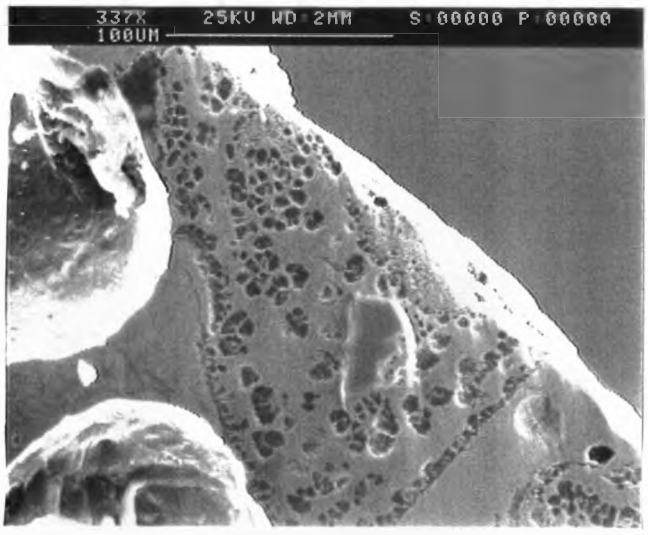

Scanning electron micrograph of partially dissolved SiC particle

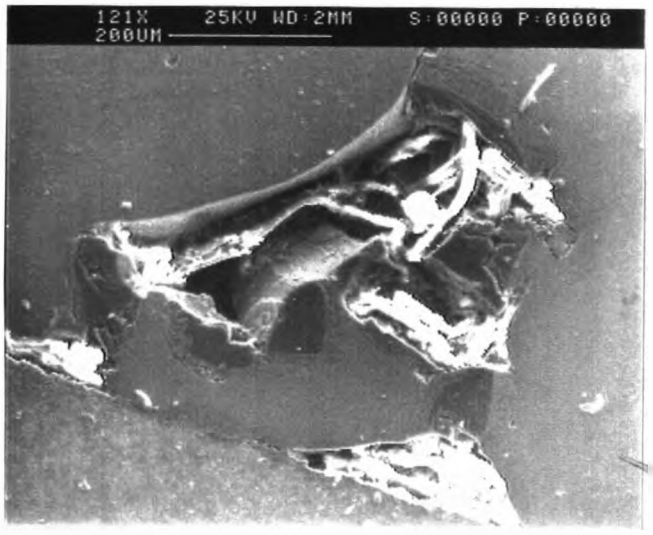

Scanning electron micrograph of undissolved SiC particles, close to interface

Scanning electron micrograph of undissolved SiC particle, near surface

Fig. 7.19

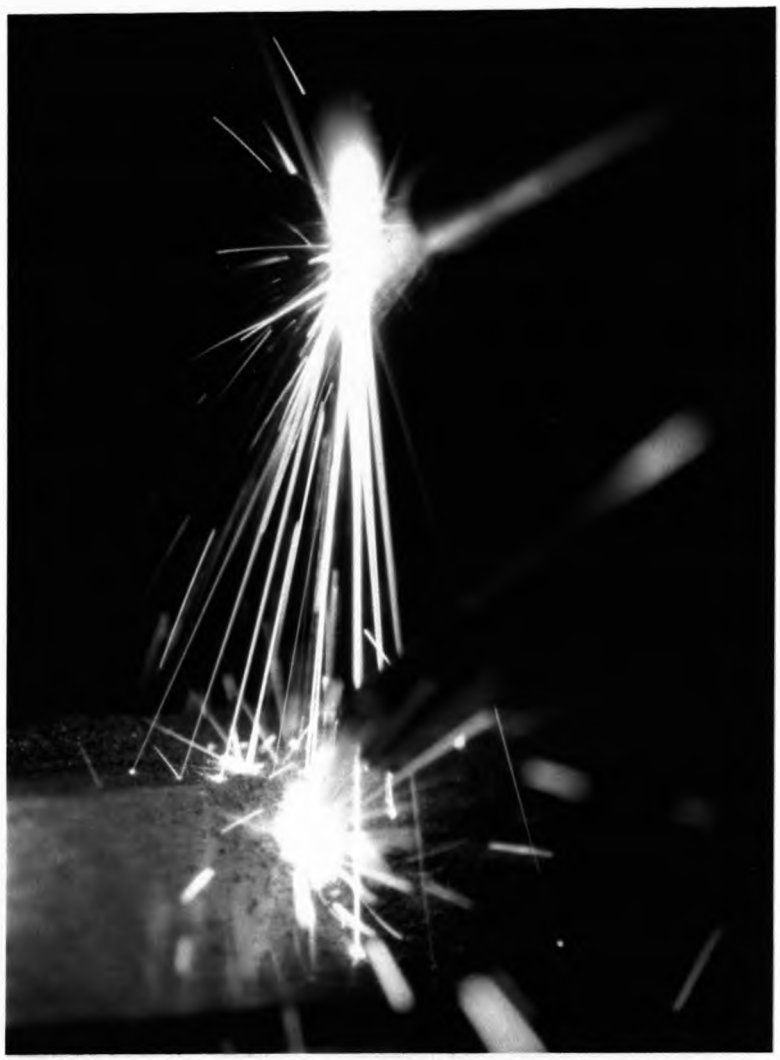

Fig. 7.20 Two geometries used for cladding of Stellite 35 and ceramic powders

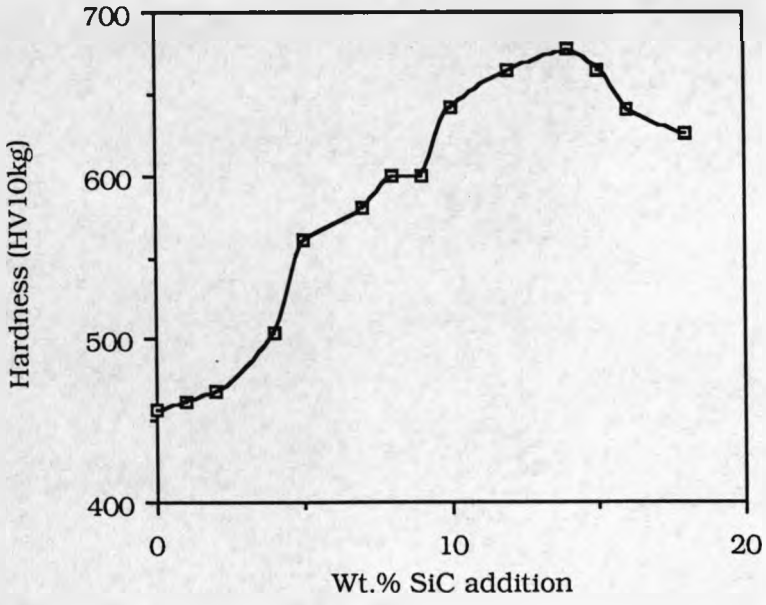

Fig. 7.21 Hardness of deposit as a function of SiC added (reservoir mixing)

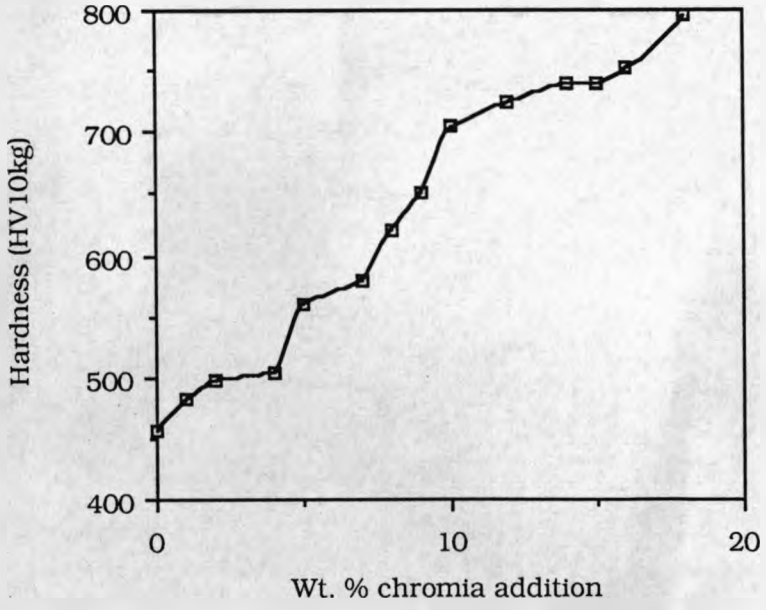

Fig. 7.25 Hardness of deposit as a function of chromia added (reservoir mixing)

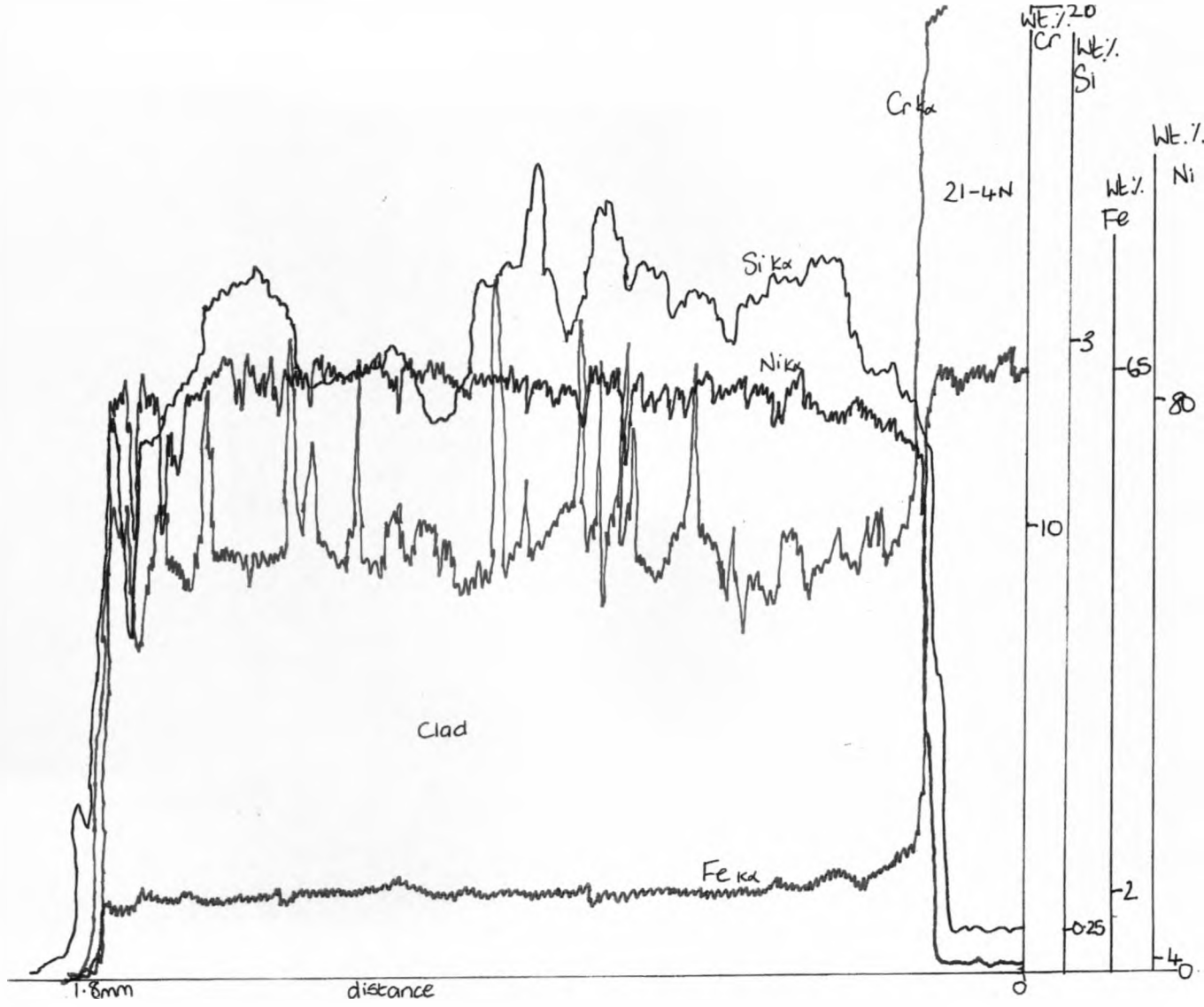

Fig. 7.22 EPMA trace for clad made with Stellite 35 + 10 Wt.% chromia, premixed

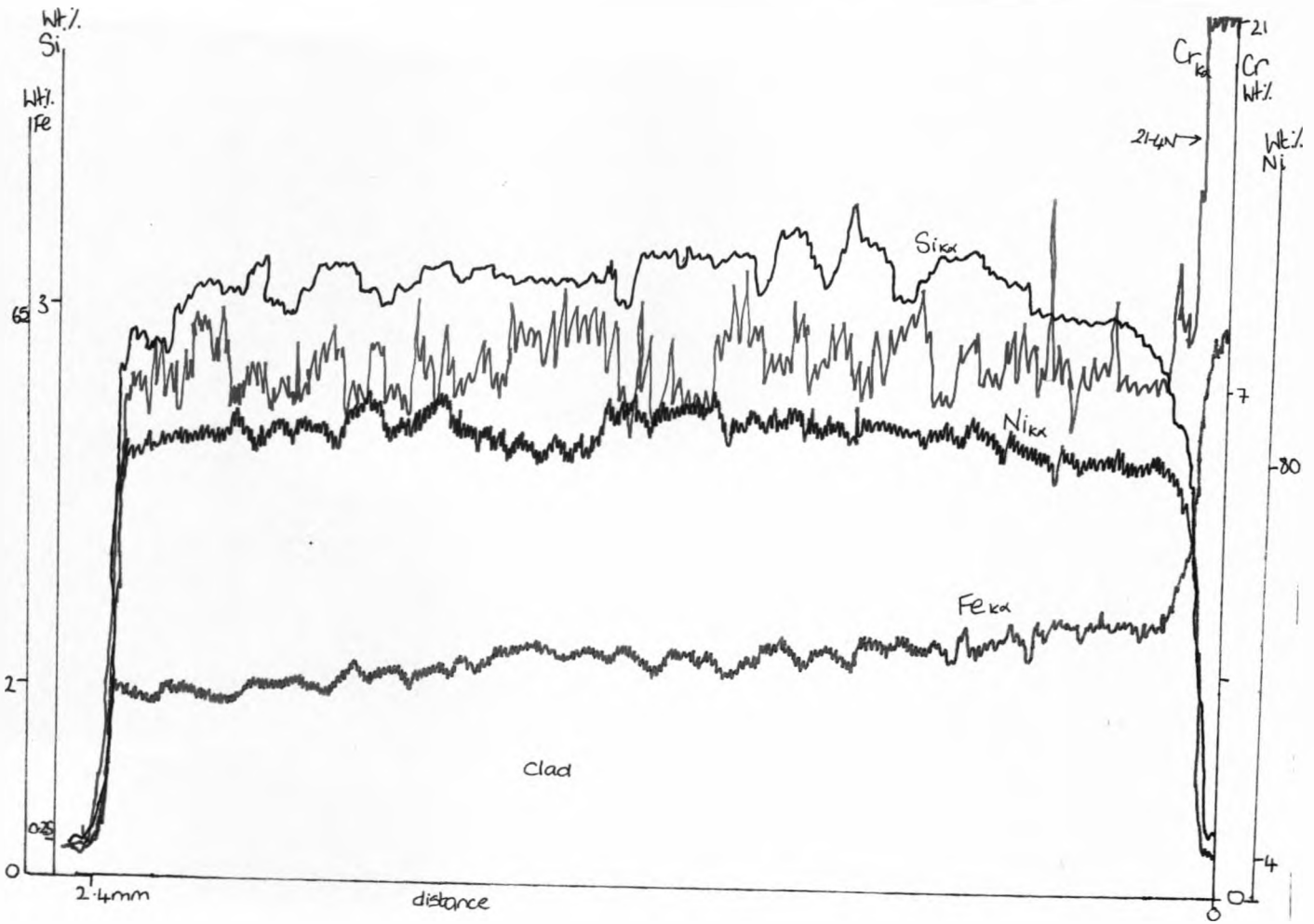

Fig. 7.23 EPMA trace for clad made with Stellite 35 + chromia, twin feed system

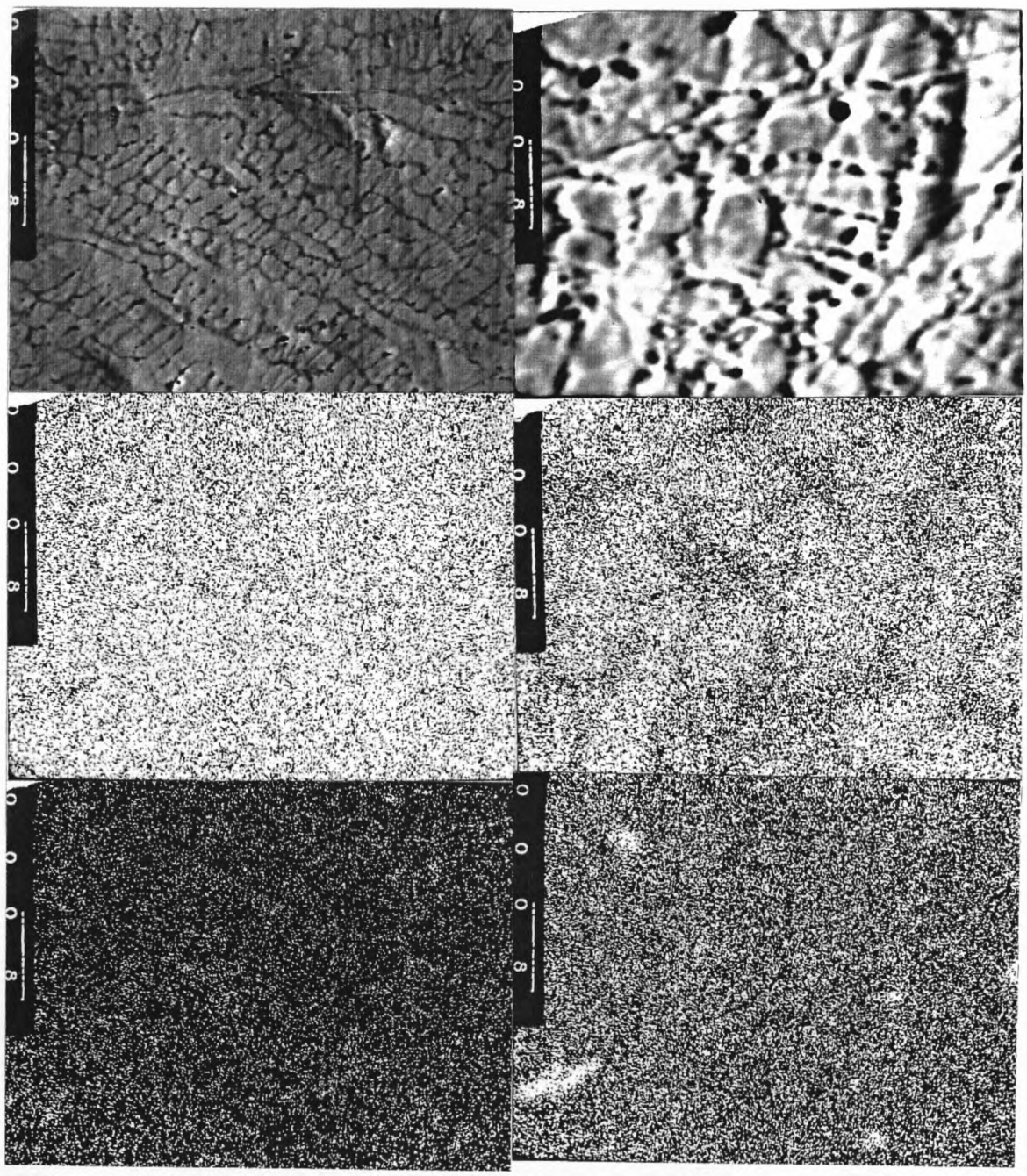

Fig. 7.24 Dot mapping for 10 Wt.% chromia + Stellite 35, premixed

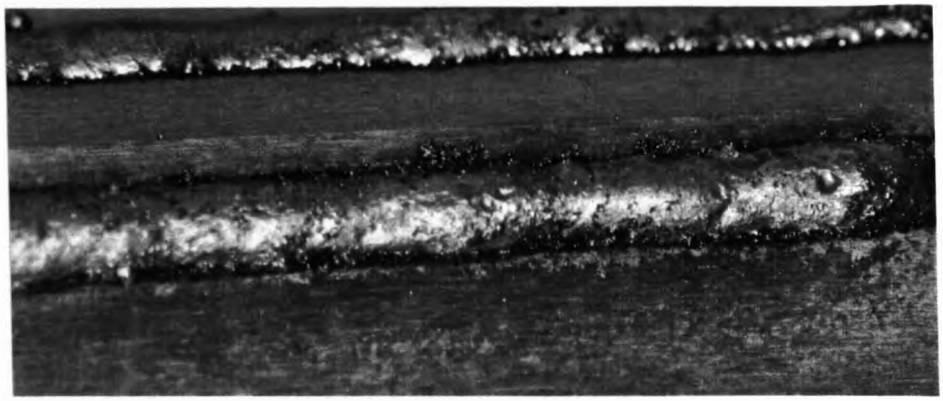

Fig. 7.26 Typical clad of Stellite 35 + chromia, no evidence of slagging of chromia. Also shown some examples of undissolved ceramic inclusions at clad surfaces.

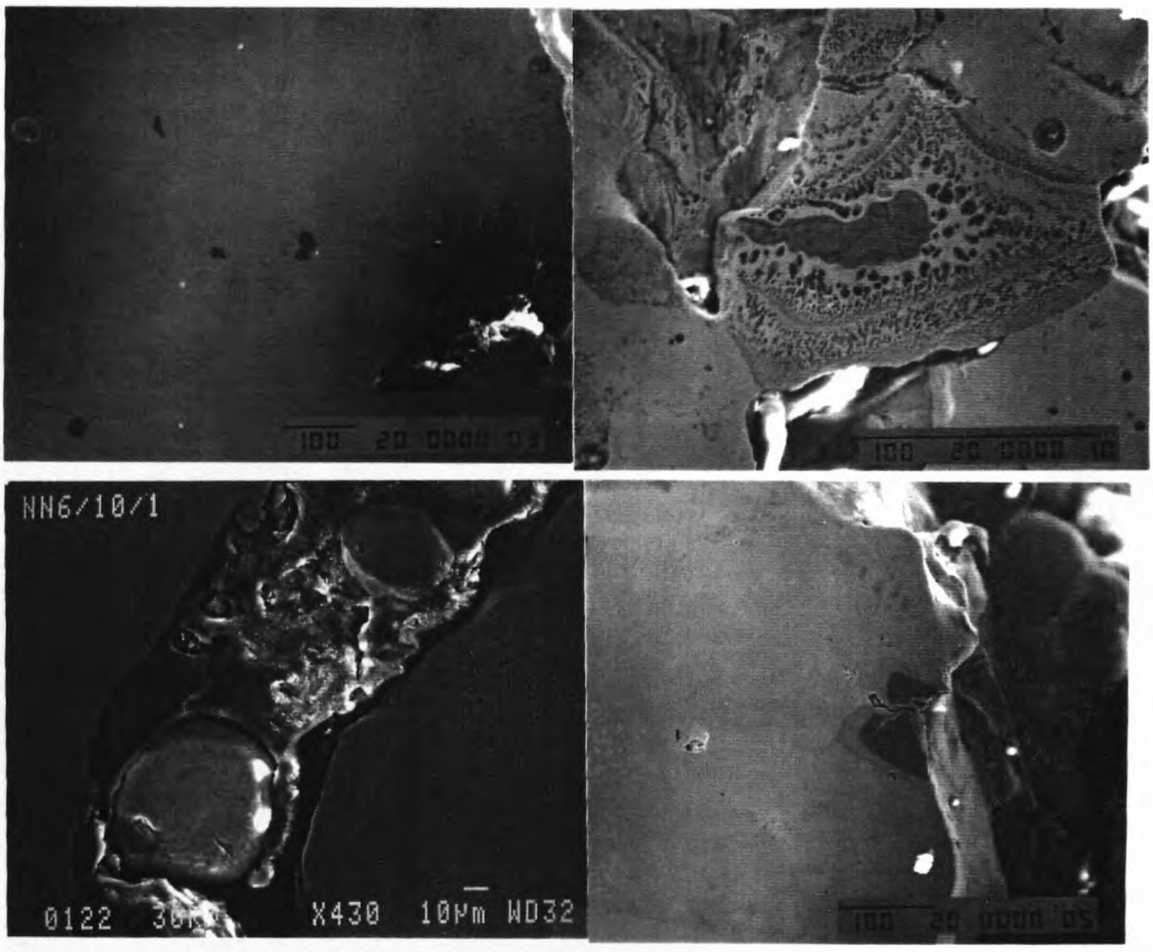

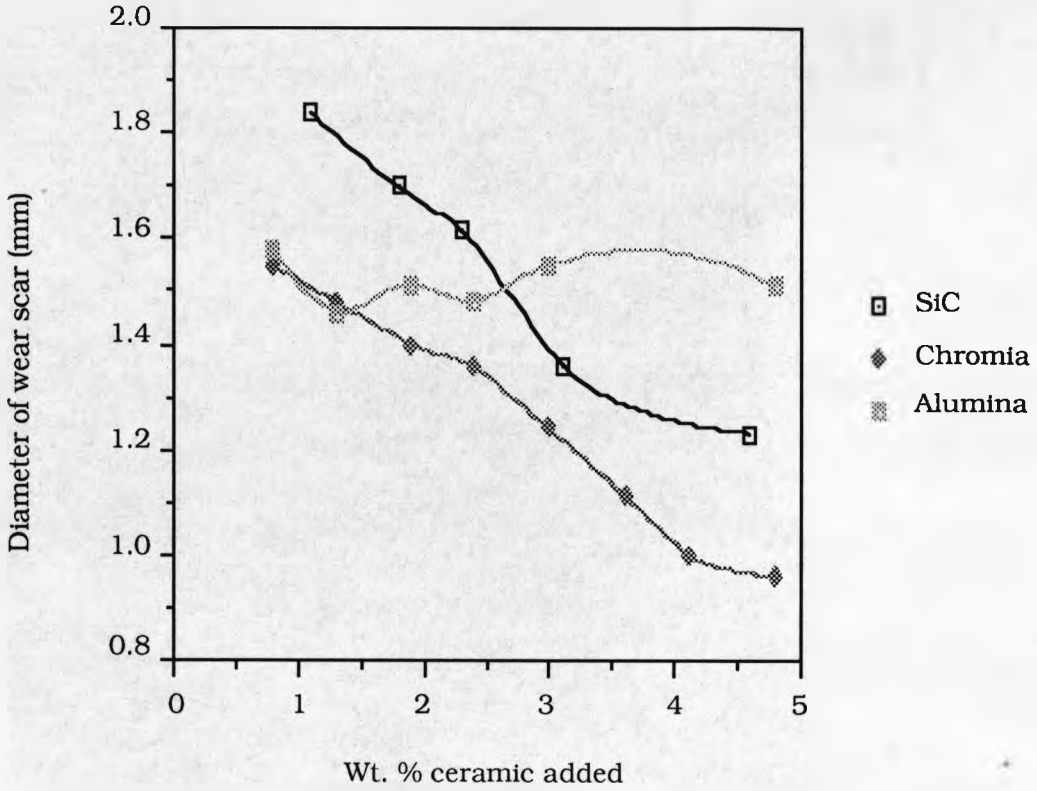

Fig. 7.27 Wear scar diameter against Wt.% ceramic addition, clads deposited at 2kW, d=5mm, v=8mm/s

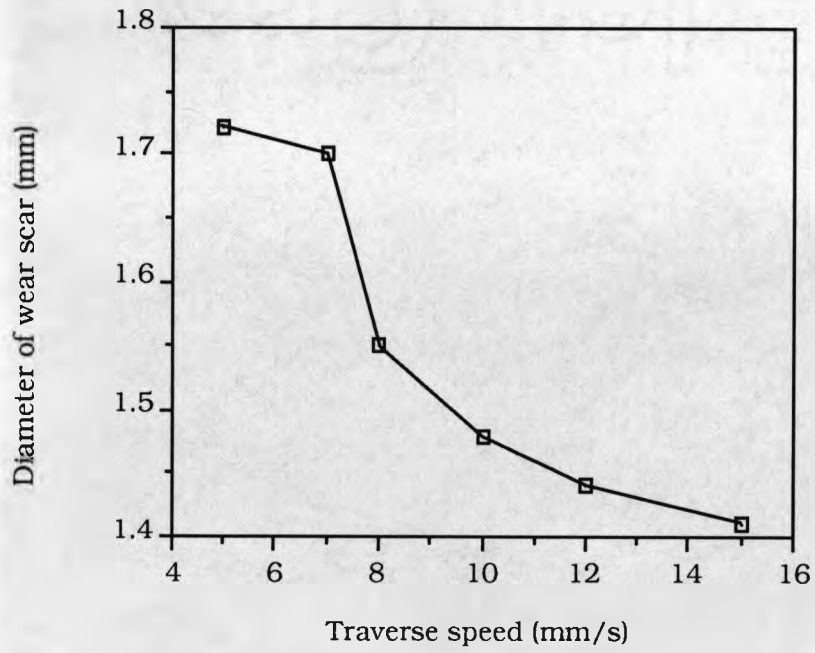

Fig. 7.28 Wear scar diameter against traverse speed for Stellite 35 clads at constant flow rate 0.32g/s, parameters as above

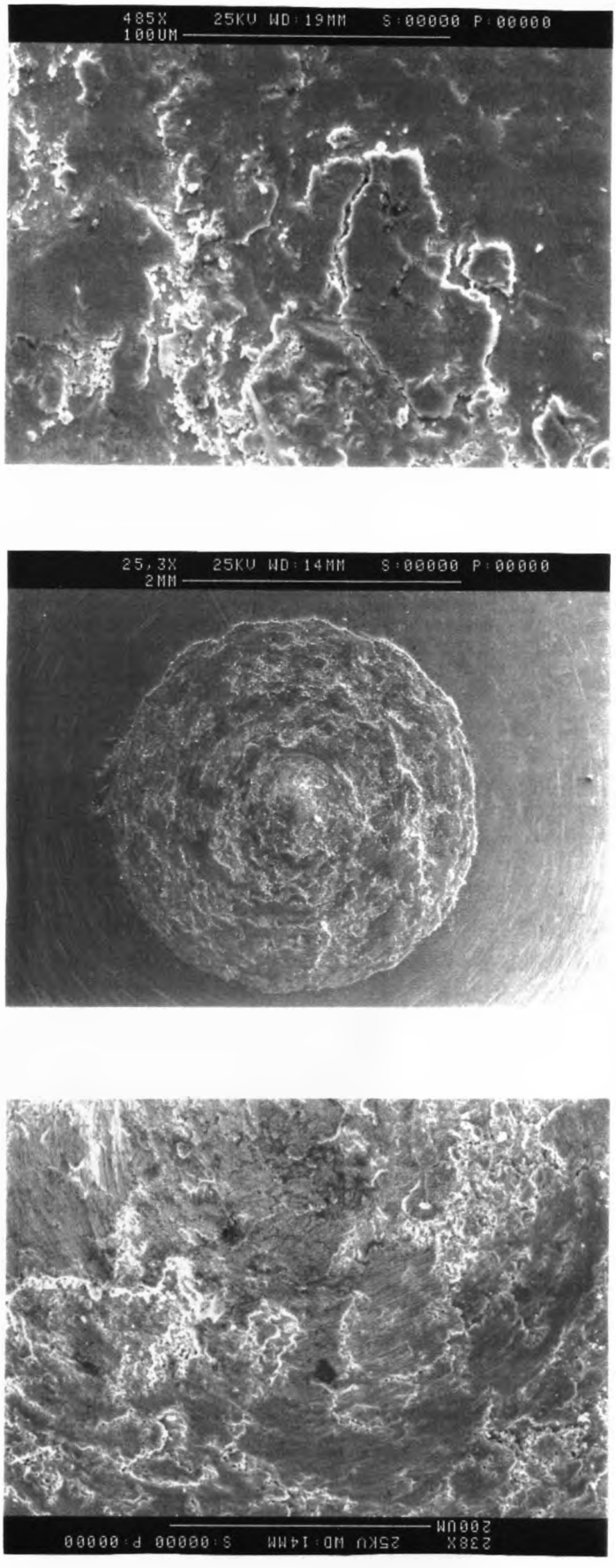

Fig. 7.29 (a), (b) and (c) (a) wear scar on substrate (NN4/6/3), (b) and (c) wear scar on pin (NN4/6/3). Conditions: q=2.5kW, v=18mm/s, d=5mm, 10Wt.% SiC in Stellite 35 premixed.

Reference Number	Laser Power (kW)	Beam Diameter (mm)	Traverse Speed (mm/s)	Powder Flow Rate (g/s)	Observations
K1	1.27	6.5	10.0	29.14	Heavily diluted
K2	1.27	6.5	5.0	29.14	Dilution and melting
K3	1.17	6.5	10.0	29.14	Thin clad still dilution
K4	1.23	6.5	10.0	29.14	Dilution
K5	1.23	6.5	10.0	20.61	Dilution
K6	1.23	6.5	15.0	20.61	Good clad
K7	1.17	6.5	15.0	29.14	Good clad
K8	1.17	6.5	15.0	37.67	Good Clad
K9	1.17	6.5	10.0	37.67	Excessive melting
K10	1.17	6.5	10.0	29.14	Excessive melting
K11	0.54	6.5	10.0	29.14	No powder melting
K12	0.90	6.5	10.0	29.14	No powder melting

Table 7.1 Operating parameters for cladding of Stellite 6'W' on mild steel.

No	power kW	speed mm/s	spot size mm	Wt. % SiC added	aspect ratio	Wt. % SiC measured
1	2.03	10	6.0	0	1.2	2.6
2	2.03	10	6.0	2.5	1.2	3.2
3	2.03	10	6.0	4.5	1.3	3.9
4	2.03	10	6.0	5.0	1.4	3.8
5	2.03	10	6.0	10.0	1.6	4.9
6	2.03	10	6.0	20.0	1.6	6.4

No	power kW	speed mm/s	spot size mm	Wt. chromia added	aspect ratio	Wt. % chromia measured
1	2.05	10	6.0	0	1.25	5.8
2	2.05	10	6.0	2.5	1.25	6.3
3	2.05	10	6.0	4.5	1.25	7.4
4	2.05	10	6.0	5.0	1.25	7.6
5	2.05	10	6.0	10.0	1.40	10.5
6	2.05	10	6.0	20.0	1.55	15.3

Wt. % Si in stellite 35 = 3.16, average measured Wt. % = 2.2
Wt. % Cr in stellite 35 = 5.41, average measured Wt. % = 5.8

Table 7.1 EPMA analysis of Stellite 35 plus ceramic clads.

Reference Number	Laser Power (kW)	Beam Diameter (mm)	Traverse Speed (mm/s)	Powder Flow Rate (g/s)	Observations
R1	1.43	6.5	2.65	22.31	No shroud. Powder not sticking.
R2	1.41	6.5	1.59	22.31	No shroud. Valve glowing red hot.
R3	1.93	6.5	12.0	22.31	No shroud. Clad baubled.
R4	1.93	6.5	20.67	22.31	No shroud. Clad sticking in parts.
R5	1.89	6.5	1.13	22.31	No shroud. No clad formed.
R6	1.92	6.5	1.24	22.31	No shroud. Valve red hot, clad baubled.
R7	1.92	6.5	1.24	22.31	No shroud. Clad smooth, oxidised.
R8	1.92	6.5	1.24	22.31	Smooth clad, no oxidation. Red hot.
R9	1.92	6.5	1.59	22.31	Thicker clad, no oxidation. Promising.
R10	1.89	6.5	2.14	22.31	Clad flat in groove. Very promising.
R11	1.91	6.5	2.65	22.31	Baubled clad, too narrow.
R12	1.85	6.5	3.15	22.31	Baubled clad.
R13	2.56	6.5	2.65	22.31	Misaligned feed.
R14	2.51	6.5	2.65	22.31	Misaligned feed.
R15	2.45	6.5	2.14	22.31	Good track, slightly baubled.
R16	2.45	6.5	1.82	22.31	Good track.
R17	2.45	6.5	3.15	22.31	Baubled clad.
R18	2.18	6.5	2.14	22.31	Good track, slightly misaligned.
R19	2.17	6.5	2.65	22.31	Baubled clad.
R20	2.17	6.5	1.82	22.31	Good track, thicker than R18.

Table 7.2 Operating parameters for cladding Stellite 6'W' on valve seat faces.

Reference Number	Laser Power (kW)	Beam Diameter (mm)	Traverse Speed (mm/s)	Powder Flow Rate (g/s)	Observations
W1	2.02	6.5	2.14	22.31	Good clad but shutter fault disrution.
W2	2.02	6.5	2.14	22.31	Slightly off-line and baubled.
W2i	2.02	6.5	1.98	22.31	Better alignment.
W3	2.04	6.5	1.98	22.31	Misaligned.
W4	2.09	6.5	1.98	22.31	Clad patchy but promising.
W5	2.09	6.5	1.98	22.31	Good track, valve edge slightly distorted.
W6	2.07	6.5	2.14	22.31	Baubled clad.
W7	1.99	6.5	1.82	22.31	Good track.
W8	1.99	6.5	1.82	22.31	Good track.

Table 7.3 Operating parameters for cladding Stellite 6'W' on valve seat faces.

Ref.No.	P (kW)	d (mm)	v (mm/s)	Flow rate(rpm)	Observations
1.1	2.00	5.0	10.0	1000	Baubled clad
1.2	1.99	5.0	10.0	1000	Incomplete melting
1.3	2.02	5.0	10.0	1000	Incomplete melting
1.4	1.97	5.0	5.0	1000	Good-baubled edges
2.1	1.97	5.0	7.0	1000	Good-baubled edges
2.1	1.97	5.0	8.0	1000	Good-baubled edges
2.3	1.97	5.0	7.0	600	Insufficient powder
2.4	1.97	5.0	7.0	600	Insufficient powder
3.1	1.92	5.0	5.0	600	Good clad, smooth
3.2	1.95	5.0	5.0	500	Good clad, smooth
3.3	1.95	5.0	5.0	500	Good clad-flatter
3.4	1.95	5.0	5.0	600	Incomplete melting

Table 7.4 Operating parameters for cladding Stellite 35 on mild steel.

CHAPTER 8

DISCUSSION - LASER SURFACE CLADDING

8.1 Cladding of Stellite 6'W' on mild steel

The first section of this discussion relates to the cladding of Stellite 6'W' on mild steel substrates and grooved engine valve seat faces.
A variety of clad shapes can be produced, depending on the operating conditions. This is in accordance with observations made by Powell (16), who found that three basic bead geometries exist for a range of conditions. These are illustrated in Fig. 8.1. The profile in Fig. 8.1(a) is produced with a large (>5mm) beam diameter and sufficient or excessive powder mass flow. Geometry 8.1(b), on the other hand, results from a small beam diameter (<2.5mm) and again, sufficient or excessive powder mass flow. Beam diameters <6mm coupled with low traverse speed (<7mm/s) produced shape 8.1(c), which exhibits high dilution. Powell was interested in producing overlapping clad tracks and therefore the optimum shape was (a), for smooth surface finish, minimum dilution and no inter-run porosity (i.e. angle θ acute). For the purposes of cladding engine valves, geometry (a) is still optimum as this geometry will lead to superior surface quality, minimum dilution and a geometry which will successfully fill the machined groove in the valve seat.

Increasing the power results in thicker, wider tracks due to more efficient powder melting. Similarly, increasing the powder flow rate or decreasing the traverse speed produces more substantial clads. The optimum conditions for the combination of Stellite 6'W' powder and a mild steel substrate are as follows: traverse speed=5mm/s, power=1.95kW and powder flow rate=0.35g/s.

In all cases, the clads exhibit the characteristic constitutionally supercooled hypoeutectic alloy solidification structure, consisting of a dendritic solid solution surrounded by carbide containing eutectic. The columnar dendrites clearly indicate the direction of heat flow and solidification as away from the substrate surface, as shown in Fig. 7.4.

Considering the Co-Cr-W-C alloy system, chromium and tungsten have similar affinities for carbide formation (98), and since the relative percentages of the two elements in the alloy are 28.7:4.4, it can reasonably be assumed that chromium carbides will be present to a much greater extent than will tungsten carbides, and the system can be estimated by considering the Co-Cr-C alloy system. Since both chromium and tungsten have high solid solubilities in cobalt, any excess, which

does not form carbides is used to strengthen the cobalt matrix by solid solution strengthening (195). Antony (57) showed that the pseudo-binary Co-(CrW)-C system, with approximately 30 wt% Cr and 4-17 wt% W has a eutectic nature where the eutectic occurs between 1.5 and 2% carbon. This involves the formation of M_7C_3 carbides and metastable α (fcc) cobalt solid solution, rather than the hcp type cobalt structure which is generally stable at room temperature. This is a result of the presence of the alloying elements which suppress the transformation. The carbide phase approximates to $(Cr_{0.8}Co_{0.15}M_{0.05})_7C_3$ where M is tungsten or other residual elements. EDX analysis of the dendritic structure observed in the deposits produced here substantiates the above with cobalt being detected in the dendritic regions at slightly higher levels than the bulk composition would indicate. Considering Fig. 8.2, which shows an isothermal section of the C-Co-Cr system at 800°C (54), it is obvious that the composition under consideration exhibits the M_7C_3 type carbide structure.

Variations in the scale of the microstructure are due to differences in the cooling rates. The scale of the dendritic strucures is too fine to determine microhardness of the phases, but the macrohardness of the deposits ranges from 500-750 HV_{10}. The microstructure becomes finer with increasing processing speed, the secondary dendrite arm spacing decreasing almost linearly from 2μm to just below 1μm for an increase in speed from 5-20mm/s.

A HAZ similar to that produced by LTH was observed in the substrate. A progression of martensite, through bainite, pearlite and a ferritic base was observed. This is the classic structural change expected from a rapidly quenched mild steel substrate.

Some of the tracks exhibit slight porosity (pore size 2-10μm) towards the centre of the clad bead. This is likely to be caused by incomplete powder melting since the pores are not smooth and spherical as one might expect if trapped vapour were the cause. The solution to this problem is to adjust the specific energy (P/vd) incident on the powder and work piece such that complete melting occurs prior to the clad solidifying.

8.2 Valve cladding

Clads made onto 21-4N valve seat faces show very encouraging results. As above, the slower processing speeds result in larger deposit dimensions. This effect was shown to be linear upto a certain point (16) due to the Guassian nature of the beam. The point at which linearity breaks down is defined by the point at which conduction from the melt pool limits the melting threshold diameter. i.e. as the interaction time increases, the molten pool diameter also increases as an increasing beam area is capable of causing melting. At some point this effect becomes limited as the melting threshold diameter increases only a small

amount and conduction becomes more significant. The depth of deposit has also been shown to increase linearly with interaction time (16), a factor which is limited by the value of P/vd. At some critical value of P/vd, keyholing dominates reducing the effectiveness of the deposit. This effect is more commonly associated with laser welding. Keyholing occurs when boiling is initiated in the molten pool. The subsequent release of vapour results in an increase in the coupling of the energy to the substrate thereby increasing the rate of vapourisation. A surface depression forms which acts as a 'black body' absorbing a very high proportion of the incident energy. In addition to reducing the value of P/vd to below that critical for keyhole formation, increasing the powder flow rate may be used to avoid such defects. A higher flow of powder effectively acts to shield the substrate surface from the incident energy. Keyholing was not noted in this series of experiments.

No porosity is observed in the valve cladding experiments. It is therefore reasonable to assume that the energy density, interaction time and powder flow rate are close to their optimum values so that just enough powder is melted to produce a homogeneous, dense clad. Porosity can be detrimental to the performance of clad layers in terms of strength, corrosion and wear properties and is to be avoided where possible. However, the presence of porosity is difficult to detect without sectioning.

The hardness of Stellite 6 'W' clad layers peaks at around $800HV_{10}$. This compares with $350HV_{10}$ for the base material, 21-4N. Similar layers prepared by the traditional plasma arc deposition route give hardness values of around 475 HV_{10} (51). This represents a considerable improvement in hardness and is likely to be a function of the fine scale of the microstructure.

A major factor of importance to the valve manufacturer, in addition to overall clad quality, is the level of machining necessary after processing. Elimination of one stage in the production process can be highly cost-effective. Some clad deposits produced here on machined grooves show a flat surface finish i.e. the groove is completely filled with cladding material and a smooth, defect-free surface finish is observed. This would probably require only a very light surface grinding operation, if any. A flat deposit, as illustrated in Fig. 7.2 (a), is the result of altering the delicate force balance in the melt pool. This is illustrated in Fig. 8.3 (16). The results are similar to those obtained by Kupper *et al* (151) and Grigor Yants *et al* (150), who both show that blown powder cladding results in homogeneous, low-dilution clads without substrate distortion. Kupper *et al* (151) have shown deposits of a Co-based alloy whilst Grigor Yants (150) used a Ni-based alloy and achieved comparable results. One further interesting point is that no differences in either microstrucuture or hardness are reported in the overlap zone. The composition of the deposits, in both cases, as indeed is the case in this work, correspond to the composition of the initial powder.

One problem which is inherent in this process is ensuring a uniform deposit in the overlap region. Kupper *et al* (151) have successfully overcome this problem by ramping the power in the overlap region to avoid non-uniformity of thickness and also oxidation and porosity in the start-up region. This method limits the overlap region to a very small area. Unfortunately, this facility is not available on the laser used in this study.

A costing analysis for the laser cladding process for engine exhaust valves compared to plasma arc hardfacing, by Williams (196) indicates a number of advantages:

1) Increased productivity.
2) Elimination of back machining.
3) Less labour intensive.
4) Decreased powder consumption and scrap rate.
5) Deposits with zero porosity, low dilution and hardness in excess of $750HV_{10}$.

Monson *et al* (51) compared deposits laid down by laser with other techniques and found that laser cladding was one of the few processes offering a fusion bond with low dilution and deposits with significantly higher hardnesses than those produced by other techniques.

The remainder of this discussion relates to laser cladding of Stellite 35 on 21-4N substrates, and the addition of ceramics to this system.

The search for cost-effective high performance alloys and the need for strategic materials conservation is driving the automotive industry to look outside the conventional Co-base materials for valve seat wear applications. In addition, there is a need to utilise the minimum quantity of powder. Stellite 35 is one such alloy which may be able to replace the more traditional Stellite 6 and Stellite F for diesel engine exhaust valves. Nickel-base hardfacing alloys are known to have excellent wear resistance (62). As previously discussed, the major requirements of a hardfacing alloy for this application are high hot hardness, thermal resistance and stability, creep resistance and adhesive/abrasive wear resistance which requires sufficient carbide volume fraction and suitable size and distribution of the carbide phase. The morphology of the deposit is vitally important in terms of wear resistance (51) and the fine scale microstructures characteristic of laser hardfacing are desirable from this perspective. The aim of the work using Stellite 35 was to assess its suitability for the blown powder laser cladding process and to attempt to alloy it with various ceramic powders to further improve wear resistance.

8.3 Laser cladding of Stellite 35

Cladding of Stellite 35 was found to be extremely successful, requiring less precision on operating parameters than Stellite 6. One initial idea, to allow future incorporation of ceramic particles into the deposit with consideration of their melting points and densities, was to melt the Stellite 35 powder in the beam focus, above the substrate and drop it down onto the surface whilst still molten. This method was thoroughly tried but did not produce a suitable deposit. Although powder melting did occur and the powder fell upon the surface in its molten state, no wetting occured and the powder balled up to form a spheroidal deposit, as shown in Fig. 8.5. This suggests that the surface tension is too high to allow wetting at the surface and the most energetically favourable structure is in the form of balls of alloy deposit. Such deposits are obviously non-uniform and rough with a poor interfacial bond.

Having determined that under most possible geometries whereby Stellite 35 is melted above the substrate surface, there are none which are conducive to good deposits, due to the poor wettability, the optimum parameters for clads made by blowing the Stellite 35 directly into the melt pool are as follows: q=2kW, v=10mm/s, d=6mm, powder flow rate=0.24g/s.

Stellite 35 forms uniform, smooth deposits with relative ease, i.e. the coditions are less restrictive than for the Co-base Stellite 6'W'. Nickel is often added to alloys to improve the weldability and this effect is substantiated by the experiments conducted here. A wide range of conditions can be used to produce clad layers, unlike Stellite 6 which has a very narrow operating window for successful deposits Successful clads of this type were also made by Lugscheider *et al* (60, 62), who found improved wear resistance over plasma sprayed coatings.

8.3.1 Microstructure

The microstructure of the Ni-Cr-Si-B-C alloy system is somewhat complicated due to the fact that carbon, boron and also silicon are able to form intermetallic compounds with nickel and chromium. Additionally, chromium can combine with nickel to form a solid solution. The microstructure of laser deposits of this system differs greatly from the microstructure of layers produced by other methods (150). The behaviour is normally dominated by a Ni/Ni_3B binary eutectic (51), the eutectic occurring at 4% boron and a temperature of $1080^{o}C$. Silicon acts to lower the eutectic temperature and to improve self-fluxing of the alloy, it would seem then that the eutectic is in fact of the form $Ni_3(B,Si)$. Hence the microstructure consists of a solid solution of Cr and Si in nickel with a $Ni_3(B,Si)$ type eutectic containing M_7C_3 carbides, borides and other complex phases. Laser deposition, on the other hand, is reported (150) to result in dissolution of the large carbides and borides and supersaturation of the solid solution, leading to a two phase microstructure of the $\gamma + Ni_3B$ type. This is supported by Monson (51) who reported that the fcc nickel based solid solution

and the orthorhombic Ni_3B were the major phases present. The complex constitution of the alloy is based on the Ni-B system (Fig. 8.5). Dot mapping analysis (Fig. 7.9) is in agreement with this, the Ni content being spread between the dendrites and the eutectic with, Si and Fe concentrated in the dendrites and Cr and C in the eutectic. Similar observations using EDX probe substantiate this. The addition of ceramic particles to this already complex system further complicates the situation. Partial or complete dissolution of the ceramic particles serves to enrich the matrix in the relative elements, as shown in table 7.5, changing the constitution.

8.3.2 Porosity

A limited amount of porosity occurs in the clads made in this study. Abbas (58) noted porosity when cladding a variety of systems and classified it into macro surface porosity and micro internal porosity. The former, noted for composite clads only, has also been found in this study. The clad surfaces tend to diminish in quality with increasing proportion of ceramic addition. The reason for such a decrease in surface finish from smooth to relatively porous is the ejection of the ceramic particles from the melt pool during the process. The extent of such porosity is fairly small and tends to be confined to the outer surface of the deposit. This does not become a problem until >15 wt.% ceramic is added. Micro internal porosity resulting during solidification has also been found. Such porosity is thought to be caused by entrapped argon (carrier gas) or by the decomposition of moisture from the powders on melting. This type of porosity is almost completely eliminated by storing the powders in in airtight container at 50-60^{o}C prior to use. No solidification cracking has been found at the clad interfaces in this study. This is to be expected as the melting points of the substrate and the Stellite are fairly close in magnitude. However, evidence of some shrinkage effects is apparent around a small number of the embedded ceramic particles, as shown in Fig. 7.19. This effect tends to be associated with clusters of ceramic particles rather than those which are isolated in situation and is possibly caused by resticted flow of the molten Stellite in the immediate area.

8.3.3 Cracking

Some macro-cracking occurs for deposits which exhibit large depths of substrate melting, this is due to the inability of the substrate to cope with the residual stresses induced in the surface as the sample cools. An additional form of cracking is noted with large feed rates. This is illustrated in Fig. 8.6. The clad itself undergoes cracking in two directions, perpendicular to the interfaceand along the interface due to thermal contraction. Both types of cracking in this case occur on cooling and are accompanied by a loud noise.

Abbas (58) noted the presence of cracking in the matrix regions of composite clads of Stellite and SiC. The increased Si and C content of the matrix in such clads has an effect on the thermal stresses produced in the clad zone. No such cracking has been found here. This is thought to be a function of the similar thermal properties of the clad and substrate. 21-4N, unlike the mild steel generally used as a substrate exhibits high hot strength and hardness. It is unlikely that cladding will induce thermal stresses as high as those induced in mild steel since this material is specifically chosen for its high temperature performance. Similarly, no cracking of individual ceramic inclusions is noted.

8.3.4 Dilution

In all cases, clads with minimal dilution can be produced. The results of EPMA analysis indicate a sharp interface for all of the samples investigated. A full analysis of the heat balance for the process for the production of zero dilution clads was given by Monson (51), and will not be discused here. The general trends in dilution are somewhat obvious. Dilution tends to increase with decreasing traverse speed as more heat is available for substrate melting. This trend still applies for Stellite + ceramic clads where the thermal balance is complicated by the range of thermal properties of the materials. Dilution is not a problem with high flow rates as the beam is effectively blocked from melting the substrate. The addition of increasing amounts of ceramic to the melt pool tends to increase the level of dilution slightly. There are a number of possible explanations for this, (a) ceramic powder exhibits lower weldability, (b) ceramic powder is more widely dispersed by the carrier gas due to its lower density decreasing the sheilding effect, or (c) simply a cumulative effect of substrate heating over the long (400mm) track length.

8.3.5 Powder feed system

The tripple hopper feed system (THS) used to provide the requested powder composition for laser cladding has recently been assessed for its weight composition error and repeatability (79). The absolute weight composition error lies within 3% of the preset value by computer and the repeatability within 98% of that predicted. It is not possible to make a direct association for the purposes of the ceramic-Stellite clads between the weight composition requested and the EPMA determined composition of the clads since not all of the powder is necessarily incorporated into the clad. This is especially true for the ceramic powders as the flow tends to splay out on leaving the feed tube and therefore, not all of the powder enters the melt pool. However, for the Stellite powders alone, the clad compositions determined are uniform and are in line with the base alloy composition. Prblems were found with the triple hopper system when feeding the low density ceramic powders at low motor speed ($\leq$ 200 rpm). Pulsing of the powder produced cyclic deposits of varying height and width.

8.3.5(i) Effect of injection geometry

Of the various methods of injection of the ceramic powder into the melt pool the least successfulwas addition via separate feed tubes. This process was extremely difficult to set up, alignment was a problem and one or other powder tended to fall on top of the clad layer producing a poor quality surface finish. This geometry exaccerbates the slagging phenomenon for ceramic layers. The trials made using alumina as a clad layer, directly onto 21-4N resulted some kind of surface reaction and were not successful. Premixing of the powders or in-situ mixing in the reservoir were equally successful both in terms of clad quality and incorporation of ceramic into the clad matrix. The usual observations for laser cladding were made in terms of correct injection geometry with optimum feed angle being 40^0 to the horizontal, optimum argon flow rate 1l/min. and powder directed into the base of the melt pool.

8.4 Solidification

The rapid heating and cooling rates inherent in the laser cladding process have been found to produce novel structures, not restricted to the appropriate phase diagram. The high cooling rate ($\geq 10^3$ K/s) can lead to increased solubility of the solute atoms, an effect which depends upon mass, energy and momentum transfer (197). Partitioning at the solid-liquid interface can significantly alter the composition of the solidified material. Mazumder and Kar (197) modelled the extension of solid solubility based on mass and energy transport, using a non-equilibrium partition coefficient to model the solute segregation at the freezing front. Monson (51) found that the cooling rates in laser cladding were so high that increased solid solubility, increased distribution coefficients and greater degrees of undercooling were all produced during processing. The fundamentals of the solidification process are highly complex and are more fully discussed by Flemmings (198) and Mazumder (199). The observation of enhanced solid solubilities in this study is borne out by the results of laser cladding of Stellite 35 where the volume fraction of eutectic decreases with increasing cooling rate.

The increased hardness of the laser deposits compared to those conventionally deposited by the plasma arc method further indicate the validity of this enhanced solid solubility theory, the hardness probably a result of solid solution strengthening of the bulk Ni matrix (or Co matrix in Stellite 6'W'). The decrease in volume fraction of carbides with increased cooling rate does not therefore decrease the hardness of the deposit as one might expect, due to this enhanced solid solubility, which seems to have the over-riding effect as hardness is observed to increase with cooling rate. Furthermore, the presence of dilution in a deposit produces hardness values below those found for undiluted samples. The incorporation of iron from the substrate provides no solid solution

strengthening and seems to reduce the effectiveness of the other elements in improving hardness by this mechanism.

The microstructures induced by laser cladding are generally characterised by a shallow featureless region at the clad-substrate interface (Fig. 7.7(a)), the presence of which indicates that constitutional undercooling must occur. For planar solidification to occur, the ratio of G/R, (the ratio of the temperature gradient in the liquid ahead of the moving interface to its velocity), must exceed a certain stability criterion as follows (198, 200):

$$\frac{G}{R} \geq \frac{m\, c_o}{D} \cdot \frac{(1 - k_o)}{k_o} \qquad (8.1)$$

Where: m = slope of liquidus
c_o = initial concentration of solute
k_o = ratio of solute concentration in solid:solute concentration in liquid
D = diffusivity of solute in the liquid

The dependence of solidification morphology on G/R is shown in Fig. 8.7. As shown, values of G/R below the critical value produce cellular morphologies and still lower G/R ratios produce dendritic growth. Kear *et al* (201) investigated the effect of laser treatment on the G/R ratio and found varying ratios depending on the position within the molten zone. The maximum G/R values were found at the bottom and sides of the melt zone where the solidification rate is low, lower values of G/R occur at the top and centre of the melt zone. It is therefore reasonable to expect a high value of G/R at the clad-substrate interface since after the beam has passed any given point, melting will have ceased and freezing not yet begun giving an infinite value of G/R (R is zero). This explains the observed featureless region in the clads observed at the interface. The value of G/R then decreases and the familiar cellular and dendritic types of solidification occur.

A further consequence of constitutional supercooling theory is that the product G.R gives the cooling rate of the deposit (200). The larger the value of G.R, the finer the microstructural scale of the deposit. This is confirmed by a measured decrease in secondary dendrite arm spacing with increasing traverse speed (increasing G.R value) for Stellite 35 clads, a comparison of the observed and calculated secondary dendrite arm spacings using a relationship derived by Kear *et al* (201), was discussed by Abbas (58). Where:

$$\lambda = b \cdot \varepsilon^{-n} \qquad (8.2)$$

And λ is the secondary dendrite arm spacing, ε is the value of G.R, the cooling rate and b and n are constants (200). The values of experimental compared to calculated results compared fairly well according to Abbas (58).

8.5 Addition of ceramic powders

The introduction of ceramic particles into a metallic clad matrix, in the geometries discussed earlier presents three major difficulties:

(1) The differences in density of the Stellite and ceramic powders presents a problem. It is difficult to blow the ceramic powder using the THS at a rate suitable for laser cladding as it tends to bounce off the substrate surface.
(2) The ceramic powder tends to slough off the surface on solidification. In some cases, high quality stellite clads are encased in a surface layer which is brittle and poorly bonded.
(3) Melting of the ceramic occurs in the laser beam.

These will be discussed at greater length in the following section.

Ceramic cladding with alumina powder does not result in any noticeable presence of aluminium in the deposit. Clads tend to consist of two layers, the upper of which is black and EDX analysis shows that this layer contains only aluminium. Some clads containing enhanced Si and Cr contents are produced when cladding with SiC and chromia respectively, as determined by EPMA. As expected, this has the effect of improving the deposit hardness in both cases. The most significant imp[rovements are noted with SiC. In some cases, clads containing undissolved or partially dissolved ceramic particles result, with the particles situated close to the clad surface or trapped at the interface.

The impingement position of the ceramic powder with respect to the melt pool is critical in terms of clad quality for both types of feed geometry. The optimum geometry for incorporation into the deposit is to introduce the powder behind and slightly below the Stellite. This geometry helps to minimise the difference in densities of the powders. There appears to be a greater tendency for chromia to dissolve, suggested by the EPMA results which show the relative increase in composition of the deposits compared to the base alloy.

Dissolution of the ceramic particles in the melt pool is a function of the alloy powder in question, the particular ceramic and the particle size, as well as the process parameters, specific energy, interaction time and melt pool stirring. As reported by Ayers and Tucker (144), the dissolution of ceramic particles (TiC in this case is also strongly dependent on the nature of the matrix. Dissolution occurred in most cases in the experiments reported, as verified by EPMA analysis of the clads which indicate enrichment in Si and Cr for the SiC + Stellite and

Chromia + Stellite clads respectively. Previous work on the SiC + Stellite 6 system (58) also shows a strong dependence on the particle size with particles in the range 50-150μm showing almost complete dissolution whilst larger (450-750μm) particles are less prone to dissolution.

In many cases, a crust of the ceramic powder is formed on top of the clad. The particles of powder appear to have floated out of the deposit and solidified on the top. To a first approximation, the terminal velocity of a particle can be calculated using Stoke's Law. For a sphere of radius a, dropped into a viscous liquid, coefficient of viscosity, η, the terminal velocity, v_t for a small spherical object in an infinite volume of viscous liquid, can be calculated using the following formula:

$$v_t = \frac{2}{9} \cdot g \cdot \frac{(\rho - \sigma)}{\eta} \cdot a^2 \qquad (8.3)$$

Where σ is the liquid density, g is the acceleration due to gravity and ρ is the density of the particle.

Therefore for a ceramic particle in a molten Ni alloy clad, the dynamic viscosity of the alloy is $\approx 5 \times 10^{-3}$ $kgm^{-1}s^{-1}$ and the terminal velocity is about 1mm/s. Therefore, assuming a particle gets to the depth of the interface, it would take 1s to float to the surface. This is unlikely due to the vastly differing densities and the ceramic particles, as observed tend to be trapped in the surface of the deposit.

An additional factor of importance in considering the behaviour of the ceramics at elevated temperatures is their stability. Alumina has many applications as coatings for protection against erosion, wear and heat. The melting point of alumina (α)is 2051^{o}C and the boiling point 3530^{o}C. Under the laser beam, the alumina particles may well experience temperatures well in exces of the melting point and possibly greater than its boiling point. The reason for this is that the ceramic particles have a higher absorptivity for CO_2 radiation than do metals (>60% (14)) and hence will experience higher temperatures than the Stellite particles. SEM micrographs in Fig. 7.11 indicate the appearance of alumina after melting and re-solidification on the surface of a clad. The stability of alumina is further indicated by the Ellingham diagram (Fig. 8.8). However, aluminium is highly reactive in the elemental form at high temperatures and is likely to react with the other components of the alloy system to form additional phases.

Silicon carbide and chromia are similarly absorptive to the 10.6μm radiaition. This explains the observed changes in the melt pool as the weight percent of ceramic added is increased. Fig. 8.9 shows the standard free energies of formation

of some carbides as a function of temperature. This indicates the high stability of chromium carbide compared to silicon carbide and explains the observations from dot mapping and EPMA that the carbon rich areas correspond with those rich in chromium and do not relate to the silicon content. Hence, chromium carbides are formed on alloying SiC + Stellite 35. The changes in melt pool size are indicated in Fig. 8.10 for a clad of Stellite 35 + SiC from 0-10%. The melt pool was filmed using an Ektapro Camera. The melt pool grows substantially in both size and intensity over this range and molten droplets are ejected from the plume as the size increases. This clearly shows that the ceramic particles are melting in the path of the beam. This problem is not easily overcome. There is only a certain power density (in this case around 70W/mm^2) which will melt the Stellite powder and even at this low level, ceramic melting occurs. This is evident in all of the configurations attempted. There seems to be no method of prevention of ceramic melting with the particle sizes studied here. One further point to note is that in some instances, holes approximately the size of the powder particles are seen in the upper part of the clad. EDX analysis in the areas shows high levels of the metallic constituent of the relevant ceramic. This suggests that ceramic inclusions are sometimes torn from the clad during metallurgical preparation. Examination of a typical SiC inclusion using confocal laser scanning microscopy (Fig. 8.11) shows that the ceramic particles stand proud of the matrix slightly (probably due to their high hardness), it would therefore seem plausible thatthey are occasionally torn out during grinding/polishing.

8.6 Wear Resistance of Laser Clad Layers

The wear resistance of the Stellite 35 clads assessed fairly crudely using the hammer drill rig is encouraging and comparable to tests on standard clads of Stellite 6. Very similar values are noted for the same processing conditions. The relationship between processing velocity and wear performance shows a trend where wear resistance improves with increasing procesing velocity up to about 20mm/s, after which, it was not possible to produce homogeneous deposits. This is in agreement with Mazumder (99) who found a similar trend and also better wear properties for deposits produced with lower laser power (3kw cf 6kw).

Dilution of the deposit from the base layer, diminishes its performance to a remarkable degree, the wear scar diameter being almost twice the size for a 30% level of dilution.

Wear resistance of layers produced by the addition of ceramic particles also exhibit improved wear properties using the hammer drill test. Stellite + alumina deposits show comparable wear resistance to Stellite clads alone. However, those produced from Stellite + SiC or Cr_2O_3 show improved wear resistance upto 15 and 10% by weight respectively, after which, the clads become brittle and porous and show poor wear resistance, breaking off under test conditions. This fits in well

with the observed improvements in hardness for the ceramic + Stellite clads. The cause of this increased hardness, as discussed by Abbas (51) can be attributed to a number of factors:

(a) solid solution strengthening due to ceramic particle dissolution
(b) dispersion hardening due to resolidified fine particles from the partial dissolution of the ceramic particles
(c) matrix hardening through microstructural refinement

As mentioned earlier, the hardness falls offer at higher levels of ceramic addition, as does the wear resistance due to the increasingly brittle and porous nature of the deposits.

Cobalt base alloys are generally used to hardface diesel valves due to their high wear hardness and resistance to sulphur attack. However this study has shown that hardnesses inexcess of 700 HV(10kg) can be achieved by increasing the chromium content of Stellite 35. These clads show a corresponding improvement in wear resistance and nickel base alloys are known to have excellent corrosion resistance (3) which is likely to be futher enhance by the addition of chromium.

This demonstrates the potential of laser surface cladding for improving wear resistance - a technique which offers the possibility of numerous applications due to the wide variety of materials available. In the particular case studied here, a more judicious choice of ceramic particle for addition to the melt pool for improved wear resisitance might have been tungsten carbide or cubic boron nitride, which may have been less likely to dissolve in the Stellite matrix. However, this was not possible due to the availability of materials.

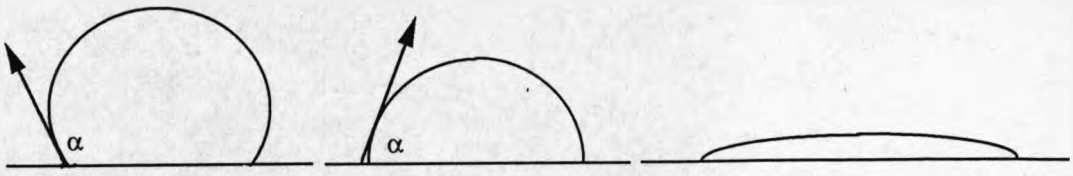

(a) (b) (c)

Fig. 8.1 Three basic bead shapes formed during laser cladding. Beam diameter > 5 mm.

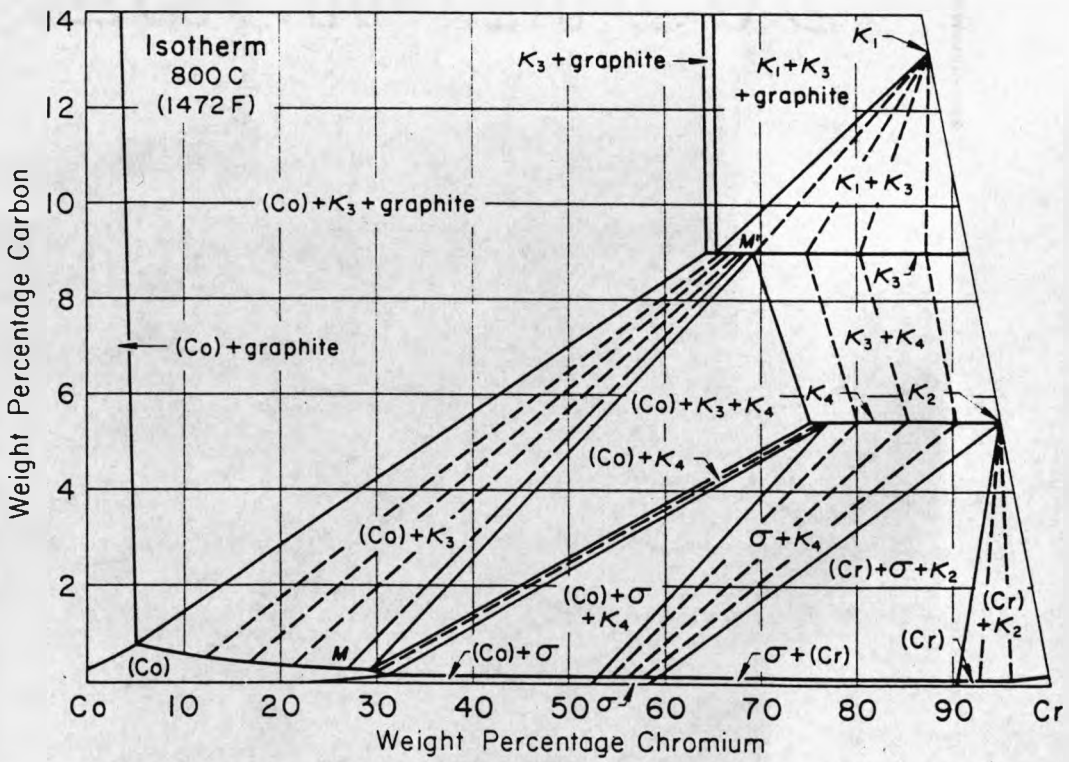

Fig. 8.2 Isothermal section of C-Co-Cr system at 800 °C.

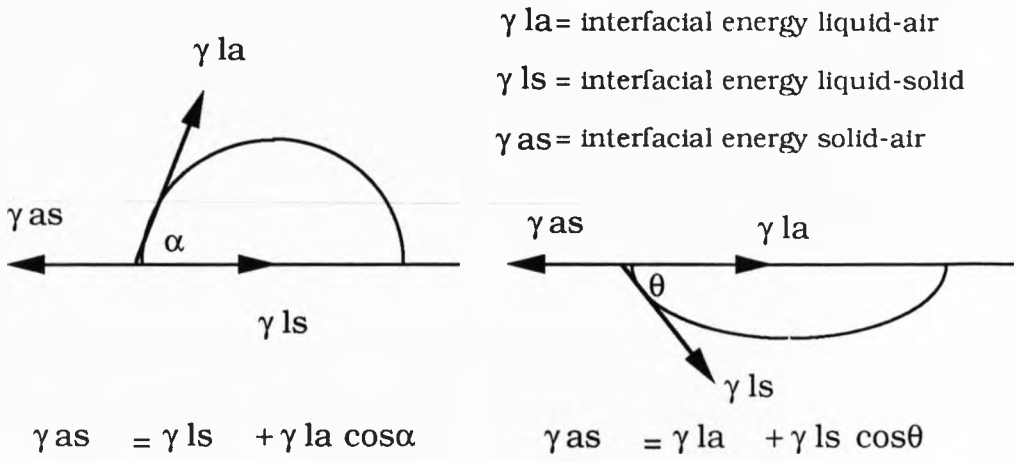

Fig. 8.3. Interfacial force balance for valve groove cladding

Fig. 8.4 Spheroidised deposit - poor quality

Fig. 8.6 Heavy deposit - solidification cracking

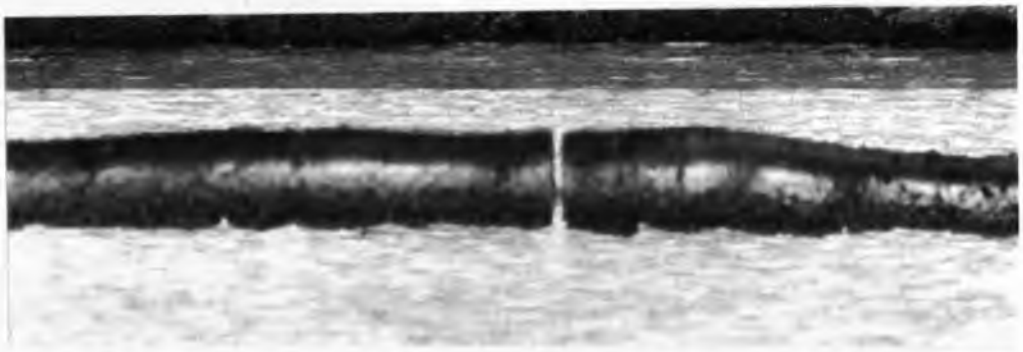

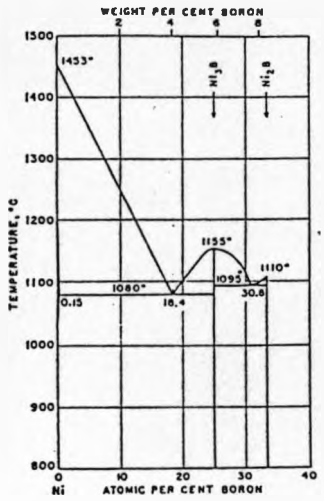

Fig. 8.5 Ni-B binary system (51)

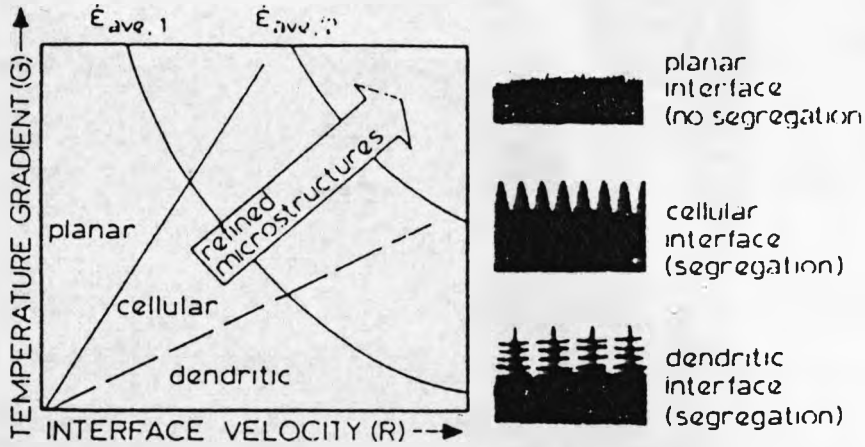

Fig. 8.7 Dependence of solidification morphology on temperature gradient G and solidification velocity R: qualitative effect of increasing average cooling rate $\varepsilon_{ave} = GR$ is indicated by a sloping arrow.

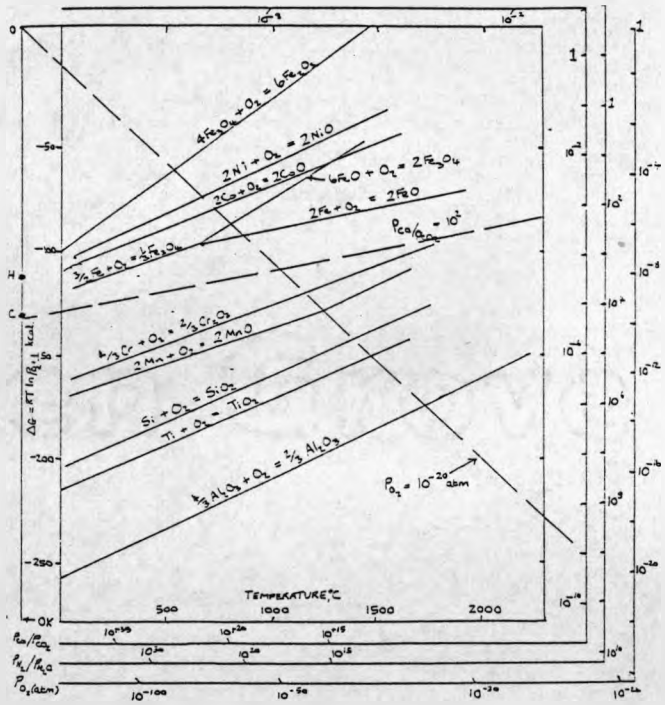

Fig. 8.8 Ellingham Richardson diagram for the oxides.

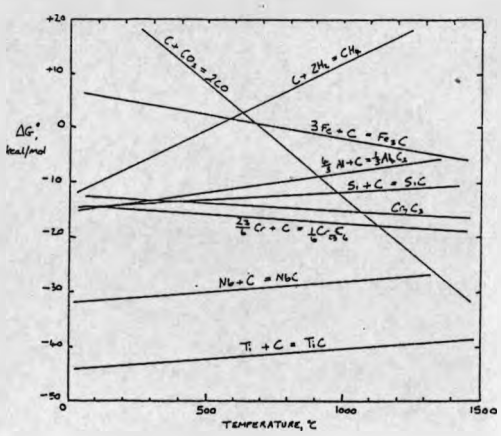

Fig. 8.9 Standard free energies of carbides as a function of temperature.

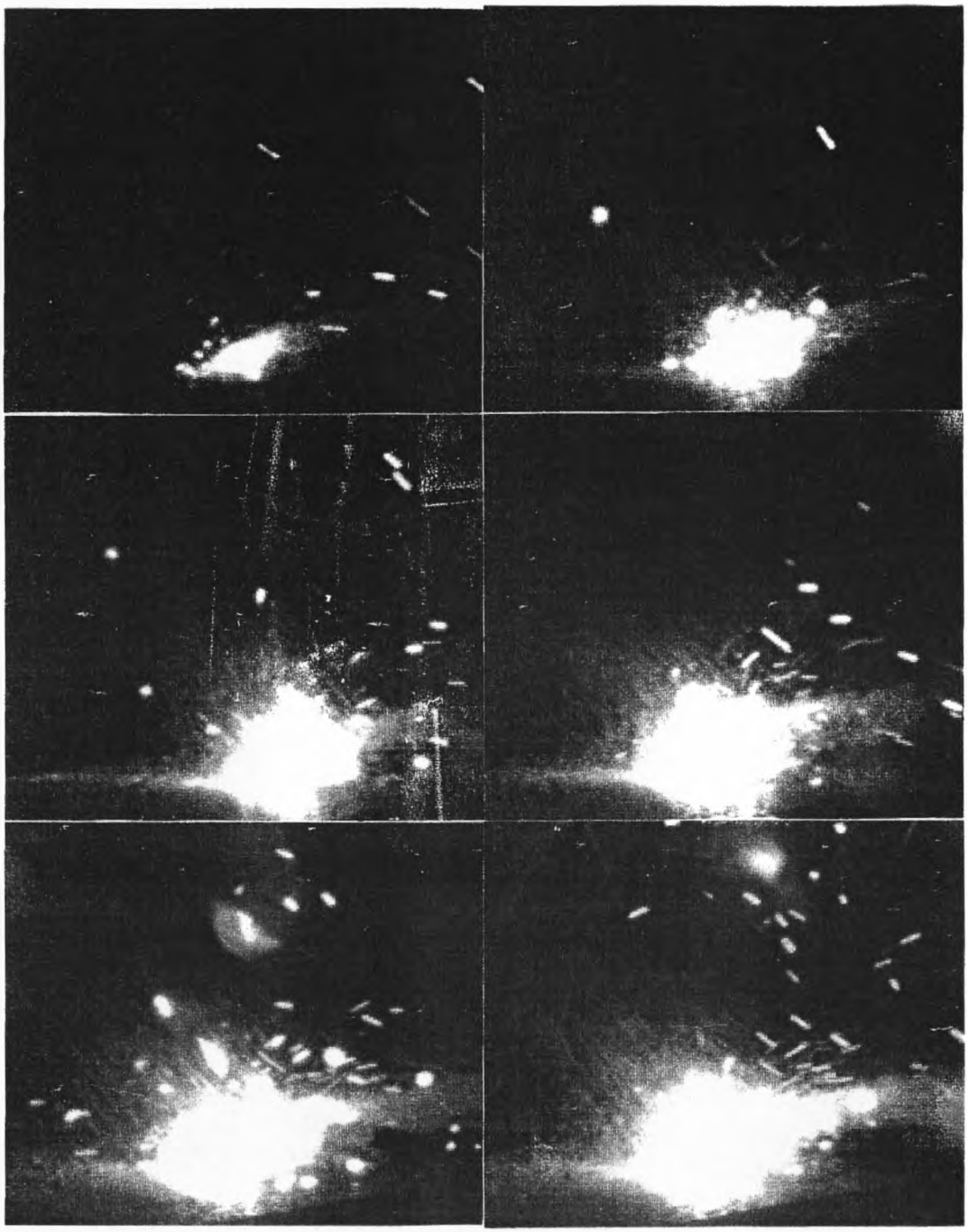

Fig. 8.10 Change in melt pool with addition of SiC to Stellite 35, 0, 1.6, 2.2, 3.4, 4.1, 4.8 Wt.% addition respectively.

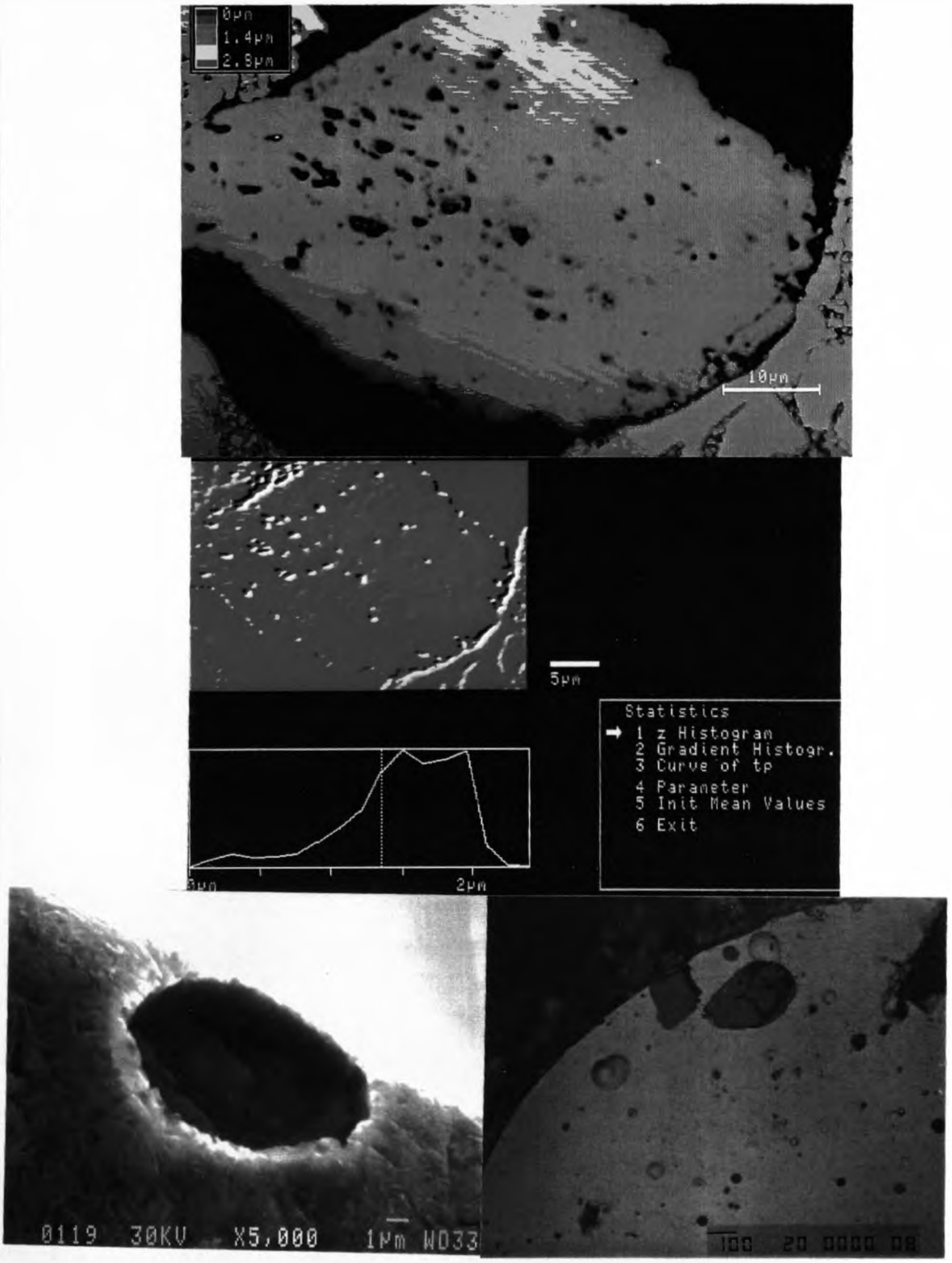

Fig. 8.1 1 Confocal laser scanning microscopy indicating elevation of ceramic particle from matrix and SEM photographs showing surface SiC particle and hole rich in Si where particle seems to have been pulled out on grinding.

CHAPTER 9

CONCLUSIONS AND FUTURE WORK

9.1 Laser Transformation Hardening

1 The as-recieved microstructures of the En24 and En52 steels supplied consist of spheroidal carbide precipitates in a ferritic matrix. In the case of En52, there is a network of intra-granular precipitates in addition to those observed at grain boundaries and all have the same ratio of Fe:Cr.

2 Both En24 and En52 can be successfully surface hardened using a high power CO_2 laser beam. However, in each case, surface coatings of some kind are required to enhance the coupling of the radiation to the surface. Of the coatings looked at, the best in terms of improving absorption were grit blasting, DAG colloidal graphite coating and excimer surface roughening. Grit blasting does not offer a practical solution, but excimer pretreatment offers the possibility of in-situ surface treatment and hardening in single a clean and fast operation.

3 Laser transformation hardening of En24 produces a martensitic surface layer with a gradual return to the base material through a region which consists of spheroidal carbide particles which are smaller and greater in number than those present in the base material but having the same composition. The carbides are of the type $(Cr,Fe)_3C$.

4 Laser transformation hardening of En52 produces a near surface microstructure consisting of martensite grains with undissolved carbide particles, below which is a region of martensite + ferrite + carbides. The carbides in this case are $(Cr,Fe)_{23}C_6$ in type and act as sites for the nucleation of austenite.

5 Laser transformation hardening of both steels produces hard highly wear resistant surfaces which exhibit a 2-3 fold improvement over the untreated material in many cases

6 Wear performance does not seem to depend upon the depth of the hardened layer as long as that depth is greater than the depth of the wear scar and the surface is martensitic.

7 Valve stems hardened with spiral patterns of varying pitch show extremely promising wear characteristics with small back tempered zones in the overlap region. Laser hardened valve stems show comparable wear performance to those

which have been hard chromium plated. The LTH process therefore offers a clean, quick and effective method of improving wear resistance which is like;y to be more economic per component than existing processes.

8 The back tempering effect for spirally hardened valve stems is greater for En24 than for En52. This is due to the lower percentage of alloying elements in En24 steel. This indicates that by changing the composition of the alloy, the backtempering effect can be minimised to around 10% change in hardness.

9 Modelling of the process using the Shercliff and Ashby model shows a reasonably good fit with experimental results, although the curves are slightly shifted due to the difference in thermal properties. The results do not fit well to the Courtney and Steen empirical model.

10 Similar modelling using finite difference methods show close agreement with experiment. However, the finite component size used in the study limits the accuracy of such models.

11 Re-working of the mathematical model to produce diagrammatic output yielded fruitful representations of the heat flow within the substrate and allows direct readings of the temperature profiles at any point within the substrate.

12 Further modification of the boundary conditions of the F.D. model to allow for the finite size of the specimens in this study revealed a different heat flow pattern and case depth results which more closely match those determined experimentally. The convective boundary condition allows the whole of the substrate to become heated, matching experimental observations. The model is therefore powerful enough to have its boundary condition changed to suit the experimental parameters.

9.2 Laser Cladding

1 Successful deposits were produced by the blown powder laser cladding technique for both the conventional Co-based Stellite 6'W' alloy and the more modern (with reference to valve seat hardfacing) Ni-based Stellite 35 alloy.

2 The operating window for successful cladding is less restrictive for the Ni-based alloy, clads can be produced over a range of parameters.

3 Addition of ceramic particles to the melt pool generally results in dissolution of the ceramics in the clad. In some cases, a layer of ceramic is formed over the top of the clad. Such layers are brittle and poorly adhered and slag off on cooling.

4 Clads produced by alloying either Stellite 35 + SiC or Stellite 35 + Cr_2O_3 show improved wear resistance and hardness over Stellite 35 clads alone. The wear resistance improves with ceramic addition up to around 15 Wt.%, after which clad quality diminishes and the wear resistance decreases.

9.3 Valve Cladding

1 Cladding of 21-4N poppet valves using Stellite 6'W' produces uniform, homogeneous clads with minimal dilution and good surface finish. In addition, laser cladding of engine valves produced no distortion in the valve seat face.

2 Analysis of the process indicates that it is a feasible method for cladding the valves. The process is far quicker and more efficient than existing techniques.
3 Valve cladding using the blown powder technique results in smooth deposits. The level of after machining required is minimal and a step in the production process can be eliminated using this technique.

9.4 Future Work

1 Sensitive investigation of the wear behaviour of En24/52 after different laser treatments to determine whether a correlation exists between wear performance and nuances in the microstructure.

2 Full scale engine testing of hardened valve stems to assess the potential of the process for component manufacture.

3 Feasibility study to determine the cost saving of laser surface treatment and the capital expenditure involved.

4 Extensive wear testing of spiral hardened stems to find the optimum pitch for hardening and the mechanism of wear.

5 Closed loop power control system to allow power ramping for valve seat face cladding, thereby eliminating problems in the overlap area.

6 Investigation of microstructure in the clad overlap region to assess whether problems occur.

7 Mathematical modelling of laser cladding with two powders to determine thermal loading, relative absorptivities and optimum flow conditions.

8 Extensive wear testing of clad deposits and subsequent corrosion testing to assess the potential for cladding as a manufacturing method.

9.5 Publications

N.Mckeown, W.M.Steen and G.McCartney, Laser Hardening of Valve Steels, Metals and Materials, Liverpool, U.K., 1990.

N.Mckeown, W.M.Steen and G.McCartney, Laser Transformation Hardening of Engine Valve Steels, ICALEO '90, Boston,. U.S.A., 1990.

N.Mckeown, W.M.Steen and G.McCartney, 5th International Conference on Surface Modification Technologies, Birmingham, U.K., 1991.

N.Mckeown, W.M.Steen and G.McCartney, Variable Composition Cladding for Improved Wear Resistance, submitted for publication, Materials Science and Technology.

Appendix A

Block Diagram Showing Finite Difference Model (23)
(boundary conditions shaded)

START
Define Common Blocks
Set Output Flags
Set T1,T2 For Reflectivity Changes
Input Experimental Variables (Speed, Power, Reflectivity)
Set ALPHA=COND/DENS x SPHT
Read Number of Iterations Before Reset (IJRESET) and Maximum Number of Iterations (LIMIT)
Store Initial Value of Reflectivity for Main Calculation
Set Reflectiviity to Zero
Call SUBROUTINE RANGE (calculates initial mesh parameters, DELTA, IX, IY, IZ, KI
KI= (IX+1)/3+1
Call SUBROUTINE SETTEMP (resets temperature array to ambient temperature)
Call SUBROUTINE POWDIST (establihes the surface power distribution)
Call SUBROUTINE DELTIM (calculates the delay time or waiting factor)
Initialise Grid Calculation Limits and Iteration Counters
Set the Dynamic Convergence Criterion, CONVTEM=1.0 E-06
IF ITER=IJRESET (Start of Main Calculation Loop)
T / F
Call SUBROUTINE RESET (checks for reset)
Set REFLEC=RSAVE, IOUTDAT=1, NLT=

Set Increment Iteration Counter		
IF ITER > 3		
T	F	
Call SUBROUTINE GRDLIM (calculates grid calculation limits)		
Start of Main F.D. Calculations		
IF ITER=IPRINT		
T	F	
IPRINT=IPRINT + 10, IPR=ITER		
Call SUBROUTINE CALC (finite difference calculations)		T
TIME=TIME + DELTIME		
Check for Convergence (BIG is maximum temperature change in iteration		
IF BIG > CONVTEM		
T	F	
CONVTEM=BIG		
IF ITER=IJRESET		
T	F	
Write 'Convergence Crit. to be Reached (compare with value of 'BIG')', CONVTEM/500.		
Until BIG > CONVTEM/500 AND ITER < LIMIT is FALSE		
IF ITER < LIMIT		
T	F	
Write 'Convergence Crit. :', CONVTEM/500., 'Iteration No.:', ITER	Write 'Iteration Limit Reached. Convergence not Assured'	

IF IOUT=1	
T	F
Call SUBROUTINE PROFILE (calculates weld profile)	
IF IOUT3=1	
T	F
Call SUBROUTINE SUMMARY (outputs summary information)	
IF IOUT2=1	
T	F
Call SUBROUTINE OUTPUT (ouputs data to printer or data file	
Write 'GLAZE8 FINISHED'	
END	

SUBROUTINE FUNCTION POWERIN	
Define Common Blocks	
Dimension F(11,11)	
Set FUN(R)=EXP(-2.0*(R/BEAM)**2, A=2.0*PTOTAL/(3.142*(RBEAM)**2)), SUM=0.0, G=(X2-X1)/10.0, H=(Y2-Y1)/10.0	
Set I=1, J=1	
Increment I, J	
X=FLOAT(I-1)*G+X1, Y=FLOAT(J-1)*H+Y1, R=SQRT((X**2)+(Y**2)), F(I,J)=FUN(R)	
Until I=11, J=11	
Set I=1, J=1	
Increment I, J, STEP 2	
SUM=F(I,J)=F(I+2,J)+F(I,J+2)+F(I+2,J+2)+SUM SUM=F(I+1,J+1)*8.0+SUM	
Until I=9, J=9	
POWERIN=A*G*H*SUM/3.0	
End	
SUBROUTINE FUNCTION TA	
Define Common Blocks	
Set TA=X	
IF TA < RMPT THEN STOP	
IF TA < (RMPT+VM)	
T	F
TA=TA+((TA-RMPT)/VM)*(QMEL/SPHT)	IF TA < BPTK

<table>
<tr><td rowspan="3"></td><td>T</td><td colspan="2">F</td></tr>
<tr><td rowspan="2">TA=TA+(QMEL+QVAP)/ SPHT</td><td colspan="2">IF TA < (BPTK+VB)</td></tr>
<tr><td>T</td><td>F</td></tr>
<tr><td colspan="2">TA=TA+(QMEL/ SPHT)+((TA-BPTK)/ VB)*(QVAP/SPHT)</td><td></td></tr>
<tr><td colspan="4">End</td></tr>
</table>

SUBROUTINE CALC

Define Common Blocks

Dimension TEMP (IX, IY, IZ), POWER (IX, IY)

Set TRFLUX=0.0, BIG=0.0, K=KS, I=1, L=1

Increment K, I, L

KM=K-1, KP=K+1, IP=I+1, IM=I-1, LP=L+1, LM=L-1

IF L=1

T	F	
LM=1	IF L > 1 AND L < IZ	
TEMPT=TEMP(K,I,L) DELTAM2=1.0/(DELTA**2)	T	F
DZDF=2.0*DELTAM2 * (TEMP(K,I,LP)-TEMPT) HLOSS=(SIGMA*ABSORP * (TEMPA**4-TEMPT**4)+HCONV * (TEMPA-TEMPT))/COND DZUF=2.0*HLOSS/DELTA	DZDF= DELTAM2 * (TEMP(K,I,LP) - TEMPT) DZUF= DELTAM2 * (TEMP(K,I,LM)- TEMPT)	ABSORP=1.0-RF(TEMPT) DZUF=2.0 * DELTAM2*(TEMP(K,I,LM)-TEMPT) HLOSS=(SIGMA*ABSORP * (TEMPA**4-TEMPT**4) + HCONV*(TEMPA-TEMPT)) /COND DZDF=2.0*HLOSS/DELTA

IF K > 1 AND K < IX

T	F	
	IF K=1	
DXEF=DELTAM2*(TEMP(KP,I,L) -TEMPT) DXWF=DELTAM2*(TEMP(KM,I,L) -TEMPT)	T	F
	DXEF=DELTAM2* (TEMP(KP,I,L) - TEMPT) DXWF=DELTAM2* (TEMPA-TEMPT)	DXEF=DELTAM2* (TEMPA-TEMPT) DXWF=DELTAM2* (TEMP(KM,I,L) - TEMPT)

IF I > 1 AND I < IY

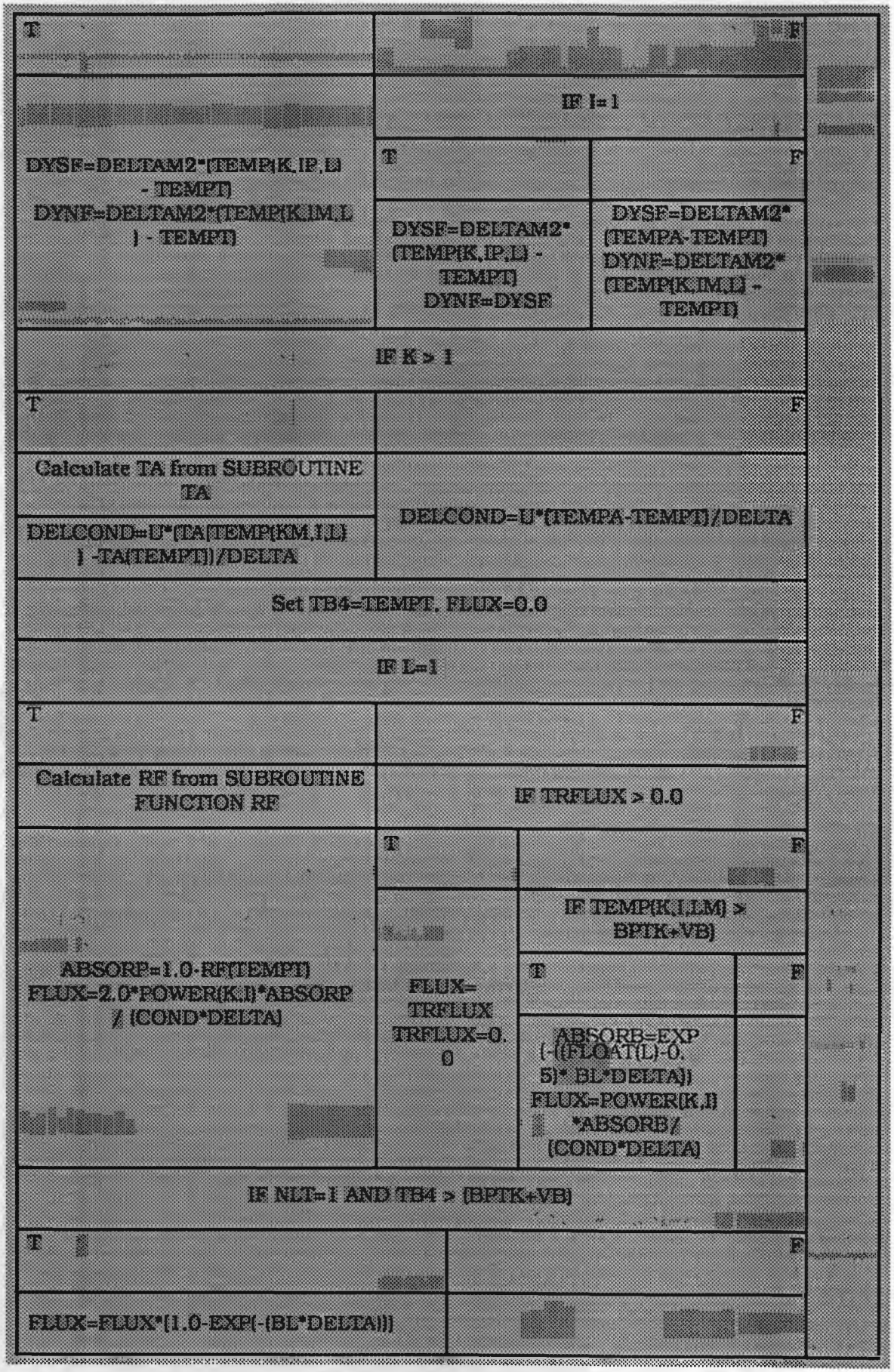
T
F
IF I=1
DYSF=DELTAM2*(TEMP(K,IP,L) - TEMPT)
DYNF=DELTAM2*(TEMP(K,IM,L) - TEMPT)
T
F
DYSF=DELTAM2*(TEMP(K,IP,L) - TEMPT)
DYNF=DYSF
DYSF=DELTAM2*(TEMPA-TEMPT)
DYNF=DELTAM2*(TEMP(K,IM,L) - TEMPT)
IF K > 1
T
F
Calculate TA from SUBROUTINE TA
DELCOND=U*(TA(TEMP(KM,I,L)) -TA(TEMPT))/DELTA
DELCOND=U*(TEMPA-TEMPT)/DELTA
Set TB4=TEMPT, FLUX=0.0
IF L=1
T
F
Calculate RF from SUBROUTINE FUNCTION RF
IF TRFLUX > 0.0
T
F
ABSORP=1.0-RF(TEMPT)
FLUX=2.0*POWER(K,I)*ABSORP / (COND*DELTA)
FLUX= TRFLUX
TRFLUX=0. 0
IF TEMP(K,I,LM) > BPTK+VB)
T
F
ABSORB=EXP (-((FLOAT(L)-0. 5)* BL*DELTA))
FLUX=POWER(K,I) *ABSORB/ (COND*DELTA)
IF NLT=1 AND TB4 > (BPTK+VB)
T
F
FLUX=FLUX*(1.0-EXP(-(BL*DELTA)))

<table>
<tr><td colspan="4">HFLOW=DXEF+DXWF+DYNF+DYSF+DZUF+DZDF</td></tr>
<tr><td colspan="4">RESDU=(HFLOW+FLUX)*ALPHA+DELCOND</td></tr>
<tr><td colspan="4">RES=RESDU*DELTIME</td></tr>
<tr><td colspan="4">TEMPT=TB4+RES</td></tr>
<tr><td colspan="4">IF TEMPT < TEMPA THEN TEMPT=TEMPA</td></tr>
<tr><td colspan="4">IF TB4 < (RMPT+VM) AND TEMPT > RMPT</td></tr>
<tr><td>T</td><td colspan="3">F</td></tr>
<tr><td rowspan="4">Call SUBROUTINE LATTRAP (calculates latent heat of melting)</td><td colspan="3"></td></tr>
<tr><td>T</td><td colspan="2">F</td></tr>
<tr><td rowspan="2">TRENGY=0
TRFLUX=0</td><td colspan="2">IF TB4 < BPTK</td></tr>
<tr><td>T</td><td>F</td></tr>
<tr><td>TIME1=(BPTK-TB4)/ RESDU
TIMEREM=DELTIME - TIME1 AND
TOLD=BPTK</td><td>TOLD=TB4
TIME1=0.0
TIMEREM = DELTIME</td></tr>
<tr><td colspan="4">DTR=TIMEREM/10.0</td></tr>
<tr><td colspan="4">SET M=1</td></tr>
<tr><td colspan="3">M1=M</td><td rowspan="6"></td></tr>
<tr><td colspan="3">Increment M</td></tr>
<tr><td colspan="3">FLUX1=FLUX*(1.0-((TOLD-BPTK)*EXP(-(BL*DELTA))/VB))
TNEW=TOLD+SPHT*VB*((HFLOW+FLUX1)*ALPHA+DELCOND)*DTR/QVAP
TRENGY=TRENGY+(FLUX-FLUX1)*DTR</td></tr>
<tr><td colspan="3">IF TNEW > (BPTK+VB)</td></tr>
<tr><td>T</td><td colspan="2">F</td></tr>
<tr><td></td><td colspan="2">TOLD=TNEW</td></tr>
</table>

Until M=10	
TIME2=DELTIME-TIME1-DTR*FLOAT(M1)	
IF TIME2 < 0.0	
T	F
TRFLUX=O.O, TEMPT=TNEW	
Set RES=TEMPT-TB4, TEMP(K,I,L)=TEMPT	
IF ABS(RES) > BIG	
T	F
BIG=ABS(RES), IPK=K, IPI=I, IPL=L, CRESDU=RESDU, BIGTEMP=TEMPT	
Until K=KF, I=IYL, L=IZL	
IF IPR > 0 then write to data file valuesfor IPR, IPK, IPI, IPL, CRESDU, BIG, BIGTEMP, KS, KF, IYL, IZL, (TEMP(J,1,1), J=KI+3)	
IPR=0	
End	
SUBROUTINE FUNCTION RF	
Define Common Blocks	
IF T < T1	
T	F
RF=REFLEC	RF=REFLEC*(T2-T)/(T2-T1)
IF RF < 0.0 THEN RF=0.0	
End	

SUBROUTINE DELTIM
Define Common Blocks
DELTIME=0.1/{(ALPHA/(DELTA**2))+(U/(6.0*DELTA))}
Write to data file, DELTIME
END
SUBROUTINE GRDLIM
Define Common Blocks
Dimension TEMP(IX, IY, IZ), PROF(100)
TEMP20=TEMPA+20.0
Set J=1
PROF(J)=TEMPA
Increment J
Until J > IY+IZ
Set K=2
KS=K
Increment K
IF (TEMP(K, 1, 1) > TEMP20 THEN KS=KS-1
Until K=KI-1
Set K=KI+2
KF=K
Increment K

Until K=IX OR (TEMP(K, 1, 1) < TEMP20)
Set I=1, K=KS
Increment I, K
IF (TEMP(K, I, 1) > PROF(I) THEN PROF(I)=TEMP(K, I, 1)
Until I=IYL, K=KF
Set L=1, K=KS
Increment L, K
IF (TEMP(K, 1, L) > PROF(L+IY)) THEN PROF(L+IY)=TEMP(K, 1, L)
Until L=IZL, K=KF
Set L=1
L1=IZ-L
Increment L
Until L=IZ OR (PROF(L1+IY) > TEMP20
IZL=L1+1
Set I=1
I1=IY-I
Increment I
Until I=IY-1 OR (PROF(I1) > TEMP20
IYL=I1+1
END

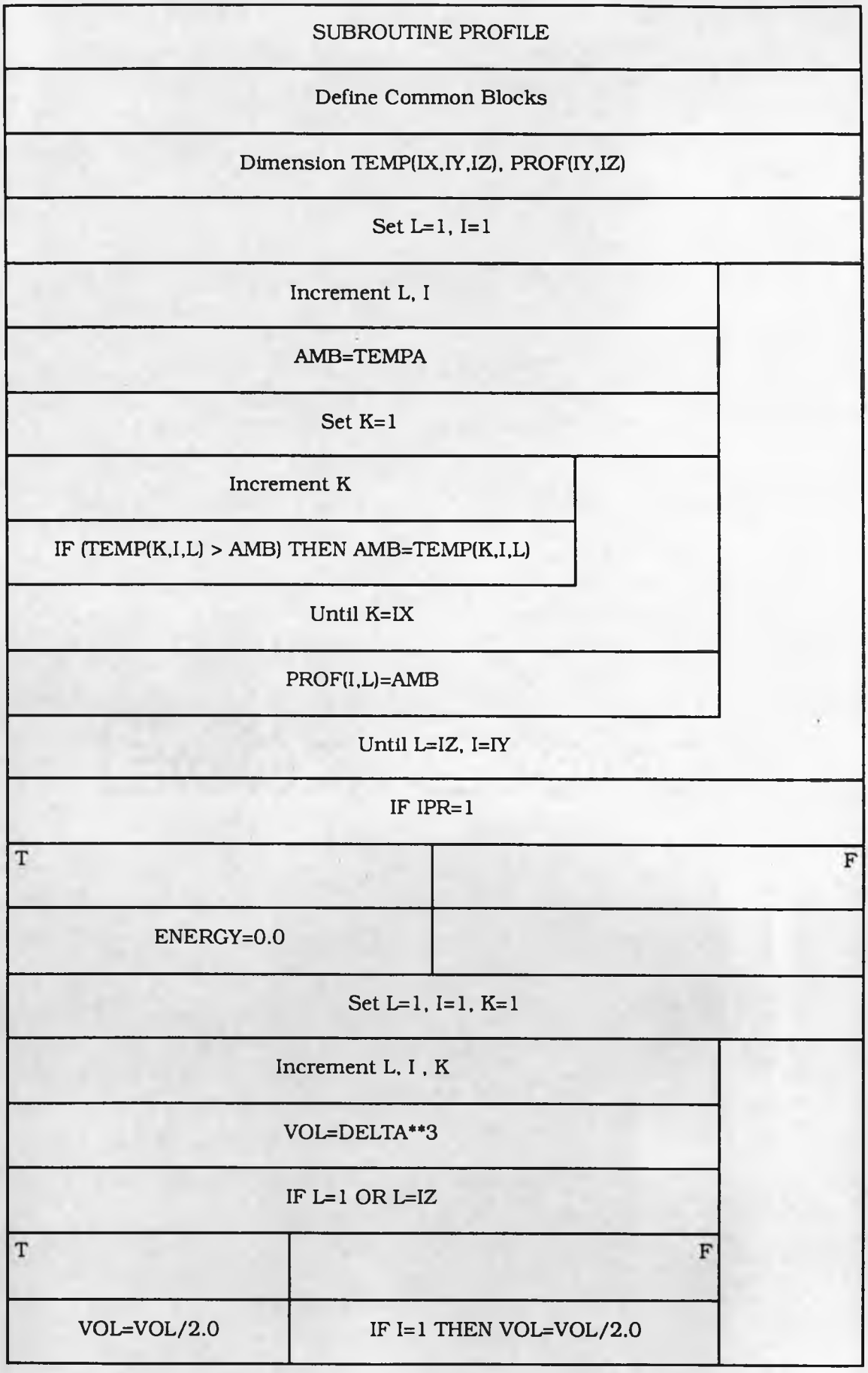
SUBROUTINE PROFILE
Define Common Blocks
Dimension TEMP(IX,IY,IZ), PROF(IY,IZ)
Set L=1, I=1
Increment L, I
AMB=TEMPA
Set K=1
Increment K
IF (TEMP(K,I,L) > AMB) THEN AMB=TEMP(K,I,L)
Until K=IX
PROF(I,L)=AMB
Until L=IZ, I=IY
IF IPR=1
T
F
ENERGY=0.0
Set L=1, I=1, K=1
Increment L, I , K
VOL=DELTA**3
IF L=1 OR L=IZ
T
F
VOL=VOL/2.0
IF I=1 THEN VOL=VOL/2.0

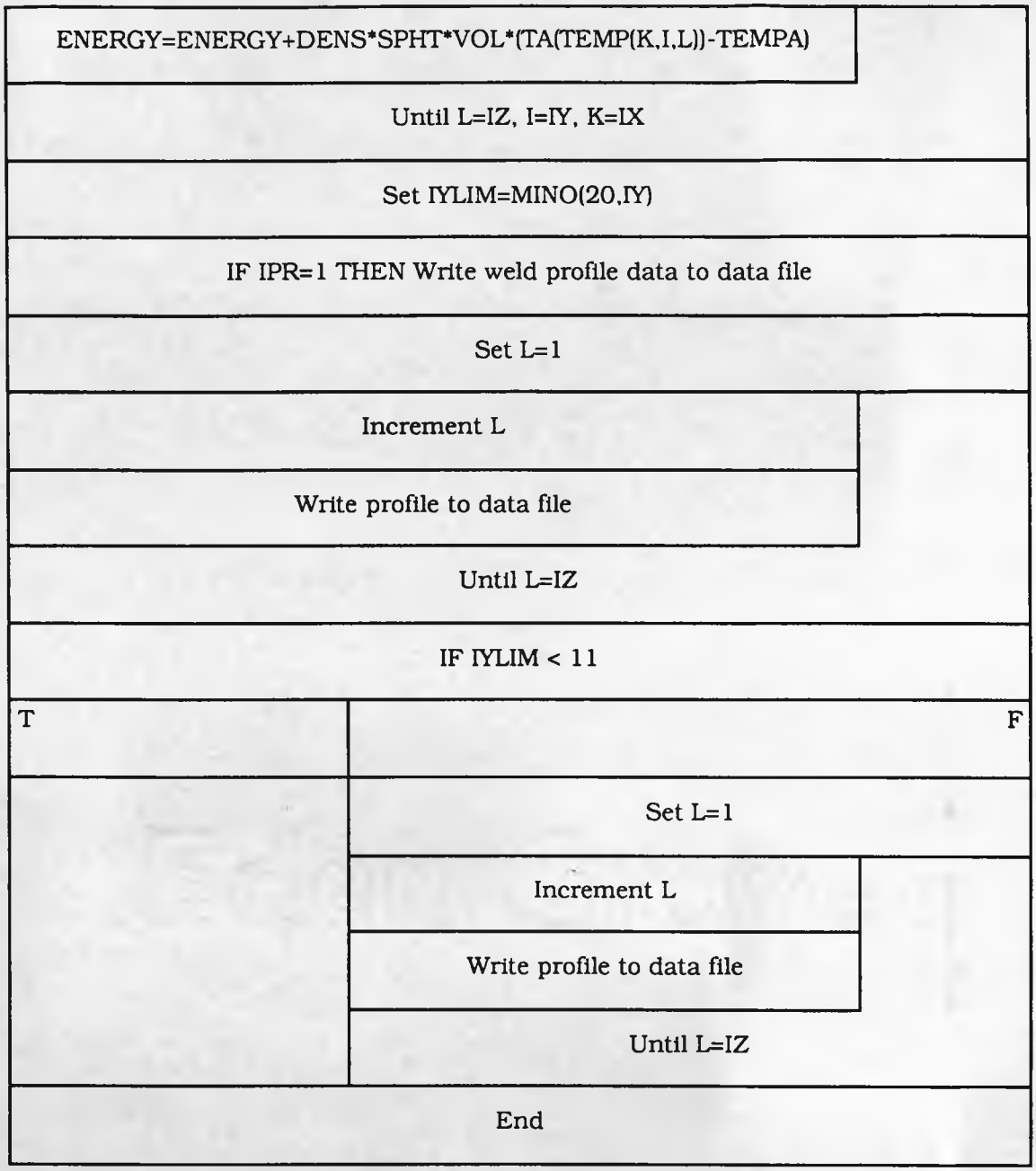
ENERGY=ENERGY+DENS*SPHT*VOL*(TA(TEMP(K,I,L))-TEMPA)
Until L=IZ, I=IY, K=IX
Set IYLIM=MINO(20,IY)
IF IPR=1 THEN Write weld profile data to data file
Set L=1
Increment L
Write profile to data file
Until L=IZ
IF IYLIM < 11
T
F
Set L=1
Increment L
Write profile to data file
Until L=IZ
End

SUBROUTINE RANGE		
Define Common Blocks		
Read Beam Radius (RBEAM)		
Calculate mesh parameters, DELTA=RBEAM/6, IX=XR/DELTA, IY=YR/DELTA, IZ=ZR/DELTA, AND ITOT=IX x IY x IZ		
IF ITOT < 8250		
T	F	
Re-calculate mesh parameters using DELTA=DELTA x 0.95		
Until ITOT > 8250		
IF ITOT > 9000		
T	F	
Re-calculate mesh parameters using DELTA=DELTA x 1.05		
Until ITOT < 9000		
IF IZ < 3		
T	F	
THEN, IZ=3, DELTA=ZR/2.0, IY=IFIX(SQRT(3000. x YR/XR)), IX=IFIX(3000./IY)-1		
Write 'Subroutine Range Completed' (writes values for IX, IY, IZ , MESH SIZE in mm)		
END		

SUBROUTINE RESET		
Define Common Blocks		
Dimension TEMP(IX, IY, IZ), PROF(IY, IZ), POWER(IX, IY)		
Call SUBROUTINE PROFILE (0, TEMP, PROF)		
K1=KI-5		
IF k1 < 1 THEN K1=1		
Write to data file (TEMP(J, 1, 1), J=K1, KI+5)		
TSET=TEMPA+10.0		
IF PROF(1,1) < TSET THEN STOP		
Set I=1		
N=I		
Increment I		
IF (PROF(N, 1) > TSET AND PROF(N+1,1) < TSET)		
T	F	
	N=IY	
Until I=IY-1		
IF N=IY		
T	F	
YR=DELTA*(FLOAT(N-1)+((PROF(N, 1)-TSET)/(PROF(N, 1)-PROF(N-1,1)))	YR=IY*DELTA	
IF (IWELD = 0)		

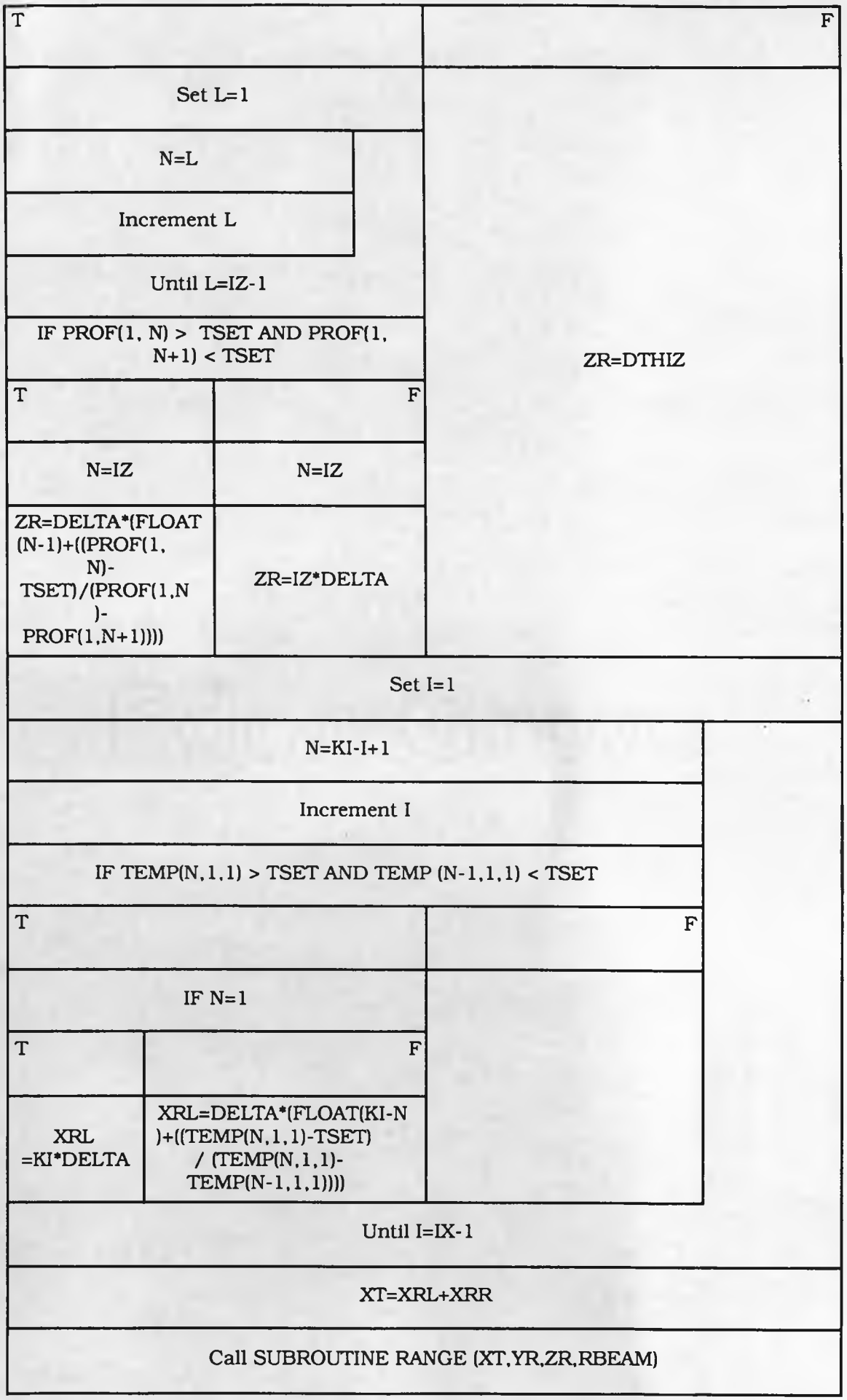
T
F
Set L=1
N=L
Increment L
Until L=IZ-1
IF PROF(1, N) > TSET AND PROF(1, N+1) < TSET
T
F
N=IZ
N=IZ
ZR=DELTA*(FLOAT (N-1)+((PROF(1, N)- TSET)/(PROF(1,N)- PROF(1,N+1))))
ZR=IZ*DELTA
ZR=DTHIZ
Set I=1
N=KI-I+1
Increment I
IF TEMP(N,1,1) > TSET AND TEMP (N-1,1,1) < TSET
T
F
IF N=1
T
F
XRL =KI*DELTA
XRL=DELTA*(FLOAT(KI-N)+((TEMP(N,1,1)-TSET) / (TEMP(N,1,1)- TEMP(N-1,1,1))))
Until I=IX-1
XT=XRL+XRR
Call SUBROUTINE RANGE (XT,YR,ZR,RBEAM)

<table>
<tr><td colspan="4">KI=INT(FLOAT(IX)*XRL/XT)</td></tr>
<tr><td colspan="4">Call SUBROUTINE POWDIST (POWER)</td></tr>
<tr><td colspan="4">Call SUBROUTINE DELTIM</td></tr>
<tr><td colspan="4">Set Time=0.0</td></tr>
<tr><td colspan="4">Call SUBROUTINE SETTEMP</td></tr>
<tr><td colspan="4">Set Mesh Parameters and Dimensions</td></tr>
<tr><td colspan="4">Write to data file, mesh parameters</td></tr>
<tr><td colspan="4">End</td></tr>
<tr><td colspan="4">SUBROUTINE LATTRAP</td></tr>
<tr><td colspan="4">IF (TB4 < TLAT)</td></tr>
<tr><td colspan="2">T</td><td colspan="2">F</td></tr>
<tr><td colspan="2">IF ((TNEW-TLAT) > (QLAT/SPHT)</td><td colspan="2">FRAC=((TNEW-TB4)*SPHT/QLAT) + ((TB4-TLAT)/VLAT)</td></tr>
<tr><td>T</td><td>F</td><td colspan="2">IF FRAC < 1.0</td></tr>
<tr><td rowspan="2">TNEW=TNEW-QLAT /SPHT</td><td rowspan="2">TNEW=TLAT+VLAT *(TNEW-TLAT) * SPHT/QLAT</td><td>T</td><td>F</td></tr>
<tr><td>TNEW=TB4 + (TNEW-TB4)*VLA T * SPHT/QLAT</td><td>TNEW=TLAT+VLAT -(TLAT+VLAT-TB 4)*QLAT/(VLAT*S PHT)+(TNEW-TB 4)</td></tr>
<tr><td colspan="4">End</td></tr>
</table>

SUBROUTINE SETTEMP		
Define Common Blocks		
Dimension TEMP (IX, IY, IZ)		
Do 100 I=1, IX, Do 100 J=1,IY, Do 100 K=1,IZ		
TEMP (I,J,K)=TEMPA		
END		
SUBROUTINE POWDIST		
Define Common Blocks		
Dimension POWER (IX, IY)		
DELTA2=DELTA**2, RB2=(RBEAM**2)*16, POT=0.0		
Do 100 K=1, IX, Do 100 I=1, IY		
RSQD=((K-KI)**2+(I-1)**2)*DELTA2		
IF RSQD < RB2		
T		F
X1=FLOAT(K-KI)-0.5)*DELTA, X2=X1+DELTA, Y1=(FLOAT(I-1)-0.5)*DELTA, Y2=Y1+DELTA		POWER (K, I)=0.0
Call FUNCTION POWERIN (POWERIN is a variable calculated for use in this subroutine)		
AVPOW=POWERIN(X1, X2, Y1, Y2), POWER(K, I)=AVPOW/DELTA2		
IF I > 1		
T	F	
POT=POT+AVPOW	POT=POT+AVPOW/(2.0)	
Write to data file, POT*2.0		
END		

Appendix B

Operating Parameters for LTH

Sample	Power	Speed	Diam.	P/vd	t_i
.25A1	1730	12.0	5.0	28.9	0.42
.25A2	1690	20.0	5.0	16.9	0.25
.25A3	1640	50.0	5.0	6.6	0.10
.25B1	1730	60.0	5.0	5.8	0.08
.25B2	1690	55.0	5.0	6.2	0.09
.25B3	1370	50.0	5.0	5.5	0.10
.25C1	1450	30.0	5.0	9.7	0.17
.25C2	1450	40.0	5.0	7.2	0.13
.25C3	1480	45.0	5.0	6.6	0.11
.5A1	1480	30.0	5.0	9.9	0.17
.5A2	1490	40.0	5.0	7.5	0.13
.5A3	1480	50.0	5.0	5.9	0.10
.5B1	1411	52.0	5.0	5.4	0.10
.5B2	1440	55.0	5.0	5.3	0.09
.5B3	1490	58.0	5.0	5.1	0.09
.5C1	1410	50.0	5.0	5.6	0.10
.5C2	1390	45.0	5.0	6.2	0.11
.5C3	1390	40.0	5.0	6.9	0.13
.75A1	1380	30.0	5.0	9.2	0.17
.75A2	1440	25.0	5.0	11.5	0.20
.75A3	1410	30.0	5.0	9.4	0.17
.75B1	1430	32.0	5.0	9.0	0.16
.75B2	1540	35.0	5.0	8.8	0.14
.75B3	1360	28.0	5.0	9.7	0.18
.75C1	1550	35.0	5.0	8.9	0.14
.75C2	1510	38.0	5.0	7.9	0.13
.75C3	1560	40.0	5.0	7.8	0.13
1.0A1	1510	35.0	5.0	8.6	0.14
1.0A2	1520	30.0	5.0	10.1	0.17
1.0A3	1470	25.0	5.0	11.8	0.20
1.0B1	1530	20.0	5.0	15.3	0.25
1.0B2	1530	10.0	5.0	30.6	0.50
1.0B3	1520	5.0	5.0	60.7	1.00
1.5A1	1450	5.0	5.0	58.2	1.00
1.5A2	1500	10.0	5.0	30.1	0.50
1.5A3	1420	8.0	5.0	35.5	0.63

All of above were En52 pretreated using excimer laser at the speed indicated in the sample name e.g. .75A3 represents a sample treated at .75mm/s.
Laser used = Laser Ecosse AF5L. Focussing system = off axis parabolic mirror.

Sample	Power	Speed	Diam.	P/vd	t_1
.25A1	1550	45.0	5.0	6.9	0.11
.25A2	1540	45.0	5.0	6.8	0.22
.25A3	1510	40.0	5.0	7.6	0.13
.25B1	1490	40.0	5.0	7.4	0.13
.25B2	1520	40.0	5.0	6.7	0.11
.25B3	1490	50.0	5.0	6.0	0.10
.25C1	1450	55.0	5.0	5.3	0.09
.25C2	1440	52.0	5.0	5.5	0.10
.25C3	1520	45.0	5.0	6.8	0.11
.5A1	1400	45.0	5.0	6.2	0.11
.5A2	1420	40.0	5.0	7.1	0.13
.5A3	1460	42.0	5.0	7.0	0.12
.5B1	1440	48.0	5.0	6.0	0.10
.5B2	1490	50.0	5.0	6.0	0.10
.5B3	1460	55.0	5.0	5.3	0.09
.5C1	1390	55.0	5.0	5.1	0.09
.5C2	1410	52.0	5.0	5.4	0.10
.5C3	1390	50.0	5.0	5.6	0.10
.75A1	1470	45.0	5.0	6.5	0.11
.75A2	1410	40.0	5.0	7.1	0.13
.75A3	1570	43.0	5.0	7.3	0.12
.75B1	1510	48.0	5.0	6.3	0.10
.75B2	1500	50.0	5.0	6.0	0.10
.75B3	1580	52.0	5.0	6.1	0.10
.75C1	1590	45.0	5.0	7.1	0.11
.75C2	1590	50.0	5.0	6.4	0.10
.75C3	1610	55.0	5.0	5.9	0.09
1.0A1	1550	45.0	5.0	6.9	0.11
1.0A2	1590	48.0	5.0	6.6	0.10
1.0A3	1550	50.0	5.0	6.2	0.10
1.0B1	1650	50.0	5.0	6.6	0.10
1.0B2	1650	55.0	5.0	6.0	0.09
1.0B3	1630	55.0	5.0	5.9	0.09
1.5A1	1640	45.0	5.0	7.3	0.11
1.5A2	1680	55.0	5.0	6.1	0.09
1.5A3	1600	50.0	5.0	6.4	0.10
.15A1	1600	55.0	5.0	5.8	0.09
.15A2	1530	50.0	5.0	6.1	0.10
.15A3	1520	45.0	5.0	6.7	0.11

All of above were En24 pretreated using excimer laser at the speed indicated in the sample name e.g. .75A3 represents a sample treated at .75mm/s.

Laser used = Laser Ecosse AF5L. Focussing system = off axis parabolic mirror

Sample	Power	Speed	Diam.	P/vd	t_i
CG1/1	1690	20.0	6.0	14.1	0.30
CG1/2	1690	10.0	6.0	28.2	0.60
CG1/3	1690	5.0	6.0	56.3	1.20
CG1/4	1690	7.0	6.0	40.2	0.86
CG1/5	1690	9.0	6.0	31.3	0.67
CG2/1	1690	12.0	6.0	23.5	0.50
CG2/2	1690	10.0	6.0	28.2	0.60
CG2/5	1690	14.0	6.0	20.1	0.43
SB1/1	1670	10.0	6.0	27.8	0.60
SB1/2	1670	8.0	6.0	34.8	0.75
SB1/3	1670	6.0	6.0	46.4	1.00
SB1/4	1670	8.0	6.0	34.8	0.75
SB2/1	1630	10.0	6.0	27.2	0.60
SB2/2	1630	7.0	6.0	38.8	0.86
SB2/3	1630	5.0	6.0	54.3	1.20
SB2/4	1630	9.0	6.0	30.2	0.67

All of above are En52, treated with DAG colloidal graphite (prefix CG) or grit blasted (SB). Laser used = BOC control. Focussing system = off axis parabolic mirror.

Sample	Power	Speed	Diam.	P/vd	t_i
CG1/3	1490	10.0	6.0	24.8	0.60
CG1/4	1490	15.0	6.0	16.6	0.40
CG1/5	1500	5.0	6.0	50.0	1.20
CG1/6	1500	5.0	6.0	50.0	1.20
CG2/1	1480	4.0	6.0	61.7	1.50
CG2/2	1480	6.0	6.0	41.1	1.00
CG2/3	1480	8.0	6.0	30.8	0.75
CG2/4	1480	2.0	6.0	123.3	3.00
SB1/1	1510	10.0	6.0	25.2	0.60
SB1/2	1510	10.0	6.0	25.2	0.60
SB1/3	1470	12.0	6.0	20.4	0.50
SB1/4	1460	8.0	6.0	30.4	0.75
SB2/1	1410	14.0	6.0	16.8	0.43
SB2/2	1530	12.0	6.0	21.3	0.50

SB2/3	1510	14.0	6.0	18.0	0.43
SB2/4	1510	16.0	6.0	15.7	0.38
SB2/5	1510	18.0	6.0	14.0	0.33

All of above are En52, treated with DAG colloidal graphite (prefix CG) or grit blasted (SB). Laser used = BOC control. Focussing system = off axis parabolic mirror.

Sample	Power	Speed	Diam.	P/vd	t_1
P1D1/1	1400	5.0	3.5	80.0	0.70
P1D1/2	1400	10.0	3.5	40.0	0.35
P1D1/3	1400	25.0	3.5	16.0	0.14
P1D1/4	1400	50.0	3.5	8.0	0.07
P1D1/5	1400	100.0	3.5	4.0	0.04
P2D1/1	1000	5.0	3.5	57.1	0.70
P2D1/2	1000	10.0	3.5	28.6	0.35
P2D1/3	1000	25.0	3.5	11.4	0.14
P2D1/4	1000	50.0	3.5	5.7	0.07
P2D1/5	1000	100.0	3.5	2.9	0.04
P3D1/1	800	5.0	3.5	45.7	0.70
P3D1/2	800	10.0	3.5	22.9	0.35
P3D1/3	800	25.0	3.5	9.1	0.14
P3D1/4	800	50.0	3.5	4.6	0.07
P3D1/5	800	100.0	3.5	2.3	0.04
P1D2/1	1400	5.0	5.5	50.9	1.10
P1D2/2	1400	10.0	5.5	25.5	0.55
P1D2/3	1400	25.0	5.5	10.2	0.22
P1D2/4	1400	50.0	5.5	5.1	0.11
P1D2/5	1400	100.0	5.5	2.5	0.06
P2D2/1	1000	5.0	5.5	36.4	1.10
P2D2/2	1000	10.0	5.5	18.2	0.55
P2D2/3	1000	25.0	5.5	7.3	0.22
P2D2/4	1000	50.0	5.5	3.6	0.11
P2D2/5	1000	100.0	5.5	1.8	0.06
P3D2/1	800	5.0	5.5	29.1	1.10
P3D2/2	800	10.0	5.5	14.5	0.55
P3D2/3	800	25.0	5.5	5.8	0.22

P3D2/4	800	50.0	5.5	2.9	0.11
P3D2/5	800	100.0	5.5	1.5	0.06

All above are En24 DAG colloidal graphite coated. Laser used = Electrox.
Focussing assembly = off axis parabolic.

Sample	Power	Speed	Diam.	P/vd	t_i
24C1	2040	20.0	6.0	17.0	0.30
24C2	2050	20.0	6.0	17.1	0.30
24C3	2040	22.0	6.0	15.4	0.27
24C4	2020	24.0	6.0	14.0	0.25
24C5	2030	26.0	6.0	13.0	0.23

All of above were En24 coated with graphite (oxy-acetylene).
Laser used = Laser Ecosse AF5L. Focussing system = off axis parabolic mirror.

Sample	Power	Speed	Diam.	Motor	Overlap%
1	1050	5.6	5.0	9.08	0
2	1100	5.6	5.0	9.08	0
3	1120	7.8	5.0	9.37	0
4	1230	7.8	5.0	9.37	0
5	1220	7.0	5.0	9.37	10
6	1220	6.2	5.0	9.37	20
7	1210	8.1	5.0	9.37	-5
8	1230	8.5	5.0	9.37	-10
9	1230	9.3	5.0	9.37	-20
10	1210	9.7	5.0	9.37	-25
11	1220	10.1	5.0	9.37	-30
A	1580	6.3	5.0	9.24	0
B	1610	7.8	5.0	9.37	0
C	1580	7.0	5.0	9.37	10
D	1540	6.2	5.0	9.37	20
E	1580	8.1	5.0	9.37	-5
F	1610	8.5	5.0	9.37	-10

G	1550	9.3	5.0	9.37	-20
H	1530	9.7	5.0	9.37	-25
I	1650	10.1	5.0	9.37	-30
J	1660	11.6	5.0	9.37	-50

Above samples are as followed: A-J En24 DAG colloidal graphite coated.

1-11 En52 DAG colloidal graphite coated.

Laser used = Laser Ecosse AF5L. Mirror focussing assembly.

REFERENCES

1. R.D.Mogford and F.A.Ball, Inst.of Mech Eng., A.D.Proc., 1955-56(5), p.147.
2. J.A.Polson, Internal Combustion Engines, J.Wiley & Sons Inc., New York, 1942.
3. W.S.Giles, Fundamentals of Valve Design and Materials Selection, SAE Paper No.: 660471.
4. J.E.Morgan, Inst.of Mech Eng., A.D.Proc., 1955-56(5), p.138.
5. R.P.Worthen and T.N.Tunnecliffe, Temperature Controlled Engine Valves, SAE Paper No.: 320601.
6. R.P.Worthen and D.G.Rauen, Measurement of Valve Temperature and Strain in a Firing Engine, SAE Paper No.: 860356.
7. A.Ball and J.J.Ward, Tribology International, 1986, Butterworth & Co. Ltd.. pp. 347-262.
8. P.Hartley, Design and Components in Engineering, May 7, 1969.
9. Exhaust Valve Steels, Automobile Engineer, March, 1962.
10. S.J.Matthews and P.Crook, Hardfacing Materials and Processes for Valve Applications, Welding Technology for Energy Applications, Oak Ridge Nat. Lab., USA, September 1982, ed. S.A.David and G.M.Slaughter.
11. W.M.Steen, Applied Laser Tooling, ed.M.Perez-Amor, Martinus Nijhoff Publishers, Dordrecht, Netherlands, 1987.
12. P.Pizzi, Applications of Laser Processes in Automobile Production, 1991.
13. W.M.Steen, Metals and Materials, December 1985. pp.730-736.
14. J.F.Ready, Industrial Applications of Lasers, Academic Press , New York, 1978.
15. W.W.Duley, CO_2 Lasers, Effects and Applications, Academic Press, New York, 1976.
16. J.Powell, Ph.D. Thesis, University of London, 1983.
17. Industrial Laser Handbook, ed. D.Belfotre and M.Levitt, Pennwell Books, 1987.
18. T.Bell and H.W.Bergmann, Transformation Hardening of Ferrous Materials, Surface Engineering with Lasers, London, May, 1985.
19. M.Sharp and W.M.Steen, Investigating Process Parameters for Laser Transformation Hardening, Proc. 1st. Int. Conf. on Surface Engineering, paper 34, publ. Welding Institute, Cambridge, 1985.
20. D.M.Roessler, An Introduction to the Laser Processing of Materials, The Industrial Laser Handbook, ed. D.Belforte and M.Levitt, 1986.
21. C.Breck Hitz, Review of Laser Modes, Lasers and Applications, November 1985.
22. M.Sharp, W.M.Steen, P.Henry and G.C.Lim, An Analysis of the Effect of Mode Structure on Laser Material Processing, Proc. Conf. Laser Opto-Electronik, ed. W.Waldelich, Munich 1983.
23. M.Sharp, Ph.D. Thesis, University of London, 1985.
24. V.M.Weerasinghe, Ph.D.Thesis, University of London, 1985.
25. C.Courtney and W.M.Steen, J.Appl.Phys. 17, 1978, pp.303-307.
26. H.Kogelnic and T.Li, Proc. IEEE, 54, 1312, 1966.
27. M.Young, Optics and Lasers, Springer Series in Optical Sciences, 3rd Edition.
28. M.Von Allmen, Laser Beam Interactions with Materials-Physical Principles and Applications, publ.Springer-Verlag, 1987.

29. J.F.Ready, Effects of High Power Laser Radiation, Academic Press, 1971.
30. F.Dausinger, M.Beck, J.H.Lee, E.Meiners, T.Rudlaff and J.Shen, Energy Coupling in Surface Treatment Processes, Proc. Conf. ICALEO 1989, Orlando, 1989.
31. F.Dausinger and T.Rudlaff, Novel Transformation Hardening Technique Exploiting Brewster Absorption, Proc. Conf. LAMP '87, Osaka, May 1987.
32. W.W.Duley, Laser Material Interactions of Relevance to Metal Surface Treatment, Laser Surface Treatment, publ. Martinus Nijhoff Publishers, 1986. pp.3-16.
33. W.O'Neill, Ph.D. Thesis, University of London, 1990.
34. R.Dekumbis, H.Mayer and P. Fernandez, A Fast Experimental Method of Measuring Laser Beam Absorption as a Function of Temperature in Solids, Proc. 3rd. Int. Conf. on Lasers (iitt), Kongresshaus, Zurich 1987.
35. G.Stern, Absorptivity of cw CO_2, CO and YAG Laser Beams by Different Metallic Alloys, Proc. Conf. ECLAT '90, Erlangen, Germany, September 1990.
36. W.W.Duley, Laser Processing and Analysis of Materials, Plenum Press, New York, 1983.
37. W.M.Steen, Laser Surface Cladding and Alloying, Industrial Laser Handbook, 1986.
38. A.D.Mclachlan and L.B.Whitburn, J.Appl.Phys., 53(6), 4038, 1982.
39. H.G.Dreeshen et al, J.Appl.Phys., 56, 238, 1984.
40. W.O'Neill and W.M.Steen, Mixed Wavelength Processing, SPIE Vol.957, Laser Beam Treating and Coating, 1988.
41. G.Kinsman and W.W.Duley, Excimer Laser-Induced Oxidation and Roughening of Metal Surfaces, SPIE Vol.957, Laser Beam Treating and Coating, 1988.
42. G.Herziger, Physics of Laser Materials Processing, SPIE Vol650, High Power Lasers and Their Industrial Applications, 1986.
43. A.R.Lansdown and A.L.Price, Materials to Resist Wear-A Guide to their Selection and Use, Pergamon Press, 1986.
44. T.S.Eyre, Wear Mechanisms, Symp. of the Condition Monitoring Grp. of NDT, Wear Diagnosis in Internal Combustion Engines, Brunel University, January 1981.
45. D.Godfrey, Diagnosis of Wear Mechanisms, Wear Control Handbook, pp.283-311, Am.Soc.Mech Eng., 1980.
46. Wear Resistant Surfaces in Engineering-a guide to their production, properties and selection, Department of Trade and Industry, HMSO Publications, 1986.
47. T.S.Eyre, Wear Characteristics of Metals, Tribology Int., Vol.9, Oct. 1976.
48. E.Rabinowicz, Wear Coefficients-Metals, Wear Control Handbook, pp.475-506, Am.Soc Mech.Eng., 1980.
49. J.F.Archard, J.Appl.Phys., 24, p.981, 1953.
50. S.Jahanmir, Onthe Wear Mechanisms and the Wear Equations, Pro. Int.Conf., Fundamentals of Tribology, Cambridge, USA, 1980. Ed. N.P.Suh and N.Saka.
51. P.Monson, Ph.D. Thesis, University of London, 1988.
52. F.Borik, Metallurgy of Ferrous Materials for Wear Applications, Wear Control Handbook, Am.Soc.Mech.Eng., 1980.
53. G.Steven and J.P.Caitlin, Journal of Materials, Vol.1, No.2, June 1966, p.293.

54. The Metals Handbook, 9th Edition, ASM, 1983.
55. W.Glaeser, Wear Resistant Materials, Wear Control Handbook, pp.313-325, Am.Soc. Mech.Eng., 1980.
56. W.L.Silence, Effect of Structure on Wear Resistance of Co-, Fe- and Ni-base Alloys, Proc. Conf. Wear of Materials, ASME, New York, 1977. pp.77-85.
57. K.C.Antony, J.Metals, February 1983. pp.52-60.
58. A.Abbas, Ph.D.Thesis, University of London,1990.
59. P.J.E.Monson and W.M.Steen, Laser Hardfacing/Cladding, Proc.Conf. ECLAT '86, Bad Neuheim, 1986.
60. E.Lugscheider and B. Oberlander, Rapidly Solidified Ni-base Hard Alloys Produced by Laser Treatment, 3rd. Int. Conf. on Surface Modification Technologies, Neuchatel, September 1989.
61. E.Eiholzer, C.Cusano and J.Mazumder, Wear Properties of Laser Alloyed and Clad Fe-Cr-Mn-C Alloys, Proc. Conf. ICALEO 1984, Boston 1984. pp.159-167.
62. E.Lugscheider and H.Bolender, Laser Cladding for Wear and Corrosion Protection, Proc. Conf. ECLAT '90, Erlangen, Germany, September 1990.
63. T.R.Tucker, A.H.Clauer, I.G.Wright and J.T.Shopki, Laser Processed Composite Metal Cladding for Slurry Erosion Resistance, Thin Solid Films, 118, 1984. pp. 73-84.
64. R.Dekumbis, Use of the Laser in Coating Technology, Sulzer Technical Review, January, 1990. pp.27-29.
65. K.P.Cooper and J.D.Ayers, Laser Melt-Particle Injection Processing, Surface Engineering, Vol.1,4, 1985. pp.263-272.
66. A.Schubler and K.H.Zum-Gahr, Incorporation of TiC/TiN Hard Particles into Steel Surfaces using Laser Radiation, Proc.Conf. ECLAT'90, Erlangen, Germany, 1990.
67. J.D.Ayers, Particulate Composite Surfaces by Laser Processing, Proc. of Symp., 10th AIME Annual Meeting, Chicago, Illinois, February 1981. pp.115-125.
68. T.Puig, M.Cantarel and M.Condat, Surface Hardening by Precipitation of Chromium Carbides after Laser Beam Treatment of Ni-Cr Substrate, Proc. 3rd. Int. Conf. on Surface Modification Technologies, Neuchatel, 1989.
69. A.Belmondo and M.Castagna, Wear Resistant Coatings by Laser Processing, Thin Solid Films, Vol.64, 1979. pp.249-256.
70. G.Abbas and D.R.F.West, Laser Surface Cladding of Stellite and Stellite-SiC Composite Deposits for Enhanced Hardness and Wear, to be published in Wear.
71. G.Abbas and D.R.F.West, Wear Studies of Variable Composition Stellite-SiC Laser Clad Deposits, Proc. Conf. ICALEO '89, Orlando, 1989.
72. M.Karlsson Gabel and D.Donovan, Wear Resisitant Coatings and Treatments, Wear Control Handbook, pp.343-371, Am.Soc.Mech.Eng., 1980.
73. Speich et al, Trans. Metallurgical Soc. of AIME, Vol.245, May, 1969, p.1063.
74. J.F.Miller and J.A.Wineman, Laser Hardening at Saginaw Steering Gear, Metal Progress, 111, no.5, 38.
75. V.G.Gregson, Laser Heat Treatment, Vol.3, Laser Materials Processing, ed. M.Bass, North Holland, Amsterdam, 1983.
76. T.Bell, Surface Heat Treatment of Steel to Combat Wear, Metallurgia, 49(3),

pp.103-111, March 1982.
77. W.M.Steen, Laser Surface Cladding, Proc. Indo-US Workshop on Principles of Solidification and Materials Processing, Hyderabad, India, publ. ONR, AIBS, 1988.
78. W.M.Steen, V.M.Weerasinghe and P.Monson, Some Aspects of the Formation of Laser Clad Tracks, Proc. SPIE Conf., Innsbruck, Austria, April 1986. Publ. SPIE, PO Box 10, Bellingham, Washington, vol.650, pp.226-234.
79. J-Y.Jeng, Ph.D. Thesis, University of Liverpool, 1992.
80. T.Takeda, W.M.Steen and D.R.F.West, Laser Cladding with Mixed Powder Feed, Proc. Conf. ICALEO '84, Boston 1984.
81. J.Kusinski, Metallurgical Transactions A, Vol.19A, February 1988, p.377.
82. G.Christodoulou, P.Henry and W.M.Steen, Proc. 4th Int.Conf. on Rapidly Quenched Metals, Sendai, 1981.
83. Z.D.Chen, Ph.D. Thesis, University of London, 1987.
84. J.D.Ayers and K.P.Cooper, Laser Melt Particle Injection Processing, Surface Eng. with Lasers, London, May 1985.
85. J.Fournier, R.Fabbro, J.L.Strudel and D.Ayrault, Proc. Conf. LAMP, Osaka,1987.
86. H.W.Bergmann and E.Schubert, Proc. 2nd Int. Seminar -Surface Eng. with High Energy Beams, ed. CEMUL, Lisbon, Portugal, 1989.
87. J.D.Ayers and R.J.Schaefer, Consolidation of Plasma Sprayed Coatings by Laser Remelting, SPIE vol.198, Laser Applications in Materials Processing, 1979, pp.57-64.
88. The Metals Handbook, Desk Edition, ASM, 1991.
89. T.Bell, Survey of Surface Hardening Processes, Proc. Conf. on Surface Hardening, Lanchester Polytechnic, June 1972.
90. Steel and It's Heat Treatment, Bofors Handbook, K.E.Thelning, Butterworths, 1975.
91. H.C.Child, Surface Hardening of Steel, Engineering Design Guides, 37, OUP, 1980.
92. J.E.Jenkins, Some Factors that Influence Electron Beam Hardening, Heat Treating, December 1981.
93. A.J.Hick, Advances in Surface Heat Treatments, Proc. 1st. Int. Conf. on Surface Engineering, Brighton, England, June 1985.
94. R.Zenker, Materials Aspects of Surface Modification by Electron Beams and Industrial Applications Today, Proc. Conf. ECLAT '90, Erlangen, Germany, September 1990.
95. P.A.Dearnley and T.Bell, Surface Engineering, Vol.1, No.3, pp.203-216, 1985.
96. W.M.Matlock, J.F.Kocis and E.T.Vitcha, Plasma-Arc Hardfacing Exhaust Valves with an Iron Base Alloy, Metal Progress, May 1978.
97. E.Seekins, A.E.Valves, Personal Communication.
98. E.C.Bain and H.W.Paxton, Alloying Elements in Steel, ASM, 2nd edition, 1961.
99. V.G.Rivlin, Int. Metals Reviews, Vol.29, no.4, 1984. pp.299-326.
100. R.Lundberg, M.Waldenstrom and B.Uhrenius, CALPHAD, Vol.1, no.2, 1977, publ.Pergammon Press, Great Britain. pp.159-199.
101. W.D.Forgeng and W.D.Forgeng Jr., C-Cr-Fe Ferrous Ternary System, Metals

Handbook, 9th Edition, ASM, 1983.
102. H.J.Goldschmidt, J.I.S.I., 163, December 1949. pp.381-387.
103. J.M.Vitek and R.L.Klueh, Metallurgical Transactions A, Vol.14A, June 1983. pp.1047-1055.
104. G.Krauss, Principles of Heat Treatment of Steel, A.S.M., 1980.
105. G.A.Roberts and R.F.Mehl, Transactions ASM, Vol.31, 1943. pp.613-650.
106. M.A.Grossman and E.C.Bain, Principles of Heat Treatment, 5th Edn.,ASM, USA, 1964.
107. F.D.Seaman, Laser Heat-Treating, Industrial Laser Handbook, ed. D.Belforte, M.Levitt, 1986.
108. L.Karmazin, Materials Science and Eng., A142, 1991. pp.71-77.
109. H.W.Paxton, The Formation of Austenite,
110. C.I.Garcia and A.J.DeArdo, Formation of Austenite in Low-Alloy Steels,
111. G.R.Speich, A.Szirmae and R.M.Fisher, Advances in Electron Metallography, Vol.6, ASTM-STP 396, 1966. pp.97-114.
112. S.F.Dirnfield, B.M.Korevaar and F.Van't Spijker, Metallurgical Transactions, Vol.5, June 1974. pp.1437-1444.
113. R.R.Judd and H.W.Paxton, TMS-AIME, Vol.242, February 1968. pp.206-215.
114. J.E.Pavlick, W.W.Mullins and H.W.Paxton, Trans.AIME, 236, 85, 1966.
115. J.Agren, H.Abe, T.Suzuki and Y.Sakuma, Metallurgical Transactions A, Vol.17A, April 1986. pp.617-620.
116. U.R.Lenel and R.W.K.Honeycombe, Metal Science, Vol.18, April 1984. pp.201-205.
117. A.W.Bowen and G.M.Leak, Metallurgical Transactions, Vol.1, June 1970, p.1695.
118. M.Hillert, K.Nilsson and L.E.Torndahl, J.I.S.I., January 1971. pp.49-66.
119. F.V.Nolfi Jr., P.G.Shewmon and J.S Foster, Metallurgical Transactions, Vol.1, August 1970. pp.2291-2298.
120. M.Nemoto, Metallurgical Transactions A, Vol.8A, March 1977. pp.431-437.
121. J.M.Beswick, Metallurgical Transactions A, Vol.18A, November 1987. p.1897.
122 J.R.Bradley and S.Kim, Scripta Metallurgica, Vol.23, 1989. pp.131-136.
123. J.R.Bradley and S.Kim, Metallurgical Transactions A, Vol,19A, August 1988. pp.2013-2025.
124. J.S.Kirkaldy, B.A.Thompson andE.A Baganis, Hardenability Concepts with Applications to Steel, TMS-AIME, Warrendale, PA, 1978.
125. G.Palombarini and G.Sambogna, J.Materials Science, V0l.26, 1991. pp.3396-3399.
126. G.A.Chadwick, Metallography of Phase Transformations, publ.Butterworths, 1972.
127. R.W.K.Honeycombe, Steels:Microstructure & Properties, publ.Edward Arnold, 1982.
128. G.Ricciardi and M.Cantello, SPIE, Vol.957, Laser Beam Surface Treatment and Coating, 1988.
129. A.Camoletto, G.Molino and S.Talentino, Materials and Manufacturing Processes, 6(1), 1991. pp.53-65.
130. M.Lovene and M.Everett, Development of a Laser Cladding Process for Shrouded Turbine Blades, SAE Paper, 892300.

131.J.Bach, R.Damaschek, E.Geissler and H.W.Bergmann, Proc. Conf. ECLAT'90, Erlangen, Germany, 1990.
132.R.Menin, E.Ramous and M.Magrini, Proc. 4th. Int. Conf. on Rapidly Quenched Materials, Sendai, 1981. pp.193-196.
133.P.Ding, Z.Zou and H.Yin, Proc. 2nd Int. Seminar-Surface Eng. with High Energy Beams, ed.CEMUL, Lisbon, Portugal, 1989.
134 W.M.Steen and C.Courtney, Metals Tech., December 1979. pp.456-462.
135. S. Mandziej, M.C. Seegers, J. Godijk, Effect of Laser Heating on Substructure of 0.4%C Steel, Materials Science and Technology, Vol. 5, April 1989, pp 350-355.
136.D.S.Gnanamathu, Cladding: US Patent No.: 3,952,180. 1976.
137.S.J.Matthews, Laser Fusing of Hard-facing Alloy Powders, Proc. Conf. ASM-Lasers in Materials Processing, 1983.
138.W. M. Steen, and C. Courtney, Surface Coating Using a 2kW CO2 Laser, Proc. Conf. Laser `79, Munich, Germany. 1979.
139.J. Powell and W.M. Steen,Heat and Mass transfer in Laser Cladding, Proc. Conf. Manufacturing and Materials Processing, Dubrovnik, Yugoslavia, 1990.
140.J. Clarke, L. Tapia-Villanueva, W.M. Steen, Report to BSC Scottish labs, Imperial College, University of London 1979.
141.Rolls Royce, personal communication.
142.R.M.Macintyre, Laser Hard-Surfacing of Turbine Blade Shroud Interlocks, Proc. Conf. ASM-Lasers in Materials Processing, 1983.
143.V. Weerasinghe and W.M. Steen, Laser Cladding by Blown Powder Injection, Proc. Conf. LIM1, Lasers in Manufacturing, Brighton, U.K. 1983.
144.T.R. Tucker, A.H. Clauer, I.G. Wright, J.T. Stropki, Thin Solid Films, 118, 1984, pp73-84.
145.P.J.E. Monson, W.M. Steen and D.R.F. West, Rapid Allot Scanning by Variable Composition Laser Cladding, Proc. Conf. LAMP `87, Osaka, Japan, 1987.
146.W.M. Steen, Laser Cladding, Alloying and Melting, Industrial Laser Handbook, 1986, pp158-174.
147.L.Li, Ph.D. Thesis, University of London, 1989
148.L.Li, W.M.Steen and R.D.Hibberd, Computer Aided Laser Cladding, Proc.Conf. ECLAT'90, Erlangen, Germany, 1990.
149.Caterpillar Tractor Co., Method and Apparatus for Fusibly Bonding a Coating Material to a Metal Article, U.S. Patent No.: 1,482,044. 1977.
150.A.G.Grigor-Yants, Weld Prod. USSR, Vol.32, No.8, 1985. pp. 11-13.
151.F. Kupper, A. Gasser, K. Wissenbach, E.W. Kreutz, Cladding of Valves with CO2 Laser Radiation, Proc. Conf. ECLAT `90, Erlanger, Germany, 1990.
152.A.A.Mangalay, M.A.Everett and A.H.Hammeke, Laser coating Technology: a commercial reality, SPIE Vol.957, Laser Beam Surface Treating and Coating, 1988.
154.J.Hernandez, A.Vannes, J.Com-Nougue and E.Kerrand, Laser Surface Cladding and Residual Stresses, proc.Conf. LIM 3, 1986.
155.M.Pilloz, C.Sahour and A.B.Vannes, Proc. 2nd Int. Seminar-Surface Eng. with High Energy Beams, ed. CEMUL, Lisbon, Portugal, 1989.
156.A.B.Vannes, J.Hernandez and L.Maiffredy, Proc. Conf. LAMP'87, Osaka, May

1987. pp.371-376.
157. Fletcher book
158. B.Scholtes and B.L.Mordike, Proc. 2nd Int. Seminar-Surface Eng. with High Energy Beams, ed. CEMUL, Lisbon, Portugal, 1989.
159. J.Barralis, G.Mathieu, G.Barreau and L.Castex, Proc.2nd Int. Seminar-Surface Eng.with High Energy Beams, ed.CEMUL, Lisbon, Portugal, 1989.
160. G.C.Lim and W.M.Steen, Optical and Laser Technology, June 1982, publ. Butterworth and Co.. pp.149-153.
161. W.M.Steen and V.M.Weerasinghe, SPIE, Vol.668, Laser Processing: Fundamentals, Applications and Systems Engineering, 1986. pp.37-43.
162. E.Beyer, A.Donges, P.Loosen and G.Herziger, Proc. 6th. Int. Conf. Opto-Electronik, 1983. publ. Gerlin:Springer, 1984.
163. R.D.Rawlings and W.M.Steen, Optics and Lasers in Engineering, Vol.2, 1981. pp.173-188.
164. T.Rudlaff and F.Dausinger, Proc. Conf. ECLAT'90, Erlangen, Germany, 1990.
165. W.P.O.Juptner, R.Becker and G.Sepold, SPIE, Vol.957, Laser Beam Surface Treating and Coating, 1988. pp.82-85.
166. E.Nakamura, S.Kimura, M.Sasaki, M.Nishio, J.Kinoshita and M.Hoshina, Proc. Conf. ICALEO'84, Boston 1984. pp.261-268.
167. M.Melander and Y.Chang, Surface Engineering, Vol.1(4), 1985. pp.273-281.
168. V.Rubruck, E.Geissler and H.W.Bergmann, Proc. Conf. ECALAT'90, Erlangen, Germany, 1990.
169. E.Geissler and H.W.Bergmann, Proc.2nd Int. Seminar-Surface Eng.with High Energy Beams, ed.CEMUL, Lisbon, Portugal, 1989.
170. H.W.Bergmann and E.Geissler, Proc. Conf. ECLAT'90, Erlangen, Germany, 1990.
171. A.Drenker, E.Beyer, L.Boggering, R.Kramer and K.Wissenbach, Proc. Conf. ECLAT'90, Erlangen, Germany, 1990.
172. H.R.Shercliff and M.F.Ashby, Master Plots for Predicting the Case-Depth in Laser Surface Treatments, Eng. Dept., Cambridge University, October 1986. Doc.: CUED/C-Mat./TR134.
173. H.R.Shercliff and M.F.Ashby, The Prediction of Case Depth in Laser Transformation Hardening, Eng. Dept., Cambridge University, September 1989. Doc.: CUED/C-Mat./TR169.
174. D.Rosenthal, Trans. ASM, November 1946. pp.849-866.
175. H.E.Cline and T.R.Anthony, J.Appl.Phys., Vol.48 (9), September 1977.
176. Conduction of Heat in Solids, H.S.Carslaw and J.C.Jaeger, 2nd Edition, OUP, 1959.
177. M.F.Ashby and K.E.Easterling, Acta Metall., Vol.32 (11), 1984. pp.1935-1948.
178. N.Rykalin, A.Uglov and A.Kokora, Laser Machining and Welding, Chapter 3, publ. Pergammon Press, Oxford. 1978.
179. M.Bass, Physical Processes in Laser-Material Interactions, Chapter3, Plenum Press, New York, 1983. ed. M.Bertolotti.
180. H.R.Shercliff, J.C.Ion and M.F.Ashby, Process Models for Laser Surfcae Treatment, 1990, not published.
181. W.M.Steen, Ph.D.Thesis, University of London, 1976.

183. P.J.Oakley, Applications of Laser Processes in Automobile Production, 1991.
184. Powder Diffraction File, Inorganic Phases, (JCPDS), International Centre for Diffraction Data, PA, USA, 1989.
185. R.W.G.Wyckoff, Crystal Structures, 2nd edn., Vol.2, Interscience publ., J.Wiley and Sons, N.Y., 1963.
186. F.C.J.Fellowes, Ph.D.Thesis, University of Liverpool, 1991.
187. ASM Handbook, Heat Treatment, ASM, 1990.
188. A.Mulot and J.P.Badeau, Trait.Therm., Vol.136, 489, 1979.
189. W.J.Feuerstein and W.K.Smith, Elevation of critical temperatures in steel by high heating rates, Trans. ASM, Vol.46, 1954, pp.1270-1284.
190. D.A.Porter and K.E.Easterling, Phase Transformations in Metals and Alloys, publ. Van Nostrand Reinhold, 1981.
191. D.R.Bury, Ph.D. Thesis, University of Cambridge, 1985.
192. E.Ramous, L.Giordano, G.Principi and A.Tiziani, Mat. Res. Symp. Proc. Vol.21, 1984.
193. D.Turnbull, Metallurgical T.A., Vol.12A, 695, 1981.
194. H.Bande, G.L.Esperance, M.U.Islam and A.K.Koul, Materials Science and Tech., Vol.7, May 1991.
195. Centre d'information du Cobalt, Cobalt Monograph, Brussels, Belgium, `60.
196. K. Williams, MSc.(Eng.) Dissertation, Liverpool University, 1990.
197. J. Mazumder, A. Car, Journal of Metals, Feb. 1987, pp18-23.
198. M.C. Flemmings, Solidification Processing, Mcgraw Hill, London, 1974.
199. J. Mazumder, Laser Heat Treatment, The State of the Art, Journal of Metals, May 1983, pp19-21.
200. R. Mehraban, Rapid Solidification of Metals and Alloys, Monograph No.8., Institute of Metals, London 1982.
201. B.H. Kear, E.M. Breinan, L.E. Greenwald, Met. Tech., Vol. 6, 1979, pp121.